

Doctoral thesis

Doctoral theses at NTNU, 2020:408

Katie McCay

# Tin and Tin Alloys for Low Cost Bipolar Plates in PEM Fuel Cells

**NTNU**  
Norwegian University of Science and Technology  
Thesis for the Degree of  
Philosophiae Doctor  
Faculty of Natural Sciences  
Department of Materials Science and Engineering



Norwegian University of  
Science and Technology



Katie McCay

# **Tin and Tin Alloys for Low Cost Bipolar Plates in PEM Fuel Cells**

Thesis for the Degree of Philosophiae Doctor

Trondheim, December 2020

Norwegian University of Science and Technology  
Faculty of Natural Sciences  
Department of Materials Science and Engineering



Norwegian University of  
Science and Technology

**NTNU**

Norwegian University of Science and Technology

Thesis for the Degree of Philosophiae Doctor

Faculty of Natural Sciences

Department of Materials Science and Engineering

© Katie McCay

ISBN 978-82-471-9726-4 (printed ver.)

ISBN 978-82-471-9984-8 (electronic ver.)

ISSN 1503-8181 (printed ver.)

ISSN 2703-8084 (online ver.)

Doctoral theses at NTNU, 2020:408

Printed by NTNU Grafisk senter

# Preface

This thesis has been submitted to the Norwegian University of Science and Technology, NTNU, in partial fulfilment of the requirements for the academic degree Philosophae Doctor.

This thesis is the result of work performed between August 2016 and August 2020 at the Department of Materials Science and Engineering, NTNU. The work has been supervised by Professor Frode Seland and Associate Professor Hilde Lea Lein of NTNU, and Dr. Ole Edvard Kongstein and Dr. Sigrid Lædre of SINTEF.

The project has been funded by the Department of Materials Science and Engineering at NTNU.

All experimental work described in this thesis, with the exception of chapter 8.3, was performed by the author. The experimental work in chapter 8.3 was performed by bachelor students Amrinder Pal Singh Dhillon, Chido Nnoli, and Ruben Gran Nykaas, under the supervision of Katie McCay.

Parts of this thesis have been published, with the scientific papers included in Appendix A. The author of this thesis has been the main contributor to the scientific paper, although all co-authors were involved with the supervision and writing of the manuscript.

Trondheim, 9th October, 2020

Katie McCay



# Acknowledgements

I would first like to thank my late supervisor Dr Ole Edvard Kongstein. This whole thesis was born from his crazy and brilliant idea, and I am honoured that he trusted me to make it a reality. His enthusiasm for the project has been so encouraging and motivating, and I will always remember both his scientific insights which have been so valuable, and how he always knew how to lighten the mood with celebratory pastries and talk of Pokémon Go. Thank you for everything, Ole Edvard.

Thank you to my main supervisor, Professor Frode Seland. Working with you for the past four years has been a lot of fun, and I have learnt so much from you. Our collaborations on the CANOPENER project have been really interesting and I appreciate you giving me that opportunity. Your feedback has always been very thorough, and I appreciate all the time you've dedicated to helping me in this work. I hope we will be able to collaborate again in the future. And finally, I apologise for all the sarcastic comments about the cleanliness of your desk.

I would also like to thank my co-supervisor Dr Sigrid Lædre for her help and guidance throughout my PhD. You've been a wonderful combination of expertise on both bipolar plates and dealing with numerous supervisors, and I appreciate your friendship and moral support. Right at the beginning of my PhD, I was told that I was the "next Sigrid", and I hope I've managed to live up to that!

Finally, thank you to my co-supervisor Associate Professor Hilde Lea Lein. You have always been so positive and supportive towards my work, as well as providing useful feedback during the writing process, and I am very grateful for that.

Together I think we've made a great team!

My journey towards this thesis did not start when I began my PhD studies, but when I first arrived in Trondheim in August 2014 to begin an industrial placement at SINTEF. I would like to thank those people who have been here since the beginning, when I was just a master's student and barely knew what a fuel cell was. A lot has changed since then, but I would like to thank everyone at SINTEF for providing such a welcoming environment, encouraging me to come back to Norway for my PhD and eventually becoming the colleagues who provide such a welcome respite from the frustrations of working with fuel cell test stations.

I would also like to thank all my friends, both here in Trondheim and elsewhere, for their support. I have enjoyed every single film night, hiking trip, crafternoon and the many hundreds of cups of tea we've shared. I would particularly like to thank Kjersti for her endless optimism and kindness. You've made my time in Trondheim so wonderful and I will forever be grateful for that.

Thank you to my family, first and foremost for putting up with me going on about how great fuel cells are at every opportunity! Thank you for listening, for all the skype sessions, long flights and short weekends

together. I'm so grateful for your constant support, and although this PhD has brought me geographically further away from you, you have all always been in my thoughts.

Finally, thank you to Gerhard. I am grateful for every one of the adventures and cupsa we've shared. Both throughout my PhD and into the future, there's no one I would rather have by my side.

## Summary

Proton Exchange Membrane (PEM) Fuel Cells are one of the most promising futures for green energy, as they provide a sustainable alternative to combustion engines in vehicles. The bipolar plate (BPP) is a crucial component in the PEM fuel cell, providing mechanical support to the stack as well as ensuring the even flow of reactants into the cell and waste products out of the cell. Additionally, it is an important conductive medium for the transfer of electrons through the stack, and any losses occurring in the BPP will reduce the overall performance of the fuel cell.

Metallic materials for bipolar plates are nowadays favoured for their high conductivity and mechanical strength. However, given the harsh conditions inside a PEMFC, they will form a protective oxide on the surface, which reduces the cell performance over time due to an increase in interfacial contact resistance (ICR). Dissolution of the metal bipolar plate could also result in leaching of harmful metal ions which cause irreversible damage to the membrane. Therefore, metallic BPPs must be coated with a conductive and stable material to increase the lifetime and performance of the fuel cell. The current state of the art coating materials are expensive noble metals or complex multilayer systems.

This thesis explores alternative materials for use as coating materials for BPPs, starting with a new concept of soldering the gas diffusion layer (GDL) to the BPP using metallic tin (Sn). This involves forming a thin layer of Sn on a stainless steel BPP using electrodeposition, and then hot pressing the bipolar plate with the GDL at a temperature close to the melting point of Sn. This process forms excellent conduction pathways through the BPP to the GDL, drastically reducing contact resistance and improving fuel cell performance. The Sn coating will oxidise under the conditions present inside a fuel cell, leading to a protective SnO<sub>2</sub> oxide layer, which should prevent further corrosion whilst maintaining conductivity through the soldered GDL fibres. This soldering process leads to a BPP/GDL system with an excellent performance and longevity inside a fuel cell, using a simple forming method and low-cost materials.

BPPs produced in this way were optimised to give the lowest contact resistance and best corrosion resistance, as judged from electrochemical testing in a simulated PEMFC environment. An optimisation of the deposition and hot pressing was performed and led to the following procedure: A 30 µm thick layer of Sn is electroplated onto a stainless steel BPP using a current density of 15 mA cm<sup>-2</sup>, before hot pressing with a Freudenberg H23 C6 GDL. The sample was hot pressed at a temperature of 230 °C, and a pressure of 0.5 bar for 20 minutes, before being slowly cooled to room temperature. The optimised Sn/GDL BPP was found to perform much better than stainless steel (SS316) alone, with an ICR of 6.5 mΩ cm<sup>2</sup> and 13.2 mΩ cm<sup>2</sup> obtained before and after corrosion testing, respectively. The increase in ICR after electrochemical testing was attributed to the dissolution and precipitation of the Sn to form a SnO<sub>2</sub> layer, which was not completely protective.

Additional modifications to the Sn/GDL system can be made to improve the stability of the protective oxide layer, and the interface between the Sn and the GDL. The first of these tested was the addition of bismuth (Bi) as an alloying element to the Sn layer. The electrodeposition of SnBi layers containing less than 6 % Bi was performed, and these layers were tested in a simulated PEMFC environment. The amount of bismuth and the hot pressing parameters were optimised to produce a SnBi coating containing 4.0 % Bi that was hot pressed with a GDL for 8 minutes and then cooled slowly. Adding more Bi or hot pressing for longer times led to separation of the Sn and Bi phases, which had a detrimental effect on performance. The optimised SnBi/GDL sample exhibited a reduction in corrosion current density, smaller oxidation peaks and a lower ICR after electrochemical testing than the comparable Sn/GDL sample, indicating that the addition of Bi is beneficial for performance.

Indium (In) was also identified as an alloying material due to its low melting point, good conductivity and the stability of its known oxides with Sn, for example, indium tin oxide (ITO) is a well-known transparent conducting oxide. The co-deposition of a SnIn alloy containing less than 10 % In was attempted but proved difficult due to the large difference in deposition potentials. Many different deposition baths, parameters, additives and operating conditions were attempted but a deposit that fit the requirements for use in a PEMFC was not obtained. Hot-dipping of a SnIn melt onto a stainless steel substrate was performed successfully, but the scalability and corrosion resistance of such a coating was unsuitable for testing inside a working fuel cell.

An investigation into the impact of the GDL properties on the Sn/GDL interface was performed. The presence of a hydrophobic treatment on the GDL fibres was preferential as it led to less contact between the Sn and the electrolyte and therefore less oxidation. It was also found that GDLs with stiffer fibres penetrated deeper into the Sn, preserving the conduction pathways and maintaining a low ICR for longer.

The final modification to the Sn/GDL system involved the addition of a carbon nanolayer to the interface between the Sn and the GDL. This was hypothesised to improve the conductivity due to a larger number of contact points. Additionally, carbon is stable in normal PEMFC conditions, and is used in multiple places within PEMFCs, therefore the addition to the BPP could also be beneficial. The presence of a layer of multiwalled carbon nanotubes (MWCNT) with an optimised loading of 0.2 mg cm<sup>-2</sup> mitigated the increased ICR after electrochemical testing, with the elongated shape of the carbon particles being more beneficial than carbon spheres (carbon black) or platelets (graphite).

Three of the different Sn/GDL concept bipolar plates were tested inside a working fuel cell to compare to standard stainless steel and gold coated stainless steel bipolar plates. All three Sn/GDL, SnBi/GDL, and Sn/C/GDL BPPs performed better than stainless steel alone, with a higher cell voltage and lower ICR at all points during the 200 hours (600 drive cycles) of testing. The Sn/GDL performed the best of the three overall, with a lower degradation rate and small increase in ICR after testing. Although the SnBi and Sn/C BPPs performed well over the first 500 cycles, the harsh conditions experienced during the shut down and start-up procedures led to enhanced degradation during the final 100 cycles. It was predicted that the performance of the Sn/GDL BPP would meet and even surpass the performance of the Au coated BPP if cycling were to continue.

Finally, the suitability of the Sn/GDL system on an industrial scale was analysed using a series of guidelines from the US Department of Energy and Argonne National Laboratory. Sn/GDL as a BPP material was found to be a much cheaper alternative to Au coated BPPs, with an estimated cost of 7 \$ / kW compared to over 100 for gold. This is still more expensive than the industrially produced BPPs, which cost around 5 \$ / kW, but with small improvements in performance and large scale production, the Sn/GDL BPP could meet the targets outlined by the US DoE. Additionally, a unique high-throughput joining method to form fuel cell stacks by using the Sn as a solder material is proposed. This would provide a low-cost manufacturing method and inevitably lead to further cost reductions.

Therefore, the results in this thesis show that the novel Sn/GDL concept for BPPs is both high performance and low cost, and represents a promising alternative to traditional coated bipolar plates for use in PEM Fuel Cells.



# Abbreviations

AES	Auger Electron Spectroscopy
ATO	Antimony Tin Oxide
CA	Chronoamperometry
CTAB	Cetyl Trimethyl Ammonium Bromide
CV	Cyclic Voltammetry
BPP	Bipolar Plate
USDoE	United States Department of Energy
ECSA	Electrochemical Catalytic Surface Area
EDS	Energy Dispersive Spectroscopy
EIS	Electrochemical Impedance Spectroscopy
EU	European Union
FCEV	Fuel Cell Electric Vehicle
GDL	Gas Diffusion Layer
GHG	Greenhouse Gas
HSE	Health, Safety and Environment
ICR	Interfacial Contact Resistance
ITO	Indium Tin Oxide
LCD	Liquid Crystal Display
LSV	Linear Sweep Voltammetry
MEA	Membrane Exchange Assembly
MPL	Microporous Layer
MWCNT	Multiwalled Carbon Nanotubes
OCV/P	Open Circuit Voltage / Potential
PBR	Pilling Bedworth Ratio
PEM	Proton Exchange Membrane
PEMFC	Proton Exchange Membrane Fuel Cell
PGM	Platinum Group Metal
PTFE	Poly Tetra Fluoro Ethylene

RHE	Reversible Hydrogen Electrode
SAWM	Simple Additive Weighting Method
SEM	Scanning Electron Microscopy
SHE	Standard Hydrogen Electrode
SS 304	Stainless Steel grade 304
SS 316	Stainless Steel grade 316
XPS	X-Ray Photoelectron Spectroscopy

# Contents

Preface.....	iii
Acknowledgements.....	v
Summary.....	vii
Abbreviations.....	xi
1. Background.....	1
1.1. Motivation.....	1
1.2. Aim of Thesis.....	1
1.3. Outline of Work.....	2
2. Introduction.....	5
2.1. Proton Exchange Membrane Fuel Cells.....	5
2.2. Electrodeposition.....	22
2.3. Tin as a solder material to join the BPP and the GDL.....	39
3. Experimental Procedure.....	47
3.1. Sample Synthesis.....	47
3.2. Sample Analysis.....	52
4. Soldering a Gas Diffusion Layer to a Bipolar Plate Using Tin.....	57
4.1. Introduction.....	57
4.2. Optimisation of the electrodeposition process.....	57
4.3. Optimisation of the hot pressing process.....	62
4.4. Discussion.....	66
4.5. Conclusions.....	67
5. A Preliminary Study on the Alloying of Sn.....	69
5.1. Melting Point.....	69
5.2. Electrochemical Testing.....	70
5.3. Interfacial Contact Resistance.....	70
5.4. Electrodeposition.....	71
5.5. Conclusion.....	72
6. Tin-Bismuth Alloys for Bipolar Plates in PEM Fuel Cells.....	73
6.1. Why Bismuth?.....	73
6.2. Optimising the Deposition of SnBi.....	75
6.3. Hot pressing the SnBi alloy.....	80

6.4. Conclusions.....	84
7. The Co-deposition of Sn and In for Bipolar Plates in PEMFCs.....	85
7.1. Why Indium?.....	85
7.2. Co-deposition of Sn and In.....	88
7.3. Hot dipping in a SnIn melt.....	107
7.4. Summary.....	109
8. The Influence of Carbon on the Sn/GDL System.....	111
8.1. Carbon Materials for PEMFCs.....	111
8.2. The Influence of the GDL Type on the Sn/GDL System.....	112
8.3. Carbon nanolayer to enhance the Sn/GDL interface.....	117
9. <i>In-situ</i> analysis of Bipolar Plates.....	123
9.1. Introduction.....	123
9.2. Interfacial Contact Resistance.....	124
9.3. Polarisation curves.....	128
9.4. Electrochemical Impedance Spectroscopy.....	135
9.5. Post-mortem Analysis.....	140
9.6. Conclusions.....	142
10. The feasibility of Sn/GDL BPPs on an industrial scale.....	143
10.1. Introduction.....	143
10.2. Requirements for robust coating materials.....	143
10.3. Meeting the requirements for robust coating materials.....	146
10.4. Conclusions.....	153
11. Conclusions and Future Work.....	155
References.....	159
Appendices.....	173

# 1

## Background

### 1.1. Motivation

Climate change is the most pressing problem faced by today's society.

Hydrogen is positioned to play a key role in a future where greenhouse gas (GHG) emissions are reduced to acceptable levels. As an energy carrier, hydrogen has the ability to influence all sectors, from providing power to large scale industry to replacing natural gas in our homes. In particular, the transport sector is primed for a hydrogen revolution. According to the International Energy Agency, transport including shipping, aviation and road travel account for 23 % of global GHG emissions [1]. In Proton Exchange Membrane Fuel Cells (PEM fuel cells; PEMFCs) hydrogen is used as a fuel that reacts with oxygen in air to produce electricity. PEMFCs can replace traditional internal combustion engines, and exhibit many of the same advantages without the drawback of high emissions of CO<sub>2</sub>, NO<sub>x</sub> and SO<sub>x</sub>, as well as noise pollution. PEMFC vehicles have long range and quick refuelling times, and their only by-product is water. Moreover, PEMFCs have a specific energy (Wh/kg) and energy density (Wh/l) up to 20 times higher than a standard lithium-ion battery [2], and do not have the same susceptibility to decreased performance in cold environments [3]. This is of particular importance to long-range vehicles such as commodity trucks, which need to use space for goods transport rather than large and heavy battery packs.

A transport revolution is already taking place. Worldwide, there are currently over 18,000 fuel cell cars on the roads, as well as over 2,000 hydrogen powered busses, 30,000 forklifts and numerous trains, boats and trucks. In just ten years, there are predicted to be more than 11 million fuel cell vehicles globally, which will be serviced by 12,000 public and even more private filling stations [4].

This large increase in uptake will be possible mainly due to mass production of fuel cell components which will bring the price down significantly. Nevertheless, further cost reductions are needed before fuel cells can reach the mass-market, and this must be done through innovations in the development of high performance, low cost components.

### 1.2. Aim of Thesis

This work will attempt to aid the implementation of hydrogen fuel cells into society, by increasing the longevity and affordability of PEM fuel cells. This thesis specifically looks at the bipolar plate (BPP), which accounts for around 30 % of the cost [5] and up to 55 % of the weight of the fuel cell [6]. The BPP has many important functions within the fuel cell: it provides mechanical support, as well as distributing reactants and products across the membrane, electronically connecting individual fuel cells together,

and managing the heat and water produced during the fuel cell's operation. Finding suitable materials for the bipolar plate that are inexpensive and durable enough to be used for transport applications is difficult due to these many requirements. Metals are promising BPP materials, but they are prone to corrode and form poorly conducting oxides on the surface due to the acidic environment produced by the membrane. This leads to increases in the contact resistance and worsens performance over time. By tackling these challenges in a novel way, this thesis will aim to produce bipolar plates that are durable, affordable and high-performance.

The idea investigated in this thesis is the electrodeposition of a layer of metallic tin (Sn) or a tin alloy onto a stainless steel bipolar plate substrate, followed by hot pressing with a gas diffusion layer to join the two together by soldering. This produces an uninhibited conduction pathway through the bipolar plate to the gas diffusion layer (GDL) due to direct contact with the metallic Sn, whilst any oxide layer that forms on the outer surface of the Sn provides protection from further corrosion. In this way, the oxide layer acts as a protective barrier instead of being detrimental to performance, therefore maintaining the conductivity and increasing the lifetime of the plates.

The main aim of this thesis is therefore to investigate, optimise and finally test this coating technique against commercial gold-coated stainless steel bipolar plates inside a working fuel cell.

### 1.3. Outline of Work

This thesis is written as a monograph, starting with an introduction to fuel cells and electrodeposition and then showing how these two can be combined by the Sn/GDL concept to produce cheap bipolar plates with an enhanced lifetime.

In chapter two, the basics of PEM fuel cells are introduced, including the current state of the art in bipolar plates and methods used for coating and testing them. Specifically, electrodeposition can be used to produce an even coating in an easy way, and chapter two also takes an in-depth look into the theory of electrodeposition of metals and alloys, including the specific case of tin (Sn).

The experimental methods used throughout this thesis are described in chapter three, starting with the fabrication of the bipolar plate using electrodeposition and hot pressing. Analysis techniques used on the bipolar plate include the measurement of interfacial contact resistance, *ex-situ* corrosion tests and the setup of an *in-situ* cell to perform accelerated stress tests and *in-situ* electrochemistry.

Chapter four describes how Sn can be used as a coating material through soldering the GDL to the stainless steel bipolar plate substrate for use in PEMFCs. The deposition of Sn was optimised in terms of Sn layer thickness, hot pressing time, temperature and pressure. A modified version of this chapter has been published in the International Journal for Hydrogen Energy [7].

After an investigation into the stability of the Sn/GDL system, it was determined that the stability of the SnO<sub>2</sub> oxide layer was insufficient, so additional alloying elements should be added to enhance the stability of the protective Sn oxide layer and improve the longevity of the BPPs. A number of possible

alloying elements were identified, and in chapter five, these elements are evaluated based on criteria such as stability in a simulated PEMFC environment, melting point, and contact resistance.

In chapter six, the alloying of Sn with bismuth (Bi) is investigated. Firstly, the influence of various deposition parameters on the bismuth content was investigated, then electrochemical tests were used to determine the optimum bismuth content. Additional hot pressing parameters were optimised, and the best combination was tested *in-situ*.

The influence of indium (In) on the Sn layer was investigated in chapter seven. Several different co-deposition techniques were attempted, including four types of electrodeposition bath and hot dipping in a Sn/In melt. However, a reliable coating was not achieved. Therefore, this was not transferred to bipolar plates, nor was any long-term *in-situ* testing done.

As well as changing the content of the Sn layer to enhance stability, it was hypothesised that adding a carbon (C) nanolayer between the GDL and the Sn could increase the conductivity and stability of the system. This hypothesis was investigated in chapter eight, with different types carbon nanolayer being sprayed onto the GDL. The experimental work in this section was performed by three bachelor's students under the supervision of Katie McCay. Chapter eight also describes work done to determine the influence of the GDL type on the Sn/GDL system.

In chapter nine, *in-situ* analysis of all the bipolar plates was performed. The Sn/GDL BPP was compared against standard gold and stainless steel BPPs, as were the Sn/C/GDL and SnBi/GDL BPPs. Drive cycles obtained from the European commission [8] were performed for 200 hours, with polarisation curves and EIS analysis of the samples taken every 50 cycles. Fitting of the EIS data was performed by Frode Seland. After *in-situ* cycling for 200 hours, the BPPs were analysed using post-mortem analysis including ICR and SEM with EDS mapping.

Finally, chapter ten deals with the scaling up of the Sn/GDL system, and how suitable it is for industrial application. A series of requirements for robust coating materials were identified during a bipolar plate workshop, organised in 2017 by the U.S. Department of Energy and Argonne National Laboratory [9]. Meeting these requirements is essential to producing commercially viable bipolar plates and fuel cells, so in order to get some perspective about the position of this thesis in a hydrogen future, the Sn/GDL concept bipolar plates are assessed in regard to the requirements outlined at the workshop.

Chapter eleven concludes this work and identifies some areas of future interest.



# 2

## Introduction

### 2.1. Proton Exchange Membrane Fuel Cells

#### 2.1.1. The Basics

A fuel cell is an electrochemical energy conversion device that continuously converts chemical energy into electrical energy (and some heat) for as long as it is fed with fuel and oxidant [10]. In a Proton Exchange Membrane (PEM) fuel cell, the fuel (hydrogen) is separated from the oxidant (oxygen) by a proton conducting membrane, sandwiched between an anode and a cathode. This assembly is the heart of a fuel cell and is referred to as the membrane electrode assembly, or simply MEA. Hydrogen is oxidised at the anode generating protons and electrons. The protons are transported through the membrane to the cathode side, while the electrons are forced through an external circuit, where work can be done, to the cathode. At the cathode, electrons and protons are consumed in the reduction of oxygen producing water, essentially the only product from such a fuel cell. The electrode reactions that occur in a PEMFC are given in eq. 2.1.1-3 along with the respective standard potential at 298 K [11]:

Equation 2.1.1: The anodic reaction in the PEM Fuel Cell



Equation 2.1.2: The cathodic reaction in the PEM Fuel Cell



Equation 2.1.3: The overall reaction in the PEM Fuel Cell



The theoretical output of a single fuel cell at 25°C and standard states is 1.23 V, however this is not achieved in a real system mainly due to a number of overpotentials that cause the real cell voltage to be lower than the thermodynamic one. Figure 2.1.1 shows a typical polarization curve of a PEM fuel cell. These irreversible loss mechanisms can be categorized as activation, ohmic and concentration overpotentials [10]. At low current densities, the activation overpotential dominates. It arises from the voltage required to start the reaction, and is influenced by sluggish electrode kinetics and charged species migration [12]. The activation overpotentials are present at both the anode and the cathode;

however, oxygen reduction is a much slower process than hydrogen oxidation, so the cathodic overpotential dominates.

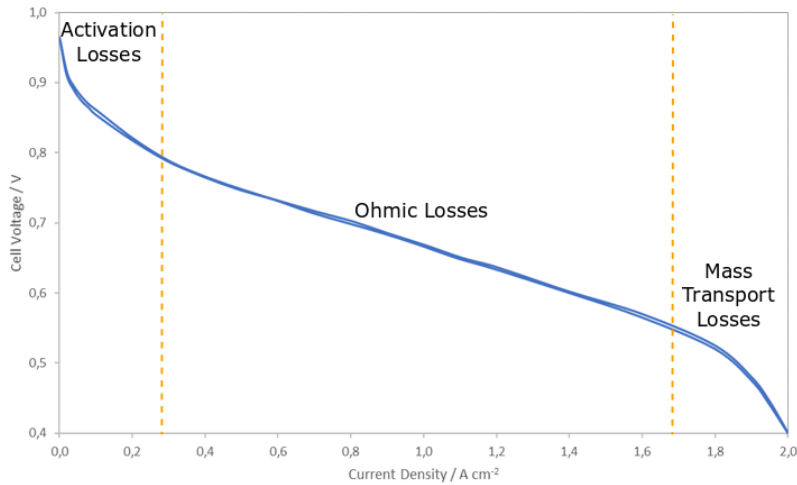


Figure 2.1.1. A typical polarisation curve from a PEM Fuel Cell.

At high current densities, the mass transport or concentration overpotential dominates. The concentration overpotential occurs when reactant is rapidly consumed at the electrode, establishing a concentration gradient [10]. As the current density increases, the amount of reactant consumed increases until the replenishment of it at the surface from diffusion is slower than the consumption of it. This limits the reaction rate, and if the current density is increased, the overpotential also rapidly increases [12]. Impeded transport of water out from the catalytic layer can also result in mass transport limitation due to flooding of the porous structure with liquid water.

The ohmic overpotential is proportional to the current density, as it obeys Ohm’s law. It arises due to resistance towards ion transport in the membrane and transport of electrons through interfaces and bulk components in the cell [10]. Minimising the bulk and contact resistances of cell components is the most effective way to reduce the ohmic overpotential, as seen in Equation 2.1.4.

Equation 2.1.4: The ohmic overpotential as a function of current density [10]

$$\Delta V_{ohm} = \eta_{IR} = jR_i$$

$$\text{where } R_i = R_{i,i} + R_{i,e} + R_{i,c}$$

$\Delta V_{ohm}$  = Ohmic overpotential, V

$j$  = Current density, A cm<sup>-2</sup>

$R_i$  = Total cell internal resistance, Ω cm<sup>2</sup>

$R_{i,i}$  = Ionic resistance of cell, Ω cm<sup>2</sup>

$R_{i,e}$  = Electronic resistance of cell, Ω cm<sup>2</sup>

$R_{i,c}$  = Contact resistance of cell, Ω cm<sup>2</sup>

The total voltage drop for the cell at any given current density is a combination of the above overpotentials, however, additional voltage losses in a PEMFC may come from reactant crossover and internal currents. Reactant crossover describes the transport of hydrogen gas through the membrane or bipolar plate to the cathode side where it is oxidized or reacts with oxygen gas, lowering both cell performance and fuel utilization. . These losses are most prevalent at open circuit voltage, OCV. In fact,

a noticeable activation overpotential at the cathode must be added just to overcome the small contributions from internal currents (from e.g. carbon or catalyst corrosion) and cross-over of reactants. This is the reason why the polarization curve starts at 1.0 V or below, significantly lower than the thermodynamic cell voltage. Electrons may also find a more efficient pathway through the membrane, short-cutting the external circuit and thereby lowering the voltage produced by the cell, a process called ‘stray current’ [10]. Though stray currents continue during operation, they are usually not large enough to impact performance, and if they are, this is an indicator of a larger problem within the cell, for example a short circuit.

The output from a single, real fuel cell is not substantial enough to be of much practical use, so a number of fuel cells can be connected in series to produce a workable output. This is called a fuel cell ‘stack’, the size of which can be tailored to suit the application, and a number of stacks can be connected in series or parallel depending on the mode of operation [13].

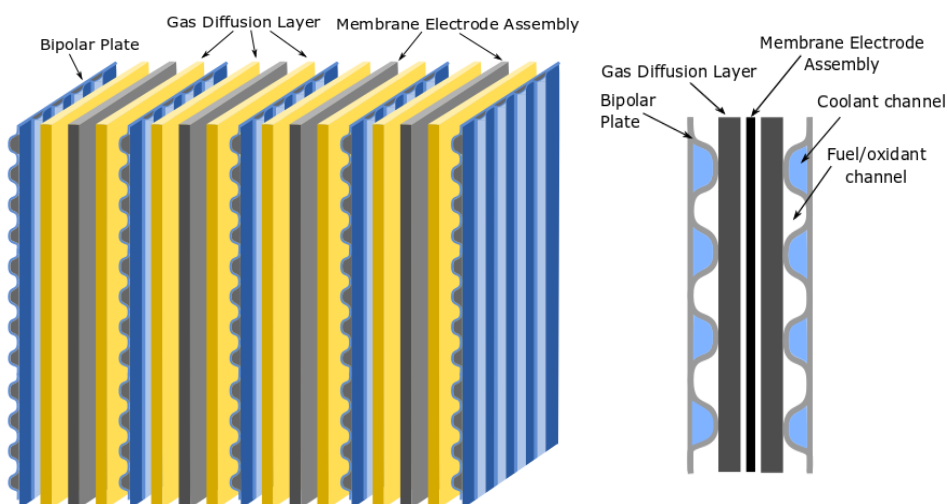


Figure 2.1.2: A schematic diagram of a PEM Fuel Cell Stack, and a single cell

The stack as a whole is made up of several single cells, and each of these single cells consists of a number of components, as seen in Figure 2.1.2. These components are the membrane electrode assembly (MEA), the gas diffusion layer (GDL) and the bipolar plates (BPP).

The MEA in a PEMFC is made up of a polymer electrolyte membrane and the electrodes with a catalyst layer mounted on them. The membrane must be highly conductive to protons, but not electrons, and must be impermeable for hydrogen gas, to avoid fuel crossover and the associated losses [14]. Typically, membranes are made from Nafion™, a copolymer of PTFE with sulfonic acid branching groups. Though the PTFE backbone is hydrophobic, the side chains containing sulfonic acid groups are hydrophilic and cluster around any water molecules present [10]. These membranes can absorb high amounts of water, and proton conductivity is facilitated through these hydrated regions [15]. The membrane must be kept well hydrated to maintain proton conductivity, meaning water management within the cell is particularly important.

Present on both sides of the membrane, the electrodes are the surfaces at which the electrochemical reactions in the cell occur. They must be permeable to gas and conductive to both electrons and protons to facilitate the electrochemical reactions. This three-phase boundary must be optimized for best possible performance [10]. A catalyst is needed in the three-phase boundary to conduct electrons and lower the activation energy of the reaction. Platinum is the most common catalyst for PEM Fuel Cells, and is usually supported on carbon [14].

The GDL, usually a carbon cloth or paper, provides a pathway for the reactant gasses to the MEA surface. It also electrically connects the BPP to the MEA surface, allowing electrons to move to and from the three-phase boundary [10]. Therefore, it must be conductive to electrons, and also porous enough to let reactants to the MEA and transport water away to avoid flooding.

These different components provide a conflicting set of requirements and it is therefore difficult to optimise all parameters within the PEM. One must also take into account the environment within the cell, and the impact this has on the lifetime of the cell components. Specifically, the sulfonic acid groups of the membrane produce a slightly acidic environment within the cell, and the PTFE groups may release fluoride ions which have been shown to locally corrode metal surfaces [16]. Coupled with the increased temperatures and high relative humidity, this produces a challenging environment for any corrosion-susceptible materials to survive within. Material selection is therefore very important, but materials that provide the most longevity are often the most costly. This is one of the current limitations with PEM technology and the task of reducing the cost of cell components whilst maintaining their corrosion resistance is one intertwined with their future commercial success.

### 2.1.2. Bipolar Plates

The bipolar plates are an important part of the fuel cell stack and have several functions. The most crucial role of the bipolar plate is the conduction of electrons throughout the stack. The bipolar plates connect each individual cell in series to produce a useable output for the stack. They connect the anode of one cell to the cathode of the adjacent cell, so electrons can move through the entire stack and then to the external circuit, therefore they must be highly conductive to avoid ohmic losses [10].

The bipolar plates also distribute and separate the fuel gasses and waste products with a flow field that has been etched or stamped into each plate to aid this process. Flow fields can be formed in a number of geometries, including pin-type, parallel, serpentine or interdigitated [17], and should homogeneously distribute reactants over the whole active electrode surface to minimise the concentration overpotential [18]. The most common flow field type is parallel serpentine, due to its superior performance, reliability and suitable pressure drop [19]. Sketches of selected flow field patterns are given in Figure 2.1.3.

With new techniques such as 3D printing, which allow more complex structures to be made, a number of new flow field patterns for the bipolar plates have been introduced. Biologically inspired tree-like, leaf-like and lung-inspired bipolar plates have been developed [20–23], as well as meshes and foams [24,25]. However, due to the complex formation processes, such BPPs are not ready for large-scale production.

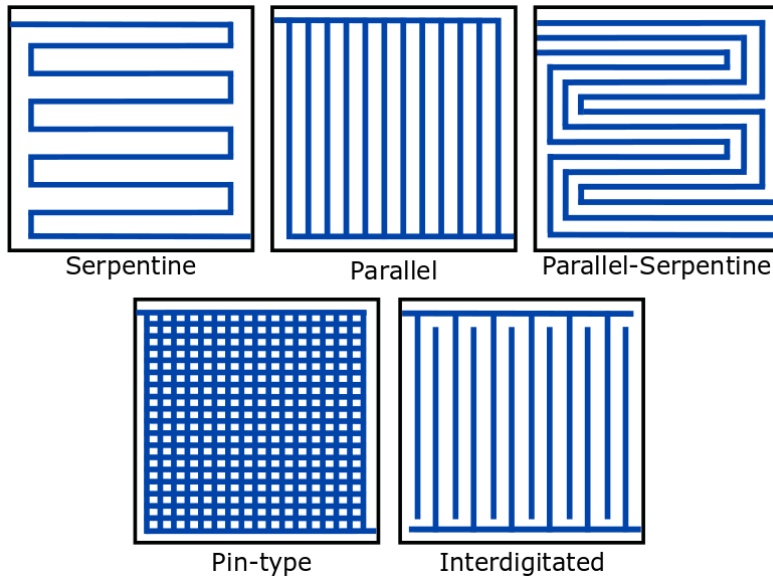


Figure 2.1.3. A diagram showing the most common types of flow fields for bipolar plates

The bipolar plates also manage heat and water distributions. If there is a local build-up of either water or heat on the membrane, mechanical stresses cause pinholes to form, leading to fuel crossover and ultimately cell failure [26].

Due to the large number of roles they play within the PEMFC, the bipolar plates need to have a variety of properties. They must be both electronically conductive and resistant to corrosion in the PEM environment. If their corrosion leads to the formation of non-conductive oxides, contact resistance will increase, and the release of ionic contaminants may poison the membrane, both of which reduce cell efficiency [27–29]. In addition, they must be mechanically durable for use in transport applications and must also provide support to the stack. Low weight and volume are also important in such applications, and gas permeability must be low to avoid fuel crossover. They must also be relatively cheap and easy to manufacture. Now that PEM technology has become commercially viable, a large volume of bipolar plates must be manufactured in a cheap and quick way.

Table 2.1.1 Technical Targets: Bipolar Plates for Transport Applications [30]

Characteristic	Units	2015 Status	2020 Targets
Cost	\$/kW <sub>net</sub>	7	3
Plate weight	kg/kW <sub>net</sub>	<0.4	0.4
H <sub>2</sub> permeation coefficient	Std cm <sup>3</sup> /(sec cm <sup>2</sup> Pa)	0	<1.3x10 <sup>-14</sup>
Corrosion, anode	μA/cm <sup>2</sup>	no active peak	<1 and no active peak
Corrosion, cathode	μA/cm <sup>2</sup>	<0.1	<1
Electrical conductivity	S/cm	>100	>100
Areal specific resistance	ohm cm <sup>2</sup>	0.006	<0.01
Flexural strength	MPa	>34 (carbon plate)	>25
Forming elongation	%	20–40	40

The US Department of Energy has produced a series of guidelines for the manufacture of bipolar plates [30], with targets for conductivity, corrosion resistance, strength and cost as outlined in Table 2.1.1.

## Materials for Bipolar Plates

Commercial bipolar plates are expensive and heavy, contributing up to 30% of the stack cost [5] and up to 55% of the stack weight [6]. Traditionally made from graphite due to its high corrosion resistance and electrical conductivity [31,32], they are stable in a PEMFC environment, and suitable for stationary applications. However, graphite is difficult to manufacture and machine so plates need to be thick and heavy, inducing a high cost and low power density [33,34]. This high thickness is also important to minimise fuel crossover and the associated degradation as graphite BPPs are semi-porous. In addition to their weight, their brittleness means that they are not suitable for transport applications and there is a drive to produce BPPs that are cheaper and more lightweight with high tolerances to shock.

Metallic bipolar plates provide a suitable alternative to previous graphite versions, as they in general exhibit excellent mechanical properties, including a low gas permeability and very high conductivities [35]. The raw materials are cheaper and the plates are easy to mass-produce [36]. A series of uncoated metallic bipolar plates have been tested for PEM applications, including aluminium, titanium, nickel alloys and stainless steels.

Table 2.1.2. A summary of the different metals that can be used to form bipolar plates, and their advantages and disadvantages

Material	Positives	Negatives	References
Aluminium	Lightweight, abundant, formable	High thermal expansion, difficult to coat, oxide formation	[37,38]
Titanium	Lightweight, strong	Hard to form, oxide formation, expensive	[39–41]
Nickel Alloys	High corrosion resistance, low ICR, formable	Very expensive	[42,43]
Stainless Steel	Formable, lightweight, low cost	Oxide formation, localised corrosion	[44–46]

In general, despite their many advantages when compared to carbon-based plates, uncoated metallic bipolar plates are not suitable for use in PEMFCs due to their corrosion properties in a mildly acidic environment at high positive potentials. When exposed to such an environment, non-conductive oxide layers are formed, increasing the contact resistance and decreasing the conductivity of the BPP [44]. In addition, corrosion products such as hydrated metal ions are formed. These can be flushed through the cell with waste water and poison the membrane by displacing  $H^+$  ions in the sulfonic acid networks, permanently reducing the proton conductivity of the membrane and therefore reducing the performance of the cell [47,48].  $Al^{3+}$  ions having three positive charges were shown to have the greatest effect [27], but almost all metal cations have a greater affinity to the sulfonic acid groups within the Nafion<sup>TM</sup> membrane than protons, meaning any ionic contaminant will have a negative effect on cell performance [49]. Corrosion products can also precipitate downstream and block the BPP channels [50]. In order to avoid these undesirable side-reactions, bare non-noble metallic bipolar plates must be coated with a conductive and corrosion resistant material to extend their lifetime in a PEMFC environment.

Due to its superior mechanical properties and low cost when compared to other BPP substrates, stainless steels are the most widely used substrate materials for coated bipolar plates. A review by Taherian in 2014 compared a number of common bipolar plates through a simple additive weighting method (SAWM) and concluded that the most favourable material for commercial BPPs was coated SS316L [51]. It provides both low cost, volume and weight, and preferable corrosion rates, with the ionic contamination vastly reduced after coating. Therefore, coated stainless steel bipolar plates are a perfect candidate for future PEM systems and most leaders in the field of fuel cell vehicles (FCEV) have chosen stainless steel bipolar plates as their substrate material [52].

### 2.1.3. Coatings

Coatings are the most effective way to improve the corrosion resistance of metallic bipolar plates whilst still maintaining the desired low resistance, volume and weight. A number of comprehensive reviews on coating materials for bipolar plates have already been published [47,51–56], with numerous different coating compositions, methods and processing steps reported in recent literature.

#### Pre-treatment of substrates

Before coating any surface, pre-treatment is often required. It has been shown that the pre-treatment of surfaces has a great impact on the morphology, thickness and wettability of coatings [57,58]. Therefore, before coating a surface, it is extremely important that the surface is reproducible. This means it should be cleaned and roughened to the desired degree, either by mechanical or chemical means, in a controlled manner.

Cleaning the surface to remove oil, dust and other particles is a necessary step to avoid delamination and ensure good adhesion. Cleaning should also remove any unwanted non-conductive oxide layers present on the substrate, which increase the contact resistance between the substrate and the coating as well as producing a surface with low roughness and low surface free-energy [59].

Roughening, or etching, of the surface can be done mechanically or chemically. Roughening the surface increases the number of anchor points for coating adhesion, as well as increasing the interaction area of the coating and substrate[60]. In general, mechanical roughening methods form a good geometrical structure but do not activate the surface, whereas chemical treatments can selectively remove certain elements or weakly bonded oxides [61].

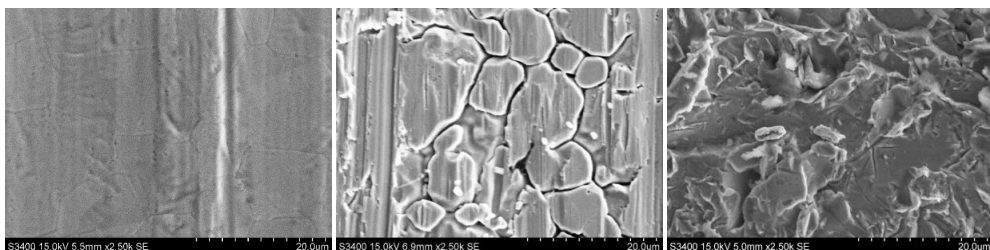


Figure 2.1.4 SEM images of (a) untreated, (b) acid etched, and (c) glass blasted SS316L substrates, used with permission from [62]

Mechanical surface treatments, for example sand or glass blasting, provide good surface roughness but may leave debris behind on the surface, which is detrimental to bonding [63]. In general, mechanical

methods are outperformed by chemical and electrochemical treatments when tested under harsh conditions [64]. Work by Husby et al. [62] showed that acid etching was a more effective pre-treatment for SS316L than glass blasting. Whilst glass blasting roughened the surface of the plates, the acid etching process corroded intergranular regions and formed deep crevices, which the coating material can infiltrate and form a strong adhesion, as seen in Figure 2.1.4.

There are, however, environmental concerns with the use and disposal of chromic acid and sulphuric acid-dichromate (FPL) baths, meaning milder acid treatments or mechanical etching are favoured.

## Coating Materials

Coatings for BPPs can be grouped into carbon based, polymer or metallic coatings. Popular research focus has recently been on carbon composites [65–68], metal nitrides [69–73], noble metals [39,74–76] and carbides [77–80], as well as multilayer coatings that can combine the advantages of each of the above.

In general, coatings for BPPs aim to provide a barrier between the bare stainless steel and the PEM environment in order to prevent corrosion. Any coatings must therefore be dense, without pinholes or cracks, and adhere to the substrate for the lifetime of the plate [81].

The applied coating must be durable, and able to withstand any post-processing steps. It is more effective in terms of both lowering ICR and ease of manufacturing to coat an entire sheet of metal and then form the BPPs through a process such as hydroforming or stamping, compared to forming the plates and then individually coating them [82]. Any coating must therefore be able to withstand this mechanical pressure as well as having enough shock-tolerance for it to perform well for transport applications. This has historically been the main drawback of carbon based bipolar plates and coatings, which often require large amounts of binder materials to meet the mechanical requirements at the expense of conductivity [65].

The coating should also be of high conductivity and ideally not form a non-conductive oxide on exposure to the PEM environment, in order to maintain a low ohmic overpotential. Oxidation of metals inside the fuel cell is a large problem, and more exotic metals such as tantalum have been investigated to obtain a stable coating that has a low contact resistance throughout its lifetime [83–85].

Modification of the contact angle of bipolar plates can be done by coating, to increase the hydrophobicity and improve the water management properties. Such coatings have successfully reached the corrosion and contact resistance requirements set out by the DoE, though have not been proven stable during long-term fuel cell operation [86].

If the coating material is not completely inert in the fuel cell environment, corrosion products could have a detrimental effect on the cell performance. This could occur through poisoning of the membrane by metal ions, blocking of flow field channels or damaging the catalyst [87].

It is obvious that a number of parameters have to be considered when choosing a suitable coating for BPPs, and most coating materials do not fulfil all of the requirements set out above. Noble metal coatings, such as Au, can reach the durability and performance requirements, but are too expensive for commercial fuel cells [39], and there is now a push from industry to find low cost, high quality bipolar

plates that are able to be mass-produced for use in the vehicles of the future. In this thesis, a series of durable, low cost coatings based on Sn and Sn alloys for use in a PEMFC have been investigated, with focus on whether they can meet the cost, performance and durability criteria.

## Coating Methods for Bipolar Plates

There are a huge number of ways of getting a coating onto a bipolar plate, ranging from the simple dip-coating to the complex and costly vapour deposition methods. The technique used depends on the type of coating and the desired surface finishes.

Dip coating and spraying are preferred for carbon based coatings, as they provide a cheap way of coating large surface areas with high volumes of coating. However, they may often produce undesirable layered microstructures, often with pinholes or other porosity [65]. Heat treating the coating after application is a way of removing such flaws, and has successfully been utilised to produce BPP coatings suitable for use on the cathode of a PEMFC [37]. High-temperature thermal spraying can instead be used for the deposition of metals such as titanium onto the BPP substrate, and has been shown to produce coatings that have low contact resistance and better water management properties, with good performance even after 1000 hours of testing [88,89].

Unlike most other coating techniques, ion implantation does not form a continuous coating layer, but modifies the existing surface up to a depth of up to 0.5  $\mu\text{m}$  through the acceleration of ions towards the surface. A uniform and stable surface is produced, that exhibits greater corrosion resistance compared to the bare substrate [53,90]. Similarly, nitriding involves the implantation of nitrogen ions into the surface of a BPP, activating the surface and improving corrosion resistance [91,92]. These processes can take long times, and often do not avoid the release of damaging metal ions from the BPP substrate into the MEA. Stainless steel bipolar plates that are modified by nitriding often struggle to meet the DoE requirements [70,72,93], and the high processing cost and temperature does not lend itself to mass-production.

Vapour deposition is a useful technique to form thin, dense films without pinholes and other imperfections. This density means that the coatings are often highly corrosion resistant and there is no release of harmful metal ions from the BPP. The vapour deposition techniques involve the vaporisation of a target made from a certain element inside a vacuum, and then the deposition onto a substrate. Therefore, they are very versatile and almost any element can be coated onto the substrate. For example, platinum has been coated onto stainless steel using physical vapour deposition (PVD), and placed inside a working fuel cell for 1000 hours, where its performance was comparable to the baseline [89]. Carbon coatings can also be deposited using chemical vapour deposition, and both graphene [94] and carbon nanotube [95] coatings were found to enhance the long-term performance of stainless steel bipolar plates. The main downside to such techniques is the requirements for expensive equipment, high vacuums and high temperatures.

The primary method used in this thesis is electrodeposition, which is a popular technique used to apply pure metal-, alloy- and metal oxide coatings on bipolar plates. Examples of coatings that can be electrodeposited onto bipolar plates include Cr-C, Ni-Mo-P, Ni-TiN and RuO [96–99], and many of these BPPs meet the DoE requirements. Electrodeposition is beneficial due to its versatility in terms of coating material and substrate, as well as its low cost and often low processing temperature. However,

organic solvents, acids and additives are commonly used and may be difficult to dispose of safely after deposition.

## 2.1.4. Testing methods for coatings and bipolar plates

When evaluating the quality of a coating, a number of common test methods are implicated. There are a series of guidelines set out by the US Department of Energy [30] advising which test methods should be used, and the performance that should be achieved in both *in-situ* (inside an operating fuel cell) and *ex-situ* (in a simulated fuel cell environment) environments. Some of the most common testing methods analyse the electrochemistry, material properties, and characterise the surfaces of bipolar plates, in an attempt to define their performance and longevity inside a fuel cell.

### Ex situ electrochemical Methods

The most common *ex-situ* electrochemical testing methods are performed using standard procedures that have been outlined by the US Department of Energy, with guidelines on conditions including pH, temperature, voltage, and impurities to effectively mimic an operating PEMFC [30]. From these tests, the stability of the bipolar plates and any regions where active corrosion is occurring can be identified, and the progressions in contact resistance over time can be obtained, indicating the longevity of the BPP *in-situ*. Common electrochemical methods for bipolar plates include Open Circuit Potential (OCP), Cyclic or Linear Sweep Voltammetry (CV or LSV) and Chronoamperometry (CA).

The OCP is the potential between the bipolar plate (working electrode) and the reference electrode (in a 3-electrode system) when there is no net current flowing in the circuit. The OCP is of limited use for fuel cell testing, as the system is rarely at open circuit and the degradation mechanisms vary with the amount of current drawn from the fuel cell.

Slow CV or LSV experiments are performed to mimic the steady state performance of a fuel cell electrode (bipolar plate) for a range of relevant operating potentials. The bipolar plate is then exposed to a sufficiently slow linear potential sweep (maximum of  $1 \text{ mV s}^{-1}$ ) that the current response can be interpreted as corrosion current from each individual scanned potential. This can be used to identify reactions occurring at the surface and the potential at which they occur, along with the OCP.

In CA measurements the bipolar plate is exposed to a potential relevant for fuel cell operation after an immediate jump from a potential where no reaction is occurring. Unlike traditional chronoamperometry (where you are typically interested in the current transients of the first milliseconds after the step to look for nucleation and growth mechanisms) the current transient at longer times, sometimes even for more than 1000 hours, is of most interest for BPPs.

These *ex-situ* electrochemical methods provide a quick and convenient way of testing bipolar plates, investigating possible failure mechanisms in an aqueous environment that mimics the conditions of a real fuel cell. However, these testing procedures may not accurately represent the *in-situ* environment experienced by a bipolar plate. For example, it is advised to use a dilute solution of sulphuric acid as an electrolyte during electrochemical tests, as sulfate ions can leech from the membrane [100]. This leads to full contact between the bipolar plate and the electrolyte, which may be much harsher than the reality, which is partial contact with an acidic environment through water droplets.

Though using harsher conditions may be useful as an accelerated testing method, it has been shown that pH of the electrolyte has a large impact on the stability of stainless steel [101]. Reducing the pH to levels below those observed inside a PEM alters the composition and thickness of the oxide layer and does not represent real conditions [44]. Feng et al [102] tested pH values from 3 to 6, showing changes in release of metal ions, passive film composition and corrosion potential. In addition, increasing levels of Cl<sup>-</sup> ions beyond those commonly found in a fuel cell initiated pitting corrosion, whereas normal contents of F<sup>-</sup> and Cl<sup>-</sup> had no effect on the ICR or polarisation of stainless steel bipolar plates *ex-situ* [44].

Commonly, voltages experienced in the *ex-situ* electrochemical test are much harsher than the actual voltages in a working fuel cell. Voltages above 1.0 V<sub>SHE</sub> only occur rarely during shut down and start up procedures, not constantly, as is the case during *ex-situ* testing at a fixed potential of 1.0 V<sub>SHE</sub>. The US DoE recommends *ex-situ* corrosion testing of BPPs to be performed at 0.6 V<sub>Ag/AgCl</sub> or 0.8 V<sub>SHE</sub> [30]. However, in work by this group, it has been shown that when comparing *ex-situ* and *in-situ* testing methods, higher *ex-situ* potentials of 0.95 V<sub>SHE</sub> [44] or even 1.4 V<sub>SHE</sub> [103] most closely matches the level of degradation found *in-situ*. Despite this, Hinds and Brightman [104] found that the *in-situ* potential experienced by the cathode BPP is closer to 0.6 V, regardless of the cell potential. Although spikes in the observed potential reaching a maximum of 0.8 V were seen under dynamic cycling conditions. Prolonged exposure to voltages higher than this may alter the surface of the BPP in ways uncommon during normal operation

Therefore, although *ex-situ* electrochemical tests are a useful preliminary study to compare different bipolar plates against one another, they are often not representative of the *in-situ* testing conditions, and the most accurate way of determining the performance of a bipolar plate is to place it inside a working fuel cell.

## Surface Characterisation of Coatings

The coating material can be analysed to determine the elemental composition, the presence of oxide layers and the morphology of the surface.

Scanning Electron Microscope (SEM) analysis with Energy Dispersive Spectroscopy (EDS) mapping is a popular technique which accelerates a beam of electrons towards a surface to map its topography and composition. It provides an excellent depth of field and is a useful tool for visualising the morphology bipolar plates, with areas exposed to corrosion or other surface irregularities easily seen. Cross-sectional imaging with high-resolution SEM allows for more in-depth observation of the coating and plate interface, whilst EDS analysis provides elemental mapping of the top approx. 2 µm of the surface.

Surface sensitive methods such as Auger Electron Spectroscopy (AES) or X-ray Photoelectron Spectroscopy (XPS) can provide information about coatings without interference from the metal substrate. XPS is particularly good for showing the oxidation state of elements in the sample and the relative amounts, which is important for understanding the oxide layer formation on bipolar plates.

## Interfacial Contact Resistance (ICR) Measurements

Contact resistances occur at every interface in the cell, with the most important contribution from the bipolar plate/GDL interface. Many factors including surface roughness, pressure and any impurity layers, e.g. oxides, can impact the contact resistance between two surfaces, and minimising this resistance is crucial to the effective performance of fuel cell stacks.

The measurement of interfacial contact resistance has become a standard method to use when characterising bipolar plates. This method can obtain the contact resistance between the BPP and the GDL by applying a fixed current through the sample and measuring the resulting voltage. Ohm's law gives you the total through-plane resistance of the system directly:

$$R \text{ (m}\Omega \text{ cm}^2\text{)} = \frac{V \text{ (mV)}}{I \text{ (A)}} \times A \text{ (cm}^2\text{)}$$

where  $V$  is the measured voltage,  $I$  is the applied current and  $A$  is the area of the bipolar plate in contact with the GDL. The contact resistance between the BPP and GDL can be isolated by removing all other system resistances from the measured value. These include resistances between the GDL and the top plate, the bulk resistance of the GDL, and any resistances in the wires and system, and were calculated by placing a single GDL into the setup and measuring the resistance as a function of pressure.

This method has been standardised by the US DoE [30], primarily adapted from the original work by Wang et al [105]. It is standard to quote resistances at 140 Ncm<sup>-2</sup>, or 1.4 MPa, equal to the standard compaction pressure *in-situ*, and in general, resistances below 10 m $\Omega$  cm<sup>2</sup> are considered to be acceptable.

## Contact Angle Measurements

The hydrophobicity of coatings can be analysed by measuring the contact angle of a drop of water on the coating surface. Hydrophobicity is an important property as bipolar plates must be able to transfer water away from the three-phase boundary and out of the fuel cell. Accumulation of water can lead to blocked channels, which can result in reduced gas flow, or hot-spots on the membrane which may cause damage and in the worst case holes. Therefore there have been multiple studies into whether changing the hydrophobicity of the bipolar plate will have an impact on long-term performance [106–109].

Hydrophobicity measurements are performed by dropping a water droplet onto the BPP surface, then measuring the angle between the surface and the water droplet. Any angles below 90° indicate that the coating is hydrophobic, which may be beneficial to the BPP, and any angles above 90° show that the coating is hydrophilic, as shown in Figure 2.1.5. Although contact angles are not reported in this thesis, they can be tuned to optimise BPP performance.

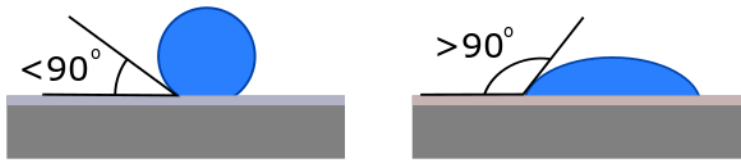


Figure 2.1.5. An image showing the contact angle of a water droplet on a hydrophobic surface (left) and a hydrophilic surface (right).

### *In-situ* Characterisation

The *in-situ* analysis of bipolar plates is performed inside a working fuel cell. This is an extremely useful technique for determining long-term performance of the bipolar plates in the exact conditions they will be used in, compared to *ex-situ* testing which attempts to simulate the conditions.

During *in-situ* testing, it is impractical to use 5000 hours to simulate the ‘normal’ operation of a fuel cell, so an accelerated testing protocol is often used and coupled with analysis techniques. This testing protocol has been designed by the European commission to simulate a fuel cell vehicle driving on European roads [8].

### Drive cycles

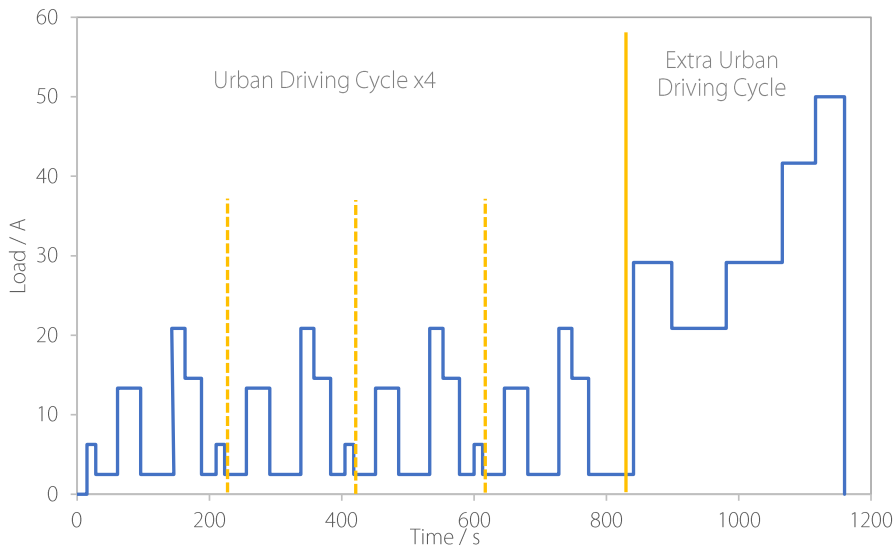


Figure 2.1.6. A single drive cycle used for *in-situ* fuel cell testing, consisting of four short urban driving cycles followed by an extra-urban driving cycle

Each drive cycle, seen in Figure 2.1.6 is designed to simulate both urban and extra-urban driving, with regions of high and low current density, corresponding to high and low vehicular speeds. These drive cycles are applied to the fuel cell in sets of 50, with diagnostic analysis including polarisation curves and Electrochemical Impedance Spectroscopy (EIS) performed before and after each set. The dynamic nature of the drive cycle, with large jumps between high and low current densities, leads to higher degradation rates than equivalent constant current operation.

After 250 drive cycles, the cell is shutdown completely with no gas flowing for at least 17 hours, and then started up again. Voltages as high as 1.4 V<sub>SHE</sub> can be experienced during these start-up and shutdown procedures, often leading to accelerated degradation that simulates real-life fuel cell operation. 500 hours of drive cycles are the equivalent of a vehicle being driven for 16 000 km, with each single cycle equivalent to a theoretical distance of 11 km driven in 20 minutes.

## Polarisation curve

The polarisation curve is an important analytical tool that can provide information about the performance of the fuel cell as a whole, and specific regions of the polarisation curve can also be used to determine which parts of the cell are causing any observed performance degradation.

A single polarisation curve is shown in Figure 2.1.7, annotated with the dominating process in three regions. At low current densities, the cell voltage is dominated by the activation losses, with the ohmic losses becoming more important at medium current densities, and then the mass transport losses dominating at the highest current density [10]. With this knowledge, one can compare the different polarisation curves taken over the lifetime of the fuel cell to determine where the main degradation modes take place, and how the cell performance is impacted by this degradation.

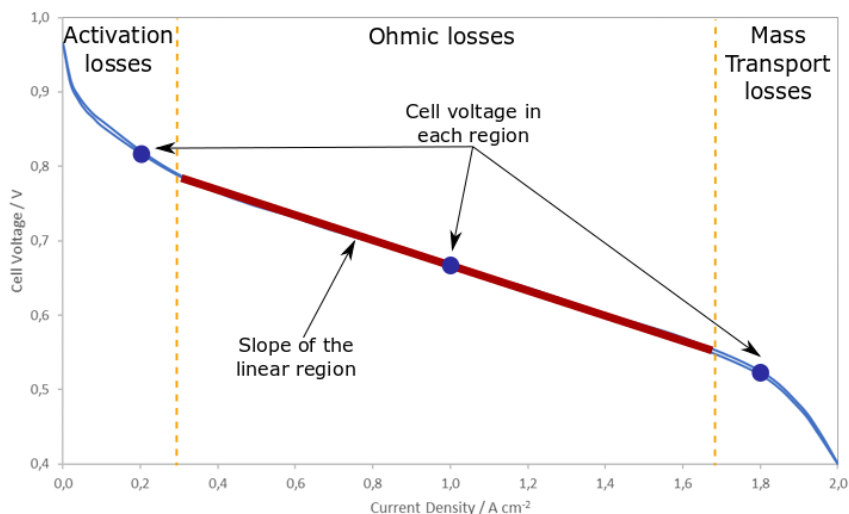


Figure 2.1.7. An annotated polarisation curve showing the dominating loss mechanism in each region. The cell voltage in each region (blue spots) can be mapped over time to determine the fuel cell performance. The resistance of the fuel cell can be estimated by applying Ohm's law to the linear region of the polarisation curve (in red).

The analysis of the polarisation curves is also shown in Figure 2.1.7, and can be done by estimating the slope of the linear region that is dominated by ohmic losses to estimate the resistance of the fuel cell over time. This resistance will include all resistances within the fuel cell, and the change in resistance over time can show processes such as the formation of oxide layers on the bipolar plate, degradation of the GDL and conductivity changes within the membrane.

The cell voltages at a chosen current density (obtained from all the polarization curves) can be plotted over time. Each current density represents a different dominant process, and information about the

specific losses occurring in the fuel cell can thus be obtained. A typical plot of cell voltage over time (cycle number) at one specific current density is shown in Figure 2.1.8. As the number of cycles increases, the cell voltage drops, due to degradation processes in the membrane, electrodes and bipolar plate. However, after the cell has been shut down overnight, there is an increase in the cell performance, which occurs due to an expulsion of liquid water in the cell. This corrects the humidification of the membrane and removes any water droplets that block gas transport to the three phase boundary [87]. This performance recovery after each shutdown is called reversible degradation of the cell.

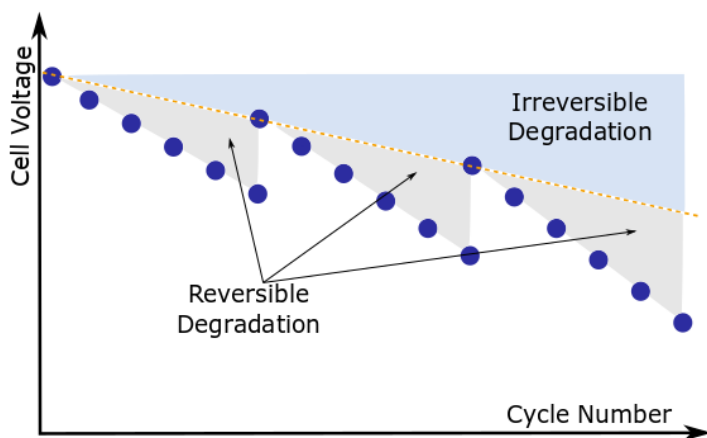


Figure 2.1.8. A typical response of a fuel cell when plotting the cell voltage against cycle number. Regions of reversible degradation are shown in grey, and the irreversible degradation is indicated by the blue region.

However, the performance will often not recover completely, and the performance of the cell will gradually get worse, even after the shutdowns. This drop in cell voltage is called the irreversible degradation. This degradation is caused by any irreversible changes happening within the fuel cell, including agglomeration of the catalyst nanoparticles, carbon support corrosion, destruction of the membrane from the presence of radicals, and oxide layer formation on the bipolar plates [87]. The slope of the yellow dashed line in Figure 2.1.8 can be used to calculate the irreversible degradation rate in mV/cycle or hour of operation, and this value can be compared against other fuel cells.

## Electrochemical Impedance Spectroscopy

Electrochemical Impedance Spectroscopy (EIS) is a very powerful technique to perform *in-situ*, as it provides a quick visualisation of the entire fuel cell and can easily monitor the progression of the different components over time. During a galvanic impedance measurement, an alternating current of varying frequency is introduced on top of a constant direct current, and the phase and amplitude of the resulting signal is monitored and plotted as a function of frequency (Bode plot), or the imaginary and real responses can be plotted against one another (Nyquist plot) [110]. The different processes within the fuel cell can be separated from one another by analysis of their time constant.

A Nyquist plot of an impedance measurement performed during fuel cell operation can be seen in Figure 2.1.9. Each of the features of the curve correspond to a different loss process occurring within the fuel cell.

The ohmic losses of the fuel cell are supposedly easy to observe from the intercept of the curve with the real axis in the high frequency region. Additionally, the anode and cathode activation losses can be deduced by fitting the curve to a series of semicircles. The first of these at the highest frequency represents the anode activation losses, which are much smaller than the cathode activation losses because the hydrogen oxidation reaction is much quicker than the oxygen reduction reaction that takes place on the cathode [111]. Additionally, the mass transport losses can be deduced from the low frequency feature of the impedance spectrum [112]. These features can be fitted to an equivalent circuit to obtain an accurate value for each loss process.

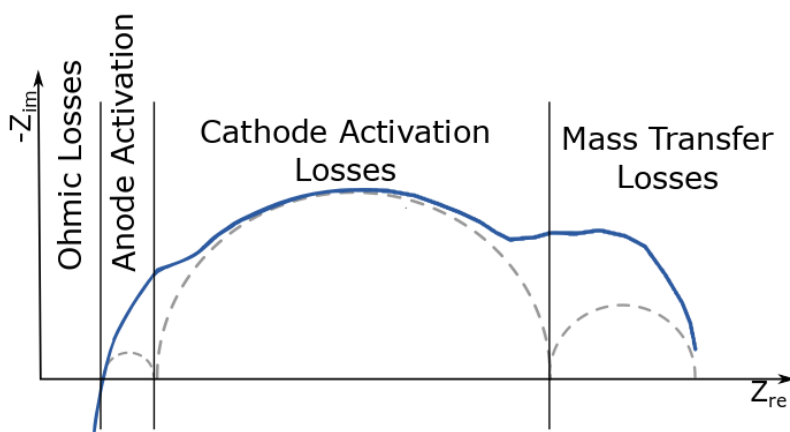


Figure 2.1.9. An example EIS spectrum, showing the features and the corresponding loss mechanism, adapted from [113] and [114].

In general, the interpretation of fuel cell impedance data can be difficult [113]. Therefore, the fitting of impedance spectra to equivalent circuit models should be performed to extract electrochemical parameters, for example the equivalent circuit shown in Figure 2.1.10 has been used in this work.

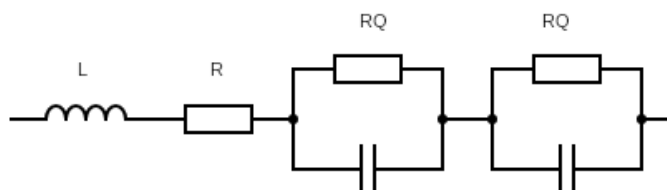


Figure 2.1.10. The equivalent circuit model used to fit EIS data in this work.

By monitoring these parameters and the shape of the impedance curve over time, the losses occurring during each process can be seen. This can be a very useful diagnostic tool to determine where the performance losses observed are specifically occurring. However, it is important to be aware that artefacts due to the cables or connections may be introduced when performing impedance with high DC loads [111]. Chapter 8 includes more details on the fitting performed and the equivalent circuit employed in this thesis.

## Additional *in-situ* techniques

Other common *in-situ* analysis techniques can specifically focus on characterisation of the catalyst layer (ECSA), membrane (H<sub>2</sub> crossover) or the bipolar plate (*In-situ* ICR), however these have not been used in this thesis.

The Electrochemical Catalytic Surface Area (ECSA) measurement uses cyclic voltammetry performed in the hydrogen underpotential deposition (H<sub>UPD</sub>) region to determine the surface area of the catalyst [115]. This surface area can be compared before and after cycling for different types of fuel cell to determine what kind of performance decrease comes from catalyst agglomeration or loss of active area due to carbon support corrosion.

Hydrogen crossover measurements analyse the permeability of the membrane, detect any pin-holes or thinning, damage due to radical formation. They involve performing a linear sweep with hydrogen on the anode and nitrogen on the cathode, and calculating the amount of hydrogen that has crossed over the membrane from the current density measured [116].

*In-situ* ICR can also be performed by placing gold wires in the fuel cell and measuring the voltage through the BPP to the GDL, then converting this to a resistance in the same way as is done *ex-situ*. It can be difficult to perform such measurements due to local variations in thickness of oxide layer and current distribution over the plates, leading to a good but not perfect correlation between *in-situ* and *ex-situ* ICR measurements [117].

## 2.1.5. Conclusion

The overarching theme of this PhD thesis is to improve the quality of commercial PEM fuel cells through innovation of the bipolar plate. A new coating method based on the electrodeposition of metallic Sn will be investigated. The aim is for it to fulfil the criteria for bipolar plates outlined in this chapter, including the US DoE 2020 targets. The evaluation of the coatings developed in this thesis will use many of the characterisation techniques outlined above, including SEM and EDS mapping, ICR analysis, and both *ex-situ* and *in-situ* electrochemical testing.

## 2.2. Electrodeposition

### 2.2.1. Introduction

Electrodeposition is a technique that is widely used to create a layer of metal on a conductive substrate, via the reduction of metal ions from an electrolyte. It provides a simple, highly tuneable method, which can be applied to a huge variety of metals and substrates, and is the main technique used in this thesis to create coatings for bipolar plates.

This thesis will specifically look at the case of Sn electrodeposition, which is simple at low pH but may become challenging when additional alloying elements are added. The feasibility of electroplating Sn and Sn alloys onto steel substrates for use in bipolar plates in PEM fuel cells is investigated in this thesis work.

### The concept of electrodeposition

Electrodeposition is the reduction of metal ions from electrolytes, with the necessary electrons being provided by an external power supply or a reducing agent in the solution (known as electroless deposition) [118]. In aqueous solutions, the following equation (eq.2.2.1) holds:



A simple sketch of a standard electrodeposition setup is shown in Figure 2.2.1, where the necessary components are: Anode (where the oxidation process occurs, often a bulk electrode of the same metal as being deposited), cathode (where the reduction occurs, hence the substrate that the deposition will occur on) and the electrolyte (comprised of ions, including metal cations to be deposited on the cathode), as well as an external power supply that completes the circuit and is needed to drive the electrodeposition.

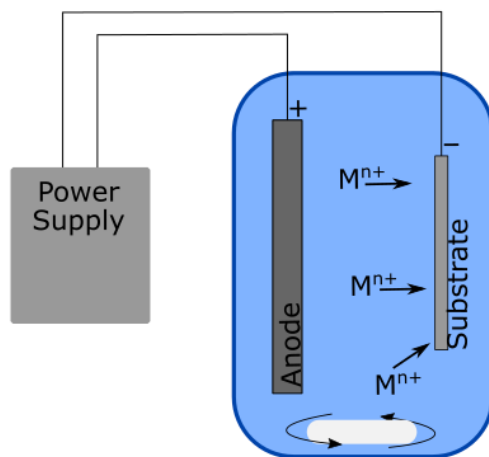


Figure 2.2.1. A standard electrodeposition setup, where an external power supply forces the movement of electrons and metal ions from the electrolyte to the cathode (substrate), where they are reduced to form a layer of metal.

During electrodeposition, the amount of deposit produced is directly proportional to the amount of charge passed, and can be calculated using Faraday's equation for electrolysis (eq.2.2.2, assuming constant current electrodeposition):

$$m = \frac{M I t}{n F} \quad (2.2.2)$$

, where  $m$  is mass of deposit (g),  $M$  is the molar mass of the deposit ( $\text{g mol}^{-1}$ ),  $I$  is the current (A),  $t$  is time or duration of the electrodeposition (seconds),  $F$  is Faraday's constant ( $96485 \text{ C mol}^{-1}$ ) and  $n$  is the valency of the ions being deposited (i.e. number of electrons being transferred per deposited metal atom). However, if some of the current is used to other processes, such as hydrogen evolution, the deposited metal will be less than expected from the Faraday's equation. Current efficiency,  $CE$ , is defined as the ratio of the actual mass deposited to the theoretical mass from Faraday's equation (eq. 2.2.3) and is an important quantity in electrodeposition of metals.

$$CE = \frac{\text{measured mass}}{\text{theoretical mass}} \cdot 100\% \quad (2.2.3)$$

## The deposition potential and overpotentials

In general, for the electrodeposition reaction to occur, the metal ions must move from the bulk solution to the electrode, where they adsorb onto its surface and undergo the above reduction reaction (eq. 2.2.1), before being added to the crystal lattice of the deposited metal. The Nernst equation determines the thermodynamic (minimum) potential,  $E$ , needed for this reaction to take place (eq. 2.2.4), where  $E^0$  is the equilibrium potential at standard states (i.e. all activities equal to 1),  $n$  is the number of electrons being transferred during the reaction,  $T$  is the reaction temperature,  $R$  is the universal gas constant ( $8.3145 \text{ J K}^{-1} \text{ mol}^{-1}$ ),  $F$  is the Faraday constant and  $Q$  is the reaction quotient.

$$E = E^0 - \frac{RT}{nF} \ln Q \quad (2.2.4)$$

If this potential is reached, the reaction can theoretically take place, but some overpotential is needed in order to allow the electrode reaction to occur. This overpotential, or kinetic limitation, relies on how well the surface promotes electron transfer (catalyses the reaction) and kinetic considerations must be taken into account to determine whether the reaction will actually take place, and how quickly it will occur [118].

The overpotential (eq. 2.2.5), which is needed to allow the electrode reaction to occur, is the difference between the actual potential at the electrode (deposition potential) and the equilibrium potential calculated using the Nernst equation.

$$\eta = E(\text{actual}) - E(\text{equilibrium}) \quad (2.2.5)$$

The total overpotential is comprised of all hindrances observed in the cell, relating to charge transfer ( $\eta_c$ ), diffusion ( $\eta_d$ ), reaction ( $\eta_r$ ) and crystallisation ( $\eta_{cr}$ ), as observed in eq. 2.2.6 [119].

$$\eta = \eta_{ct} + \eta_d + \eta_r + \eta_c \quad (2.2.6)$$

Each overpotential contributes to slowing down the kinetics of the reaction and describes a physical phenomenon that occurs when deposition takes place.

- The charge transfer overpotential relates to the movement of electrons or charged species across the electrical double layer at the surface of the electrode. For highly conductive solutions, as are the norm for electrodeposition, this overpotential is minimal.
- The diffusion (also known as concentration) overpotential relates to the concentration difference between the bulk of the electrolyte and the electrode surface, where the reaction happens. Movement of species between the bulk solution and the electrode surface can be slower than the charge transfer kinetics at high overpotentials, creating a concentration gradient. If all the reactant species are used up immediately as they approach the electrode surface, the rate of reaction is controlled by the movement of the species to the surface, and therefore the rate of diffusion. When at high overpotentials (fast kinetics), the reaction is diffusion controlled, the surface concentration is zero. This limiting current density,  $j_b$  can be used to calculate the diffusion overpotential (eq. 2.2.7):

$$\eta_d = \frac{RT}{nF} \ln \left( 1 - \frac{j}{j_b} \right) \quad (2.2.7)$$

- The reaction overpotential accounts for unwanted reactions taking place both in the bulk of the solution and at the electrodes.
- The crystallisation overpotential arises from the energy needed when metal atoms are added and absorbed into the crystal lattice.

The summation of these overpotentials shows the hindrance of the deposition and describes how quickly the reaction will take place at a given electrode potential. If the overpotential is extremely high, the rate of deposition will likely be very slow and challenging, and the likelihood of dominating side-reactions such as hydrogen evolution increases [119].

## The Butler Volmer and Tafel Equations

For a simple one-electron outer-sphere charge transfer reaction with no diffusion limitations, the current follows a simple equation, where the anodic ( $j_a$ ) and cathodic ( $j_c$ ) current densities both depend exponentially on the overpotential,  $\eta$ . This relationship is shown in the Butler-Volmer equation (eq. 2.2.8), where  $j$  is the overall current density,  $j_0$  is the exchange current density,  $\alpha_a$  and  $\alpha_c$  are the anodic and cathodic transfer coefficients, respectively, and  $\eta$  is the charge transfer overpotential [120]:

$$j = j_0 \left[ \exp \left( \frac{\alpha_a F}{RT} \eta \right) - \exp \left( \frac{-\alpha_c F}{RT} \eta \right) \right] \quad (2.2.8)$$

Electrodeposition involves inner-sphere reactions steps with no general law for the current-potential relationship. However, often a Butler-Volmer type of relation is found to hold also for such reactions, for example when the rate-determining step is an outer-sphere electron transfer or an inner-sphere electron transfer from an adsorbed species to the metal electrode. We will use the Butler-Volmer equation in the following to conceptually visualize reaction currents at the electrode and current efficiencies.

For large overpotentials (about  $70/n$  mV), the current response will be dominated by either the anodic or cathodic current. One can therefore ignore the smaller one and hence the Butler-Volmer equation reduces to the Tafel approximation[120]. Figure 2.2.2 shows a plot of the logarithm of current density as a function of overpotential based on the Butler-Volmer equation, with the Tafel approximation clearly seen as the linear regions at either high anodic or high cathodic overpotential. The slope of this linear region is called the Tafel slope and together with the exchange current density are the two most important kinetic parameters.

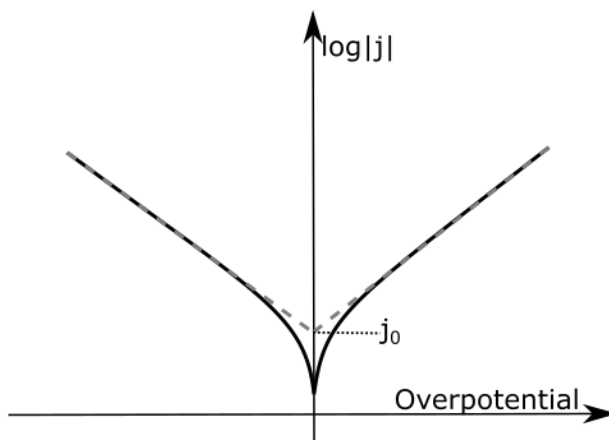


Figure 2.2.2. A visualisation of the Tafel Equation, showing the linear region where the equation is valid, extrapolated to find the exchange current density.

Extrapolating this linear region to a point of zero overpotential gives the exchange current density,  $j_0$ . This is specific to each reaction and electrode material and shows the number of electrons flowing in the backwards and forwards directions, directly telling the capability of the surface to exchange electrons. Although there is no overpotential applied (no net current), electron transfer is still occurring, and the exchange current density describes how active the surface is towards the specific reaction. If the exchange current density is high, the kinetics of the reaction are favourable and will likely continue to be favourable at all applied potentials.

It should be noted that the reaction rates for electrodeposition are very dependent on the conditions, including the substrate, pH, temperature and any additives present that may change the surface. In case of diffusion limited deposition, altering the convection by agitation also affects the electrodeposition rate.

Using these parameters is an effective way of comparing the kinetics of multiple reactions happening at the same electrode, and visualising which reaction will be favourable at certain sets of conditions. For example, if we take reaction A, which has a certain reversible potential,  $E_{rev}^A$ , and a certain exchange

current density,  $j_0^a$ , illustrative Tafel plots can be drawn as shown in Figure 2.2.3. This can visually tell us how the reaction rate changes with applied potential and effect of other electrode reactions occurring simultaneously.

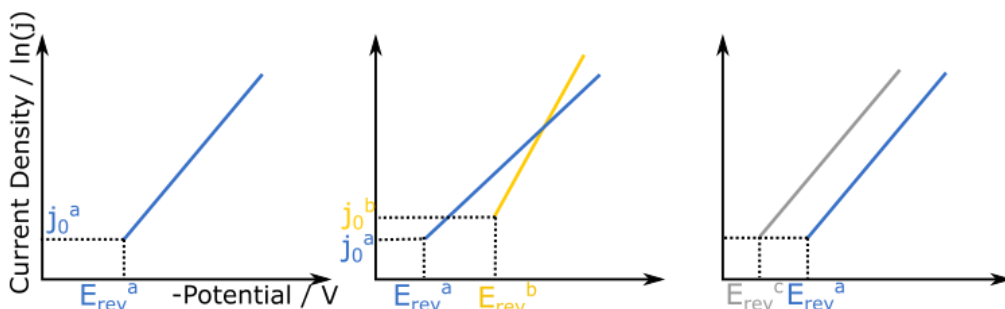


Figure 2.2.3. Kinetics diagrams showing the Tafel slopes for various hypothetical reactions. A comparison of reaction A (blue) with reactions B (yellow) and C (grey) shows that by modifying the applied potential or current, reaction B is favoured over A, however, reaction C is favoured over reaction A at all potentials.

All reactions taking place on the electrode must be considered, so if the side reaction B (this could be a secondary metal deposition or a gas evolution reaction) occurs on the same electrode, the Tafel curve can also be plotted based on its exchange current density and Tafel slope. As shown in Figure 2.2.3, for these hypothetical reactions A and B, initially the reaction of A is favoured, due to the more positive deposition potential. However, when forcing the deposition potential to be more negative, the reaction B becomes more and more favourable, and takes a larger share of the current, hence the current efficiency towards deposition of A reduces. At some point when the two Tafel curves meet, the reaction of B becomes more favourable than A, and eventually reaction B is so dominating that almost no A will be deposited. Therefore, by tuning the deposition parameters, the final deposition product can be tuned.

However, for some types of reactions, forcing the reaction to take place at a certain potential or current density will not change the ratio of the products. This occurs when the Tafel slopes are similar or diverging, for example in Figure 2.2.3, when comparing the behaviour of reactions A and C. Here, whichever current density or potential the deposition takes place at, reaction C will be favoured over A, and other parameters such as the temperature or electrode type must be altered in an attempt to obtain A.

Therefore, it is important to obtain kinetic information about the deposition potentials, exchange current densities and Tafel slopes of the deposition reaction and any side reactions and their dependence on bath composition, substrate material and temperature to determine whether the desired reaction will be favoured at any set of conditions.

## Diffusion Limitations

At some point, when the overpotential is very high and the reaction is occurring very quickly, the current is limited by the rate of mass transport to the surface of the electrode. If the rate of reaction is quicker than the diffusion of reactants to the reaction site (the electrode surface) then reactants will become depleted, and the reaction is said to be diffusion limited. This produces a concentration gradient between the electrode surface and the bulk electrolyte. The area close to the surface that

contains this concentration gradient is called the diffusion layer and the thickness of the diffusion layer,  $\delta$ , for a constant current is (not considering natural convection) given in eq. 2.2.9 [121]:

$$\delta = \sqrt{\frac{4Dt}{\pi}} \quad (2.2.9)$$

, where  $D$  is the diffusion coefficient (in  $\text{cm}^2 \text{s}^{-1}$ ) of the active species, and  $t$  is the time (in seconds) held at the constant current. The limiting current density,  $j_l$  (eq. 2.2.10) occurs when the concentration of reactants at the electrode surface is zero, and the rate of reaction is controlled by the transport of reactants to the surface.

$$j_l = \frac{nFDc_b}{\delta} \quad (2.2.10)$$

, where  $c_b$  is the bulk concentration (in  $\text{mol dm}^{-3}$ ). By combining the contribution from the B-V equation (eq. 2.2.8) whilst taking into account diffusion limitations, the steady state current density / potential characteristics for a wide range of overpotentials can be obtained. This is schematically illustrated in Figure 2.2.4.

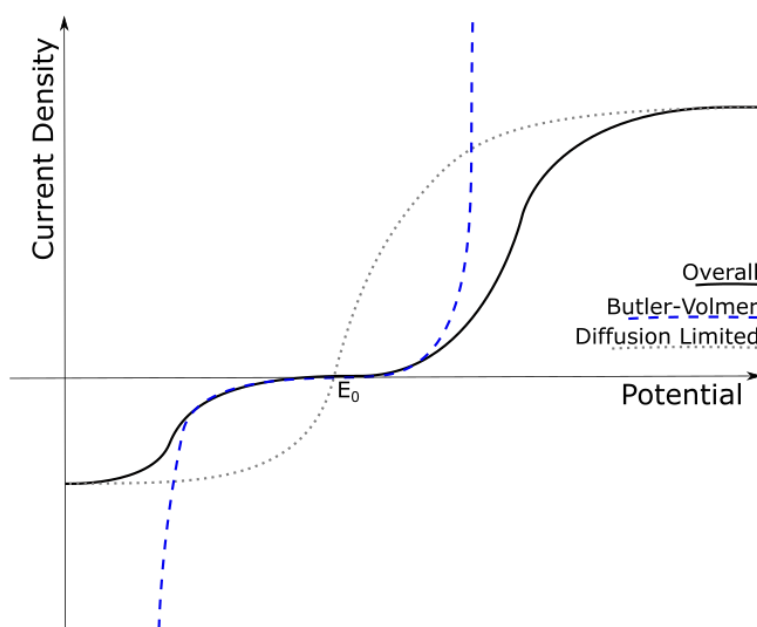


Figure 2.2.4. A characteristic current density profile showing the overpotential regions limited by mass transport (diffusion) and electron transport (Butler Volmer).

## Nucleation and Growth

The first stage in the electrodeposition of a deposit onto a surface is the arrival and adsorption of atoms onto that surface. Metal ions in solution are hydrated, so must lose their hydration sphere before adsorbing onto the surface. Once adsorbed onto the surface, the ions undergo a charge transfer

reaction, to become metallic adatoms. These adatoms can move around the surface by diffusion until they reach a favourable site, attaching to the crystal and forming clusters or adding onto the edge of steps [122].

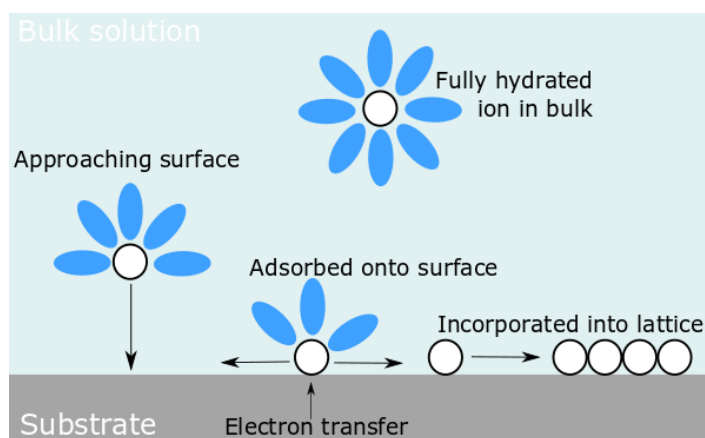


Figure 2.2.5: The stages involved in depositing an atom from the bulk solution to the lattice of a deposit.

The nucleation of each atom is composed of a bulk energy contribution and an interface energy contribution. As an atom is added to the surface, the interface energy of the surface increases due to an increase in the surface area. However, the bulk energy of the surface decreases as ions are transferred from the solution to the crystal phase. An atom alone on the surface has a very high interfacial energy, so in order to become energetically favourable it needs to form a cluster to reduce the bulk energy, reducing the relative surface area compared to the bulk size. The size at which the overall energy of the cluster starts to decrease is called the critical size, and has a critical radius ( $r_c$ ) of [122]:

$$r_c = \frac{2\sigma V_m}{nF\eta} \quad (2.2.11)$$

, where  $V_m$  is the molar volume of the atom ( $\text{L mol}^{-1}$ ),  $\sigma$  its surface energy ( $\text{J m}^{-2}$ ) and  $n$  the number of electrons needed to completely reduce it. From this equation, it is clear that at high overpotentials, it is easier to form a critical nucleus as the critical radius needed becomes smaller. This phenomenon allows grain size to be tuned by changing the overpotential, however if the overpotential is too high and a limiting current is reached, a dendritic deposit is likely to form.

There are two types of nucleation, distinguished by the size of the nucleation constant [123]. A high nucleation constant leads to instantaneous nucleation, where all the nucleation sites are covered almost immediately. The nuclei then proceed to grow until they contact one another, and a monolayer is formed. If there is a small nucleation constant, the number of nuclei is a function of time, i.e. they form and grow gradually, eventually overlapping to form a monolayer with clusters on top. This is called progressive nucleation. In both cases, nucleation occurs first at the defect sites on the crystal, as they are energetically preferential.

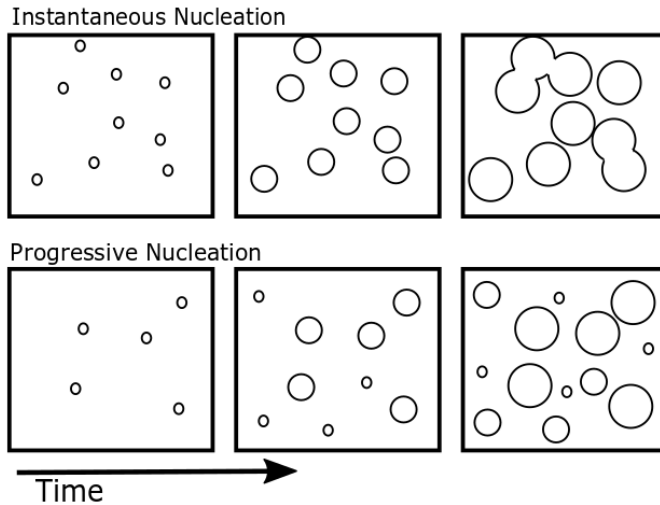


Figure 2.2.6: The growth of nuclei in instantaneous and progressive modes.

Each of these nucleation methods can proceed to form multilayers. At low nucleation rates, when the overpotential is low, layer-by-layer growth is preferred. Atoms energetically prefer to add to a nucleus instead of forming a new one, creating layers of atoms, like steps that grow along the surface. At high nucleation rates and high overpotentials, multinuclear growth is preferred. Isolated islands of atoms grow together to form a linked structure, which is 'filled in' after further deposition [123]. This growth type produces deposits that have small grains and are more likely to have voids or dislocations at grain boundaries.

Kinetics also plays a role in the type of nucleation. There is an energy barrier for atoms to move up or down steps, and atoms can move around on top of steps, before either adsorbing onto a step edge or dropping down to a lower step. If the amount of movement on top of a step is much larger than the size of the step, then multinuclear growth will proceed, as atoms add to the top of each step/nucleus and do not necessarily fill in the whole step first (3D growth). If the amount of movement of the atom is low, it will quickly adsorb onto the step edge and growth will proceed in a layer-by-layer way (2D growth) [124,125].

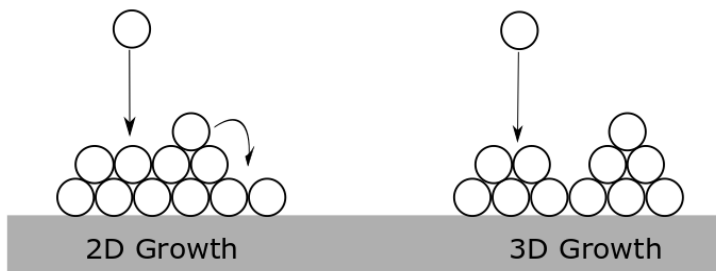


Figure 2.2.7: 2D and 3D growth mechanisms.

## 2.2.2. The Practicalities of Electrodeposition

The final deposit achieved from electrodeposition is defined by a number of factors. Although the nucleation and growth modes determine the microstructure and therefore influence the properties of the final deposit, other parameters must be considered [126]. Primarily, a suitable plating bath including anode type and substrate material must be identified. Specific metal salts, complexing agents and other additives are needed to obtain the desired grain size and material properties. Furthermore, bath variables have a large effect on the deposit and must be tuned. The pH, concentrations, current density, temperature and agitation amongst others are important and should be specifically tailored to achieve the correct surface finish and properties.

Most metals have previously been deposited from aqueous solutions, so a simple literature search can identify a good bath formulation, as well as suitable anodes and substrate materials.

### Anodes and Current Distribution

Anodes can be grouped into two types: soluble and insoluble.

- Soluble anodes are made of the same material as is being deposited. For every metal ion deposited onto the cathode, an ion is dissolved from the anode to maintain the concentration in the plating bath. However, the anode may react with the bath, generating a parasitic current and increasing the wear of the anode.
- Insoluble anodes are made from an inert material that is not being deposited and will not react with the solution. They retain their dimensions and do not produce any suspended particles in the bath, however, the metal concentration and pH (in case of oxygen evolution at the anode) of the bath will decrease over time. Therefore, careful monitoring and maintenance of the bath is needed.

The positioning of the anode is very important to obtain a high quality deposit. The anodes should be large enough to provide sufficient current for the deposition and should be positioned far from the cathode to achieve an even current distribution. However, the current distribution will be higher at any edges and points of the cathode due to the 'bunching' of current lines, meaning more deposition will take place in these areas, and the thickness of the layer will be increased [127]. If necessary, supporting anodes can be added to even out the current distribution, and any edges on the cathode can be rounded off. The electroplating solution itself should have a high conductivity and polarizability, and a low current density should be used to form an even film. The effect of current distribution can be experimentally studied using a Hull Cell [128].

### Additives

Additives have many specific functions including stabilising or complexing ions in solution, and brightening, refining or reducing stress in the deposit. Additives compete with water and other species to adsorb on the surface of the cathode, and there is generally a potential range in which the adsorption of the additive is preferred. Increasing the concentration of additive increases the potential range in which it is stable, however this only occurs when the surface is at a potential of zero charge. If not, the adsorption of charged species is preferred. Any adsorbate will selectively adsorb on a fraction of the

high-energy surface sites, blocking them and reducing the number of sites available for nucleation. They can therefore slow the growth or alter the morphology of the surface [129].

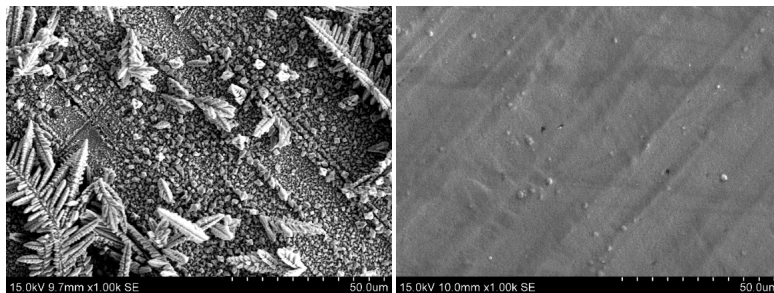


Figure 2.2.8: SEM images of the structure of a Sn layer deposited A - without and B - with levelling and brightening agents.

Specific additives have different functions, for example a uniform deposit can be obtained by adding a levelling agent to the bath. These agents accumulate at the peaks as they are more accessible under mass transfer control, thus inhibiting deposition in the protruding areas and producing a more levelled out deposit. Grain refiners can produce bright surfaces with a small grain size by selectively blocking deposition onto the large particles, leading to the growth of new and smaller particles. Other additives can stabilise certain complexes in the solution, favouring the deposition of certain elements in an alloy, or suppress hydrogen evolution to obtain deposition at a greater current range and high current efficiency.

Additives are not used up in the electrodeposition process; therefore, they must be able to adsorb and desorb from the surface. If the rate of adsorption/desorption is slow, additive molecules can become trapped in the deposit, leading to brittle deposits with higher resistance [130]. If the electrode kinetics become slow, some additives may also undergo unwanted oxidation at the anode.

## pH

The pH has an impact on the deposit for a number of reasons. Firstly, the pH can change the deposition potential of a metal in a way that can be predicted from the Pourbaix diagram. It is common for the deposition potential to decrease with an increase in pH. It is also possible that the stable species in the bath can change with a change in pH. This can lead to solid precipitates in the bath, therefore reduced deposit quality, or a reduced current efficiency due to higher valency ions being deposited [131].

Any deposits that are in oxide form can be rough, dull and have a worse adhesion to the substrate, being of overall lower quality. This can be seen for the deposition of Sn under different pH, in the SEM images in Figure 2.2.9. The deposit goes from being bright with small grains at low pH to being dull and rough at higher pH, with long needles of SnO<sub>2</sub> obvious in the SEM image at pH 3.0.

Additionally, complexing agents or additives in a bath may be sensitive to small changes in pH, which can change their stability, solubility or ability to complex certain ions.

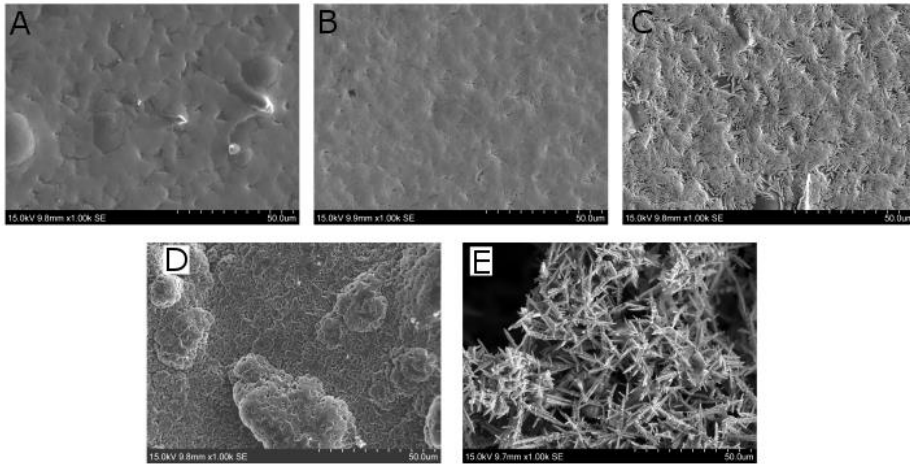


Figure 2.2.9: SEM images of the structure of a Sn layer deposited at various pH: A - pH -1.0; B - pH 0.0; C - pH 1.0; D - pH 2.0; E - pH 3.0.

## Temperature

Small fluctuations in temperature can harm the deposit quality and the rate of deposition; however, a well-formulated bath can operate within a larger range of temperatures. In such baths, increasing the temperature often increases plating rates [131]. The temperature will also have an impact on the deposition potential, as predicted by the Nernst equation, and also on the Tafel slope and exchange current density [132].

In Figure 2.2.10, it can be seen that increasing the deposition temperature increases the roughness of the surface. This is because at higher temperatures, electrode kinetics are much faster, so the ions add on top of one another instead of in a layer-by-layer way. Additionally, at higher temperatures it is likely that the adsorption strength of additives at the surface reduces, so will not have the same levelling effect that they do at lower temperatures [133].

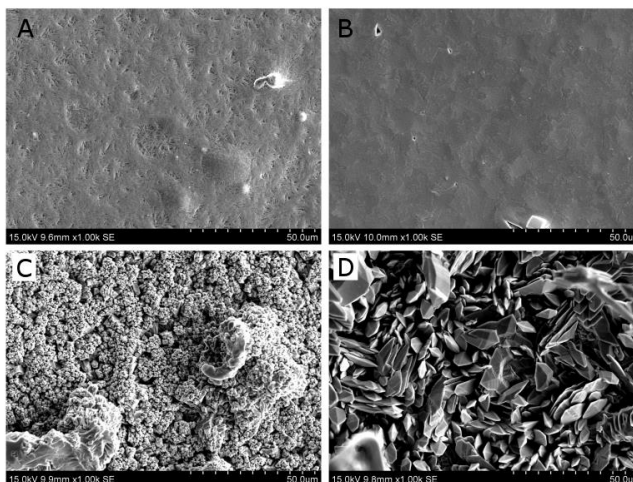


Figure 2.2.10: SEM images showing structure of a Sn layer deposited at various temperatures: A - 20 °C; B - 40 °C; C - 60 °C; D - 80 °C.

## Agitation

Agitation of the bath reduces the thickness of the diffusion layer and therefore increases the limiting current density. It increases the concentration of metal ions in the diffusion layer, until it approaches the concentration of the bath, but does not change the bulk properties of the bath. Controlling the agitation is most important for the deposition of alloys, as it can alter the alloy composition [134]. Due to the reduction in the size of the diffusion layer, increasing the agitation of the bath leads to a higher nucleation rate, which decreases the grain size of the deposit, as seen in Figure 2.2.11.

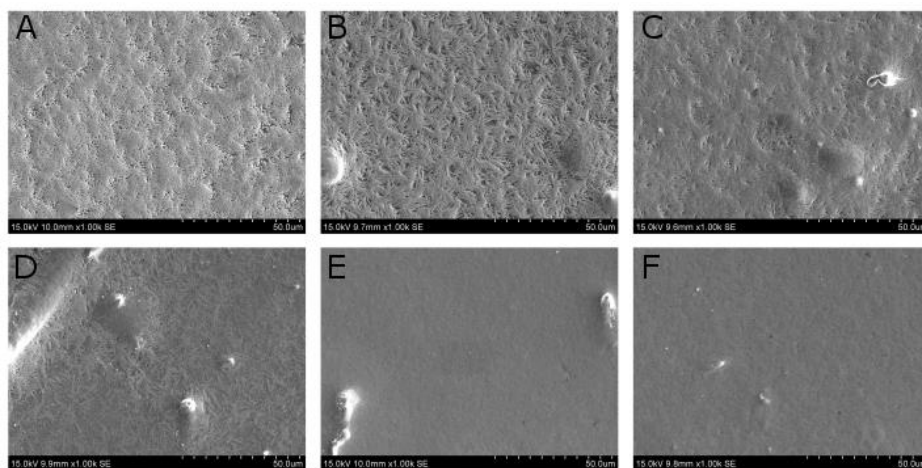


Figure 2.2.11: SEM images of the structure of a Sn layer deposited at various stirring speeds: A - 0 rpm; B - 100 rpm; C - 150 rpm; D - 200 rpm; E - 300 rpm; F - 500 rpm.

## Current Density

The current density of the bath has a great impact on the deposit. If the current density is too low, the deposit may have poor coverage and a low plating rate. However, if the current is too high, hydrogen evolution can take place, forming uneven deposits due to gas bubbles on the surface, and increasing the local pH, perhaps including hydroxide impurities in the deposit.

The impact that the current density has on the deposition can be predicted from the Tafel plots, as seen in Figure 2.2.3. The kinetics of the hydrogen evolution and metal deposition must be compared to determine the specific effects. However, as the Tafel equation is only valid at lower overpotentials. As the overpotential increases, the metal deposition reaction will become mass transport limited, but the hydrogen evolution will not, or not to the same degree, therefore it will eventually dominate. This is clearly seen from the measured current efficiencies as a function of current density in Figure 2.2.12. In the current density range used here the current efficiency decreased with increased current density due to a larger contribution to the current from hydrogen evolution.

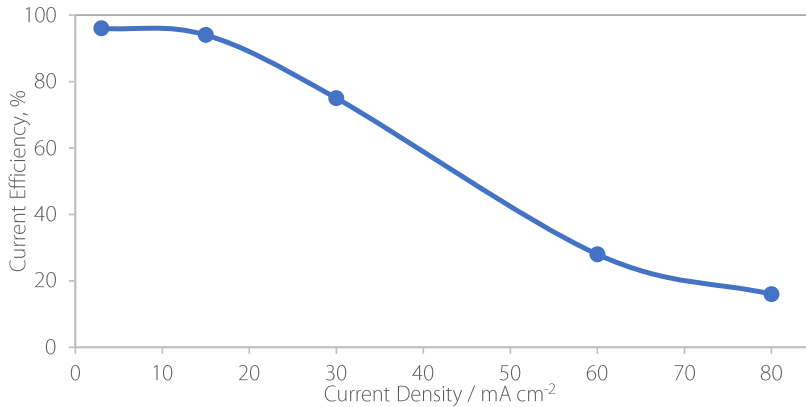


Figure 2.2.12: The effect of current density on the current efficiency of deposition, for the deposition of Sn from a sulphate bath at 25 °C.

Without being excessively high, increasing the current density increases the overpotential and leads to smaller grain sizes. However, when moving to higher current densities, hydrogen evolution has more of an impact and a rougher deposit is obtained, because of the presence of hydrogen bubbles on the surface of the deposit.

## 2.2.3. Electrodeposition of Alloys

### Co-Deposition of Alloys

Two or more different types of metal ion can be co-deposited to form an alloy. Here, the kinetics of the two deposition reactions are very important to determine whether deposition is possible, and the impact that changing certain deposition parameters will have. Generally, any factor that impact the kinetics of the deposition has the potential to change the composition of the alloy produced.

Firstly, in order to co-deposit two different metals, their deposition potentials should be close to one another, otherwise the more noble metal will deposit exclusively [135]. If the deposition potentials are not close together, there are some ways by which they can be brought together. Firstly, one can reduce the concentration of the more noble metal, however, when the concentration of the bath becomes very low, deposits become unreliable. In general, the dependence between concentration and potential is logarithmic, meaning very large reductions in concentration need to be made to have a significant impact on the deposition potential [131]. Therefore, a better way to approximate two potentials is by using a complexing agent. All metals have a more negative potential when complexed, which crowds the potentials closer together allowing easier co-deposition [133]. In 'mixed baths', multiple different complexing agents can be used, each of which forms a complex with a different metal. In general, complexing agents are very useful, however they should not be used with less noble metals as they can reduce the deposition potential into the hydrogen evolution region, lowering efficiency.

### Types of Co-deposition

If co-deposition can be achieved, it will fall into one of five different types of co-deposition, defined by their response to various bath conditions and control mechanisms [136].

In regular co-deposition, the bath is under diffusion control, so any changes of metal concentration in the cathode diffusion layer affect the metal ratio in the deposit. Any parameters that increase the amount of a metal ion in the diffusion layer will increase the amount of that metal in the deposit, such as increasing the temperature, agitation of the bath or increasing the total metal concentration in the bath. All of these favour the metal that was already depositing preferentially, and tend towards the ratio of the bath.

Irregular co-deposition is controlled more by the metal potentials than the diffusion. This is most likely to occur in solutions of complex ions of metals with similar static potentials, and metals that can form a solid solution together. The effects of plating variables on deposit composition are smaller for metals that co-deposit irregularly than those that do so regularly.

Equilibrium co-deposition is achieved when the ratio of the two metals in the deposit is the same as the ratio of metals in the bath. The amounts of metal in the diffusion layer are already the same as those in the bath, and the deposition is in equilibrium, so the effects of temperature and agitation are minimised. The current density has an unpredictable effect on the deposit composition, dependent on the individual metals and other bath parameters.

In anomalous co-deposition, the less noble metal deposits preferentially, but only under certain bath concentrations and operating variables. This type of deposition is rare.

Induced co-deposition is the deposition of alloys containing metals that cannot be deposited alone (reluctant metals) with metals that induce the deposition. In general, the influence of plating parameters on the metal content of such alloys is small and inconsistent.

## Practical considerations

A number of bath variables can be tuned to deposit an alloy of desired composition [131]. Increasing the amount of a metal ion in the bath will increase the exchange current density [132], indicating more active kinetics and favourable deposition. However, as many baths use complexing agents to approximate the deposition potentials and allow co-deposition, the concentration of any complexing agent has a great influence on the metal ratio in the deposit. Increasing the complexing of a metal lowers its deposition potential, so it is less readily deposited. If the complex is the same for both metals in a bath, little effect is seen, however for mixed baths, the amount of metal in a deposit varies with the concentration of 'free' complexing agent.

Changing the pH has a more specific effect, depending on which complexes the metal ions form in solution. Simple metal ions are usually unaffected by pH, but the stability of many complex ions can change with pH. The Pourbaix diagram can indicate whether changing the pH will impact the deposition potential of any simple ions in the bath. If there are multiple different complexes in a bath, changing the pH will affect each to a different extent, changing the composition of the deposit.

Temperature has a variety of effects on the bath, some of them competing. Firstly, deposition potentials can change with temperature, but these effects are specific to certain metals, and hard to predict. The concentration of the metal ions in the diffusion layer increases with bath temperature, favouring the metal that was already preferentially deposited. Finally, the cathode current efficiency is affected by

temperature, in a specific way. Therefore, the effects of temperature are specific to the alloy and bath, so are hard to predict.

Increasing the current density will firstly impact the kinetics of the deposition as predicted by the Tafel plots, however once the current density increases to the point of diffusion control, further increases can encourage the less noble metal to deposit (as the more noble metal is already at its diffusion limit). This effect reaches a limiting value at some point, and the composition of the deposit tends towards the composition of the bath. Additionally, side-reactions such as hydrogen evolution may become more prevalent as the current increases far beyond the diffusion limitations, as indicated in Figure 2.2.12.

Finally, agitation reduces the thickness of the diffusion layer, and increases the concentration of metal ions in the diffusion layer. This favours the metal that was already preferentially depositing, but the magnitude of the effect is determined by the type of co-deposition. If the composition changes greatly with agitation, the system is under diffusion control.

## 2.2.4. Electrodeposition of Sn

Commercial electroplating of Sn was developed in the 1850s and has become a popular technique due to its low cost, simplicity and good controllability of coating morphology and thickness. It is very easy to electrodeposit Sn in acidic media, using soluble anodes of pure (> 99.9 %) Sn. At pH < 1, the dominating reaction is [137]:



Under ideal conditions, the current efficiency should be close to 100 %, however side reactions such as hydrogen evolution can occur. As the pH increases above 1, Sn<sup>4+</sup> becomes the dominating ion in solution. Although this can be deposited, the amount of current that needs to be passed is twice as much, reducing the current efficiency by 50 %, so it is preferential to deposit at low pH.

There are many industrial plating baths available nowadays, allowing for a variety of finishes on different substrates. Sulphate baths are commonly used as they have high current efficiencies at low current densities. They are also low cost and easy to maintain, in part because they operate at room temperature and are generally lower toxicity than other acid baths, making waste management easier. Sulphate baths have a high throwing power, however they can undergo anodic passivation at high current densities, and are highly susceptible to Cl<sup>-</sup> impurities [137]. Other common Sn deposition baths are fluoroboric acid, phenolsulphonic acid or hydrochloric acid based.

### Tin Whiskers

Whiskers are hair-like single crystal filaments that spontaneously grow from electroplated Sn and Sn alloys [138]. When a surface is under compressive stress, whiskers can extrude from the surface after a certain incubation time that can range from days to years, causing problems such as short-circuiting of electrical equipment. Whiskers usually have very high conductivity and strength, up to 1000 times higher than other Sn single crystals [137].

It is not entirely well-know how whiskers form. The growth phase of whiskers requires Sn atoms to diffuse from the bulk to the nucleation sites, so having smaller grains and more grain boundaries leads

to more diffusion and more whiskers [138]. The interfaces between Sn and its substrate or the air above it can also lead to the growth of whiskers. It is thought that surface oxide layers that form immediately after deposition can reduce whisker formation as they act as a physical barrier to stop whiskers erupting from the surface. However, it has also been said that whiskers propagate through defect sites in the surface oxides. The whiskers themselves often contain oxygen, which may come from the surface oxide or from Sn being oxidised after formation. Additionally, the intermetallic compounds that form between the Sn and the substrate through diffusion can increase the stress in the Sn layer and lead to whiskers. However, like the surface oxides, if the intermetallic is regular and dense, it can act as a physical barrier and inhibit the growth of whiskers.

To prevent whiskers from forming, an alloying element can be added to the Sn, which may reduce residual stress in the coating and stop whiskers from growing. Reflowing the coating after deposition can also have this effect, as can using a barrier layer to stop the formation of intermetallics and the build-up of stresses. It is only compressive stress that leads to whisker formation, meaning that by maintaining tensile stress in the deposit also suppresses growth.

## Tin Alloys

Sn can be alloyed with many different materials for a variety of different purposes. Alloys deposited at their eutectic point have a lower melting temperature than other compositions, so are widely used as solder materials. Some examples of these, seen in Figure 2.2.13, are Sn-Cu containing 0.7 % Cu, with a melting point of 227 °C, it is used for low-cost electronics applications. Sn-Ag at 3.5 % Ag has a melting point of 221 °C and exhibits good fatigue resistance, and Sn-Bi eutectic at 57 % Bi has a very low melting temperature of 139 °C. However, eutectic SnBi can be brittle with low ductility, so the alloy containing 2-3 % Bi is most widely used.

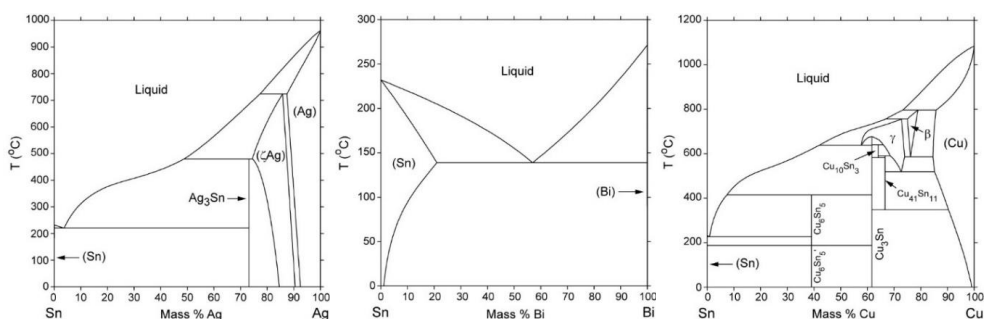


Figure 2.2.13: Phase diagrams of binary Sn alloys. A, SnAg [139]; B, SnBi [140]; C, SnCu [141].

Compared to Pb, these alloying elements have substantially higher redox potential than Sn, meaning that to deposit the alloy, complexing agents are needed, or conditions must be kept in the diffusion-limited region. In this case, the more noble metal does not have time to completely deposit, and a mixture of the more and less noble metal can be obtained.

### 2.2.5. Electrodeposition in this thesis

It has been demonstrated that electrodeposition is a powerful technique that can be used to form a thin layer of a range of metals and alloys onto a conductive substrate of any shape and size. In this thesis,

electrodeposition in aqueous plating baths was used to create layers of coatings onto bipolar plates for use in PEM fuel cells. With the information in this introduction chapter, the electrodeposition of tin and tin alloys can be performed, and the importance of fine control of certain electroplating parameters is described, thereby allowing specific compositions, surface finishes and microstructures to be obtained.

## 2.3. Tin as a solder material to join the BPP and the GDL

Tin has been in use since as early as 3500 BC, where during the Bronze age it was alloyed with copper to produce bronze icons, tableware and weapons. In more modern times, tin has been used for several major applications, including protective coatings for food containers (tin cans), solder materials, in the glass making process, and in the chemical industry.

Its major use today is as a solder in the electronics industry, where it is suitable due to its high electrical conductivity, good wettability, low cost and reliability [142,143]. It also has a low melting point, 231.9 °C [144], and has historically been alloyed with lead to increase solderability by reducing this further, but more recently with elements such as bismuth, copper and silver due to the negative health effects of lead exposure. Another emerging use of tin is in the same industry, where Indium Tin Oxide (ITO) is a popular material for LCD screens, anti-icing coatings and solar panels due to its transparent and conducting nature.

In this thesis, we investigate whether the long history of tin at the forefront of technology could continue with its use for bipolar plates for PEM fuel cells, and the ushering in of the green revolution in sustainable technology.

### 2.3.1. Tin for use in PEMFCs

Firstly, to understand whether tin would be suitable material for use in a PEMFC, it is important to look at the Pourbaix diagram to determine if it would be stable within the range of operating conditions. This range for a PEMFC is from around 0 to 1 V, with slightly higher and lower voltages during start-up and shutdown conditions, and a pH between 3 and 5 [145].

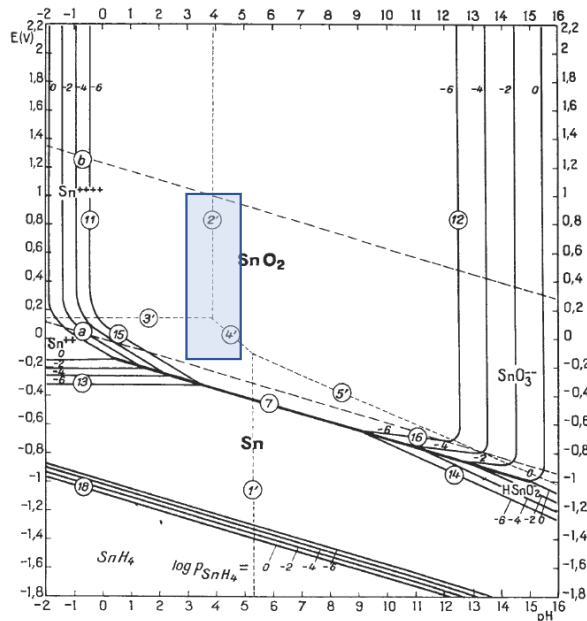


Figure 2.3.1. The Pourbaix diagram for the Sn / H<sub>2</sub>O system at 25 °C, reproduced with permission from [146], and modified to show the operation region of a PEMFC.

When looking at the Pourbaix diagram for tin [146], it clearly has one stable oxide, SnO<sub>2</sub>, throughout this range. This is beneficial as this oxide will passivate the surface and provide a stable barrier to further oxidation (corrosion), as is also the case for iron-based materials used for BPPs. The SnO<sub>2</sub> has the added benefit of being more conductive than similar passivation layers that form on metals like stainless steel, or aluminium, as seen from the respective metal and metal oxide resistivities in Table 2.3.1.

Table 2.3.1. Resistivity values for several metals and their respective dominant oxides, as identified from the relevant Pourbaix diagrams.

Metal	Metal Resistivity / $10^{-8} \Omega \text{ cm}$	Dominant Surface Oxide(s)	Oxide Resistivity / $\Omega \text{ cm}$
Tin	11.5 [144]	SnO <sub>2</sub>	0.59 [147]
Aluminium	2.71 [144]	Al <sub>2</sub> O <sub>3</sub>	$2 \times 10^{11}$ [144]
Stainless Steel (316)	7200 [144]	Cr <sub>2</sub> O <sub>3</sub>	$3 \times 10^3$ [148]
		Fe <sub>2</sub> O <sub>3</sub>	$2 \times 10^4$ [149]
		NiO	$8 \times 10^4$ [150]
		Cr <sub>2</sub> FeO <sub>4</sub>	$3 \times 10^6$ [151]

However, the Pourbaix diagram does not tell the whole story about whether the Sn oxide will provide a good protective barrier. Some oxide formation processes involve such a large lattice expansion that the resulting oxide is pushed away from the metal surface and flakes off, for example iron [152]. Other oxide formations result in a contraction of the lattice parameter, leading to an oxide that is thin and has cracks in it, and is therefore not protective, for example Magnesium [152]. This phenomenon can be described by the Pilling Bedworth Ratio (PBR), and metals with  $1 < \text{PBR} < 2$  should form a protective oxide [152]. Sn has a PBR of 1.31 [153], implying that the oxide formed will remain on the surface and form an effective barrier. It should be noted, however, that the PBR is not always an accurate measure of the protective oxide formed on alloys [154].

Therefore, according to the Pourbaix diagram, SnO<sub>2</sub> should be stable within the PEMFC operating range, and the PBR indicates that it should stick to the Sn surface to form a protective oxide. Despite this, there are multiple theories on the oxidation of metals, and there have been conflicting reports as to whether the oxide formed on tin is actually protective. It has been observed that in aqueous, sulphuric acid media (often used to simulate the PEM fuel cell environment), a two-stage passivation process, through Sn(II)O to Sn(IV)O<sub>2</sub> occurs [155]. Though passive, this oxide film does not prevent further dissolution of the underlying metal, possibly due to easy ion diffusion through the film [156]. However, during similar tests in various media including 4 molar sulfuric acid, tin has in fact been proven to improve the corrosion properties of stainless steels through the formation of a dense SnO<sub>2</sub> passive layer, which inhibits further corrosion [157–159]. Although these tests aim to simulate a PEMFC environment, some major differences in the contact of the electrolyte with the BPP surface mean that such *ex-situ* tests are not always accurate. Specifically, when *ex-situ* testing, the electrolyte is in full contact with the BPP, however when *in-situ*, we expect a series of slightly acidic droplets to flow through the BPP channels. These differences mean that *in-situ* tests in a working fuel cell are the most accurate way to determine the long-term performance of Sn-coated bipolar plates.

The stability of the tin oxide layer is not the only consideration that should be made to determine whether Sn makes a suitable BPP material. The leaching of metal ions from bipolar plates is a well-known cause of membrane degradation in PEMFCs, with divalent cations having a strong negative impact on membrane transport properties, water flux and radical formation [49,160,161]. However, there have not been any specific studies done on the influence of  $\text{Sn}^{2+}$  ions on membrane degradation, and in fact Sn and its oxides have found use in multiple different components within the fuel cell [162], including the catalyst [163], catalyst support [164] and composite membranes. Iwai et al. [165] reported no decomposition of nafion membranes when exposed to Sn ions, in fact, the proton conductivity and Young's modulus of nafion membranes is improved upon small additions of Sn [166]. It has been reported that  $\text{SnO}_2$  modified MEAs have improved durability, reduced release of F<sup>-</sup> ions and retained a higher Pt loading through the cell lifetime [167,168], indicating that Sn has positive impact on the catalyst and membrane during operation.

A small number of studies have investigated  $\text{SnO}_2$  as a coating material for bipolar plates. Yang et al. [169] showed that a  $\text{SnO}_2$  film formed by a sol-gel dip coating method improved the corrosion performance of 304 stainless steel. Additionally, a thin fluorine doped  $\text{SnO}_2$  film was deposited using chemical vapour deposition (CVD) on austenitic, ferritic and duplex stainless steels, although to mixed results [170–172]. Of these studies, only a fluorine doped zinc tin oxide film was tested *in-situ*, leading to both improved corrosion performance and lower ICR [173]. However, to our knowledge neither undoped tin oxide or nor electrodeposited tin have been tested *in-situ*. Therefore, further testing is necessary to determine the long and short term properties of tin and tin oxide in PEMFC conditions.

### 2.3.2. The Sn/GDL Concept

The novel concept in this thesis is to use Sn as a solder material to join the gas diffusion layer with the bipolar plate. A layer of Sn will be electrodeposited onto the stainless steel bipolar plate, which has been treated to remove the naturally formed oxide layer. The coated plate is then hot pressed with a gas diffusion layer, so the fibres of the GDL become embedded into the tin coating of the BPP, as visualised in Figure 2.3.2.

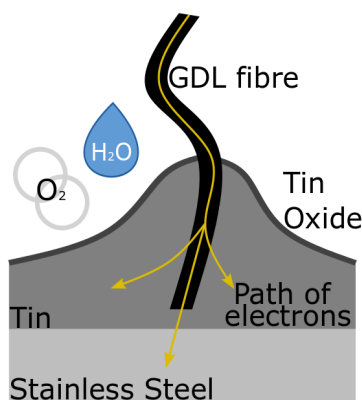


Figure 2.3.2. The Sn/GDL concept, where conductivity is maintained through the GDL fibre, whilst the Tin Oxide provides protection from further corrosion

These contacts between the GDL fibres and the tin layer will provide a significantly improved conduction pathway from the GDL to the BPP, allowing the electrons to more easily conduct through the coating, resulting in a very low contact resistance. When the system is exposed to the oxidising environment inside the fuel cell, the surface of the tin layer is oxidised to SnO<sub>2</sub>. This oxide then protects the underlying tin from further oxidation, while maintaining free conduction pathways for electrons. Furthermore, since SnO<sub>2</sub> is stable within the operating range of the fuel cell, it should in principle remain intact and enable production of bipolar plate configurations that possess a low contact resistance over the entire lifetime of the cell.

US DoE targets for BPPs in 2020 are contact resistances of < 10 mΩ cm [30], measured by placing two GDLs on either side of a sample between two copper conducting plates. A current is applied between the plates, and the voltage drop is measured then converted to a resistance. After accounting for the resistance contribution from the GDL, the contact resistance between the sample BPP and the GDL can be obtained [105].

The contact resistance between two surfaces arises from the limited area of ‘true contact’ between the surfaces, due to microscopic surface roughness that leads to only a small number of contact points [174]. In addition, there may be surface oxides or films present which further reduce the number of contact points, as electron transfer can only occur through the contact of two conducting surfaces. This leads to the constriction of the current lines to the points where the conductive surfaces are in contact, as seen in Figure 2.3.3.

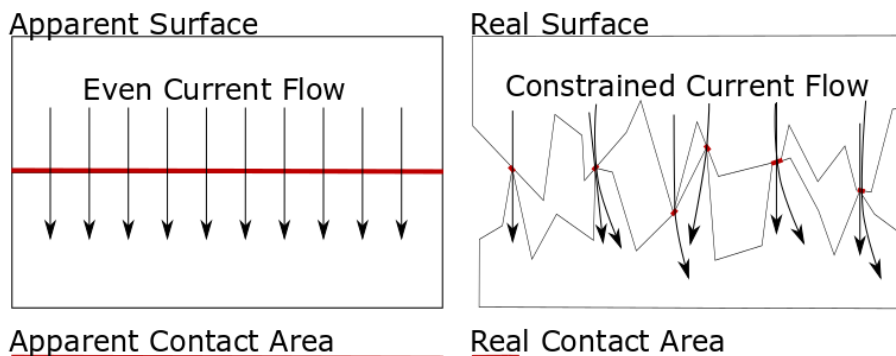


Figure 2.3.3. A diagram showing how the real surface differs from the apparent surface, leading to a much smaller ‘real’ contact area and a constrained current flow.

This model can be applied to contact resistance within PEM fuel Cells, and it is well known that the surface roughness of bipolar plates affects their electron transfer to the GDL [175,176]. If surface of the BPP is much rougher than the GDL, there are few contact points, but if the BPP surface is too smooth, the contact area increases, leading to a decrease in pressure and an increase in ICR. It is generally difficult to make broad conclusions about the most appropriate BPP surface roughness to reduce the contact resistance as it is heavily dependent on the GDL type and BPP coating [177,178].

For the Sn/GDL system, the constricted current model used for traditional BPPs becomes problematic. As seen in Figure 2.3.4, the contact area between the BPP and GDL is much larger for the Sn/GDL BPP than traditional BPPs, because of the soldering process with the Sn.

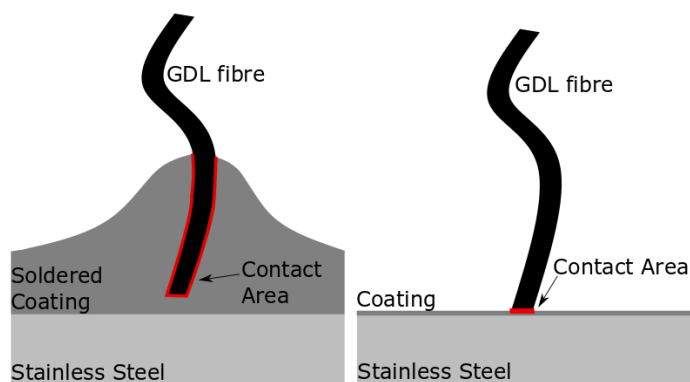


Figure 2.3.4. A diagram showing the difference in contact area between the GDL and coating for two types of BPP. The soldered coating has a significantly higher contact area than the traditional coating method.

This leads to a very low or even negligible contact resistance, and the conclusion that the ICR measurement technique popularised by Wang et.al [105] for use on bipolar plates is not useful as a comparison between the Sn/GDL system and other bipolar plate types. For the Sn/GDL system, it is often observed that when the bulk resistances of the GDL and measurement apparatus has been accounted for, the measured contact resistance is close to zero. However, the technique is still used in this thesis as a way to quantify the degradation of the BPP/GDL interface over time, as any oxidation or delamination that takes place will lead to a smaller contact area and an increase in contact resistance.

Therefore, this concept of creating a combined bipolar plate with GDL through soldering with metallic Sn represents an interesting alternative to conventional metallic bipolar plates. Experimental validation will be performed throughout this PhD thesis, to determine whether the combined BPP/GDL will function inside a working fuel cell, and provide a low-cost, high-performance alternative to gold-coated stainless steel bipolar plates.

### 2.3.3. Development of the Sn/GDL Concept

Modifications of the Sn/GDL interface can be made in an attempt to improve the performance and longevity. These modifications can be grouped into three categories, as shown in Figure 2.3.5.

1. Alloying the Sn to form an oxide that has greater protective character and increased durability.
2. Changing the type of GDL, focussing on the structure and wetting properties to form a better contact with the Sn during soldering.
3. Altering the Sn/GDL interface properties by adding various carbon nanoparticles prior to soldering.

Each of these modifications are investigated and reported in the upcoming chapters of this thesis.

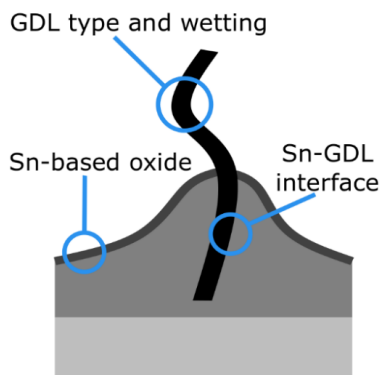


Figure 2.3.5. A diagram showing the areas of interest when designing modifications to the Sn/GDL system

## Alloying

The Sn oxide that forms on the surface of the metallic Sn solder should in theory be protective and stable in the PEM environment. However, there are ways to increase the oxide stability and one suggestion is to add an alloying element to the Sn to form a more stable and protective oxide, increasing the longevity of the system and making a better bipolar plate. Some examples of stable tin-based oxides are ATO (antimony tin oxide) and ITO (indium tin oxide), both of which have good conductivity and stability.

When identifying promising alloying elements, certain characteristics are desired. Such characteristics are:

- Low melting point
- High conductivity
- Stable oxide within the PEMFC operating range
- Able to be co-deposited with Sn as a homogenous metallic layer

Certain alloying elements that seem to fulfil these criteria were identified, and preliminary tests were performed to determine their contact and corrosion resistance in chapter 5 of this thesis. If promising, these elements were moved onto the next stage, which is attempting the co-deposition with Sn. Chapters 6 and 7 of this thesis report the co-deposition of tin with bismuth and indium, respectively, and the impact these additions have on the coating properties including the suitability and longevity of the Sn/GDL system.

## GDL type

The Sn/GDL system can also be modified by changing the type of GDL. As the Sn is in direct contact with the GDL, the type of carbon fibres, porosity and pre-treatment (e.g. hydrophobic treatment and/or added microporous layer) can influence the infiltration, adhesion and corrosion of the Sn/GDL interface. Firstly, the mechanical strength, flexibility and conductivity of the carbon fibres changes with the type of carbon paper used. As an example, Toray carbon papers have very stiff fibres that are likely to protrude more deeply into the Sn layer, whereas the Freudenberg non-woven carbon papers have flexible fibres that will not go as deeply into the Sn, as demonstrated in Figure 2.3.6.

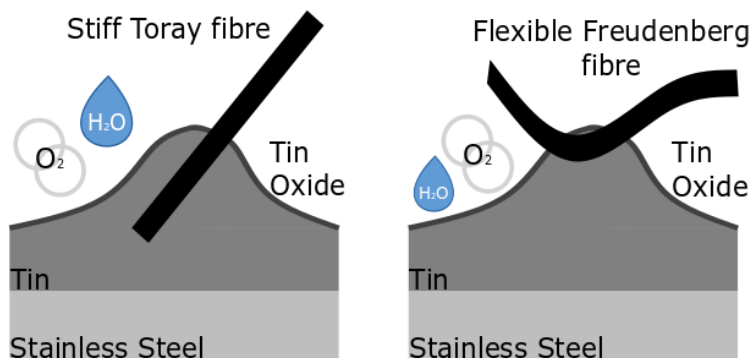


Figure 2.3.6. A diagram showing how the GDL type can affect the interface between the Sn and the GDL, with the stiff Toray fibre penetrating deeper into the Sn than the flexible Freudenberg fibres.

The carbon fibres are often treated with PTFE to make them hydrophobic. This aids the water management in the cell, however it may be detrimental to the adhesion and total contact area between the Sn and the GDL fibre during hot pressing. If the fibre is hydrophilic, the Sn may adhere better to the fibre than if it has had hydrophobic treatment in the form of PTFE. This hypothesis is outlined in Figure 2.3.7.

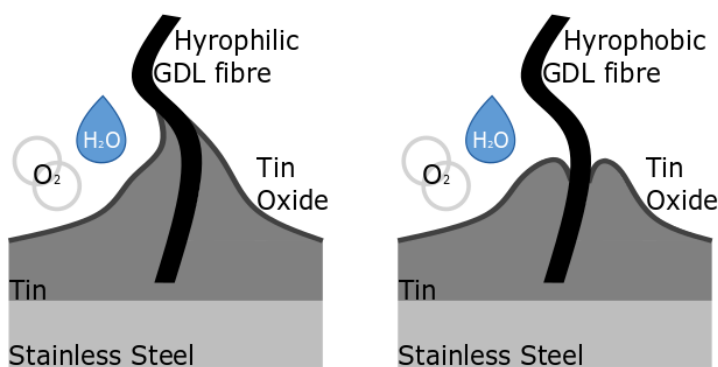


Figure 2.3.7. A diagram showing how the hydrophobicity of the GDL fibre will affect its contact with the Sn, with the hydrophilic GDL fibre, left, predicted to have better contact with the Sn than the hydrophobic GDL fibre, right.

Chapter 8.1 of this thesis explores how the type of GDL used affects the contact between the Sn and the GDL, and the impact this has on the performance of the BPP.

## Sn/GDL Interface

Finally, the interface between the Sn and the GDL can be modified by the addition of conductive particles on the nanoscale. This will ideally increase the number of contact points and improve the adhesion between the Sn and the GDL, and slow down the loss of Sn-oxide at this location, increasing the longevity of the system.

Chapter 8.2 of this thesis looks at the addition of various types of carbon nanoparticles to the Sn/GDL interface.



# 3

## Experimental Procedure

The experimental procedures performed in each chapter of this thesis are laid out below. The scientific methods used in this thesis were carefully chosen to ensure reproducibility of coatings and BPPs, and to provide a thorough analysis of the relevant properties. The synthesis of the samples has varied depending on the type of metal being deposited, the type of GDL used and the presence of any additional carbon on the BPP. Additionally, the deposition was varied slightly to produce larger BPPs for *in-situ* testing. The detailed procedures for each of these alternatives can be found in chapter 3.1. The analysis methods used on all samples have been consistent throughout this thesis, and an overview of the procedures used for each analysis method can be found in chapter 3.2.

### 3.1. Sample Synthesis

#### 3.1.1. Pre-Treatment

The substrates used for deposition were either a stamped stainless steel BPP (SS316, 13 x 1.2 cm, ElringKlinger) with a parallel flow field, a flat, square stainless steel coupon (SS316, 3.5 x 3.5 cm, ElringKlinger), or a large BPP (SS316, 9.5 x 9.5 cm, flow field 7 x 7 cm, ElringKlinger) with a parallel serpentine flow field. All BPPs, shown in Figure 3.1.1, were provided by ElringKlinger as part of the STAMPEM European project (FCH JU, 303449).

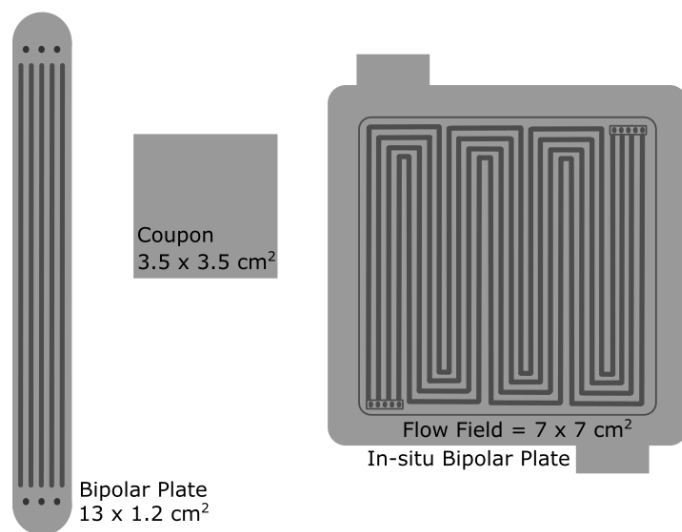


Figure 3.1.1. An illustration of the three different substrate types used in this thesis. The standard bipolar plate has parallel channels, and an elongated shape. The coupon is square with no channel structure, and the *in-situ* bipolar plate has a larger channel structure, of a parallel serpentine geometry. The flow field shown above is not identical to the flow field on the *in-situ* bipolar plate, which is proprietary. All substrates are made from 316 stainless steel, provided by ElringKlinger.

The pre-treatment of all the substrates used for electrodeposition was performed as follows:

A solution of 12.5 % HCl was prepared by diluting HCl (30 ml, 37.5 %, Sigma Aldrich) with deionised water (60 ml, Milli-Q Integral pure water system, 18.2 M $\Omega$ ), and stirring. Immediately before electrodeposition, the substrate was submerged into the HCl solution for 15 minutes before being removed, rinsed with deionised water and dried with a lint-free paper towel.

### 3.1.2. Electrodeposition

Electrodeposition was performed in all experimental chapters of this thesis, from 4 to 8. These electrodeposition procedures were largely based on the commercial SLOTO TIN bath produced by Schlötter. To allow the deposition of Sn-based alloys, adjustments to the bath were made, and in the case of the SnIn deposition, multiple different baths were attempted.

For the different geometries of substrates, the electrodeposition procedure was identical, with adjustment of the applied current performed to maintain the required current density.

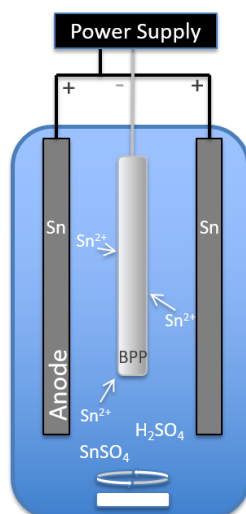


Figure 3.1.2. A diagram of the electrodeposition setup, showing the two Sn anodes, suspended on either side of the stainless steel substrate, in a sulfuric acid based electrolyte.

#### Pure Sn samples

The electrodeposition of Sn to form a coating on a stainless steel substrate, as done in chapters 4 and 7 of this work, was performed as follows:

An electroplating solution was made by adding sulfuric acid (100 ml, 98%, Sigma Aldrich) slowly to deionised water (700 ml, Milli-Q Integral pure water system, 18.2 M $\Omega$ ) whilst stirring. The solution was left to cool to room temperature before the addition of tin (II) sulfate (36.17 g, purity  $\geq$  95 %, Sigma Aldrich), SLOTO TIN 71™ (20 ml, Schlötter), then SLOTO TIN 72™ (3 ml, Schlötter) with thorough stirring between each addition. The solution was topped up with deionised water to a total volume of 1 l. A pair of Sn (99.99 % purity, Sigma Aldrich) electrodes were fixed in the bath and connected to the

positive pole of a power supply to act as the anodes during deposition. Two anodes were used to obtain an even deposit on both sides of the substrate.

A platinum wire was connected to a pre-treated, pre-stamped stainless steel 316 bipolar plate of surface area 39.2 cm<sup>2</sup> by point-welding. The substrate was immersed in the electroplating solution and connected to the negative pole of the current source, in the configuration shown in Figure 3.1.2. A current was applied between the anodes and cathode in order to deposit a layer of Sn. The current density and deposition time were varied in order to control the structure and thickness of the coating. After deposition, the plate was removed from the electroplating solution, rinsed with deionised water and dried with a lint-free paper towel.

## SnBi Samples

For the electrodeposition of SnBi samples performed in chapter 5 of this work, the deposition bath was prepared as above. Before deposition took place, the additive SLOTOLET G53 (1 to 30 ml, Schlötter), which contains between 25 and 50 % bismuth in the form Bi(SO<sub>3</sub>CH<sub>3</sub>)<sub>3</sub>, was added to the bath, which was thoroughly stirred.

## SnIn Samples

The investigation of the SnIn samples is described in chapter 6 of this work. As the deposition was performed using multiple different baths, a summary of all the bath types and their constituents is listed in Table 3.1.1. All baths are aqueous, and the additives were added to deionised water whilst stirring.

Table 3.1.1. A summary of each deposition bath type with the additives used and the quantities.

Bath Type	Additive	Supplier	Amount
Slototin bath	H <sub>2</sub> SO <sub>4</sub>	Sigma Aldrich	100 ml/l
	SnSO <sub>4</sub>	Sigma Aldrich	36.17 g/l
	Slototin 71	Schlötter	20 ml/l
	Slototin 72	Schlötter	3 ml/l
	Slotopas ZNB 62	Schlötter	Varied
Indium salt bath	H <sub>2</sub> SO <sub>4</sub>	Sigma Aldrich	100 ml/l
	SnSO <sub>4</sub>	Sigma Aldrich	36.17 g/l
	Slototin 71	Schlötter	20 ml/l
	Slototin 72	Schlötter	3 ml/l
	In <sub>2</sub> (SO <sub>4</sub> ) <sub>3</sub>	Sigma Aldrich	Varied
Indium salt and anode bath	InCl <sub>3</sub>	Sigma Aldrich	Varied
	In <sub>2</sub> (SO <sub>4</sub> ) <sub>3</sub>	Sigma Aldrich	10 g/l
CTAB bath	Na <sub>2</sub> SO <sub>4</sub>	VWR	10 g/l
	In <sub>2</sub> (SO <sub>4</sub> ) <sub>3</sub>	Sigma Aldrich	5 g/l
	CTAB	Sigma Aldrich	5 g/l
	SnSO <sub>4</sub>	Sigma Aldrich	Varied

After preparation of the bath, the pre-treated substrate (SS 316, 3.5 x 3.5 cm<sup>2</sup>, ElringKlinger) was suspended into the solution using a platinum wire secured by point-welding. The substrate was connected to the negative pole of the current source and the selected deposition parameters were applied. A testing matrix containing all the different parameters used for each deposition bath type can be seen in Table 3.1.2

Table 3.1.2. A summary of the parameters used during the deposition of SnIn from each deposition bath.

Bath Type	Parameter Studied	Unit	Values						
Slototin	Amount of additive	ml	1	5	10	15	20	30	
	Current Density	mA cm <sup>-2</sup>	3	15	30	60	80		
	Temperature	°C	20	40	60	80			
	pH		-1.0	0.0	1.0	1.5	2.0	2.5	3.0
	Stirring speed	rpm	0	100	150	200	300	500	
Indium salts	Salt type		InCl <sub>3</sub>		In <sub>2</sub> (SO <sub>4</sub> ) <sub>3</sub>				
Indium salts and anodes	Current density	mA cm <sup>-2</sup>	10	20	30				
	Temperature	°C	20	40	60				
	Substrate		Rough		Smooth				
			Sn layer		No Sn layer				
CTAB	Temperature	°C	20	40	60	70			
	Current Density	mA cm <sup>-2</sup>	5	10	20				
	Surface roughness		Glass blasted		As received				
	pH		0.5	1.0	1.5				
	Sn content	g l <sup>-1</sup>	1	2	5	10			

After deposition, the substrate was removed from the electroplating bath, rinsed with deionised water and dried with a lint free paper towel, before hot pressing it with a GDL.

### *In-situ* Samples

The *in-situ* BPPs were larger, with an active area of 50 cm<sup>2</sup>, therefore a larger electroplating bath of the desired composition (to make Sn or SnBi BPPs) was obtained, containing 3 L of electrolyte. The pre-treatment process was performed as described above. During deposition, the current was adjusted to maintain the required current density.

### 3.1.3. Hot Pressing

Immediately after deposition, the coated bipolar plate was placed on top of a pre-cut H23C6 GDL from Freudenberg (chapters 4, 5, 6 and 8) or a different GDL from either Toray or Freudenberg (chapter 7). The BPP and GDL were placed inside a custom made PTFE envelope, then placed inside a pre-heated hot press, as shown in Figure 3.1.3.

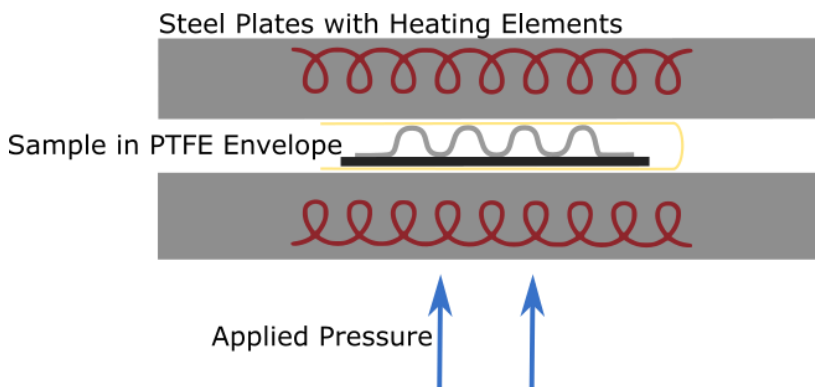


Figure 3.1.3. A diagram of the hot press used to solder the GDL to the BPP through heating under applied pressure.

The sample was pressed at a varied temperature, pressure and time, before cooling to room temperature either slowly under applied pressure or rapidly at atmospheric pressure. The plate was removed from the Teflon envelope and the GDL trimmed to size, as shown in Figure 3.1.4.

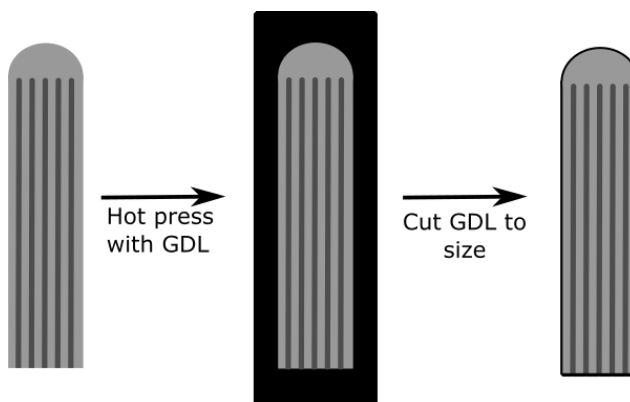


Figure 3.1.4. A diagram of the BPP before hot pressing, after hot pressing with the GDL and after the GDL has been cut to size.

### 3.1.4. Hot-Dipping SnIn

In chapter six, hot-dipping of a SS316 coupon (ElringKlinger, 3.5 x 3.5 cm) into a SnIn melt was performed.

A mix of pure Sn (109 g, Sigma Aldrich, foil, >99.99 %) and In (5.5 g, Sigma Aldrich, foil, 99.999 %) in a ratio of 19:1 was placed in a glass beaker and heated on a heating plate until a temperature of 230 °C was reached, whereby both the indium and the tin had melted. The melt was mixed with a glass rod until homogeneous, then a pre-treated (see section 3.1.1) stainless steel coupon was submerged in the melt, and slowly removed so that the melt remained on the surface of the coupon.

After cooling on a watch glass, the coupon was heated to 226 °C inside the hot press to melt the surface and provide an even distribution of coating over the surface. A mould made from PTFE sheets and aluminium foil was used to keep the SnIn alloy in place on the surface of the coupon. Surface analysis

of the sample was performed using SEM with EDS to determine the alloy content, before further analysis of the electrochemical properties. Additional Sn or In was added to the melt to adjust the composition of the final coating as required.

### 3.1.5. Spraying of Carbon

The amount of carbon particles needed to achieve a loading of  $0.25 \text{ mg/cm}^2$  was calculated and weighed out. The carbon was suspended in a mixture of isopropanol (8 g, 10.2 ml, VWR) and deionised water (2 g, 2 ml) and placed in an ultrasonic bath for 10 minutes, then further dispersed using an ultrasonic probe for 5 minutes. The mixture was spray coated by hand using a spray gun (Cocraft) onto the back side of a  $13.5 \text{ cm}^2$  Freudenberg H23C6 GDL, which was placed on a hotplate pre-heated to  $150 \text{ }^\circ\text{C}$  in order to promote evaporation of solvents. After all solvent had evaporated, the GDL was hot pressed with a freshly made BPP.

## 3.2. Sample Analysis

### 3.2.1. Interfacial Contact Resistance Measurements

Interfacial contact resistance (ICR) measurements were performed after hot pressing and after each corrosion test using a setup adapted from Wang et al [105], shown in Figure 3.2.1.

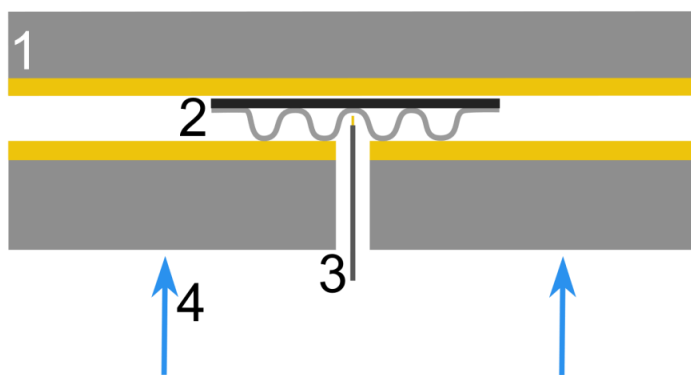


Figure 3.2.1. The setup used to measure Interfacial Contact resistance. 1 is the gold-coated copper plate, 2 is the sample (grey curved line) with GDL (black line), 3 is the gold-coated contact pin, 4 is indicating the presence of a piston used to apply pressure.

The sample was placed between two gold-coated copper plates, and a current of  $2 \text{ A}$  was passed between the bottom and top plates. Pressures from  $70$  to  $650 \text{ N cm}^{-2}$  were applied using a piston, and the exact pressure values were adjusted based on the surface area of the sample. The voltage through the sample, between the top plate and a spring-loaded gold pin isolated from the bottom plate was measured and plotted as a function of pressure. All quoted values for ICR are recorded at  $1.4 \text{ MPa}$ , which is the standard *in-situ* compaction pressure of a fuel cell [105].

This technique was used in all experimental chapters of the thesis, from chapter 4 to 8.

### 3.2.2. SEM Imaging and EDS Mapping

Both before and after corrosion testing, scanning electron microscope (SEM) images of the plates were obtained. Samples for cross-sectional imaging were prepared by cutting (LABOTOM-5, Struers) to reveal the Sn/GDL interface.

The samples were mounted inside a Hitachi S-3400 N SEM and probed with an electron beam accelerated to 15 keV. Energy Dispersive Spectroscopy (EDS) mapping of the samples was performed at a working distance of around 10 mm to analyse the elemental composition.

SEM imaging and EDS mapping of samples was performed in chapters 4 to 8 of this thesis.

### 3.2.3. *Ex-situ* electrochemistry

In chapters 4, 5, 6 and 7 of this work, the bipolar plate specimens were evaluated for their corrosion characteristics using potentiodynamic and potentiostatic techniques with a Gamry Ref 600 potentiostat. The combined BPP/GDL functioned as the working electrode and was submerged in  $\text{Na}_2\text{SO}_4$  (0.1M, Sigma Aldrich), adjusted to pH 3 using  $\text{H}_2\text{SO}_4$ . A Pt coil or mesh was used as the counter electrode, and a Gaskatel Hydroflex Pt/Pd reference electrode was used as a reversible hydrogen electrode (RHE) for all experiments. All potentials in this work are recalculated and expressed versus a standard hydrogen electrode (SHE) unless stated otherwise. Prior to testing, electrolyte was injected into the channels of the bipolar plate with a syringe. The electrolyte was heated to 80 °C and purged with nitrogen prior to all testing.

Before all electrochemical measurements, the samples were first stabilised at open circuit, before an EIS test was performed to identify the internal resistance in the solution and setup. All resulting data were corrected for 85 % of the solution resistance. For potentiostatic measurements, a voltage of 1.0  $V_{\text{SHE}}$  was applied for 1 hour and the current response was measured. For potentiodynamic measurements, a potential sweep from -0.4 to 1.0  $V_{\text{SHE}}$  and back was performed at a rate of 1 mV/s. The sweeps were repeated for either two or three cycles, depending on the experiment, and the final sweep was reported each time. After the test was complete, samples were rinsed with deionised water and dried with a lint-free paper towel.

### 3.2.4. *In-situ* Tests

For the *in-situ* fuel cell tests that were performed in chapter 8, a larger pre-stamped SS 316 bipolar plate (as received from ElringKlinger) with a parallel-serpentine flow field pattern, area 50  $\text{cm}^2$  (one side) was used as a substrate.

The pre-treatment, deposition and hot pressing procedures were performed as described in Chapter 3.1, and the interfacial contact resistance was measured. The Au and SS plates were measured through a range of pressures from 40 to 240  $\text{N cm}^{-2}$ , but the Sn/GDL, SnBi/GDL and Sn/C/GDL plates were initially only measured up to 1.4 MPa. This is to prevent the excessive compression of the GDL, which could hinder water and gas transport to the MEA and reduce cell performance. After the 600 cycles were complete, both plates were measured up to 240  $\text{N cm}^{-2}$ .

This bipolar plate combined with the GDL was used as the cathode in the cell and assembled into the fuel cell casing along with a MEA (Gore Primea® FCM with 0.1 and 0.4 mg/cm<sup>2</sup> Pt loading on the anode and cathode respectively), a GDL for the anode side (Freudenberg H23 C6), and a gold coated stainless steel bipolar plate (provided by ElringKlinger) for the anode side, as seen in Figure 3.2.2.

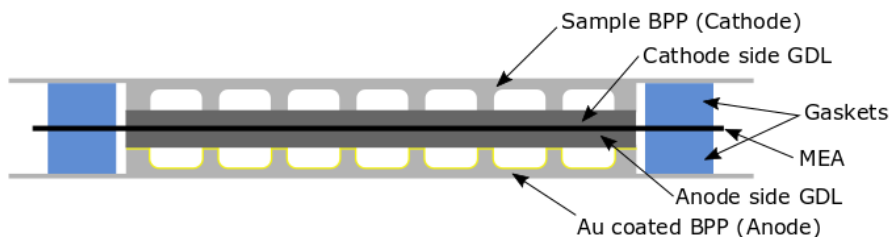


Figure 3.2.2. A Cross section of the fuel cell for *in-situ* testing.

The fuel cell was placed inside a custom-made cell housing from ElringKlinger, and a pressure of 1.4 MPa was applied as shown in Figure 3.2.3, using four springs, one in each corner. The cell was then connected up to a Greenlight G40 test station in counter flow configuration.

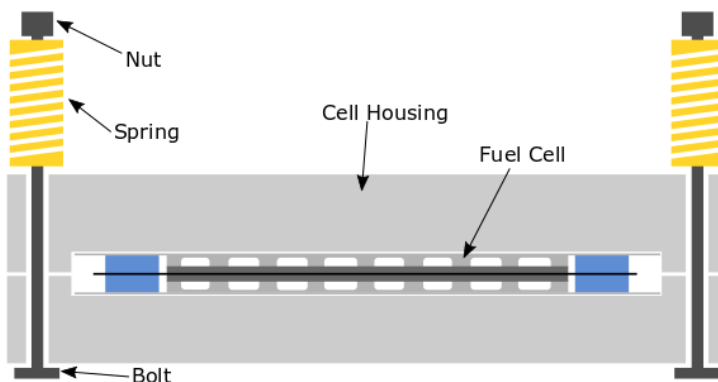


Figure 3.2.3. A cross section of the fuel cell in the cell housing.

A modified set of parameters based on the EU harmonised Automotive Reference Operating Conditions for Low Temperature PEMFC single cell testing at open end mode in counter flow configuration [8] was used:

Table 3.2.1. The parameters used for *in-situ* fuel cell testing

Parameter	Value	Unit
Nominal cell temperature	80	°C
Anode gas inlet temperature	85	°C
Cathode gas inlet temperature	85	°C
Anode relative humidity	64	°C
	50	%
Cathode relative humidity	53	°C
	30	%
Anode stoichiometry	2	-

Cathode stoichiometry	2	-
Anode Inlet Pressure (absolute)	200	kPa
Cathode Inlet Pressure(absolute)	200	kPa

After 17 hours of conditioning the cell at a current density of 1 Acm<sup>-2</sup>, initial cell characterisation was performed. This consisted of a polarisation curve, with the low current density measurements taken at 0.00, 0.02, 0.04, 0.06, 0.08 and 0.10 A cm<sup>-2</sup> having a dwell time of 60 seconds and an acquisition time of 30 seconds. Medium current density points were taken at 0.2, 0.3, 0.4, 0.6, 0.8, 1.0 and 1.2 A cm<sup>-2</sup> with a dwell time of 120 seconds and an acquisition time of 30 seconds. The forward and reverse sweeps of the polarisation curves were identical. The maximum current density was limited by the size of the load bank in the test station (60 A).

The polarisation curve was followed by electrochemical impedance spectroscopy with the following parameters:

Table 3.3.2.2. The parameters used for *in-situ* EIS measurements

Value	Parameter
50	DC Current (A)
30000	Initial Freq. (Hz)
1	Final Freq. (Hz)
10	Points/decade
2,5	AC Current (A rms)
50	Area (cm <sup>2</sup> )

After initial analysis, a series of 50 drive cycles were performed, as recommended by the EU reference testing conditions [8]. After these drive cycles had been performed, the cell was characterised again, as above. This group of 50 drive cycles plus characterisation was repeated 5 times until a total of 250 drive cycles had been performed, and then the cell was shut down for a minimum of 17 hours. The cell was then restarted, characterised and another set of 250 drive cycles performed. A total of 600 drive cycles were performed on each set of bipolar plates (200 hours of testing), before the cell was again shut down and dismantled.

Post-mortem analysis of the cell was performed, including SEM/EDS images to determine whether any metal ions or other contaminants had leached into the membrane, and *ex-situ* ICR of the bipolar plates to determine the specific degradation observed on them.



# 4

## Soldering a Gas Diffusion Layer to a Bipolar Plate Using Tin

### 4.1. Introduction

As described in chapter 2.3, it has been hypothesised that Sn is a suitable coating material for bipolar plates in PEM fuel cells due to its stability, conductivity and low cost. This chapter outlines the work done to investigate whether the novel Sn/GDL technique is suitable for bipolar plates, and the subsequent optimisation of the deposition and hot pressing process. The system was firstly optimised with respect to the lowest ICR and then to highest corrosion resistance. A number of different parameters were identified as possibly having an impact on the final performance of the Sn/GDL system, including: the hot press pressure, temperature and time, as well as deposition rate and charge (equal to the coating thickness) and cooling method. Before the Sn/GDL plates could be tested *in-situ*, each of these parameters was optimised to increase performance and longevity.

This chapter has been modified from previously published work in the International Journal of Hydrogen Energy [7].

### 4.2. Optimisation of the electrodeposition process

The first stage of the BPP construction is the electrodeposition of a Sn layer onto the stainless steel substrate. This process is highly tuneable and can be optimised with respect to the current density of deposition, and also the amount of Sn deposited onto the BPP.

#### 4.2.1. Current density

Firstly, the current density of the deposition was investigated. This important parameter determines the morphology of the deposit and the efficiency of the deposition. The deposition bath used had a recommended range of current densities, which have been optimised by the manufacturers to produce a bright Sn coating. For this application of coatings for PEMFCs, the appearance of the coating is not important, however bright coatings are normally dense with small grains, which may be beneficial here due to a more even surface coverage and less exposed substrate.

A note on nomenclature of current densities: Given the applied current during all electrodeposition is negative, when changing the current so that the value of current density becomes more negative, but the absolute magnitude of the current increases, this shall be referred to as ‘increasing the current

density'. For example, changing the applied current from 15 to 30 mA cm<sup>-2</sup> would be increasing the current density. Similarly, 50 mA cm<sup>-2</sup> will be referred to as a lower current density than 150 mA cm<sup>-2</sup>.

The different current densities used are outlined in Table 4.2.1. As expected, the time taken to produce a layer of set thickness (30 μm in this case) reduces with increasing current density, and the current efficiency of deposition reduces with increasing current density for the current densities used here (from 7.5 mA cm<sup>-2</sup> to 150 mA cm<sup>-2</sup>). This can be attributed to diffusion limiting the rate of Sn deposition whilst the hydrogen evolution reaction is continuously increasing and taking a higher percentage of the current.

Table 4.2.1. A summary of the current densities used for electrodeposition.

Current Density / mA cm <sup>-2</sup>	Plating Time / min	Efficiency / %
7.5	79	95
15	40	94
30	20	75
50	12	40
100	6	9
150	4	5

SEM images of each of the samples were taken to determine the surface morphology before hot pressing. It can be observed in Figure 4.2.1 that as expected, the current density during deposition has a clear impact on the obtained surface morphology.

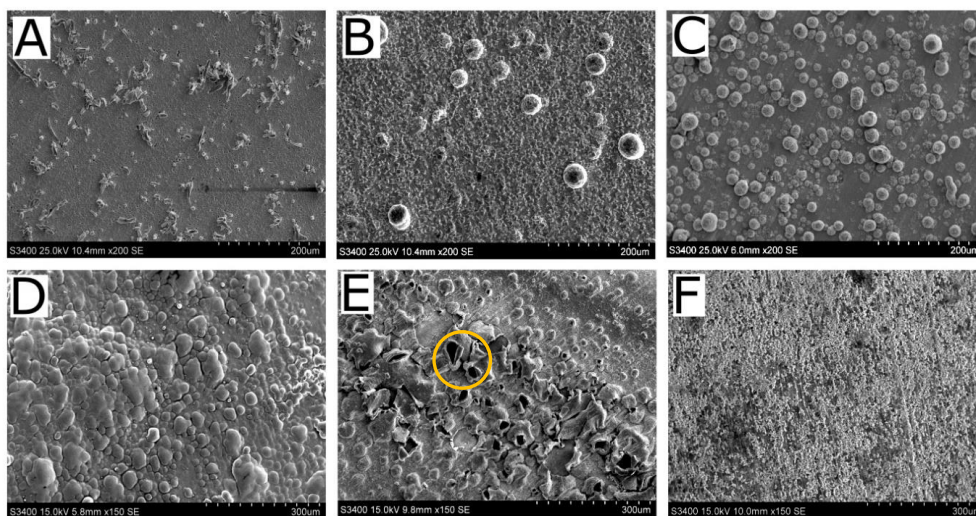


Figure 4.2.1. SEM images of Sn surfaces deposited at varying current densities, a - 7.5 mA cm<sup>-2</sup>; b - 15 mA cm<sup>-2</sup>; c - 30 mA cm<sup>-2</sup>; d - 50 mA cm<sup>-2</sup>; e - 100 mA cm<sup>-2</sup>; f - 150 mA cm<sup>-2</sup>, all images taken before hot pressing. The yellow circle in figure E emphasises the features created by gas eruptions from the substrate.

The lower current densities of up to 30 mA cm<sup>-2</sup>, as seen in Figure 4.2.1.a, b and c, have a dense base layer of Sn with few pores, and there are no visible gaps down to the substrate. There are some surface features, more of which appear at higher current densities.

As described in chapter 2.2, increasing current density too much reduces the current efficiency due to increasing contribution from hydrogen evolution readily happening at negative electrode potentials. This gas evolving side reaction can be observed in Figure 4.2.1.e and f, whereby in Figure 4.2.1.e hollow features formed by the eruption of gas from the surface can be seen. An example of this is circled in yellow. The resulting surface is porous, and the tin layer is much thinner than those produced at low current densities. At the highest current density of  $150 \text{ mA cm}^{-2}$ , in Figure 4.2.1.f, the amount of gas evolution is so high that most of the Sn deposited on the surface is removed, and the Sn that sticks on the surface is rough and unevenly distributed, shown in Figure 4.2.2.

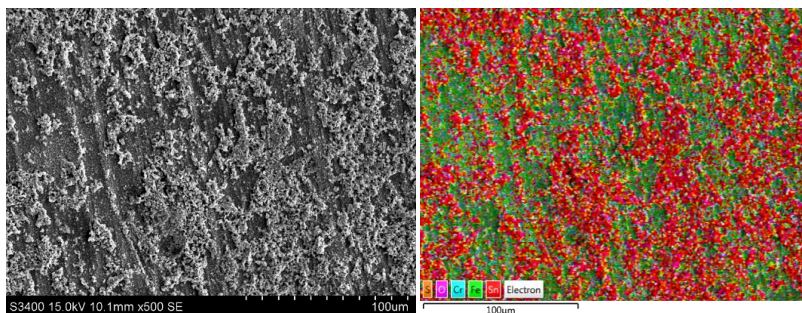


Figure 4.2.2. Zoomed-in SEM images of the sample deposited at  $150 \text{ mA cm}^{-2}$ , with a false colour-EDS image showing the Sn distribution (in red) and the Fe from the bare substrate (in green).

These samples were hot pressed, in order to melt the Sn layer and determine whether the current density would have an impact on the final layer, since the morphology should be destroyed during the melting process. SEM images of the samples after hot pressing are shown in Figure 4.2.3.

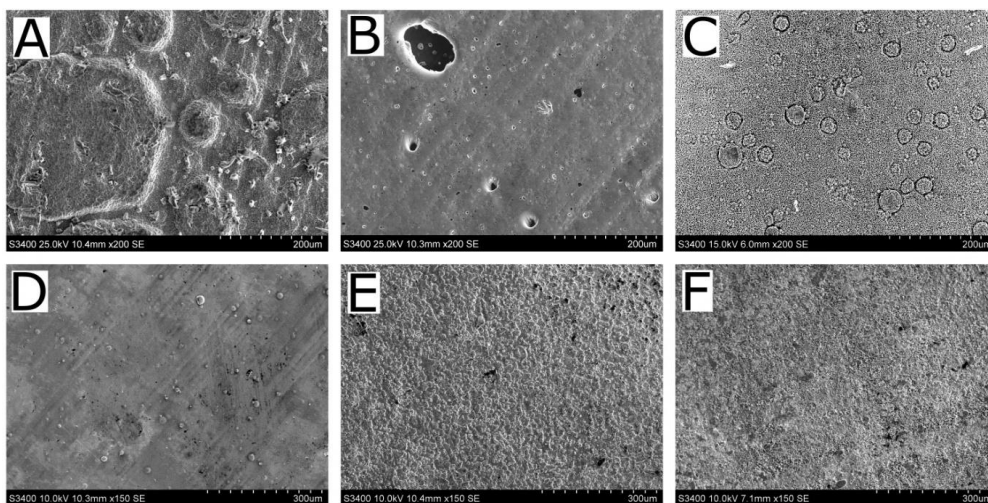


Figure 4.2.3. SEM images of Sn surfaces deposited at varying current densities. a -  $7.5 \text{ mA cm}^{-2}$ ; b -  $15 \text{ mA cm}^{-2}$ ; c -  $30 \text{ mA cm}^{-2}$ ; d -  $50 \text{ mA cm}^{-2}$ ; e -  $100 \text{ mA cm}^{-2}$ ; f -  $150 \text{ mA cm}^{-2}$ , all images taken after hot pressing.

As is observed in Figure 4.2.3, although some of the layer is melted during the hot pressing process, some of the morphological structures remain, indicating that the deposition current density will in fact have an effect on the final coating. In addition, coatings deposited at the highest current densities do not completely cover the substrate surface, despite having been melted. This leads to a poor adhesion

between BPP and GDL, with the exposed substrate having a high ICR and leaching unwanted metal ions. Therefore, the lower current densities can be seen to make the best coatings.

New BPPs were constructed with a hot pressed GDL, and the ICR of these plates before and after electrochemical testing at 1.2 V<sub>SHE</sub> for 1 hour was taken to quantify whether the structural differences seen in the SEM have an impact on the performance of the BPPs. The error bars on this and all subsequent ICR graphs are from the repetition of a bipolar plate synthesis four times under identical conditions. A percentage deviation in the ICR measurements before and after corrosion testing was obtained and applied to all further ICR values obtained.

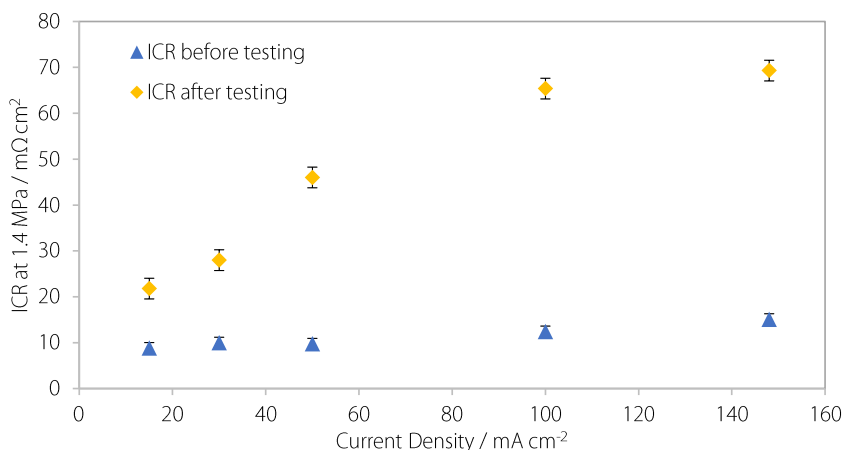


Figure 4.2.4. Comparison of current density of deposition against the ICR measured before and after *ex-situ* electrochemical testing.

The ICR measured in Figure 4.2.4 can be correlated with SEM images, with the lowest current densities producing the lowest ICR. For the samples measured before electrochemical testing, this is due to a smoother, homogeneous coating that has lots of contact points to the GDL, and a lower exposed area of Sn meaning less oxide is formed on the bare substrate.

This trend continues after chronoamperometric at 1.2 V<sub>SHE</sub> for 1 hour tests have been performed on the BPPs. At the high current densities, the exposed stainless steel substrate further oxidises, causing a large increase in ICR. The lower the current density, the higher the efficiency and therefore the more tin on the BPP. This leads to good adhesion between the BPP and GDL, with lots of contact points for good conduction of electrons, and a suitable amount of Sn to make a good protective oxide layer.

After considering the performance of the BPPs, recommendations for use of the electroplating bath, and the time taken to make the BPPs, it was decided that 15 mA cm<sup>-2</sup> would be used for all further depositions.

## 4.2.2. Thickness of the Sn layer

The second optimised parameter was the thickness of the deposited tin layer, which is important to determine how much Sn needs to be present to permeate into the GDL and form a good contact. ICR measurements before and after corrosion testing at 1.2 V<sub>SHE</sub> for 1 hour were done for a series of Sn thicknesses between 10 and 60 μm, and are shown in Figure 4.2.5.

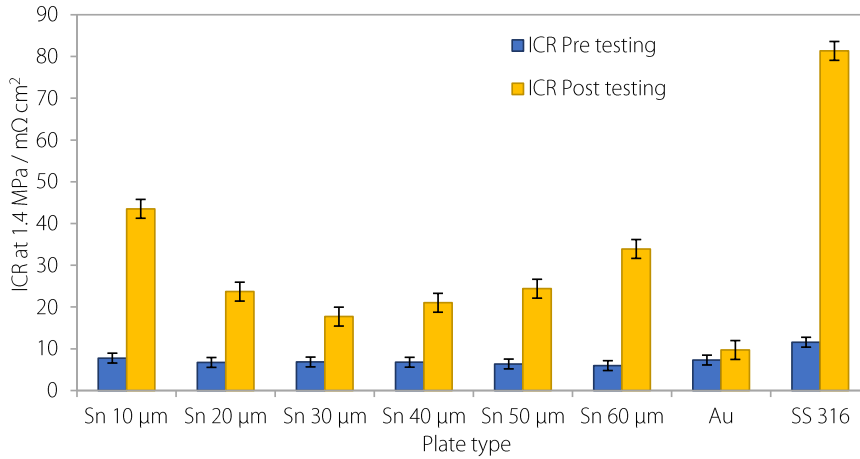


Figure 4.2.5. A comparison of the ICR of bipolar plates with varying thickness Sn layer hot pressed to a GDL, before and after *ex-situ* electrochemical testing for 1 hour at 1.0  $V_{\text{SHE}}$ .

Before corrosion testing, all ICR values were lower than DoE requirements, and decreased with an increasing tin-plating thickness. The bulk resistance of Sn is low ( $1.09 \times 10^{-7} \Omega \text{ m}$  [144]), so although the electrons travel through a thicker layer, this resistance contribution is small. The thicker Sn layers also have a greater permeation into the GDL and therefore increased electrical contact. The initial contact resistance of the Sn plates was also lower than values obtained from gold and cleaned stainless steel plates. This is a clear indication that hot pressing the tin-plated BPP with the GDL produces a better conduction pathway than simply placing the GDL on top of the BPP.

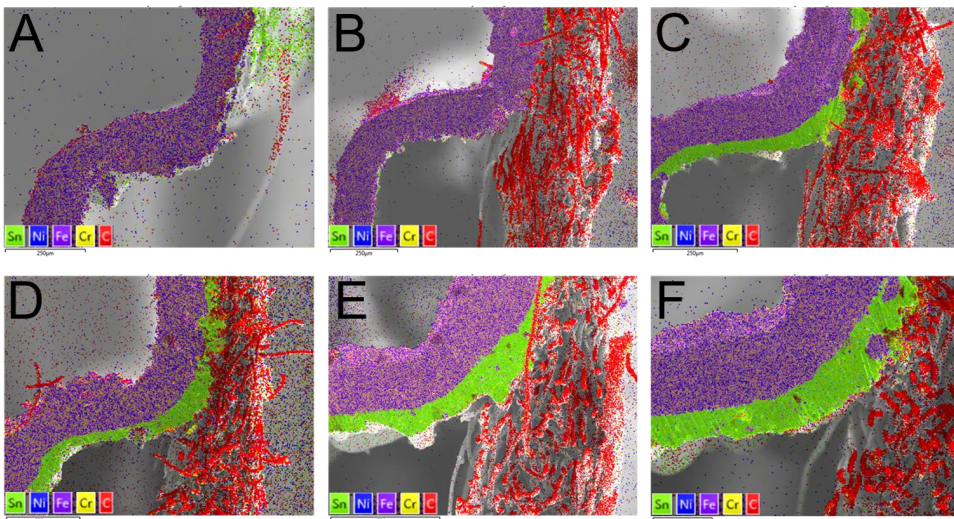


Figure 4.2.6. Cross-sectional EDS images of BPPs & GDL with varying thickness of Sn after *ex-situ* testing, purple representing the Fe in the bipolar plate, green the Sn and red the C in the GDL. The initial thickness of deposits was 10, 20, 30, 40, 50 and 60 μm on figure a to f respectively.

After potentiostatic testing for 1 hour at 1.2  $V_{\text{SHE}}$  the ICR of the samples increased vastly, up to 560 % for the thinner coatings. The significant increase in through-plane resistivity could be due to detrimental oxidation processes occurring during the high potential operation. However, since the

increase in ICR is dependent on the coating thickness, it cannot be the oxidation alone that causes the increased ICR. To gain further insight, cross-sectional EDS images were taken (Figure 4.2.6).

It is clear that the corrosion testing led to a significant removal of tin. In fact, in Figure 4.2.6 the deposited Sn layer (green colour) was reduced from a thickness of 10  $\mu\text{m}$  before any testing to being non-existent. The GDL (red colour) is also not present, as the removal of Sn during corrosion testing reduced adhesion between the GDL and BPP enough that the GDL entirely delaminated from the plate. From Figure 4.2.6 b (20  $\mu\text{m}$ ), there is also very little of the Sn layer remaining, but just enough to continue to adhere the GDL to the BPP. The mechanism behind the loss of tin will be explored in the discussion section of this chapter.

As the thickness of the Sn layer increases, in Figure 4.2.6 c, d, e and f, it is visible that there is more Sn left after corrosion and consequently greater adhesion. Interestingly, the ICR of the thickest coatings, 50 and 60  $\mu\text{m}$ , also increased by a large amount, up to 570 %, after polarization to 1.2  $V_{\text{SHE}}$  for 1 h. This can be attributed to an initially larger volume of Sn, which spreads further into the GDL during hot pressing. This leads to a larger surface area exposed to the electrolyte, and therefore a larger performance degradation.

From the ICR results in Figure 4.2.5, the best performing bipolar plate was found to have a Sn layer thickness of around 30  $\mu\text{m}$ , which was then used for all subsequent plates. As seen in the images in Figure 4.2.6 (c and d), it is obvious that the Sn has permeated into the GDL during the hot pressing stage, so despite the loss of Sn that took place during the high voltage procedure, there is still a good conduction pathway and the ICR remains low. The ICR increased by around 260 % after corrosion testing. Despite this being less than for the other thicknesses, all of which showed better performance than bare SS316L, there is still a necessity to improve the deposition process and quicken the passivation of the  $\text{SnO}_2$  layer that is formed after exposure to the PEM environment.

## 4.3. Optimisation of the hot pressing process

As well as the deposition process, the hot pressing process can be optimised. Parameters such as hot pressing time, temperature and pressure could have an effect on the adhesion of the Sn to the GDL and therefore the performance of the BPPs.

### 4.3.1. Hot press pressure

When hot pressing, the pressure was set at 1.4 MPa, equivalent to the *in-situ* pressure. There are negative impacts of either increasing or reducing this pressure, as seen in Figure 4.3.1. Lower pressures reduce adhesion between the GDL and BPP as permeation of the Sn into the GDL is lessened, reducing the length of the conduction pathway and the conductivity. At its most extreme, having not enough pressure during hot pressing leads to no contact between the GDL and BPP, meaning that when placed in a fuel cell, the top layer of Sn will oxidise between the Sn and the GDL, reducing conductivity.

The opposite phenomenon, hot pressing with too much pressure, can have equally negative effects on the performance of the BPP [179]. In Figure 4.3.1, we can see that when hot pressed at a too high

pressure, the GDL is forced into the channel of the BPP, blocking gas and water transport. Additionally, the presence of GDL fibres hot pressed to the Sn layer inside the channel indicates that the BPP was completely flattened during hot pressing. This could have a negative impact on the structural integrity of the BPP, by permanently deforming the BPP, narrowing coolant channels and breaking weld-points.

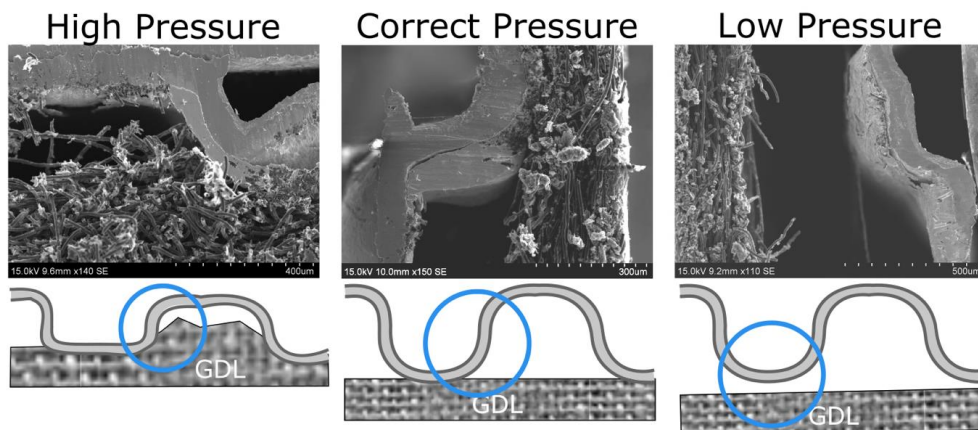


Figure 4.3.1. SEM images and figures of BPPs hot pressed at varying pressures.

Therefore, a hot pressing pressure of 1.4 MPa was determined to be optimum. As this is equal to the *in-situ* compaction pressure, the BPP substrate is designed to withstand it without deforming, the GDL will not be crushed and the infiltration of Sn into the GDL is enough to provide good contact.

### 4.3.2. Hot press temperature

When optimising the hot pressing temperature, those around the melting point of Sn (231.9°C [144]) were selected to investigate how the degree of melting of Sn could produce a best possible electronic contact between the metallic plate and the carbon based GDL. Figure 4.3.2 shows the ICR values recorded after pressing at temperatures between 226 and 232 °C.

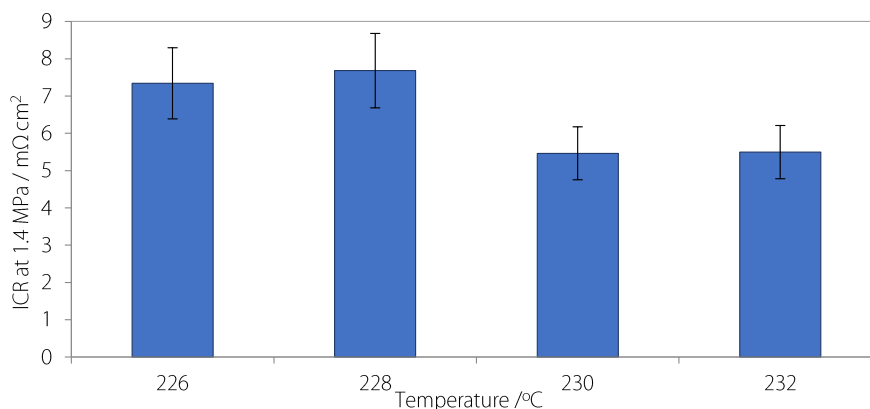


Figure 4.3.2. The correlation between the hot pressing temperature of a BPP and its ICR.

At temperatures above 230 °C, the Sn becomes ductile enough to penetrate the GDL more effectively, ensuring an increased contact area and a better pathway for current, lowering the average ICR from

7.7 mΩ cm<sup>2</sup> at 228 °C down to 5.5 mΩ cm<sup>2</sup> at 230 °C. In addition to an improved through-plane electronic conductivity, the plates prepared with a hot press temperature of 230 °C offered an improved adhesion due to the infiltration of GDL fibres into the tin, something that did not occur at temperatures lower than 230 °C.

Raising the temperature even further, up to 240 °C, causes the Sn to melt and run into the channels, as seen in the picture in Figure 4.3.3. As there is no Sn on the land areas of the BPP, there is no adhesion to the GDL.



Figure 4.3.3. A picture of bipolar plates hot pressed at 240 °C, where the Sn has collected in the channels.

Following these experiments, a temperature of 230 °C was used for all further plates.

### 4.3.3. Hot press time

The effect of the time spent in the hot press on the bipolar plates was measured. The bipolar plates were pressed for times ranging from 1 to 60 minutes, then removed from the hot press and cooled, before their ICR was measured.

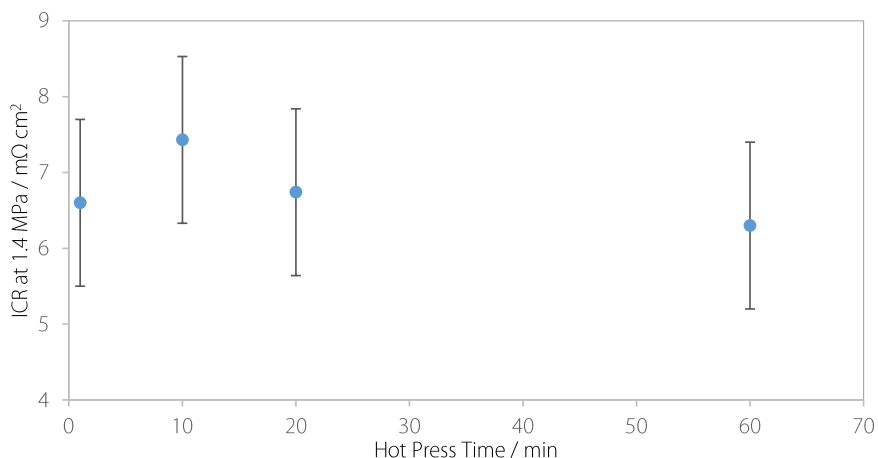


Figure 4.3.4. A comparison of the ICR of bipolar plates hot pressed for varying amounts of time.

Figure 4.3.4 shows that the effect of hot pressing time on the ICR of the BPPs was minimal. All ICR values are within the standard deviation of the others, meaning there is no statistically significant difference in performance obtained from varying the hot press time. As long as the Sn layer has enough time to reach its desired temperature, allowing soldering to take place, the subsequent time spent in the hot press does not impact the structure or properties of the combined BPP/GDL.

Therefore, a hot pressing time of 20 minutes was used for all further bipolar plate fabrication, as this leaves enough time for the temperature in the hot press to stabilise.

### 4.3.4. Cooling method

The effect on ICR of cooling the samples using two different methods was investigated (Figure 4.3.5). The ICRs for both cooling rapidly under atmospheric pressure (fast cool) or slowly under applied pressure (slow cool) were comparable before corrosion, at 6.8 and 7.1  $\text{m}\Omega \text{cm}^2$  at 1.4 MPa. After polarisation to 1.2  $V_{\text{SHE}}$  for 1 hour, a significantly improved ICR was observed for the slowly cooled plate, 13.2 compared to 17.9  $\text{m}\Omega \text{cm}^2$  at 1.4 MPa.

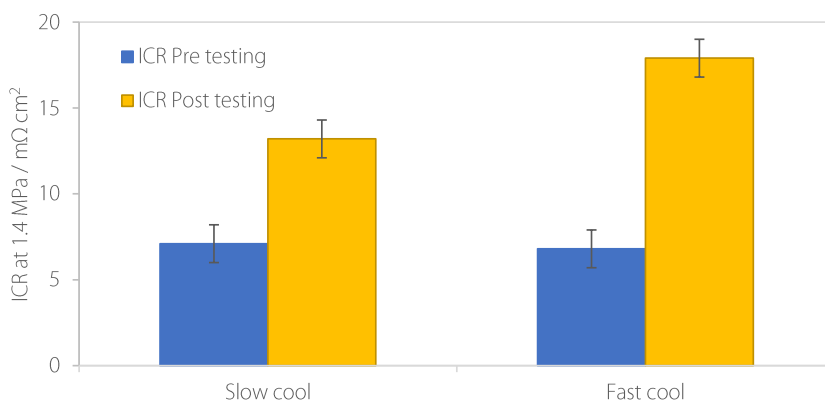


Figure 4.3.5. Comparison of the quick vs slow cooled plates before and after corrosion testing.

It is widely known that the rate of solidification of a metal has an impact on its microstructure, with the fastest cooling rates producing the smallest microstructures [180,181]. This is also the case for Sn and Sn alloys, and it has been shown that Sn films with larger grains have higher ductility and lower overall strength [182,183]. However, there is little information available on the influence of microstructure on the corrosion properties of Sn in simulated PEMFC environments.

Generally, oxide formation is preferred at the grain boundaries of metals due to the slightly lower local densities, allowing the easier penetration of oxygen or electrolyte into the metal matrix [184,185]. This can lead to the quicker formation of a protective oxide, if such an oxide is formed, or can lead to enhanced intergranular corrosion if the metal will not passivate. In the case of the Sn/GDL BPP, the smaller grain size of the quickly cooled BPP leads to a higher ratio of grain boundary to bulk. This enhances the oxide formation, so a protective layer will be produced more quickly, and BPP should be more stable.

However, this is not the trend that is observed in Figure 4.3.5. Instead, the slowly cooled plate has a better corrosion resistance than the quickly cooled plate, and this can be attributed to the pressure applied during the slow cooling, which forces the Sn to stay in contact with the GDL whilst solidifying. This produces longer conduction pathways and more contact between the Sn and GDL, so any oxidation of the Sn affects a smaller portion of the contact points.

It should be noted that for metals with an alloying element, for example stainless steels or Sn-based solder materials, the corrosion is often localised on the grain boundaries between the metal and the alloy phases due to galvanic coupling, so larger grains are better for corrosion resistance due to their



A summary of these corrosion processes occurring on Sn can be seen in Figure 4.4.1.

However, after this full passivation of the surface to SnO<sub>2</sub>, further corrosion can still occur. In the presence of certain ions such as halides or sulfates, pitting corrosion of Sn has been observed [196,197]. The rupture or detachment of the Sn corrosion product can also lead to additional corrosion through the exposure of metallic Sn [191,198], and it was found that in deoxidised electrolytes at acidic pH, complete oxidation of a thick Sn film will occur eventually (in this case, after 20 days of exposure to citric acid of pH 2-3 [198]). This leads to the conclusion that there is some ion movement through the film.

In terms of the progression of the Sn/GDL concept, with the optimisation and stabilisation of the oxide growth, the dehydration step to form SnO<sub>2</sub> is the slowest, so in order to improve the passivity of the Sn surface, this step should be sped up. It has been shown that the presence of elements with a greater valence than Sn will increase the rate of oxide formation when added to SnO [156]. The addition of just 0.1 % bismuth or antimony, amongst others, increased the rate of oxide formation, which should lead to a faster passivation of the surface and a more protective oxide. Therefore, the addition of certain alloying elements should improve the long-term performance of the BPPs.

## 4.5. Conclusions

The novel Sn/GDL soldering concept has proven to be successful in significantly reducing the interfacial contact resistance of stainless steel bipolar plates, by soldering the bipolar plate and the gas diffusion layer using metallic Sn. Very low ICR values were obtained before *ex-situ* corrosion testing, due to the uninhibited conduction pathways connecting the GDL and BPP through the soldered tin. However, the ICR increased after corrosion testing due to the dissolution and then oxidation of Sn on the BPP surface, leading to the breakdown of the conduction pathways. This shows that future modifications of the Sn/GDL system can be made to improve performance and longevity, including adding alloying elements to the Sn, or adding a layer of sprayed C between the Sn and GDL.

It was determined that a number of parameters during the deposition and hot pressing process have an impact on the final performance of the bipolar plates. The optimised conditions for the deposition of Sn onto the SS316L BPP are as follows: A plating thickness of 30 µm was deposited at 15 mA cm<sup>-2</sup> onto the pre-cleaned BPP, before hot pressing with a pre-cut Freudenberg H23 C6 GDL at 230 °C for 20 minutes at a pressure of 0.5 bar, then cooling slowly to room temperature. This procedure obtained the lowest contact resistance of 6.5 mΩ cm<sup>2</sup> at 140 Ncm<sup>-2</sup>, well below U.S DoE targets. The contact resistance increased to 13.2 mΩ cm<sup>2</sup> at 140 Ncm<sup>-2</sup> after *ex-situ* testing in Na<sub>2</sub>SO<sub>4</sub> at pH 5.5 and 80 °C, with 1.2 V<sub>SHE</sub> applied for 1 h.

*In-situ* testing was performed on Sn/GDL bipolar plates and will be discussed in chapter 9 of this thesis.



# 5

## A Preliminary Study on the Alloying of Sn

As determined in chapter four of this thesis, Sn alone is not stable enough as a coating material for BPPs in PEMFCs as its oxide does not form a protective layer fast enough and allows corrosion to continue. Therefore, there is a need to increase the rate of formation and stability of this oxide, and alloying with another element is a suitable way to do this.

The alloying metals were initially chosen for different reasons. Some (e.g. indium and antimony) are known to form stable transparent conducting oxides with tin [199]. Others, e.g. tantalum are known to be inert metals that are stable under PEMFC conditions, and bismuth is commonly used as an alloying material for Sn in lead-free solders. It has been found that the addition of bismuth and antimony in small quantities increases the rate of oxide formation on tin [156], which would hopefully lead to a more stable oxide and better performance. It has also been found that adding indium to a tin solder leads to a much better performance, with an increased fatigue resistance over the lifetime [200].

The important parameters for a successful alloying material for this application have been identified as: low melting point, low ICR after exposure to a PEM environment, and a low corrosion current density during electrochemical tests where a constant voltage is applied. Additionally, the feasibility of a one-step co-deposition with Sn should be evaluated. In this part of the thesis, these qualities for each potential alloying material have been compared against Sn alone, and SS316 to determine whether co-deposition to form a stable bipolar plate is feasible.

### 5.1. Melting Point

Firstly, the melting point was used to determine which of the candidate metals were practical for use in the hot pressing procedure, a summary of which is given in Table 5.1.1.

Table 5.1.1. A summary of the melting points of several metals, and their melting points when alloyed with Sn in a ratio of 95 % Sn to 5 % other metal.

Metal	Pure metal melting point / °C	5 % alloy with Sn melting point / °C
Sn	232	-
Bi	271	215
In	157	224
Ta	2980	850
Sb	630	242
SS316	1510	-

Immediately it is clear from Table 5.1.1 that tantalum is not a suitable alloying element, due to its very high melting point. Even at only 5 % tantalum in an alloy with Sn, the melting point is so high that hot pressing with the GDL would lead to oxidation of the carbon and destruction of the GDL properties. All other metals seem to be suitable based on melting point alone.

## 5.2. Electrochemical Testing

The pure metals were electrochemically tested in a simulated fuel cell environment by applying a voltage of  $1.0 V_{SHE}$  for 1 hour and measuring the current response, which is shown in Figure 5.2.1.

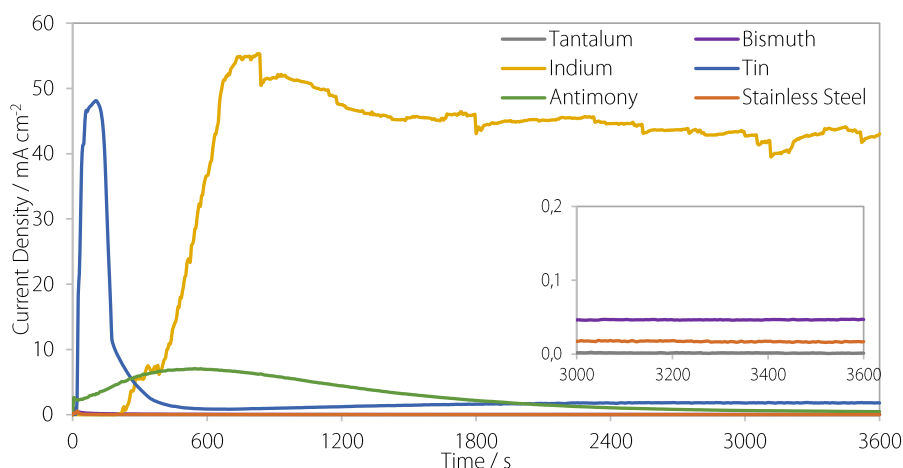


Figure 5.2.1. The current density response for pure metals exposed to  $1.0 V_{SHE}$  for one hour, with the inset showing a zoomed in section at very low current densities for the last 10 minutes.

Compared to tin, several of the potential alloying materials have a better performance, with a lower peak current density and a lower current density after one hour. Indium is the only metal that continuously corrodes without forming a protective oxide that passivates the surface, and consequently it has a higher corrosion current density throughout the test. Bismuth, stainless steel and tantalum all have very low corrosion currents, indicating that they are inert and would be stable under PEM conditions. The melting point of tantalum is too high for use in this application, but bismuth is a promising alloying element. Antimony also has a relatively low corrosion current and significantly lower than tin so it may be a useful alloying element.

## 5.3. Interfacial Contact Resistance

The ICR is one of the most important parameters for the bipolar plate, and any alloying element should preferably lead to a lower contact resistance than Sn alone. The ICR of each sample before electrochemical testing has been performed, and after they have been exposed to a voltage of  $1 V_{SHE}$  for 1 hour in a simulated PEMFC environment is reported in Figure 5.3.1.

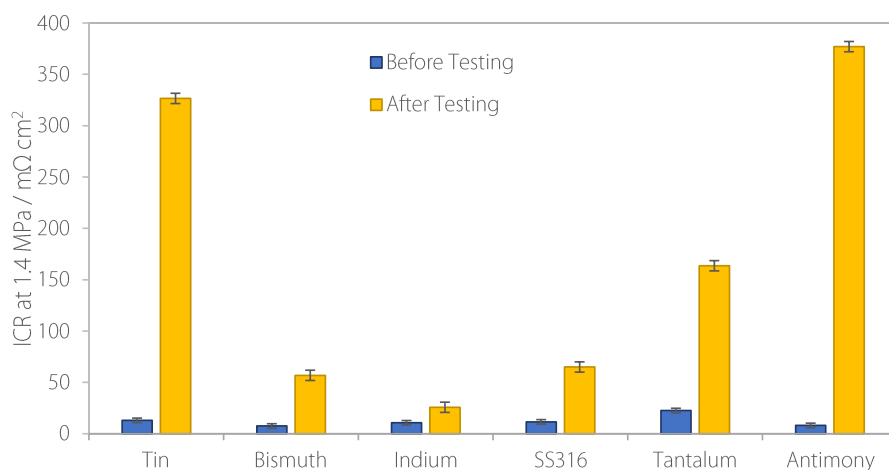


Figure 5.3.1. ICR of the different samples of metal before and after electrochemical testing at  $1.0 V_{SHE}$  for 1 hour.

It is obvious from Figure 5.3.1 that most of the samples that are stable under PEM conditions form a non-conductive oxide that increases the ICR after testing. Of the four most stable metals during the electrochemical testing, all have significant increases in ICR, however antimony is the only one that has a higher ICR than Sn-alone. Due to this large increase, it seems that adding antimony to the tin will not have a beneficial impact on the performance of the BPP.

Bismuth, which had very good corrosion performance, also has a much lower ICR than tin, so is the most promising alloying element to start investigating. Indium, despite not performing so well in the corrosion test, has a very low ICR so may be a beneficial alloying element to the Sn, especially if Sn can help stabilise In when alloyed as already shown in the very stable ITO.

## 5.4. Electrodeposition

Finally, the ability of each metal to be electrodeposited is crucial for success in this project. Although there are multiple ways to obtain a coating of a material on a stainless steel substrate, electrodeposition provides a cheap, easy and tuneable way to obtain a thin layer of metal on an irregularly shaped surface such as a bipolar plate.

Both bismuth and indium have performed well in the electrochemical and contact resistance tests, so a literature search was performed to determine whether deposition with Sn from an aqueous, ideally sulfate based bath had been previously performed.

For bismuth, the successful co-deposition of Sn and Bi from a sulfuric acid based bath has been performed [201,202], with bright SnBi alloys containing less than 5 % Bi being obtained. This is exactly the type of alloy required for this application, indicating the deposition is feasible.

Similarly, electrodeposition is a popular technique for obtaining layers of indium and its alloys. There are examples of Sn and In being co-deposited from a sulfate based bath to form SnIn alloys with less than 12 % Indium [203–205].

## 5.5. Conclusion

In conclusion, there seems to be two potential alloying elements for the Sn/GDL system, bismuth and indium. These both have good ICR properties after corrosion, low enough melting points and also seem to be able to be co-deposited with Sn to form an alloy from a simple one-step electrodeposition process. Therefore, in the upcoming chapters, SnBi and SnIn alloys will be deposited and tested to determine their suitability as coating materials for bipolar plates in PEM fuel cells.

# 6

## Tin-Bismuth Alloys for Bipolar Plates in PEM Fuel Cells

### 6.1. Why Bismuth?

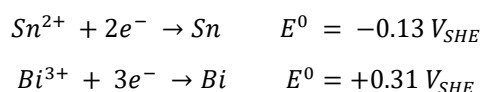
From preliminary studies using pure metals to identify possible co-deposition elements with Sn, bismuth has emerged as a promising solution. It has a suitably low melting point and exhibits a good stability in PEM environments whilst maintaining a low ICR.

Alloys of Sn and Bi have long been used as lead-free solders for electronics. SnBi alloys exhibit good corrosion resistance, low melting temperatures and good solderability [137]. A small addition of Bi has been shown to reduce the formation of Sn pest (the beta phase), as well as reducing the formation of whiskers due to a reduction in compressive strain [206]. It has been shown that the addition of Bi can promote wetting of the alloy, but too much Bi can cause reliability problems [207]. Notably, alloys with more than 4 % Bi may suffer from phase separation upon cooling, as the solubility of Bi in Sn at room temperature is only 4 % [208].

The majority of work on SnBi alloys has been done to advance the field of lead-free solder materials, with focus on the mechanical properties and soldering behaviour. However, little work has been done on the corrosion behaviour in sulfate -based electrolytes or identification of the electrochemical properties of SnBi alloys for the application of fuel cells. In one study, bismuth was found to increase the rate oxide formation on the SnBi surface, as it is of higher valence than Sn [156]. Having an oxide that forms quicker may produce a thicker protective oxide layer on the Sn BPP, which may increase the lifetime, although it may also have a detrimental effect on the electrical conductivity. Therefore, this work will attempt to quantify the effect of Bi on the long-term performance of Sn-based BPPs under simulated PEM fuel cell conditions.

#### 6.1.1. Electrodeposition of SnBi Alloys

Co-deposition of Sn and Bi is regarded as difficult due to the large differences in deposition potential, but it is possible with the help of additives.



A literature search into the co-deposition of Sn and Bi showed that there have been many examples of successful alloy formations from a variety of different bath types, some of which can be seen in Table 6.1.1.

Table 6.1.1. A summary of the available literature into SnBi co-deposition from aqueous solutions

Study	Sn Salt	Bi Salt	Bath Type	Anodes	Bath Conditions	Substrate	Deposit Composition
[209]	SnCl <sub>4</sub>	Bi(NO <sub>3</sub> ) <sub>3</sub>	Citric Acid PVA <sup>a</sup> Betaine	Steel	5 mA cm <sup>-2</sup> pH 0.4 to 6	Cu	14 to 75 % Sn
[210]	SnCl <sub>4</sub>	Bi(NO <sub>3</sub> ) <sub>3</sub>	Citric Acid EDTA <sup>b</sup> PEG <sup>c</sup>	DSA	25 °C 100 mA cm <sup>-2</sup> pH 6	Cu/Ni	0.5 to 30 % Sn
[211]	SnSO <sub>4</sub>	Bi(NO <sub>3</sub> ) <sub>3</sub>	Commercial	Sn	25 °C 40 – 60 mA cm <sup>-2</sup> pulsed	Cu	2 to 15 % Bi
[201]	SnSO <sub>4</sub>	Bi(NO <sub>3</sub> ) <sub>3</sub>	H <sub>2</sub> SO <sub>4</sub> POELE <sup>d</sup>	Pt	20 °C 2 A dm <sup>-2</sup>	Cu	> 3 % Bi
[212]	SnSO <sub>4</sub>	Bi <sub>2</sub> O <sub>3</sub>	CH <sub>3</sub> SO <sub>3</sub> H HQ <sup>e</sup> Gelatine	Pt	25 °C 18 mA cm <sup>-2</sup>	Cu	0 to 39 % Sn
[202]	SnSO <sub>4</sub>	Bi <sub>2</sub> (SO <sub>4</sub> ) <sub>3</sub>	H <sub>2</sub> SO <sub>4</sub> Sintanol Formalin Benzyl alcohol		2 to 10 A dm <sup>-2</sup>	Steel Cu	0 to 1.3 % Bi

<sup>a</sup> PVA = poly(vinyl alcohol)

<sup>b</sup> EDTA = Ethylenediaminetetraacetic acid

<sup>c</sup> PEG = Polyethylene glycol

<sup>d</sup> POELE = polyoxyethylenelaurylether

<sup>e</sup> HQ = Hydroxyquinone

During SnBi deposition, there is a tendency for the Sn anodes to undergo a displacement reaction, forming a black powdery Bi film which can passivate the anode, unbalance the Bi content in the bath and/or incorporate into the deposit [137]. To avoid this, different types of anodes or a chelating agent that binds more strongly to Bi than to Sn can be used, and it can be seen from Table 6.1.1 that insoluble anodes are indeed often used for SnBi deposition.

Electrodeposition of SnBi from deep-eutectic solvents has also been done [213,214], but for the work described in this thesis, an aqueous deposition bath at low temperatures is preferred. SnCl<sub>4</sub> salts have previously been used in aqueous deposition baths, but Cl<sup>-</sup> ions can induce pitting corrosion on stainless steels [16], so a bath using SnSO<sub>4</sub> is preferred.

The use of a sulfuric acid based deposition bath has previously been investigated by multiple authors [201,202]. Additives are required to approximate the deposition potentials of Sn and Bi, but otherwise the deposition is simple, and can take place at room temperature and with high current densities. Typically, deposition from sulfate based baths is only suitable for alloys containing less than 10 % Bi due to precipitation of Bi from the bath at higher concentrations [215]. As the work described in this thesis attempts to form alloys containing less than 10 % Bi, the sulfate bath was a suitable choice.

Experimental details including the exact composition of the electrodeposition bath used for SnBi codeposition can be found in chapter 3 of this thesis.

## 6.2. Optimising the Deposition of SnBi

As seen in Chapter 5 of this thesis, bismuth is stable under simulated PEMFC conditions. Bismuth showed improved corrosion performance compared to both tin and SS316 stainless steel, with a lower contact resistance both before and after testing, as well as a lower corrosion current than Sn during chronoamperometry at  $1.0 V_{SHE}$  for 1 hour at  $80\text{ }^{\circ}\text{C}$ . For these reasons, as well as its low melting point of  $271\text{ }^{\circ}\text{C}$ , Bi was deemed a suitable alloying element for Sn and co-deposition was attempted.

### 6.2.1. Factors affecting the Bi content

The objective of this thesis is to obtain a SnBi alloy with less than 10 % bismuth due to cost restrictions, melting point and stability in the PEM environment region of the Pourbaix diagrams [146]. Higher amounts of bismuth present in the SnBi alloy could improve the performance, but a solid solution of bismuth and tin is required and the solubility of bismuth in tin at room temperature is around 4 % [216]. The optimum amount of bismuth in the deposit was thus investigated in this work, starting with identifying the factors influencing the bismuth content of the deposit.

The most simple and effective way of varying the composition of a deposit is to change the metal content of the deposition bath [131]. Additionally, factors such as the bath temperature, addition agents, stirring, deposition potential, substrate material and substrate pre-treatment could influence both the bismuth content and quality of the deposit. However, the sulfate based Slototin bath has successfully been used to produce uniform Sn deposits on stainless steel substrates, and it is beneficial to keep using this bath type. Therefore, only certain types of addition agents are suitable without producing detrimental side reactions that affect the bath stability and deposit quality. For this reason, a compatible bismuth-containing additive was obtained. This additive has a stability range of 5 to  $40\text{ }^{\circ}\text{C}$ , so using elevated deposition temperatures would be difficult. Changing the amount of additive is therefore the easiest way to alter the Bi content of the bath.

#### Bath Composition and Stability

Slotolet G53, containing between 25 and 50 % Bi in the form  $\text{Bi}(\text{CH}_3\text{SO}_3)_3$  was added to the bath in varying quantities, and the amount of Bi in the deposit was measured. This additive is designed to be used in the Slototin bath, however only in small quantities (up to 0.3 mL/L bath) as a Sn whisker suppressant. Adding more of the additive to the bath should increase the amount of Bi in the deposit, but there could be a stability limit of the additive in the bath.

Figure 6.2.1 shows this relationship, and as more additive is added to the bath, the amount of Bi in the deposit linearly increases, until around 6 % Bi. After this point, the Bi content levels off, as the deposition of Bi is limited by the amount of additive adsorbed on the cathode surface. Adding more additive will increase the concentration in the bath but not necessarily at the surface, due to the presence of other competing Sn-containing additives.

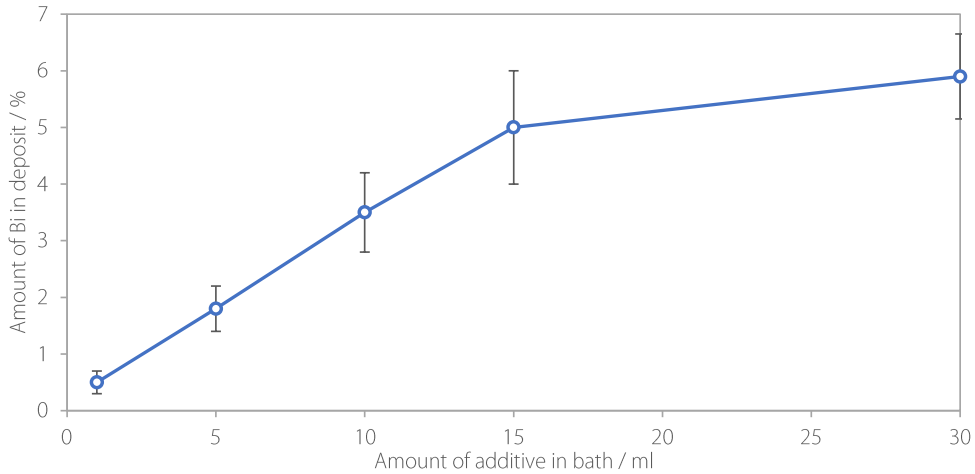


Figure 6.2.1. The relationship between the amount of Slotolet additive in the bath and the bismuth content of the deposit.

During this experiment, it was determined that the stability of the bath with respect to the expected and obtained bismuth content was limited to the first 12 hours after the addition of the Bi additive. All future deposition was done within this timeframe.

## Stirring

It is hypothesised that the amount of agitation in the bath could impact the structure of the deposit, and therefore have an impact on the corrosion properties and interaction between the BPP and the GDL. Increasing the stirring speed should encourage nucleation, leading to a smoother deposit with a smaller grain size, as well as favouring the deposition of the element that is already preferentially deposited [134].

SEM images show that the presence or absence of agitation has no notable effect on the morphology or grain size of the deposit. This can be seen in the SEM images in Figure 6.2.2, along with the backscattered electron images that clearly show the grain structure of the deposit, with both the deposit without any stirring and the deposit with 1000 rpm stirring having similar grain sizes. This implies that the nucleation rate of the majority alloy (Sn) is not affected by the agitation, as a faster nucleation would lead to more grains and therefore a smaller grain size.

However, the stirring speed of the bath does affect the bismuth content of the deposit. The sample deposited without stirring has a Bi content of  $2.3 \pm 0.3$  %, whereas when agitation of the bath is occurring the Bi content of the deposit drops to  $1.5 \pm 0.3$  %. This implies that the deposition of Sn is kinetically favoured over the deposition of Bi in this bath, and increasing the stirring speed reduces the comparative amount of Bi nucleation occurring.

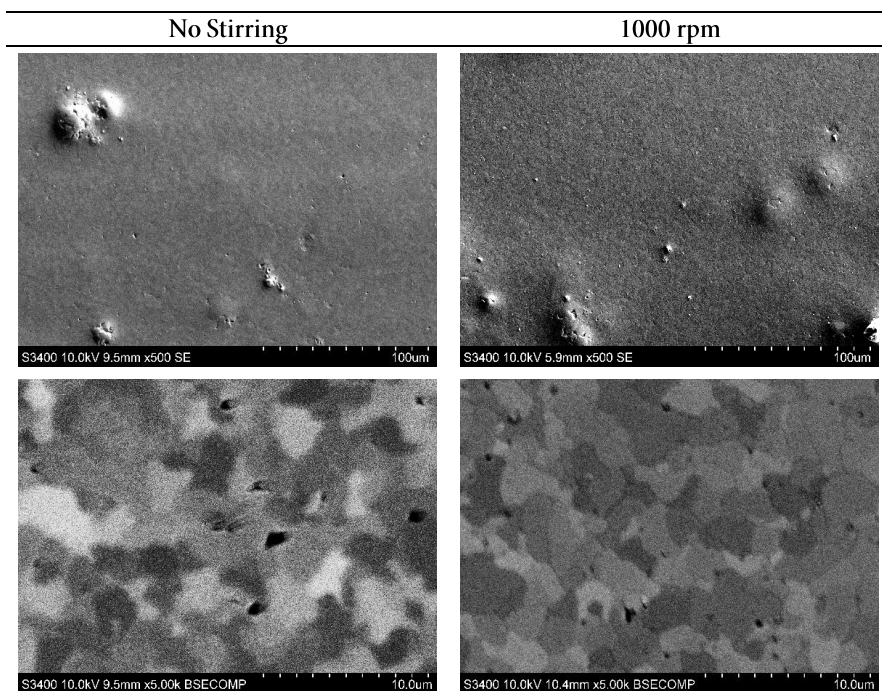


Figure 6.2.2. SEM images showing the structure of SnBi deposits with varying agitation in the bath during deposition (above) and SEM images with electron backscatter that show the detailed grain structure of the deposits (below).

Therefore, it can be concluded that the easiest way to change the composition of the SnBi alloy is to vary the amount of additive in the deposition bath, whilst keeping the stirring speed the same. There is no notable advantage to using either high or low stirring speeds, due to the similar surface morphology.

## 6.2.2. Determining the optimum Bi content

The amount of Bi in the deposit was varied by adding varying quantities (between 1 and 30 ml) of the Slotolet additive, which produced alloys containing between 1 and 6 % Bi, as seen in Figure 6.2.1 above. In order to fully characterise the SnBi surface and sample without obstruction, these coatings were deposited on stainless steel substrates, but not hot pressed with the GDL. Therefore, the ICR reported in this section is not representative of the ICR of the SnBi/GDL system but indicates the stability of the oxide layer formed.

Four samples of varying Bi content and one sample of pure Sn were tested in a simulated PEMFC environment using a 3-electrode configuration. Firstly, cyclic voltammetry (CV) was performed within the operating range of a fuel cell, with a sweep rate of 1 mV/s. Performing a CV is useful in order to map the potential behaviour of the sample and determine if there are any electrochemical processes occurring, and in this case, to indicate the effect of Bi on the processes occurring on the Sn/GDL BPP. Three sweeps were performed on each sample, and the final sweep is shown for all samples in Figure 6.2.3.

The CV for Sn alone is very typical of Sn oxidation, with a large oxidation peak starting at around  $-0.1 V_{\text{SHE}}$  which is around the thermodynamic potential of Sn oxidation in acidic medium [146]. As

seen in chapter 4 of this thesis, the oxidation of Sn does not necessarily produce a stable protective oxide, so the oxidation current remains high and continues throughout the entire forward and backwards sweep, until the subsequent reduction of tin oxides. The reduction occurs at potentials below  $-0.05 V_{SHE}$  with a small reduction peak at around  $-0.12 V_{SHE}$ .

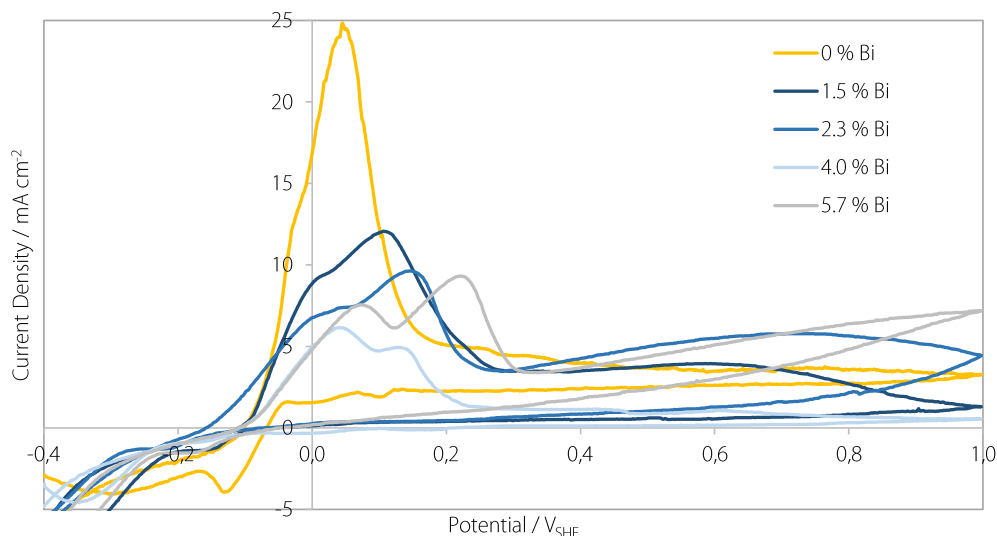


Figure 6.2.3. Cyclic voltammograms of samples of Sn containing between 0 and 6 % Bi when swept between  $-0.4$  and  $1.0 V_{SHE}$  at  $1 \text{ mV s}^{-1}$  in  $\text{Na}_2\text{SO}_4/\text{H}_2\text{SO}_4$  at pH 3 and a temperature of  $80^\circ\text{C}$ . Three cycles were performed, and the final cycle for each sample is shown here.

The addition of any bismuth to the tin seems beneficial, producing a smaller oxidation peak and in general a lower oxidation current, thereby reducing the total amount of oxide formed. The main oxidation peak is broadened with a distinct second peak, or shoulder, and shifted to more positive potentials in line with the incorporation of the more noble bismuth in the tin coating. The increasing amount of Bi in the samples improves the performance up to 4 %, which consistently performs the best at all potentials. At Bi content higher than 4.0 %, the performance apparently worsens.

The subtle differences in the potential of the onset of oxidation and peak oxidation are affected by the amount of Bi but are likely also due to variations in the sample surface and homogeneity of the Bi distribution. Although the CV measurements are interesting, it is more likely that the potentials experienced within the fuel cell will be more continuous and at a more positive potential (cathode). Therefore, the chronoamperometry measurement, which exposes the sample to a constant voltage for longer times, is likely to be of more use to determine the longevity of the BPP and the actual impact of Bi addition to the Sn coating.

Chronoamperometry measurements were performed by placing each sample in a simulated PEMFC environment with a potential of  $1.0 V_{SHE}$  applied for a total of one hour. The current response of the SnBi samples are shown in Figure 6.2.4 with the inset highlighting the last 15 minutes of the current transients.

For all the samples, the current density is very high initially after  $1.0 V_{SHE}$  has been applied, and then starts to gradually drop after a certain amount of time. As has been shown in Chapter 4 of this work,

with the pure Sn coatings, the peak in current density comes from the dissolution of the Sn surface to form  $\text{Sn}(\text{OH})_4$  species, which then slowly passivate to form a  $\text{SnO}_2$  layer on the surface of the sample.

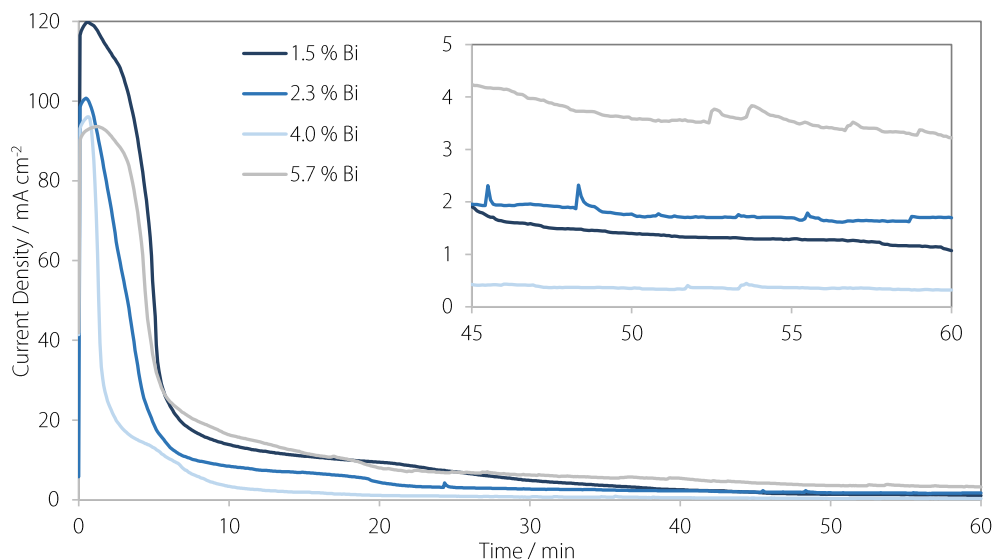


Figure 6.2.4. The current response from SnBi deposits containing various amounts of Bi, during the application of a voltage of  $1.0 V_{\text{SHE}}$  over the course of 1 hour in  $\text{Na}_2\text{SO}_4/\text{H}_2\text{SO}_4$  at pH 3 and a temperature of  $80^\circ\text{C}$ . The inset shows a zoom of the final 15 minutes of the current transients.

The amount of time taken to passivate the SnBi layer, indicated by the width of the peak, varies with varying amounts of Bi. As explained by Boggs et al [156], the addition of small amounts of Bi leads to faster passivation of the Sn layer, which is likely the reason why the oxidation charge is reduced for increasing addition of Bi to the alloy, up to 4%. This is not entirely in-line with the CVs, but the trend at  $1.0\text{ V}$  in the CVs matches the CA response in the final 15 minutes. Furthermore, when the Bi content increases above 4%, the Bi is no longer soluble in the Sn [208], leading to precipitation and the formation of Bi rich regions. This has a detrimental effect on performance, possibly because the accumulation of Bi at the grain boundaries could hinder the oxidation of Sn which occurs more quickly at the low density grain boundaries [184]. This leads to the longer passivation times, and the higher final current density, which indicates that the surface is not completely passivated, due to the presence of  $\text{Bi}_2\text{O}_3$  which could lead to poorer coverage and more film fracture.

The ICR data (Figure 6.2.5) agree with the conclusions made from the chronoamperometry tests. The oxide layer for the 4.0% sample stabilised quickly and remained fairly stable (with the lowest current density) over the course of the 1 hour corrosion test, and this is reflected in the high ICR value. The samples with less bismuth present took longer to stabilise, and were therefore dissolving for longer, leading to a thinned coating which has an inherently lower ICR. Although the samples eventually stabilised, their higher current density by the end of the constant voltage test implies that the surface was not completely passivated, and the oxide was not thick and stable.

The sample with higher Bi content took a long time to passivate, and even after 1 hour it did not passivate completely, as observed from the highest corrosion current density. This constant corrosion of the surface probably led to a very thin oxide forming, perhaps only on removal of the sample from

the electrolyte when it is exposed to air. Therefore, the ICR is the lowest of all the BPPs, despite the poorest corrosion performance.

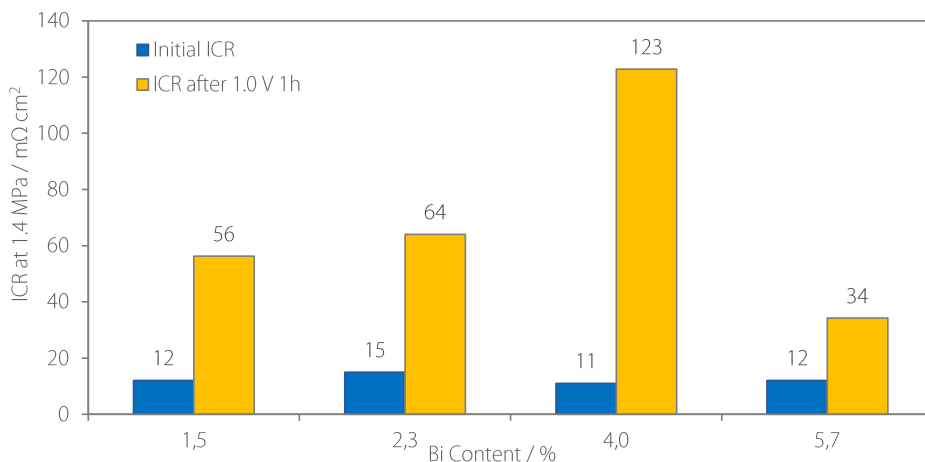


Figure 6.2.5. The ICR of samples with varying bismuth content before (blue) and after (yellow) exposure to 1.0 V<sub>SHE</sub> for 1 hour in a simulated fuel cell environment.

From these results, we can conclude that the sample with 4.0 % Bi is in the ‘goldilocks zone’ for beneficial Bi content. It has enough bismuth to quickly passivate the surface, leading to a stable oxide layer that will form a good protective barrier inside a fuel cell. However, it does not have too much bismuth, which leads to phase separation and is detrimental to the overall performance.

### 6.3. Hot pressing the SnBi alloy

After the SnBi alloy has been deposited onto a stainless steel substrate, it is hot pressed together with a GDL. This process can be tuned, with the hot pressing time and cooling procedure shown to be important parameters for the Sn/GDL system in Chapter 4. These parameters were therefore optimised for the SnBi/GDL system.

#### 6.3.1. Optimisation of the hot pressing time

Four identical samples containing 2.5 % Bi were deposited, and then hot pressed for varying amounts of time to determine the impact this had on the microstructure and electrochemical performance of the SnBi alloy. The samples were not hot pressed with the GDL in place, in order to be able to visualise the microstructure and elemental distribution, shown in the SEM images with EDS maps in Figure 6.3.1.

The samples that were hot pressed for up to 8 minutes show an even distribution of Sn and Bi, while an increase in hot pressing time results in a smoother surface. The 1-minute sample shows some holes in the coating, possibly because the surface has not fully melted in such a short time. These features are not present in the 3- and 8- minute samples, which have undergone a complete melting, leading to a smoother surface and an even distribution of Sn and Bi.

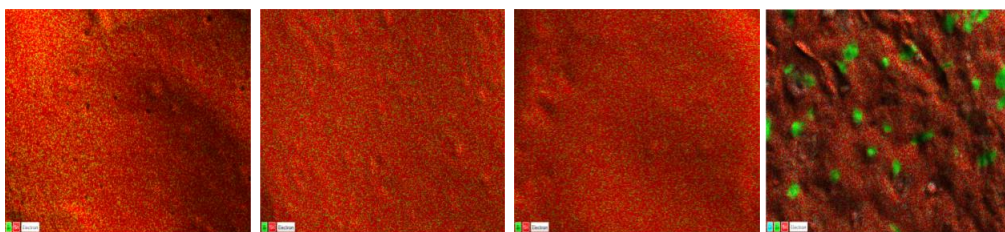


Figure 6.3.1. SEM images with false-colour EDS maps of SnBi deposits after being hot pressed at 226 °C for A - 1 minute, B - 3 minutes, C - 8 minutes, D - 20 minutes, showing the Sn distribution (in red) and Bi distribution (green).

At hot pressing times longer than 8 minutes, the surface is no longer smooth, and it is clear that hot pressing for 20 minutes results in phase separation of the Sn and Bi. This leads to both bismuth rich regions in the sample (seen in green on Figure 6.3.1d), and a depletion of Bi from the remainder of the deposit. The presence of these Bi-rich regions is detrimental to the overall performance of the BPP, as observed when the Bi content of the sample is greater than 4 in section 6.2.2. The bismuth-poor regions of the deposit should also have reduced corrosion performance compared to regions with intermediate bismuth contents.

The samples were electrochemically tested without a GDL present in a simulated PEMFC environment, to quantitatively determine the impact of hot pressing time on the corrosion performance of the SnBi deposits.

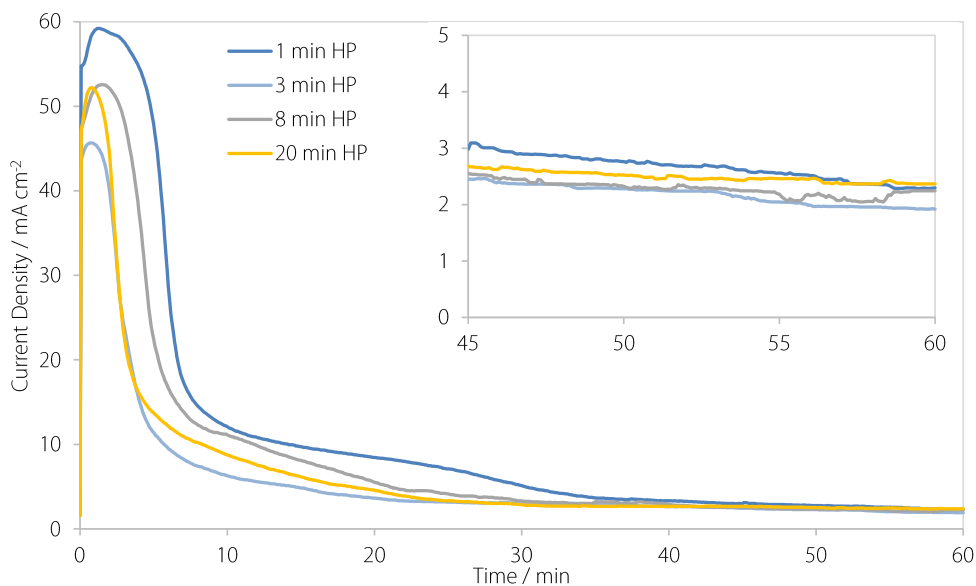


Figure 6.3.2. The current response of SnBi samples that have been hot pressed for various amounts of time without a GDL present, when exposed to 1.0 V<sub>SHE</sub> for 1 hour in a simulated PEMFC environment.

Figure 6.3.2 shows that the initial current densities can vary with the hot pressing time. The initial current is from the dissolution of Sn from the surface of the SnBi alloy, and the hot pressing time can affect the area of the sample directly exposed to the electrolyte. The one minute sample, which has pin-holes and surface roughness, has the largest exposed area initially, and thus produced the highest

currents. Once the Sn and Bi have been dissolved from the surface and begin to passivate to form oxides, the current drops and partial passivation occurs.

However, when all the SnBi surfaces have become passivated, after approximately 35 minutes, the corrosion current for each hot pressing time is almost identical. This is because small variations in surface roughness can be obstructed by the passivating film, and the surface areas of the samples become similar. Therefore, after the initial dissolution of the SnBi surface, the hot pressing time does not impact the long-term performance of the samples.

In order to understand how the different hot pressing times affect the adhesion to the GDL, the experiment was repeated with bipolar plate substrates, which were hot pressed to GDLs for between 1 and 20 minutes. This should provide more insight into the stability provided by the oxide layer and the adhesion between the GDL and BPP.

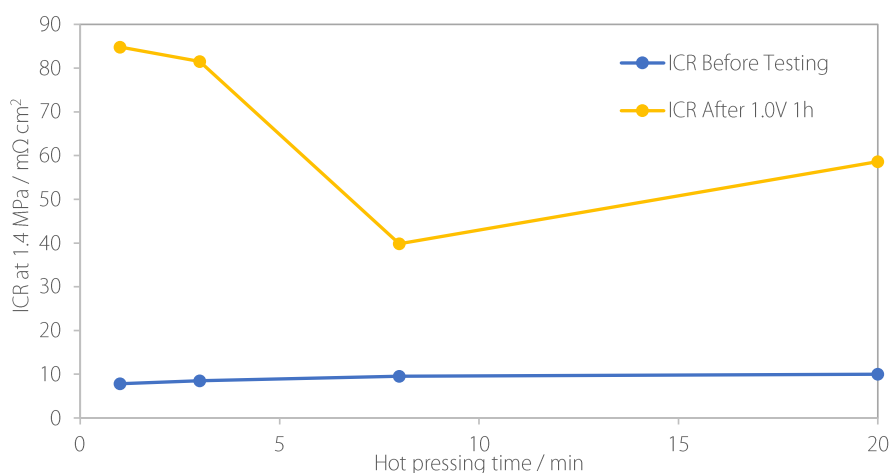


Figure 6.3.3. The ICR of BPPs hot pressed to GDLs for varying amounts of time, before (blue) and after (red) electrochemical tests at 1.0 V<sub>SHE</sub> for 1 hour.

After chronoamperometric testing at 1.0 V for 1 hour, the ICR for each of the BPPs has increased (Figure 6.3.3), but the hot pressing time of 8 minutes provides the smallest increase. This implies that the longer hot pressing time has improved infiltration of the SnBi into the GDL, leading to better adhesion and therefore a larger amount of conduction pathways for electronic transfer, even after corrosion testing. The longer hot pressing time of 20 minutes should also perform well for this reason, however as seen in the SEM images in Figure 6.3.1, phase separation has occurred as the heat treatment was too long. This leads to poorer corrosion performance including galvanic corrosion, poor stabilisation of the oxide layer and therefore more removal of the SnBi coating material. This has clearly affected the ICR negatively, with fewer conduction pathways for electron transfer, and poorer adhesion between the GDL and BPP.

Therefore, the hot pressing time of 8 minutes was long enough to produce a good adhesion whilst not being too long to lead to phase separation and the associated negative effects. This hot pressing time was used for all further samples.

### 6.3.2. Cooling procedure

Two cooling procedures were identified for when the BPP is taken out of the hot press. The plate can either be taken directly out of the hot press and quickly cooled to room temperature, solidifying the SnBi at atmospheric pressure. Alternatively, the heating elements within the hot press can be turned off and left to air-cool, with the SnBi coating cooling slowly whilst under pressure. Cooling the BPP slowly under pressure should produce a coating with greater adhesion to the GDL, in addition to better infiltration of the SnBi into the GDL, therefore a larger contact area for electron transfer and a lower contact resistance. This effect has been observed in chapter 4 of this thesis.

However, the slower cooling process will lead to greater phase separation, which could be detrimental to the long-term performance of the BPP [217]. SnBi solders with up to 5 % Bi were analysed by Mahmudi et al. [218], and it was determined that the slowly cooled solders had a much larger grain size and more precipitation of Bi from the Sn phase, which worsened the mechanical properties. Such phase separation would also be detrimental to the corrosion performance of SnBi alloys, as it would lead to galvanic coupling between the SnBi and the Bi rich phases due to differences in corrosion potentials.

In order to determine which effect dominates, and therefore which BPP would perform the best, chronoamperometric testing in pH 3 electrolytes at 80°C at 1.0 V for 1 or 6 hours was performed. Each sample was repeated three times with the error bars showing the standard deviation.

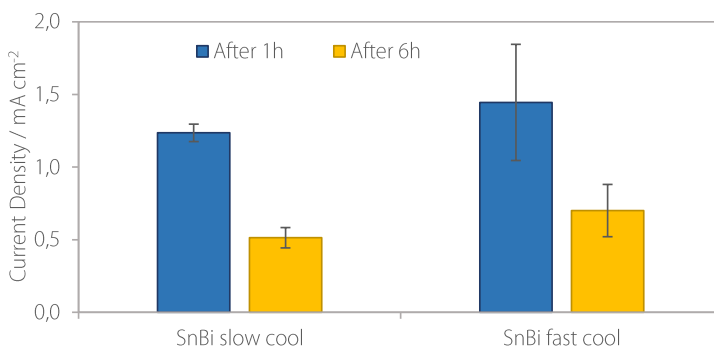


Figure 6.3.4. The current density of slowly and quickly cooled SnBi BPPs after one hour (blue) or six hours (yellow) of an applied potential of 1.0 V SHE in a simulated PEMFC environment.

From Figure 6.3.4, it can be seen that the slowly cooled plates have a slightly lower current density after one and six hours of electrochemical testing, and a smaller standard deviation than the quickly cooled plates. The results are not completely conclusive, as the current density for the slowly cooled BPP is within the standard deviation of the fast cooled BPP. However, the slowly cooled plate seems to be more consistent.

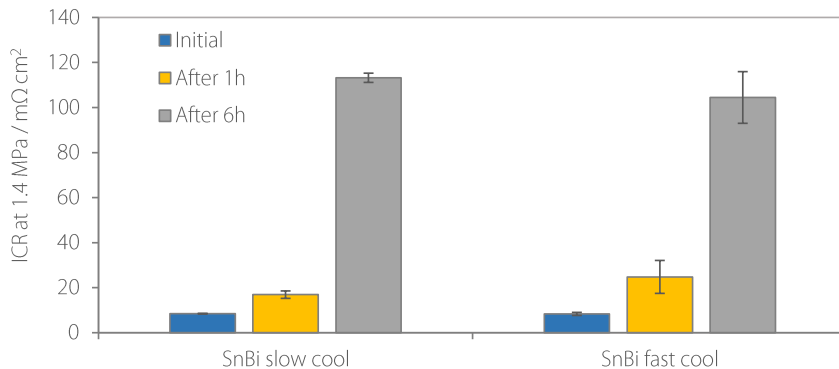


Figure 6.3.5. The ICR for slowly and quickly cooled bipolar plates after pressing (blue), after 1 hour of electrochemical testing (yellow) and after 6 hours of electrochemical testing (grey).

The ICR results, shown in Figure 6.3.5, also confirm that the slowly cooled BPP performs better over the first hour of corrosion testing. However, after 6 hours in a simulated PEMFC environment, its ICR is higher than the fast cool BPP. Again, the slowly cooled plate is more consistent, with a small standard deviation, and is also within the error bars of the fast cooled plate. Therefore, in this case, the slow cooling procedure is recommended due to the higher reliability of this method. In general, the two competing processes of better adhesion but phase separation for the slow cool plate have an opposite effect and both must be considered when deciding which cooling method to use.

## 6.4. Conclusions

The successful co-deposition of a SnBi alloy has been performed using an additive containing bismuth in the form  $\text{Bi}(\text{CH}_3\text{SO}_3)_3$  and a commercial Sn plating bath. It was determined that a SnBi alloy with 4% Bi, hot pressed with a H23C6 GDL for 8 minutes at 226 °C and then cooled slowly under pressure provided the best resistance to corrosion in an *ex-situ* simulated PEM environment. This SnBi BPP was tested *in-situ*, and the results are reported in chapter 8 of this thesis.

The results in this work have shown that any treatment of bipolar plates containing alloying materials should be done in a way that avoids phase separation. In this case, depositing more than 4 % Bi or heat treating the samples for more than 8 minutes have been shown to negatively affect the performance.

# 7

## The Co-deposition of Sn and In for Bipolar Plates in PEMFCs

### 7.1. Why Indium?

Indium is a semi-precious metal that was first discovered in 1863 and is generally produced as a by-product of zinc refinement [219]. Since 1992, the largest application of Indium has been in ITO (indium tin oxide) thin films used in LCD screens [220]. It was one of the first transparent conducting oxides discovered and has been widely used due to its stability and good conductive properties. Although ITO has a much higher indium content than desired for our application due to cost requirements, its properties indicate that SnIn alloys may be interesting for this application.

Preliminary tests, seen in chapter 5 of this thesis, indicate that pure indium has a low ICR after exposure to a PEM environment, although the Pourbaix diagram indicates that Indium may only be stable at higher pH at relevant electrode potentials [146]. Geiger et al. [221] investigated the stability of ITO in 0.1 M  $\text{H}_2\text{SO}_4$ , and found that rapid dissolution of indium and tin occurred above potentials of 2.35  $V_{\text{RHE}}$ , and even below these potentials, constant dissolution still occurred although at a lower rate. However, there is currently no information as to whether the dissolution rate of ITO is lower than that of  $\text{SnO}_2$ , and therefore whether additions of indium could enhance the stability of the Sn/GDL BPP system.

Other common uses of SnIn alloys have been as low-temperature solder materials at close to eutectic compositions [222,223], and tin with smaller amounts of In present have been used when alloyed with other metals such as silver, bismuth and zinc [208]. In addition to reducing the solder melting temperature, the addition of small amounts of In to a Sn solder can reduce the formation of whiskers due to a decrease in compressional tension at the solder surface [224,225]. Indium has a similarly low resistivity as tin ( $0.83 \times 10^{-7} \Omega \text{ m}$  for In vs  $1.09 \times 10^{-7} \Omega \text{ m}$  for Sn), therefore as well as its low melting temperature, it will provide the low ICR needed for bipolar plate applications.

To our knowledge, there is no literature on the corrosion properties of SnIn alloys with between 1 and 10 % indium, in an environment relevant to usage in PEM fuel cells. This thesis chapter will contribute with new knowledge to fill this apparent gap and attempt to show that the deposition of a thin layer of a low indium content SnIn alloy is possible on a stainless steel substrate, as well as indicating the corrosion properties of such an alloy in a simulated PEMFC environment.

### 7.1.1. Examples of Indium and Tin-indium Deposition

The electrodeposition of indium and indium tin alloys is fairly common, and a number of deposition baths have been patented since the 1940s [225–228]. Many other papers have reported the deposition of SnIn alloys under various conditions [203–205,229–233].

Some co-deposition of Sn and In at near-eutectic ( $\text{Sn}_{0.49}\text{In}_{0.51}$ ) compositions has been performed using carboxylic acid salts as chelating agents to slow down the Sn deposition [231,232], however none of the baths used are suitable for industrial electroplating, due to the presence of cyanides [231] or unsuitable processing conditions [232].

A summary of some of the available literature on SnIn or In deposition can be seen in Table 7.1.1.

Table 7.1.1: A summary of the available literature on Indium and InSn alloy deposition.

Study	In salt	Sn salt	Bath type	Anodes	Bath conditions	Substrate	Deposit composition
[203]	$\text{In}_2(\text{SO}_4)_3$	$\text{SnSO}_4$	$\text{H}_2\text{SO}_4$ Formalin Synthanol Butyenediol	Tin, Indium or SnIn alloy	18 - 50 °C Agitation 1 - 7 A $\text{dm}^{-2}$	Copper or Steel	0.5 - 9 wt% In 45 - 57 wt% In
[204]	$\text{InCl}_3$	$\text{SnSO}_4$	$\text{H}_2\text{SO}_4$ OC-20	Tin, Indium or SnIn alloy	0.5 - 1.5 A $\text{dm}^{-2}$ 20 - 50 °C	Copper or Steel	12 - 78 wt% In
[205]	$\text{In}_2(\text{SO}_4)_3$	$\text{SnSO}_4$	$\text{H}_2\text{SO}_4$ CTAB	Platinum, Pt coated Ti or graphite	1 A $\text{dm}^{-2}$ pH 1 - 3	-	12 wt% In
[227]	$\text{In}^{3+}$ salt	$\text{Sn}^{4+}$ salt	NaOH Chelating agent Organosulfonic acid	-	pH 7 - 11 0.1 - 30 $\text{Adm}^{-2}$ 60 - 100 °C	-	40 - 60 wt% In
[228]	Sulfmate Chloride Bromide Sulfate	-	$\text{H}_3\text{NSO}_3$ $\text{NH}_2\text{NaSO}_3$ Dextrose	Indium	Room temp pH < 3.5 Agitation < 10 $\text{Adm}^{-2}$	Copper	Indium
[230]	$\text{In}_2(\text{SO}_4)_3$	$\text{SnSO}_4$	Methanesulfonic acid NaOH Gluconic acid Hydroquinone	Stainless steel	pH 1.2 Room temp Agitation 2 A $\text{dm}^{-2}$	Copper	4 - 10 wt% In
[233]	$\text{In}(\text{BF}_4)_3$	$\text{SnCl}_2$	$\text{BF}_3$ , $\text{H}_3\text{BO}_3$ , $\text{NH}_4\text{F}$ , $\text{NH}_4\text{HF}_2$	-	18-25 °C 2.5-5 A $\text{dm}^{-2}$ pH 1.0 - 1.1	-	Up to 16 % Sn
[234]	$\text{InCl}_3$	-	$\text{InCl}_3$ solution	Platinum	0.03 - 0.12 A $\text{dm}^{-2}$ 35 - 65 °C	Steel	Indium

Multiple types of deposition bath have been used for In and SnIn deposition. Of the deposition baths listed in Table 7.1.1, the vast majority are acidic, with the  $\text{In}_2(\text{SO}_4)_3$  and  $\text{InCl}_3$  salts being used most frequently. Based on the complex deposition baths listed in Table 7.1.1, it is obvious that a number of additives are needed to obtain a SnIn alloy, although indium alone has successfully been deposited from a simple chloride bath [234]. The vast majority of depositions took place at room temperature or slightly above, and at current densities of around  $1 \text{ A dm}^{-2}$ , or  $10 \text{ mA cm}^{-2}$ . Many of the attempts use insoluble anodes, however the ones that do not, use soluble indium or SnIn alloy anodes to plate on copper or steel substrates.

A sulfate bath has successfully been patented and used for the deposition of a SnIn alloy [203,226], and performed better than similar baths using Indium chloride salts [204], with a bright finish being observed. It contained numerous organic additives such as formalin and butynediol and produces alloys in the range of 0.5 to 57 wt % indium. Low In alloys were obtained when the concentration of the tin salt was higher than that of the indium salt. When the content of the indium salt is increased, alloys with between 45 and 57 wt % In were obtained, however they had a narrow range of operating current density due to the small hydrogen evolution overvoltage for indium deposition which leads to more hydrogen evolution and therefore lower current efficiencies.

From this literature overview, it can be concluded that deposition of a SnIn alloy containing up to 10 wt% In from a sulfate bath should be possible.

## 7.1.2. The Kinetics of SnIn Deposition

In general, co-deposition of Sn and In is difficult due to the large difference in standard electrode potentials, which often leads to the deposition of Sn alone [230].



The approximation of the deposition potentials of Sn and In must be done, and common methods of achieving co-deposition of two metals with a large difference in deposition potential include changing the bath composition with respect to metal salt concentrations [131], using additives such as complexing agents [133], or by tuning the operating variables of the deposition [134]. Additionally, the electrochemical characteristics of the Sn and In deposition reactions can be identified to determine what effect tuning certain kinetic parameters will have on the co-deposition.

The kinetics of any reaction is very dependent on a number of factors including the substrate, bath conditions and additive types. When studying the kinetics of tin deposition from an acidic sulfate bath, Meibuhr et al. [132] found Tafel slopes within the range of  $170$  to  $230 \text{ mV decade}^{-1}$  when using a wide range of additives. The exchange current density also varied widely with the additive type, with values of between  $0.03$  and  $2.0 \text{ mA cm}^{-2}$  reported. Also in sulfate baths, Tzeng [235] reported Tafel slopes for Sn deposition of around  $105 \text{ mV decade}^{-1}$ , with varying additives present.

For indium deposition, Tafel slopes of between 250 and 300 mV decade<sup>-1</sup> have been reported by Lovrecek et al. [236] for indium deposition from an acidic indium sulfate solution, but in some cases slopes up to 480 mV decade<sup>-1</sup> have been found [237]. Changing the electrolyte will have a large impact on the kinetics. In chloride solutions, a Tafel slope of only 30 mV decade<sup>-1</sup> was reported, but this increased to 120 mV decade<sup>-1</sup> in a perchlorate electrolyte, when the dominating species in solution changed from In(III) to In(I) [238].

In general, it can be seen that the Tafel slopes of Sn and In deposition are highly variable depending on a number of factors. It is difficult to predict the exact kinetics of each reaction in each electroplating bath, but by tuning the deposition parameters, the relations between the kinetic behaviour of each metal deposition can be determined.

In this chapter, deposition from sulfate and chloride baths has been attempted, and a large number of deposition parameters were tuned to try and achieve a SnIn alloy that can be used as a coating for bipolar plates. The surface morphology and composition of SnIn deposits were investigated and optimised to obtain a homogeneous and metallic coating, which was characterised using SEM imaging with EDS analysis, ICR measurements and chronoamperometry. The experimental procedures can be found in chapter 3 of this thesis.

## 7.2. Co-deposition of Sn and In

### 7.2.1. Indium based additive for SLOTO TIN solution.

The simplest way to begin the SnIn co-deposition is to continue using the Slototin bath used for the deposition of Sn and SnBi alloys in chapters 4 and 5. The bath is designed to produce bright Sn-based coatings on stainless steel substrates, and if a small amount of indium is added to the bath, co-deposition should be possible. Thereby, SLOTOPAS ZNB 62 additive from Schlötter was obtained. This additive, which was originally designed for passivation of zinc-nickel deposits, contained between 3 and 5 % indium in the form In<sub>2</sub>(SO<sub>4</sub>)<sub>3</sub>, and should be compatible with the bath that has successfully been used to deposit Sn and SnBi alloys on stainless steel.

#### The amount of indium based additive

Initially, the indium additive was simply added to the bath in varying amounts from 1 to 30 ml and deposition was performed under the recommended conditions. The plates were then analysed in the SEM to study the morphology of the deposit and determine whether any indium was co-deposited on the surface. As can be seen from Figure 7.2.1, it is clear that the amount of additive present in the bath does not affect the indium content of the deposit.

At 30 ml of additive per L of deposition bath, the approximate ratio of tin to indium ions is 3 : 1. As the concentration of tin ions is greater than the concentration of indium ions, this should produce a Sn rich SnIn alloy [203]. However, as seen in Figure 7.2.1, none of the deposits have more than 1 % indium present, and there is no trend that indicates adding more will increase the indium content. This could

be due to the large difference in deposition potentials between Sn and In, or the strong complexation of indium in the additive, meaning there is none available for deposition.

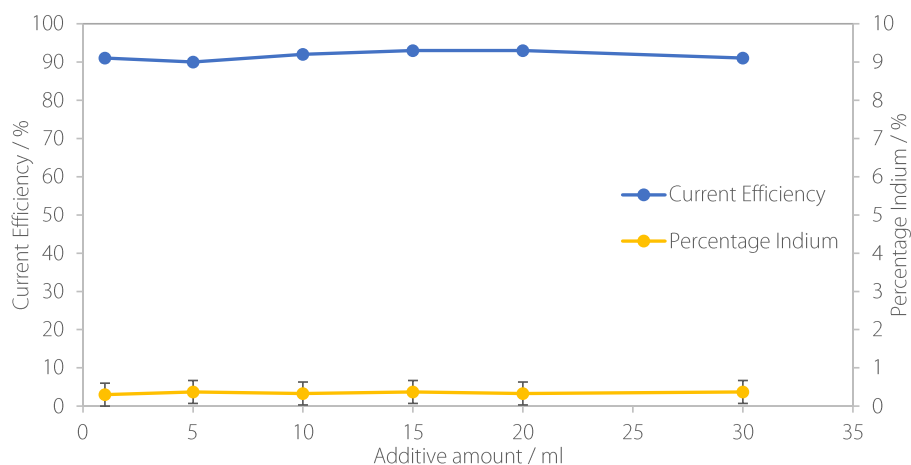


Figure 7.2.1: The influence of the amount of additive present in the bath on the current efficiency of deposition and indium percentage in the deposit. The error bars in indium percentage reflects the uncertainty in the EDS measurements.

Therefore, other parameters were used to try and force the indium present in the bath to deposit onto the surface, preferably as an alloy with Sn.

## Current Density

Firstly, the current density of deposition was varied. From the kinetic parameters of the Sn and In depositions found from literature, the indication is that increasing the current density of deposition should favour In deposition, as it often has a steeper Tafel slope. Additionally, at low current densities the deposition rate should be determined by kinetics, however when increasing the current density, the deposition quickly becomes limited by the diffusion of metal ions to the surface. This should favour the deposition of the less noble indium, as it is not at its limiting current density yet. However, if the kinetics of the indium deposition are so slow that a large increase in current density is required, hydrogen evolution will begin to dominate and a drop in current efficiency is observed.

It is clear from Figure 7.2.2 that this is the case, as increasing the current density did not change the indium composition of the deposit. Again, less than one percent indium was present in the deposit at all times, and as the current density increased past  $80 \text{ mA cm}^{-2}$ , the current efficiency of deposition was so low that there was almost no deposit present.

Therefore, the kinetics of indium deposition are so unfavourable that the current density cannot be increased enough to deposit indium, before the current efficiency becomes too low due to hydrogen evolution.

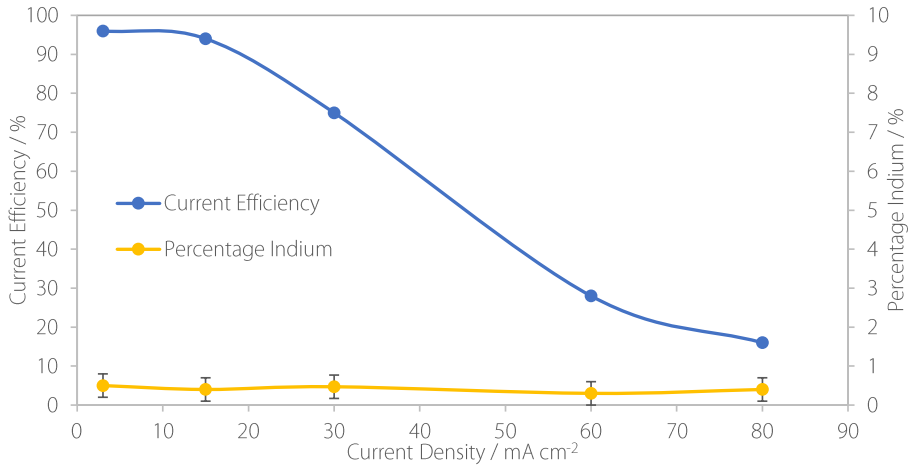


Figure 7.2.2: The influence of the current density of deposition on the current efficiency of deposition and the percentage of indium in the deposit.

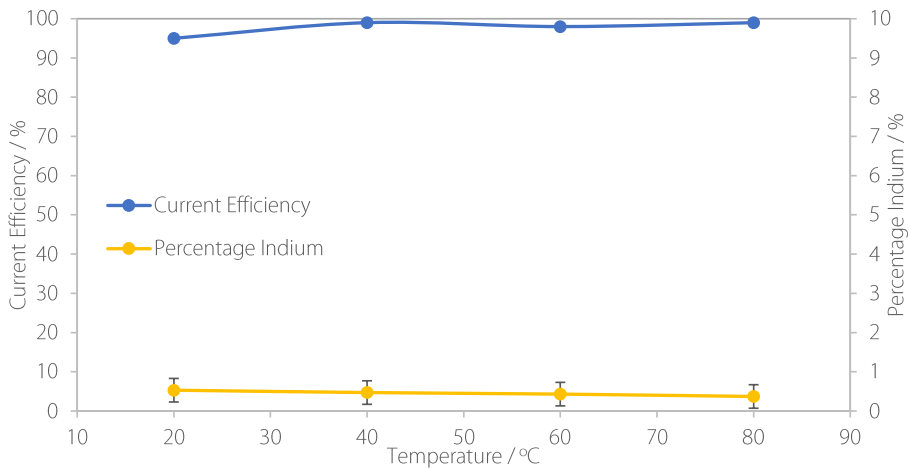


Figure 7.2.3: The influence of the temperature of the deposition bath on the current efficiency of deposition and the amount of indium in the deposit.

## Temperature

Next, the temperature of the bath during deposition was altered. The bath is designed to be operated at room temperature, and the effects of increasing temperature can be very bath-specific and deposit-specific. Therefore, it is hard to predict what effect changing the temperature will have.

Interestingly, the current efficiency of the Sn deposition increases with temperature, this is because the overpotential for electrodeposition of tin must be more dependent on the temperature than that of hydrogen evolution. It has been shown that as the temperature increases, the Tafel slope steepens and the exchange current density of the metal deposition reaction increases [239], as predicted in the introductory chapter of this thesis.

Unfortunately, increasing the temperature of the bath did not have any effect on the indium content, shown in Figure 7.2.3. The current efficiency remained high, and the amount of indium in the deposit

remained below 1 % at all temperatures. Therefore, the improvements in the kinetics of indium deposition are not enough to overcome the difference with Sn and allow co-deposition.

## Stirring

The stirring speed of the bath was also altered in an attempt to co-deposit Sn and In. Increasing the stirring speed reduces the thickness of the diffusion layer and will improve diffusion of metal ions to the surface.

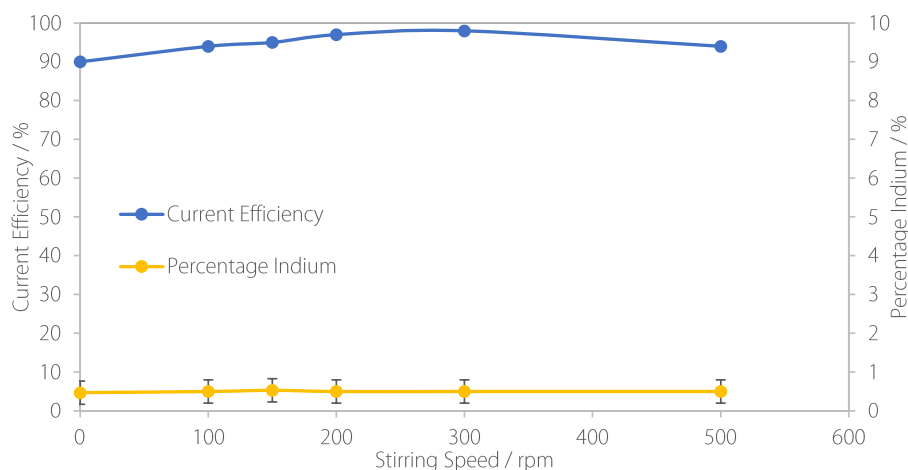


Figure 7.2.4: The influence of the stirring speed in the bath on the current efficiency of deposition and the amount of indium in the deposit.

From Figure 7.2.4, it can be seen that initially there is an increase in the current efficiency up to 300 rpm stirring speed. This is due to enhanced metal deposition kinetics, which occur due to a decreased diffusion layer thickness increasing the limiting current density (which is diffusion controlled). As the stirring speed further increases, the current efficiency once again drops, a trend that has previously been reported [240]. The decrease in current efficiency with increasing stirring speed can be attributed to enhanced hydrogen evolution kinetics [241].

However, it is clear that the stirring speed has no effect on the amount of indium in the deposit. This indicates again that indium deposition, or Sn-In co-deposition is not kinetically favourable, perhaps due to In being strongly complexed in the electrolyte.

## pH

Finally, the pH of the bath was also increased in an attempt to allow for co-deposition of both Sn and In. Inspecting the corresponding Pourbaix diagrams [146], the deposition potential of Sn reduces with an increase in pH, however the deposition potential of In remains constant within the pH-range studied here. The In deposition potential is  $-0.34$  V until around pH 5, whereas Sn reduces from  $-0.136$  at pH -1 to around  $-0.30$  V at pH 3. Therefore, increasing the pH in the electrolyte leads to the approximation of the thermodynamic deposition potentials so that co-deposition may become possible.

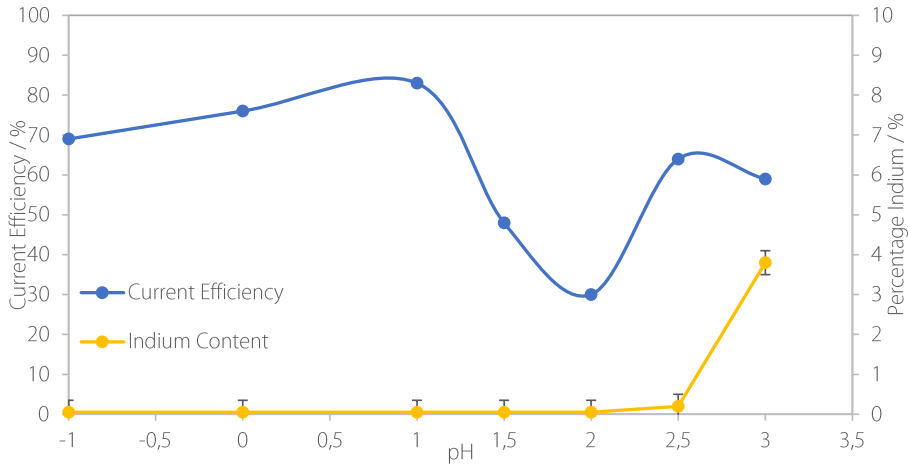


Figure 7.2.5: The influence of the pH of the deposition bath on the current efficiency of deposition and the amount of indium in the deposit.

The electroplating bath consists of numerous additives and it is important to be aware that altering the pH can also affect the complex formation in the bath, which may differ between the two metal ions. Since the deposition bath and additives are proprietary, the complexing agents and their concentrations are unknown, therefore it is impossible to directly predict the effect that changing the pH will have. Figure 7.2.5 displays the In content in the electroplated layer as well as the current efficiency as a function of pH.

As the pH increases through the addition of NaOH, the indium content of the deposit also increases. Above pH 2, the indium content of the deposit increased up to 4 %, the highest seen in any of the parameter studies. This is probably due to the approximation of the Sn and In deposition potentials, as predicted from the Pourbaix diagrams. Furthermore, hydrogen evolution kinetics is rapidly decreasing with increasing pH in this pH interval [242]. This explains the initial increase in current efficiency of the deposition from pH -1 to 1, due to the slower hydrogen evolution.

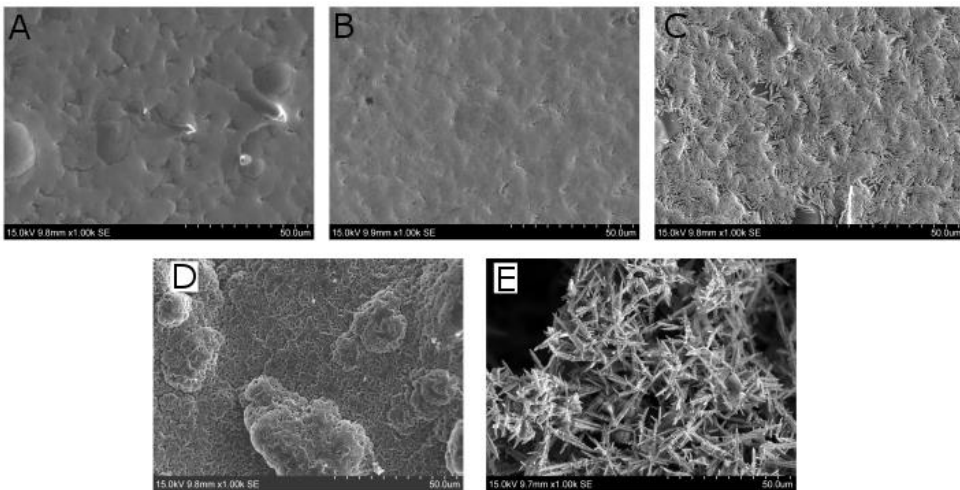
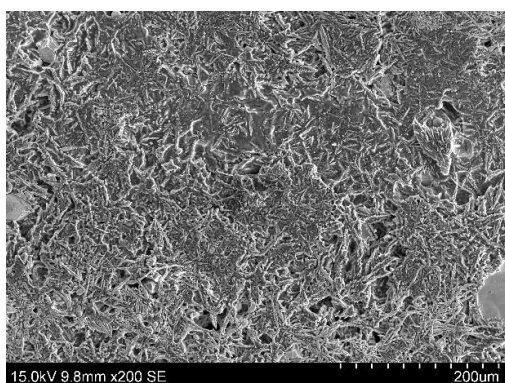


Figure 7.2.6. SEM images of SnIn alloys deposited at various pH. A = -1.0, B = 0.0, C = 1.0, D = 2.0, E = 3.0.

However, there is a very distinct and sharp reduction in current efficiency starting at pH 1, reaching as low as 30% at pH 2. This can be explained as there is a transition from the deposition of  $\text{Sn}^{2+}$  to  $\text{Sn}^{4+}$  at around pH 1. It requires twice as many electrons to reduce each atom of  $\text{Sn}^{4+}$  compared to  $\text{Sn}^{2+}$ , effectively decreasing the current efficiency. The increase in current efficiency with increase in indium content from pH 2 to 3 is due to the combined deposition of In (from  $\text{In}^{3+}$ ) and Sn (from  $\text{Sn}^{4+}$ ), reducing the average number of electrons needed to reduce each atom in the deposit.

Although the deposition at pH 3 produced an alloy of Sn and In with around 4 % indium, it is clear from the SEM images in Figure 7.2.6E that the deposit is not smooth and metallic, as required for coatings on bipolar plates. Instead, the increase in pH has produced a rough, non-homogeneous deposit that consists of needles of SnIn oxide.

The deposit was hot pressed to determine whether the melting and re-solidifying process would produce a homogeneous layer suitable for use in a bipolar plate. Seen in Figure 7.2.7, the deposit did not form a suitable layer due to its uneven and porous structure. The layer itself contained a large amount of impurities including oxygen, carbon and sulphur, and was only around 35% SnIn by weight.



Element	Wt %
Sn	31.1
O	24.9
C	23.1
Na	10.8
S	6.3
In	3.8

Figure 7.2.7. A SEM image of a SnIn layer deposited at pH 3 then hot pressed at 226 °C, with its composition as determined through EDS analysis.

Therefore, although interesting, changing the pH of the bath did not produce a viable deposit for use as a coating for bipolar plates in PEM fuel cells. Further optimization of this coating by plating outside the pH specification of the Slototin bath was considered outside the scope of this thesis.

## Conclusion

It is clear that producing a homogeneous and smooth SnIn alloy deposit that can be applied onto a BPP and hot pressed with a GDL is not possible using the deposition parameters and bath configurations employed here. Indium ions in the bath are too heavily complexed, and indium electrodeposition kinetics are too slow to be available for deposition. This complexation has most likely reduced the deposition potential of indium below that of hydrogen evolution, and it is only by increasing the pH significantly that indium can be deposited from this bath. However, by doing this the quality of the deposit is reduced so it does not form a dense and homogeneous coating, as would be required for this application. Therefore, alternative bath configurations were attempted.

## 7.2.2. Indium salts with Sn anodes + Slototin bath

Given the results of attempting co-deposition with the Slotopas additive as the indium source, it is hypothesised that indium ions with a less rigid solvation shell ('free' indium) may lead to a more successful deposition, given that they possess a less negative deposition potential. Table 7.1.1, shows that both chloride and sulfate salts have successfully been used to deposit indium or SnIn alloys. Therefore, the indium salts  $\text{InCl}_3$  and  $\text{In}_2(\text{SO}_4)_3$  were obtained to be added to the Slototin deposition bath in addition to Sn.

Soluble anodes are preferred here since they maintain the ion content and pH of the bath [135], and suitable soluble anodes to deposit a SnIn alloy would be tin, indium or a tin indium alloy. As the desired alloy composition would be over 90% Sn, the composition of the bath would be easier to maintain if Sn anodes were used, and indium salt was periodically added.

### Sn/ $\text{InCl}_3$ bath

Initially, one percent Indium by weight was added to the bath as  $\text{InCl}_3$ , and three coupons were electroplated under identical conditions and analysed in the SEM. The current efficiency of deposition at  $15 \text{ mA cm}^{-2}$  was  $93 \pm 1\%$ , and it was determined that each sample had around 0.2% Indium present. A SEM image of one of the samples is shown in Figure 7.2.8, along with a percentage composition obtained from EDS mapping. Although encouraging that some indium was present, this is not a statistically significant amount since the EDS analysis is not accurate at such low amounts [243]. Therefore, a higher amount of indium was added to the bath in an attempt to get more indium into the deposit.

More  $\text{InCl}_3$  was added to the bath until 10 wt% had been obtained, when deposition was tried again. Again, the current efficiency of deposition was very high, but the amount of indium in the deposit remained low, less than 1 % in total. Additionally, there were areas of the deposit with oxygen present, and the microstructure of the deposit had vastly changed compared to that with a lower amount of  $\text{InCl}_3$  present.

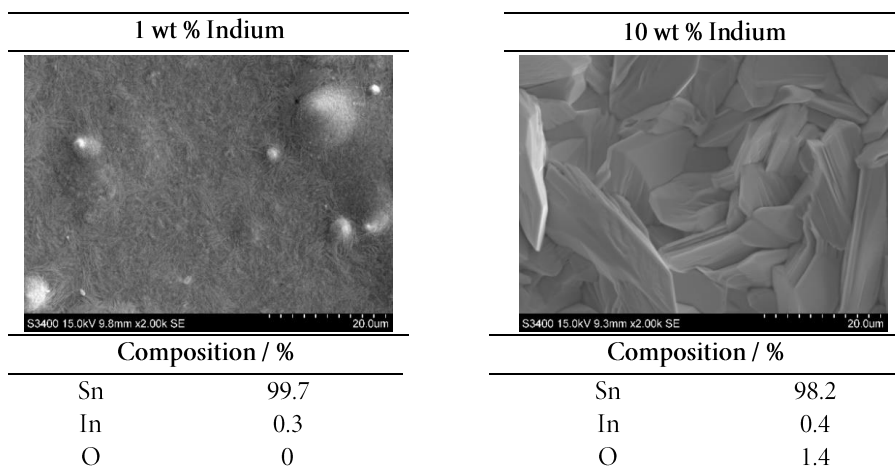


Figure 7.2.8. SEM images and compositions obtained using EDS of two SnIn alloys deposited with 1 wt% (left) and 10 wt% (right) of  $\text{InCl}_3$  salt in the bath.

From Figure 7.2.8, it can be seen that the deposit has become coarser grained and with a rougher surface. The bath is designed to produce a small-grained bright Sn deposit, and the addition of too much chloride has clearly degraded the quality of the deposit produced. This is in agreement with known consequences of adding chloride to sulfate baths for Sn deposition [137], therefore indium sulfate salts were obtained and added to the bath instead.

### Sn/In<sub>2</sub>(SO<sub>4</sub>)<sub>3</sub> bath

Indium was added to the bath in a ratio of one Indium atom to every ten tin atoms, in order to try and obtain an alloy with 10 % Indium or less. The initial deposition was performed at a current density of 15 mA cm<sup>-2</sup>, after which it was varied to try and obtain a higher amount of indium in the alloy. The results are shown in Figure 7.2.9.

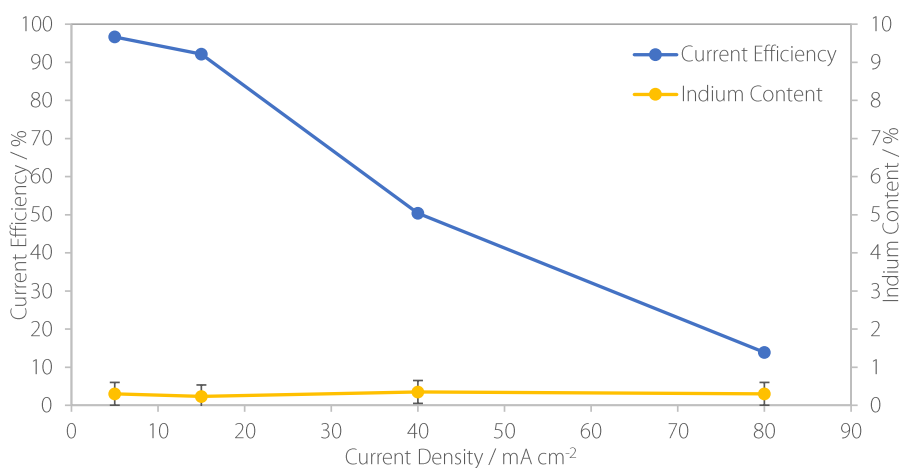


Figure 7.2.9. The influence of current density of deposition on the amount of indium in a Sn deposit and the current efficiency of deposition.

Each current density was repeated three times, and the standard deviation was calculated and added to the chart, however the errors in current efficiency are so small that they are not visible.

It can be seen in Figure 7.2.9 that the indium content of the alloy did not change with increasing current density. However, as shown previously when increasing the current density, the current efficiency decreased as the deposition becomes mass transport limited, and the rate of hydrogen evolution increases to a point at which very little deposit was present on the coupon. Based on the knowledge gained from the extensive study performed using the Slotopas additive in this bath, we can conclude that the lack on indium at high current densities indicates that the kinetics of indium deposition are too slow, and SnIn co-deposition will not occur. Other bath compositions are therefore investigated.

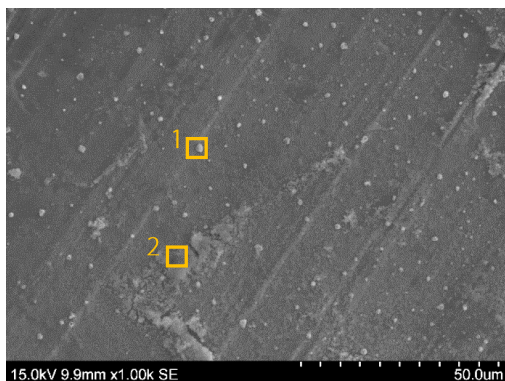
### 7.2.3. Indium anodes with Indium sulfate salt

From the previous deposition attempts, it seems that the biggest problem is getting indium into the deposit, which has until this point been essentially only Sn at all deposition conditions. Therefore, literature on pure indium deposition or the deposition of high indium content alloys was reviewed. Early patents and Russian studies have successfully used indium anodes[203,204,228]; therefore, this was tried. Initially, attempts to produce a viable layer of Indium on the surface of the substrate were made using a basic indium sulfate based bath, which has a pH of 2-3. If this is successful, Sn salts can be added to the bath to make a SnIn alloy.

As previously, certain parameters that rely on, or should change the deposition kinetics of the individual reactions in favour of indium deposition over hydrogen evolution were identified and studied, including the current density, temperature of deposition, and the substrate.

#### Varying current density

Three different current densities were used for the deposition, 10, 20 and 30 mA cm<sup>-2</sup>. For all three, the current efficiency was extremely low, with only 0.001 g of deposit being produced. There was a significant amount of hydrogen evolution occurring during the deposition, and the electroplating bath became milky white. The surface of the substrate after electroplating, Figure 7.2.10, shows some small spheres of indium deposit, and a powdery indium oxide on the surface.



Element	Wt %	Wt %
	Area 1	Area 2
In	76	51
O	0	25
Fe	16	12
Cr	5	4
Ni	2	2

Figure 7.2.10. A SEM image of a deposit obtained at 10 mA cm<sup>-2</sup>, with its composition as determined using EDS analysis of two areas of the sample. Area 1 shows a spherical indium deposit and area 2 a powdery indium oxide.

From this evidence, we can hypothesise that the following is happening: during the initial stages of indium deposition, small nuclei of indium form on the surface of the substrate. However, since the deposition potential of indium is very close to the hydrogen evolution potential, a large amount of current is used for hydrogen evolution. This increases the pH close to the electrode surface, due to the removal of H<sup>+</sup> ions. The In<sup>3+</sup> ions have a stability limit of around pH 2.5 and at pH higher than this, In(OH)<sub>3</sub> and subsequently In<sub>2</sub>O<sub>3</sub> is formed [237]. This slows down any further indium deposition, due to the lack of In<sup>3+</sup> ions close to the electrode surface, and some of the surface is also blocked by the In(OH)<sub>3</sub>, which is visible on the SEM image in Figure 7.2.10. The white precipitate in solution is also probably the insoluble In(OH)<sub>3</sub>.

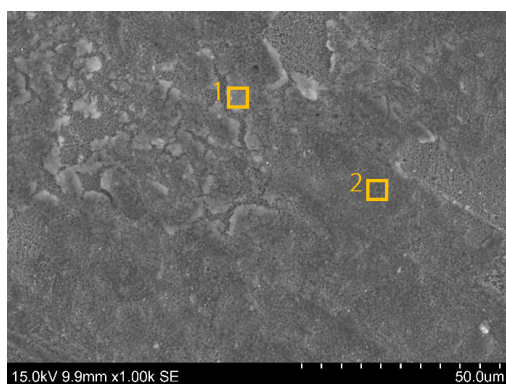
Increasing the current density only increases the rate of hydrogen evolution and therefore local pH increase, leading to the same phenomenon for the other current densities attempted. Indeed, the deposits produced at 20 and 30 mA cm<sup>-2</sup> were very similar, consisting of a few scattered particles of indium and indium oxide on the substrate. Therefore, the next step is to reduce the amount of hydrogen evolution taking place, improving current efficiency.

## Sn sublayer

The deposition of a thin layer of Sn onto the stainless steel using the Slototin bath, before deposition using the SnIn bath with indium anodes was suggested for three reasons. Firstly, the hydrogen evolution overpotential on Sn is much higher than on stainless steel [244,245], meaning that the hydrogen evolution reaction will be much slower and more current can be used for indium deposition. Additional benefits to using a Sn-sublayer could include providing more anchor points for the deposit as the surface is rougher than stainless steel, as well as promoting the deposition of In if the deposition potential of In on Sn is less negative than that of In on stainless steel.

Furthermore, if a thin layer of pure indium is deposited on the underlying Sn, then this can be subsequently heat-treated in the hot press to mix the Sn and In layers and form a SnIn alloy. This is a common way of making alloys of materials that are difficult to co-deposit [246,247].

For this deposition, a thin layer of Sn was deposited onto stainless steel using the Slototin bath, as described in chapter 4 of this thesis. The layer was deposited for 60 s at a current density of 3 mA cm<sup>-2</sup>, leading to a layer of Sn approximately 75 nm thick. After this, the sample was moved to the indium deposition bath to form a layer of In on top of the Sn. The current efficiency of this deposition was again very low (less than 1%), and only 0.003 g of coating was deposited onto the substrate. The samples were imaged in the SEM with EDS to determine whether there was any indium on the surface.



Element	Wt %	Wt %
	Area 1	Area 2
Sn	24	24
In	23	6
O	15	4
Fe	25	45
Cr	8	12
Ni	4	6

Figure 7.2.11. A SEM image of a deposit consisting of a Sn sublayer with a SnIn layer deposited on top. The composition of two different areas of the samples was determined using EDS analysis, with both area 1 and 2 consisting of an indium hydroxide layer on a Sn layer on the stainless steel substrate.

The fact that the current efficiency with the Sn sublayer is slightly higher than without proves that the hydrogen evolution reaction is indeed slightly less dominant, as predicted. However, there is still a large amount of oxygen present on the surface, indicating that the local pH has increased outside the range of In<sup>3+</sup> stability, and so In(OH)<sub>3</sub> hydroxide has formed in the bath and is sticking to the substrate.

The In:O ratio of the different areas of the sample is the same, so the composition of the deposited layer is consistent over the sample, but the thickness of the layer changes, which is why more Fe is present in area 2, as the Sn/In layer is thinner and more of the substrate is being analysed. Therefore, the indium hydroxide must be falling off the substrate, which again was observed as a milky white precipitate in the solution.

We can estimate from the coupon mass that the total deposit (Sn and In) was less than 2  $\mu\text{m}$  in thickness. This is not particularly useful for this application given that there needs to be enough coating present to form a good adhesion between the GDL and the BPP. From chapter 4 of this thesis, a coating thickness of 30  $\mu\text{m}$  was optimum, something that has clearly not been achieved here. Therefore, alternative ways of getting an indium coating onto the substrate were investigated.

## Rough substrate

The substrate was roughened by glass-blasting in order to promote adhesion of the deposit. This led to a much more uneven substrate, as seen in Figure 7.2.12, whereby there should be more anchor points for the In to deposit and remain on the surface.

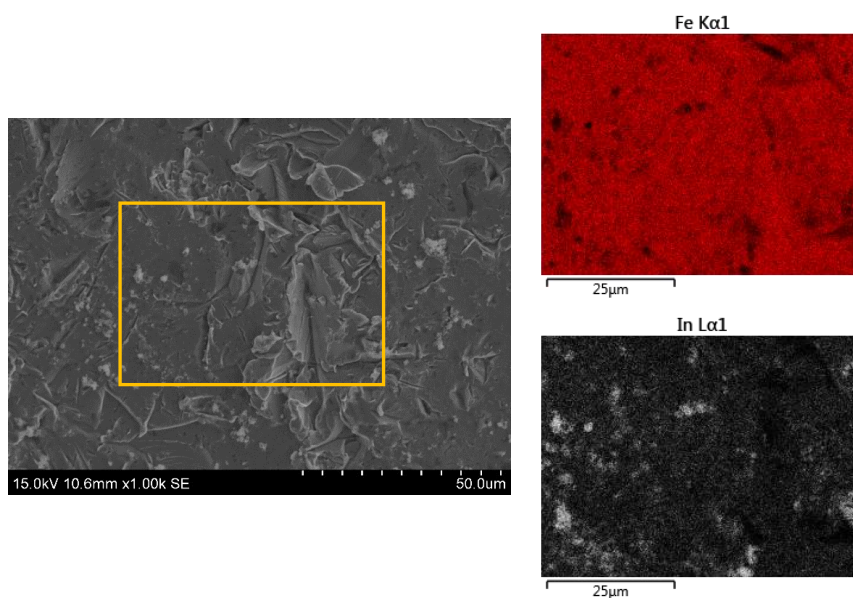


Figure 7.2.12. A SEM image of a sample of SnIn deposited onto a glass-blasted substrate at 20°C, with EDS analysis showing the Iron (Fe) and Indium (In) distribution. The yellow box on the SEM image indicates the area analysed by EDS.

With this roughened surface, the current efficiency of deposition went up slightly, to over 1 %, however this is still very low, to the point that it would be impossible to make a coating of useable thickness. As seen previously, the deposit consists of indium particles on the stainless steel substrate, shown in Figure 7.2.12. Although not visible in this EDS analysis, there was a significant amount of oxygen in the sample, indicating once again the formation of  $\text{In}(\text{OH})_3$ .

Again, this electrodeposition bath does not seem to be producing a viable coating, as the current efficiency is extremely low, metallic indium is not being deposited. Therefore, the next step is to try and increase the current efficiency, and one way of doing this is to increase the bath temperature.

## Temperature

Whilst continuing to use the roughened substrate, the bath temperature was increased. This should improve the kinetics of the reaction, reducing the size of the diffusion layer and the mass transport overpotential, and increasing the exchange current density. This could bring the deposition potential out of the hydrogen evolution range, increase the current efficiency and allow more indium to deposit.

The SEM images of the deposits from the baths at 20 °C (Figure 7.2.12) and 40 °C (Figure 7.2.13) are very similar, with small indium deposits on the surface of the substrate. The current efficiency for both bath temperatures is very low, below 2 %, and there is no homogeneous layer of deposit forming on the substrate.

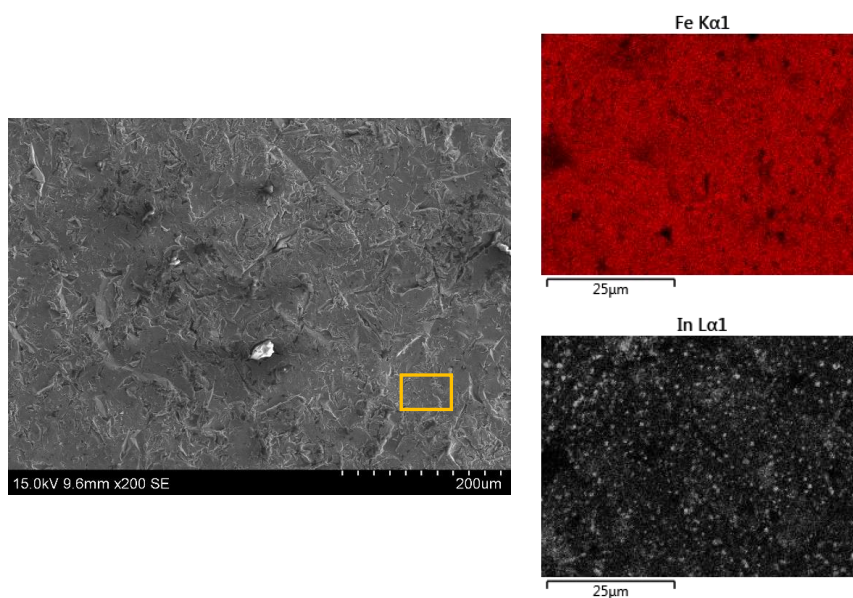


Figure 7.2.13. A SEM image of a sample of SnIn deposited onto a glass-blasted substrate at 40 °C, with EDS analysis showing the Iron (Fe) distribution in red and the Indium (In) distribution in white. The yellow box on the SEM image indicates the area analysed by EDS.

At 40 °C, the indium is more finely dispersed over the surface of the stainless steel than at 20 °C, probably due to the higher nucleation rate at elevated temperature, because of the enhanced nucleation kinetics. However, given that no or very slow growth of the nuclei is occurring, we can assume that hydrogen evolution is dominating and stopping the deposition of  $\text{In}^{3+}$ , as seen earlier.

When the bath temperature further increases to 60 °C, the current efficiency increases to over 3 %, the highest seen from this bath type. It is also clear that an actual layer of deposit has formed, shown in Figure 7.2.14, implying that the greater number of nuclei that are forming at the higher temperature are also growing to form a layer of indium. This implies that hydrogen evolution is less impacted by an increase in temperature than the In deposition, as predicted by the Nernst equation for a two electron

transfer reaction compared to a three electron transfer reaction. Therefore, a larger share of the current is going to deposition, and the current efficiency increases.

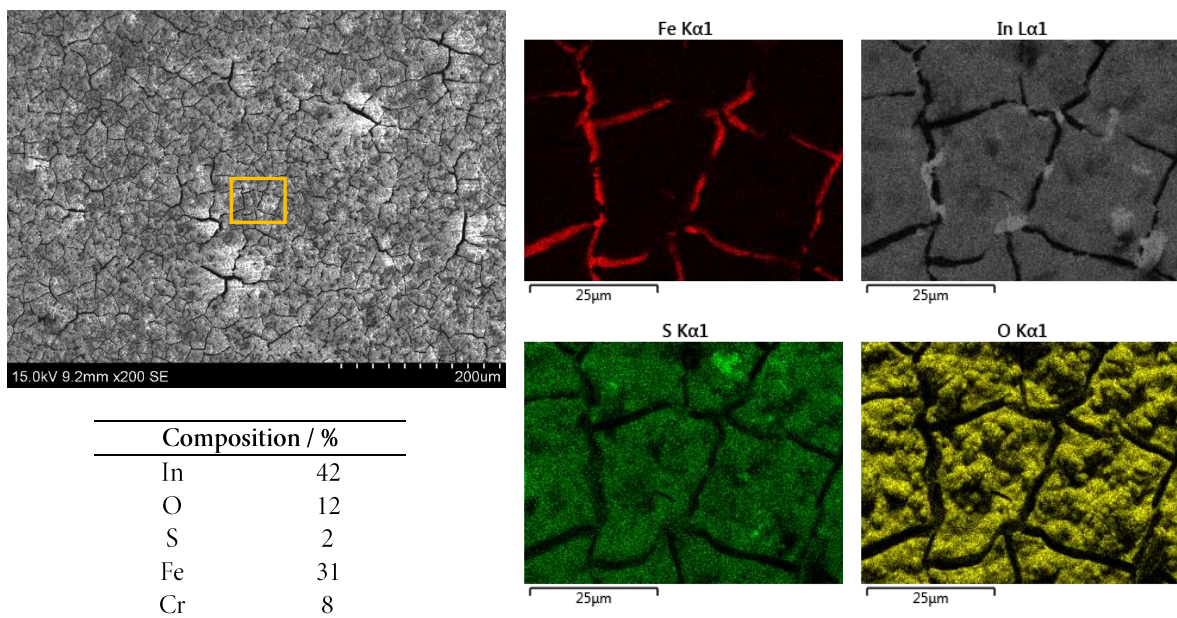


Figure 7.2.14. A SEM image of a sample of SnIn deposited onto a glass-blasted substrate at 60 °C, with EDS analysis showing the Iron (Fe, red), Indium (In, grey), Sulfur (S, green) and Oxygen (O, yellow) distribution. The yellow box on the SEM image indicates the area analysed by EDS, and the table shows the percentage composition of the area analysed by EDS.

Looking at the EDS maps of this deposit, we can note that the deposit is thick enough to stop any of the underlying substrate from being measured by EDS, with only Fe being visible through the cracks in the deposit. We can also see from the EDS analysis that the deposit contains a large amount of oxide and other impurities, so it is likely that as was the case earlier, the amount of hydrogen evolution is still high, causing a local pH increase and the precipitation of indium oxides on the surface.

Although this increase in the amount of deposit is promising, the fact that the current efficiency remains low and high amount of non-metallic impurities are present means that this coating is not suitable for use on a bipolar plate.

## Conclusion

Many attempts at effectively depositing a coating that consists of a layer of metallic indium on the stainless steel substrate have not been successful. Although some tuning of deposition parameters led to increased current efficiency, it overall remained very low due to the prevalence of hydrogen evolution. Additionally, this hydrogen evolution led to local changes in pH at the electrode surface, and unwanted side reactions, creating deposits that are largely unsuitable for the application of coatings for PEM fuel cells. The presence of oxides in the coating can lead to increases in the interfacial contact resistance and negative impacts on fuel cell performance.

Therefore, the next stage is to move on from this deposition bath configuration and explore alternative ways for SnIn co-deposition.

## 7.2.4. Cetyltrimethylammonium bromide (CTAB) additive

From the previous attempts at forming a SnIn layer on a stainless steel coupon, it seems that neither highly complexed In salts nor 'free' In ions are suitable for deposition. In order to co-deposit Sn and In, the deposition potentials must be approximated, and one way of doing this is to find a complex that binds to both the Sn and In ions in solution, and therefore allows the deposition of both ion types together. Additionally, the introduction of new components to the electrodeposition bath can change the kinetic parameters, meaning the co-deposition could become favourable.

In their review paper on the electrodeposition of indium alloys, F. Walsh and D. Gabe suggested that cetyltrimethylammonium bromide (CTAB) is a crucial additive for the deposition of SnIn alloys from sulfate baths [205,229], and has also been used for the deposition of other metals such as Co, Ni and Cu [248]. CTAB, as seen in Figure 7.2.15, is a cationic detergent with quaternary ammonium as the polar end attached to a negatively charged Br<sup>-</sup> ion. This acts as a surfactant, which can bind to the positive metal ions present in the electrolyte, reducing their deposition potential and allowing co-deposition. Ideally, the deposition potential of indium should not be reduced too much, as a too negative cathode potential would allow for even faster hydrogen evolution, making deposition very inefficient and practically impossible.

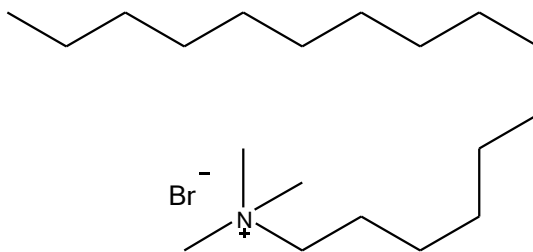
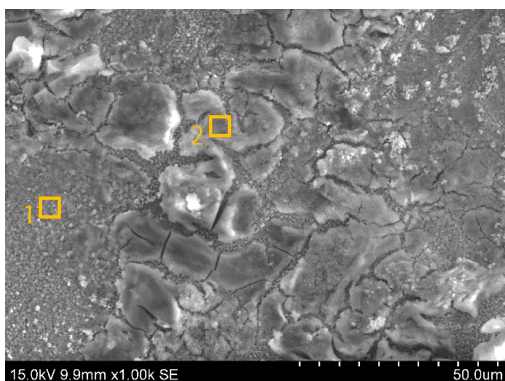


Figure 7.2.15: The structure of cetyl trimethylammonium bromide.

Deposition using CTAB was tried as suggested by Walsh et al. [229], but due to limited reporting of experimental details, a parameter study was performed to determine the best operating conditions with respect to current density, temperature and Sn content of the bath.

### Varying current density

Initially, the bath was prepared with 5 g L<sup>-1</sup> Indium as In<sub>2</sub>(SO<sub>4</sub>)<sub>3</sub>, 5 g L<sup>-1</sup> of CTAB additive and 1 g L<sup>-1</sup> of tin as SnSO<sub>4</sub>. The pH was set to 2, which is in the middle of the recommended range of the bath [205]. The first deposition was attempted with a current density of 10 mA cm<sup>-2</sup>, as recommended. However, the current efficiency of this deposition is very low, at just 3 %, and the deposit was not homogeneous. The morphology of the deposit was imaged with SEM including EDS analysis, shown in Figure 7.2.16. The deposit was determined to consist of a thin layer of Sn rich SnIn alloy with a powdery In rich SnIn oxide on the surface. The adhesion between the coupon and the oxide was poor, with some of the powder falling off during the rinsing stage.



Element	Wt % Area 1	Wt % Area 2
Sn	9	13
In	1	23
O	0	12
Fe	62	35
Cr	16	10
Ni	9	5

Figure 7.2.16: A SEM image of the deposit obtained at  $10 \text{ mA cm}^{-2}$  with its composition as determined through EDS analysis. The yellow boxes labelled 1 and 2 are representative of the different types of deposit obtained, where 1 is an area containing a thin layer of SnIn alloy, and 2 is the thicker layer of SnIn oxide.

The presence of a thin SnIn alloy layer on the substrate surface shows that in the initial stages of deposition, metal deposition is occurring, and an alloy is being produced. However, given the large amount of gas evolution that was observed during the deposition, we can hypothesise that there is a local increase in pH at the surface of the anode as has been seen for other types of deposition bath.

This pH increase changes the stability of the ions in solution, forming indium and tin oxides, which precipitate on the surface and can be observed in the SEM images (Figure 7.2.16).

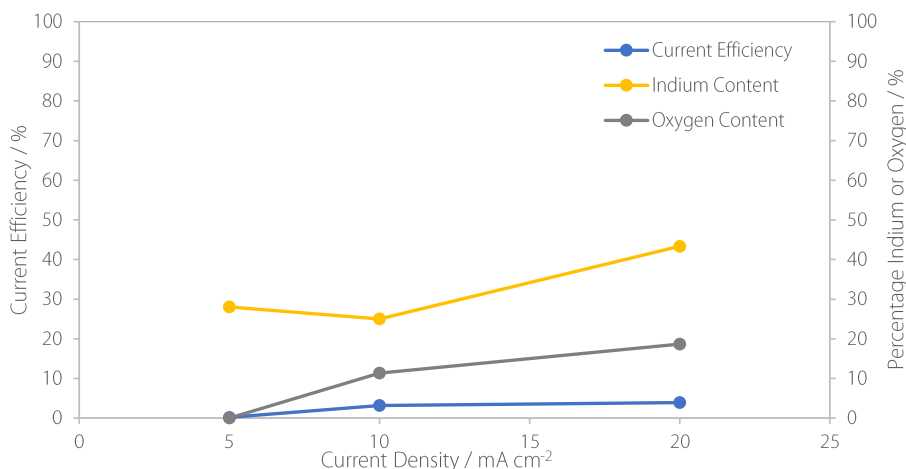


Figure 7.2.17: The influence of the current density of deposition on the current efficiency of deposition and the composition of the electrodeposited SnIn alloy.

By changing the current density, we can change the kinetics of the reaction and the contribution from hydrogen evolution. At low current densities, there is almost no deposit on the surface, but the deposit there seems to be a SnIn alloy with no oxide. This implies that the hydrogen evolution is still dominant over metal deposition but has slowed down enough that there is less pH change and oxide conversion in the bath. This is verified by the SEM images taken in Figure 7.2.18, where it is visible that the layer deposited at  $5 \text{ mA cm}^{-2}$  consists of some small balls of deposit on the surface, with no puffy oxide present.



Figure 7.2.18. SEM images of SnIn samples deposited at A - 5, B - 10, and C - 20 mA cm<sup>-2</sup>.

At a current density of 20 mA cm<sup>-2</sup>, the indium content of the deposit increases, as does the oxygen content. The increasing current density leads to more hydrogen evolution, which in turn increases the local pH at the electrode surface more quickly and leads to more oxidation of the indium and tin ions in the bath. This oxide precipitates on the surface (Figure 7.2.18) which leads to the artificially higher current efficiency but does not produce a useable deposit. Therefore, hydrogen evolution must be suppressed before a suitable deposit can be obtained.

## Varying Temperature

As reported earlier in this chapter, changing the temperature of the deposition leads to very bath-specific effects that cannot easily be predicted. An elevated temperature will speed up the deposition process, have a slight effect on the deposition potentials and change the electrode-electrolyte interface. The competitiveness of metal deposition vs hydrogen evolution will also be impacted by the temperature change.

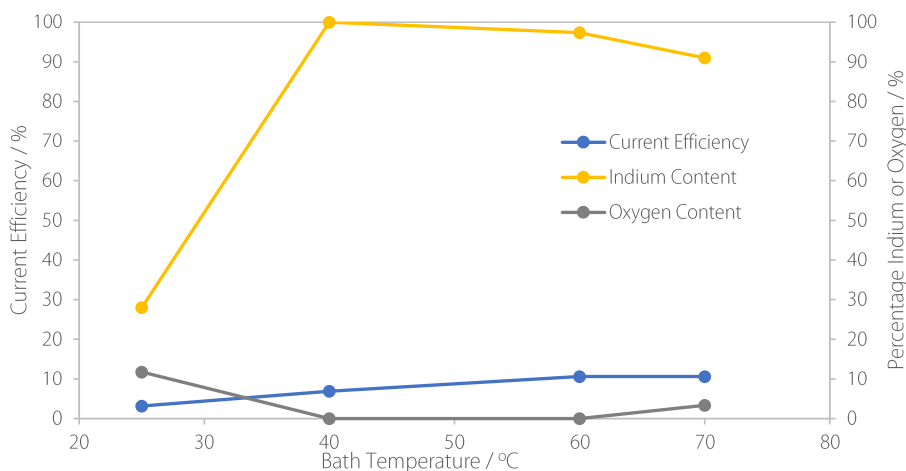


Figure 7.2.19. The influence of the bath temperature on the current efficiency of deposition and the alloy composition of a SnIn alloy.

In general, it can be seen from Figure 7.2.19 that increasing the bath temperature leads to a slightly higher current efficiency. This increases from 3 % at 25 °C to 11 % at 70 °C and is as we expect given that the two electron hydrogen evolution reaction is less temperature sensitive than the three electron indium deposition reaction.

As the temperature increases, the amount of Indium in the deposit increases and the amount of Sn decreases. At 25 °C, there is approximately 60 % Sn, which quickly reduces to 0 % at 40 °C. The ratio of indium to tin ions present in the bath is approximately 2:1. As there should be enough Sn ions left in the bath to form a deposit, we can conclude that the increase in temperature is changing the deposition potentials of Sn and In to favour the deposition of the indium ions.

As we further increase the temperature to 60 and 70 °C, the amount of Sn increases slightly. This could be due to poorer interaction with the CTAB additive at higher temperatures, or partial decomposition of the additive. Without the additive present, the deposition potential of Sn is much less negative than that of indium, therefore the deposition of Sn is once again favoured, and the amount in the deposit increases.

A bath temperature of 60 °C resulted in best deposit in terms of current efficiency and the amount (minimum) of oxygen present. However, the ratio of In to Sn in the deposit was much higher than desired for this application, so the next step was to take those conditions and increase the amount of Sn in the bath to increase tin activity in order to obtain a SnIn alloy containing between 1 and 10 % indium.

## Sn content

Whilst keeping the bath at 60 °C, which until now had produced the best quality deposit, the Sn content of the bath was varied. There was initially 1 g/l of the Sn salt SnSO<sub>4</sub> in the bath at a ratio of 1 Sn-ion to every 2 In-ions. This was increased incrementally up to 10 g/l, producing a Sn:In ratio of 5:1, which should cause a significant change in the composition of the deposit.

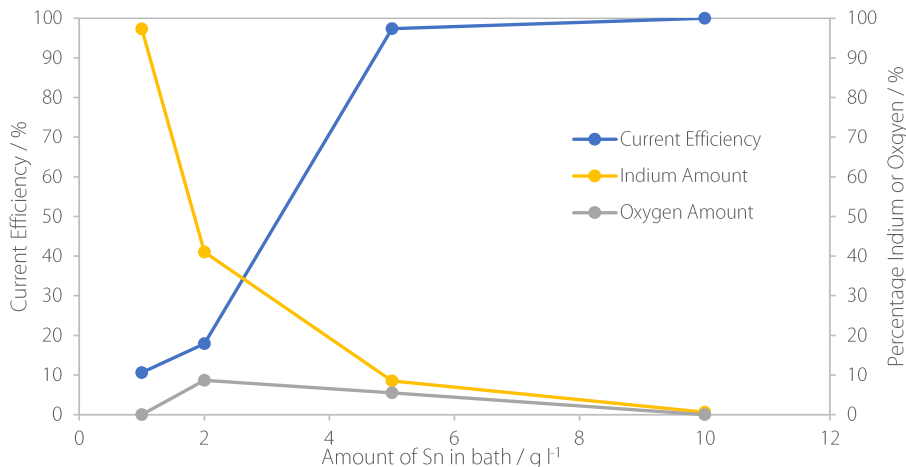


Figure 7.2.20. The influence of the Sn content of the bath on the current efficiency of deposition at 15 mA cm<sup>-2</sup> and 60 °C, and the deposit composition of a SnIn alloy.

As can be observed from Figure 7.2.20, this was indeed the case. As the amount of Sn in the bath increases, so does the amount of Sn in the deposit. This is in agreement with the findings from Medvedev et al. [203]. Increasing the amount of Sn in the bath also increases the current efficiency to values close to 100% at 5 g L<sup>-1</sup> and above. This is because the deposition of In occurs at a potential very close to the hydrogen evolution overpotential, so much of the current passed in the bath is used for hydrogen evolution. As there is more Sn present, Sn deposition becomes more favourable due to an

increase in the exchange current density [132] and the deposition potential becomes less negative, reducing the current efficiency for both hydrogen evolution as well as indium deposition.

At 2 g/l Sn, there is an approximate 1:1 ratio of Sn to In ions in the bath, yet the amount of indium in the deposit is only 41 %. Again, this confirms that the indium deposition reaction is more difficult and less efficient, due to both the more negative deposition potential and apparently more sluggish deposition kinetics, likely due to more electrons needed to deposit In than Sn.

When the amount of Sn in the bath is significantly larger than the amount of indium, at 10 g/l of Sn salts, the indium content of the deposit drops to just one percent. At this point, the current efficiency is very high, as to be expected, and the deposit produced is suitable to be used as a coating for a bipolar plate, given its low oxygen content.

Ideally, the indium content of the deposit should be slightly higher and more easily tuned to adjust the amount of In in the deposit without greatly affecting the current efficiency or oxygen content. However, this seems to be very difficult given the large parameter studies that have been undertaken without success. Therefore, the most suitable deposit obtained from this bath, with the deposition parameters: 10 g/l Sn, 60 °C, 10 mA cm<sup>-2</sup> was repeated and then used as the working electrode in a 3-electrode electrochemical cell.

## Electrochemical Testing

Electrochemical testing including ICR was performed on a deposit formed as above, which contained less than 1 % indium, as measured by EDS after deposition. The sample was placed in a simulated PEMFC environment and a potential of 1.0 V<sub>SHE</sub> was applied for 1 hour whilst the current response was measured.

The initial ICR value was very high, even before any testing. This could be due to poor adhesion between the SnIn layer and the GDL, or the presence of organic additives that have incorporated into the deposit. Additionally, the SnIn deposit was on a flat coupon rather than a bipolar plate, meaning the GDL could not be hot pressed on the BPP, thereby increasing the contact resistance.

As seen in Figure 7.2.21, the current density produced by corrosion reactions on the plates differed after one hour of applying a voltage of 1 V<sub>SHE</sub>. As is commonly seen, the stainless steel had a very low current density after 1 hour, due to the protective oxide layer forming early on and acting as a protective barrier from further corrosion. Therefore, the stable surface does not undergo very many reactions and so produces very little current. The Sn-based plates have higher current densities due to the dissolution and then passivation of the Sn by SnO<sub>2</sub>, which precipitates on the surface. This leads to partial passivation, but the SnO<sub>2</sub> layer can be fractured or incomplete, exposing the underlying Sn which again dissolves, producing some current. The SnIn has a higher corrosion current because of the contribution of the indium. As determined in the preliminary tests with pure metals, seen in chapter 5 of this thesis, the indium alone has a high corrosion current after constant potential testing, leading to the increased current density of the SnIn alloy compared to Sn alone. Conversely, the addition of Bi reduces the corrosion current density, as Bi increases the rate of the SnO<sub>2</sub> formation, thereby passivating the surface more efficiently.

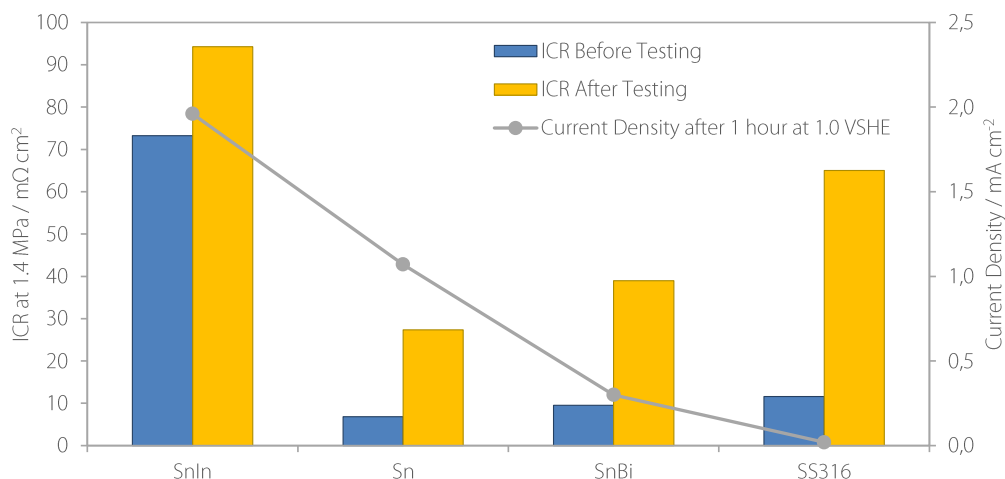


Figure 7.2.21. The interfacial contact resistance of the SnIn coating before (blue) and after (yellow) electrochemical testing as compared to the bare stainless steel (SS316), Sn coated and SnBi coated steel plates, with the final current density (grey) after 1 hour of chronoamperometric testing at 1.0 V<sub>SHE</sub>.

The ICR for SnIn, shown in Figure 7.2.21, was initially much higher than expected, and also increased significantly after the electrochemical testing. The ICR for the pure Sn plate increased by around 20 mΩ cm<sup>2</sup>, and the SnIn plate increased by 21 mΩ cm<sup>2</sup>. The small difference in ICR performance between the Sn and the SnIn plates implies that the addition of small amounts of indium neither improves nor worsens the quality of the coating. From the increase in ICR we can see that the SnIn layer has oxidised, but without producing a bipolar plate that is hot pressed together with the GDL, we cannot make any further conclusions. However, the increase in ICR after testing for all the Sn-based coatings was less than stainless steel alone, which had an increase of 53 mΩ cm<sup>2</sup>.

## Conclusions

In conclusion, the use of CTAB in the deposition bath has produced the most successful SnIn deposits that could be used for bipolar plates in PEMFCs. Despite this, it has proven very difficult to produce a series of SnIn deposits with varying indium content, as would be required to determine the optimum alloy content. Additionally, the deposits produced often have low current efficiency which means it will be difficult to produce a suitably thick coating on a bipolar plate, or may contain impurities such as oxygen which increase the contact resistance and reduce performance.

Electrochemical testing has been performed on some samples of SnIn. It has both a higher corrosion current density after 1 hour at a constant voltage of 1.0 V<sub>SHE</sub> than pure Sn does, and a higher contact resistance before and after testing. However, since no tests were performed on bipolar plates with GDLs hot pressed onto them, it is difficult to conclude how the BPPs would perform *in-situ*.

### 7.3. Hot dipping in a SnIn melt

As a final attempt to obtain a layer of SnIn alloy that would be suitable for use inside a PEM fuel cell, hot dipping of the stainless steel substrate into a molten mix of Sn and In in a mass ratio of 19:1 was performed. The densities of Sn and In are almost the same,  $7.31 \text{ g cm}^{-3}$  [144], implying that the two would mix well in a molten melt, without forming layers of one floating on top of the other. Ideally, this would produce a thin layer of SnIn alloy with around 5 % Indium onto the coupon, which could then be analysed using electrochemical techniques and ICR.

During the hot dipping process, there were some difficulties with obtaining a homogeneous layer of metal on the coupon. Due to surface tension, the molten metal gathered together to form globules instead of dispersing across the stainless steel substrate, forming a discontinued layer that was very thick in some places and non-existent in others. For this reason, each coating was re-flowed inside a mould during hot pressing to flatten it and produce a thin and even layer of SnIn alloy on the stainless steel substrate.



Figure 7.3.1. Photographs of a SnIn layer hot-dipped onto a stainless steel coupon before (left) and after (right) heating to 226 °C. Before heating, bare substrate is visible (yellow circles) and the surface is very rough, but after heating the substrate is completely covered and the surface is smoother.

Initially, many of the coatings produced had much higher indium content than expected, up to 13 %. This is unexpected given there was only 5 % indium in the bath but could be due to the slightly lower melting point of Indium or the higher wettability of indium on many surfaces[219]. Additional amounts of Sn were added to the melt to obtain SnIn alloys with less indium present. This was partially successful and a minimum of approximately 5 % indium was obtained.

After the reflowing procedure in the hot press, the sample was imaged in the SEM with EDS mapping to determine whether the hot pressing procedure had any impact on the coating. The SEM and EDS images in Figure 7.3.2 show that after the re-flowing procedure in the hot press, although the coating as a whole is more homogeneous, there is a separation of the Sn and In phases. This leads to indium rich areas with up to 30 % In, and indium poor areas with only 2 % In present, with the average over the whole area being around 6 % Indium. These large discrepancies that occur after hot pressing can be detrimental to performance of the coating.

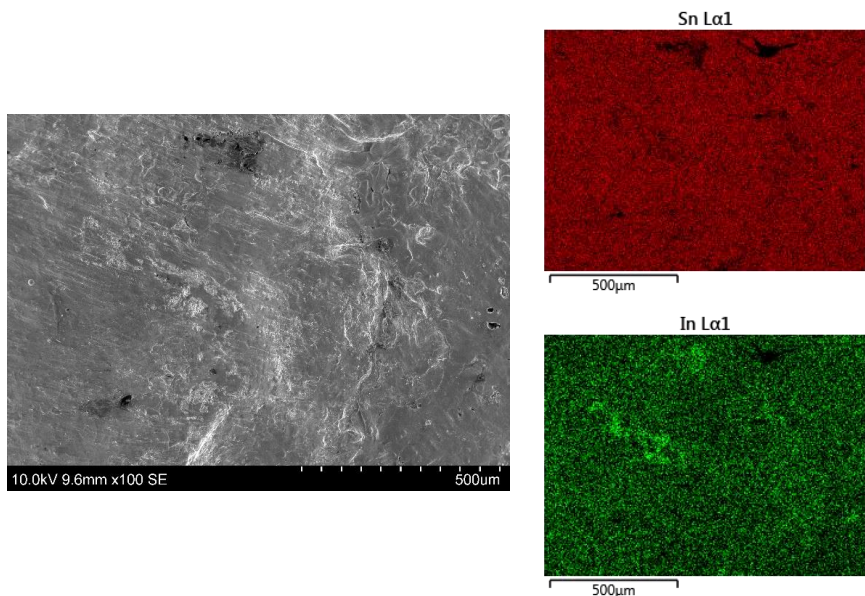


Figure 7.3.2. A SEM image of a SnIn coupon after re-flowing in the hot press, with EDS mapping showing the Sn and In density over the imaged area.

### 7.3.1. Electrochemical testing

After the coupons were hot pressed, a series of electrochemical tests were performed to determine how they compared to Sn alone. Each coupon was held at a constant potential of  $1\text{ V}_{\text{SHE}}$  for 1 hour, and the current density after this hour was plotted against the indium content of the coupon, seen in Figure 7.3.3. The blue circles represent samples that have been hot-dipped, the yellow triangle is an electroplated sample of SnIn, and the red square is an electroplated Sn reference containing no Indium.

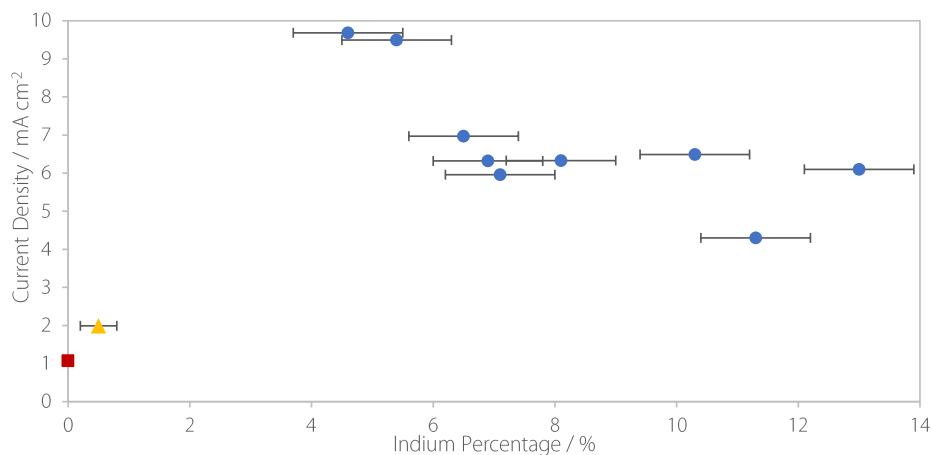


Figure 7.3.3. The influence of the Indium content on the final current density of a sample after being held at  $1.0\text{ V}_{\text{SHE}}$  for 1 hour. The blue circles are hot-dipped SnIn samples of varying In content, the yellow triangle is an electroplated SnIn sample, and the red square is an electroplated Sn sample.

Looking at Figure 7.3.3, it can be noted that comparing the two electroplated samples, a small addition of Indium leads to an increase in the corrosion current density during the *ex-situ* testing, as seen in the initial electrochemical tests performed in chapter 5 of this thesis.

When looking at the hot-dipped samples, the Indium content was very variable over each sample (as seen in the EDS images in Figure 7.3.2), so there is a large uncertainty in the x-axis. Despite this uncertainty, it seems that increasing the amount of indium in the deposit leads to a lower corrosion current density at the end of 1 hour at constant current. However, there are a few problems with drawing this conclusion.

Firstly, the surface area of each sample is not the same. Although reflowing in the hot press improves the surface coverage of the coating, it is still rough with pin-holes and cracks, as seen on the SEM image in Figure 7.3.2. Therefore, when normalising the current density for geometric area, it is very hard to be accurate about the sample area, leading to large uncertainties in the reported current densities, being significantly higher. This is not the case for the electroplated SnIn sample, which has a smooth and homogeneous surface and therefore the reported current density should be more accurate.

Additionally, it is difficult to know the exact indium content of the 1 cm<sup>2</sup> area exposed to electrolyte as the distribution of indium through the samples is not even. The indium content of the samples that is reported in Figure 7.3.3 comes from SEM images with EDS analysis of three different areas of the sample, averaged together. As seen from the images in Figure 7.3.2, this ignores local variations in indium content and therefore is not very accurate.

Finally, the adhesion between the samples and the underlying SS substrate was very poor, meaning electrolyte could get underneath the coating, increasing the surface area or even completely removing the SnIn coating from the surface, leading to no electrical contact and then the current just coming from the stainless steel and not the SnIn. Often when removing the samples from the electrolyte and then rinsing, the SnIn coating was completely removed from the underlying substrate. This is also the reason that no ICR has been reported for these samples.

These factors combined lead to the electrochemical testing of the hot-dipped SnIn samples being of limited use in comparing the performance of SnIn to Sn alone and SnBi coatings. Again, it can be concluded that hot-dipping a coating of SnIn onto the BPP does not lead to a reliable coating that can be used for *in-situ* testing due to the poor coverage and adhesion to the substrate. Proper surface preparation of the substrate could potentially increase the adhesion between the substrate and hot-dipped SnIn alloy in the future.

## 7.4. Summary

It has been demonstrated in this chapter that it is almost impossible to obtain a several  $\mu\text{m}$  thick and homogenous SnIn alloy coating suitable for BPPs, equivalent to the Sn and SnBi coatings that have previously been produced in this thesis. Although some SnIn alloy coatings were obtained, they were either powdery and oxidised, or inhomogeneous and deposited with a very low current efficiency, leading to long deposition times, excessive hydrogen evolution and inevitable bath degradation.

From the small amount of electrochemical testing that has been performed here, we can conclude that the presence of Indium in the Sn layer does not improve the performance of the coating with regards to the corrosion current density, nor ICR. However, the majority of the electrochemical testing has been performed with hot dipped coatings that were not smooth layers of a constant thickness as the electrodeposited coatings are. This leads to a varying surface area and therefore it is difficult to compare the performance of these SnIn coatings against Sn or SnBi coatings. Additionally, the hot dipped coatings had very poor adhesion in that the coating often completely delaminated after *ex-situ* testing, meaning that the ICR could not be obtained. As the ICR is an important parameter for bipolar plates, it is therefore very difficult to quantify how well the SnIn coating performed.

Due to the problems experienced with the electrodeposition of SnIn alloys, and therefore the unsuccessful electrodeposition of a suitable SnIn alloy coating, no deposition onto bipolar plates was performed, and therefore no *in-situ* testing occurred.

In the future, the co-deposition of SnIn from Cl-based baths could be attempted. Literature also suggests that the co-deposition of Sn and In using ionic liquids is possible [249–251], however this is outside the scope of this thesis work.

# The Influence of Carbon on the Sn/GDL System

## 8.1. Carbon Materials for PEMFCs

The final adjustments to the Sn/GDL system involve the optimisation and addition of carbon materials at the Sn/GDL interface. The use of carbon within PEM fuel cells has been occurring for many years [252]. It can be found in multiple places inside the fuel cell, including in the bipolar plate [253,254], gas diffusion layer [255,256], and as a support for the platinum catalyst layer [257,258].

Carbon is highly beneficial for use in the PEM environment due to its low cost, high electrical conductivity and acceptable stability [252]. However, on the cathode side of the fuel cell, carbon-based materials can be exposed to highly oxidising conditions, with potentials of up to 1.44 V during start-up and shutdown cycling [259]. If the cell has been incorrectly purged, the presence of hydrogen and oxygen together at the anode can cause a drop in the potential to -0.59 V, when electrons and protons from the hydrogen oxidation reaction can combine with oxygen to reduce it to water. This produces a negative potential, which when the cathode is also exposed to oxygen leads to a high potential difference and subsequent carbon corrosion. This corrosion process is irreversible as it occurs via the formation of CO<sub>2</sub> and subsequent removal out the exhaust [260].

The carbon corrosion mechanism is typically slow under the normal operating conditions of a PEMFC, but is catalysed by platinum and the presence of water [260]. It is therefore most relevant for carbon used as a catalyst support, where the removal of a small amount of material can have large negative effects on the amount and dispersion of the catalyst, leading to large performance losses. For the carbon based GDL, the main failure mechanisms are often mechanical, with over-compression or a change in surface hydrophobicity leading to poor water management and performance reductions [8].

For the case of bipolar plates, carbon corrosion leading to material removal can cause changes in hydrophobicity and small reductions in conductivity but does not constitute a critical failure unless physical holes or break-up of the bipolar plate occurs. Therefore, carbon is a very durable material for use in bipolar plates, and additions of carbon to the Sn/GDL system could improve both the conductivity and longevity of the system.

### 8.1.1. Carbon in Bipolar Plates

Carbon in the form of graphite has previously been used as a bipolar plate material and is advantageous due to its high conductivity and stability in a PEM environment. However, bipolar plates machined from graphite do not have the required mechanical properties for use in transport applications, as they are brittle, porous and expensive [47].

Therefore, there has recently been a movement towards moulded carbon or stamped metal bipolar plates, both of which are advantageous over graphite due to their low cost, high-throughput manufacturing methods. Carbon composite BPPs have been well researched [254,261,262], and have become well established commercial products, with Ballard Power Systems amongst others using carbon based bipolar plates for their fuel cell stacks. They consist of a carbon based filler material (for example carbon nanotubes, graphite, fibres, platelets or carbon black) of varying shape and size, suspended in a polymer matrix. Although they have a generally lower conductivity than metallic BPPs, this is highly dependent on the type and amount of filler material, and the BPP forming and processing parameters [263]. Additionally, they do not undergo the same increase in ICR over time that metal plates suffer from.

Alternatively, carbon coated metallic BPPs are suitable for use in PEMFCs for their high corrosion resistance, good conductivity and ease of manufacturing. There have been numerous studies on the use of carbon as a coating material for stainless steel bipolar plates [17,47,253], with the major types of carbon based coatings being amorphous carbon, metal doped carbon and metal carbides [253]. There are multiple different ways of applying carbon coatings to a BPP, with popular techniques including spraying [65], CVD [264], sputtering [265] or using a polymer binder [266] amongst others.

The use of carbon in fuel cells and specifically on the bipolar plate is very versatile, indicating that when used properly, it has the potential to be a low cost and highly stable component. Although carbon is not used as a bipolar plate material in this thesis, understanding the interface between the Sn coating and any carbon based components is important for the optimisation of the BPP. The introduction of carbon to the Sn/GDL interface in the form of a thinly sprayed layer can improve the conductivity of the BPP by increasing the number of contact points. Additionally, the longevity of the BPP could also be improved due to the stability of carbon in the PEM environment, which may have a beneficial effect on the formation of the protective Sn oxide. Therefore, analysing the effect of the GDL type on the Sn/GDL interface, and the addition of a carbon nanolayer at the same interface are interesting ways to determine the role of carbon on the Sn/GDL system.

## 8.2. The Influence of the GDL Type on the Sn/GDL System

### 8.2.1. Introduction

In previous chapters of this work, the properties of the Sn layer in the Sn/GDL system have been optimised, with deposition and hot pressing parameters tuned, and alloying elements introduced into the system to improve the longevity. However, there is another component that can also be optimised, the GDL. There are several types of GDL available, with multiple different carbon fibre types, treatments and additional layers.

Two types of GDL have been identified as being of interest in this work. Firstly, the Freudenberg H23 series of GDL are non-woven carbon papers that are available with or without a hydrophobic treatment and microporous layer (MPL). Since the MPL is in direct contact with the MEA and not the BPP, the

presence or absence should not interfere with the Sn/GDL system, although it has been shown to reduce the conductivity of the GDL as a whole [252].

Two types of Freudenberg H23 GDL have been identified, the C6 carbon paper which has been hydrophobically treated by impregnation with PTFE, and the C2 paper that is untreated. The structure of the two papers can be seen in Figure 8.2.1.

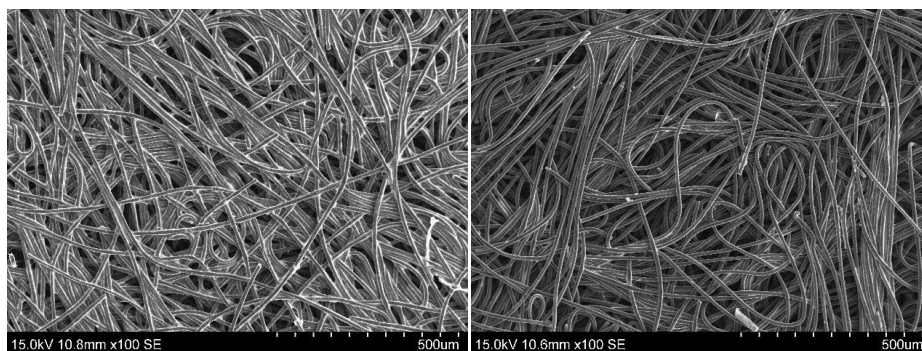


Figure 8.2.1. The two types of Freudenberg H23 papers used in this thesis. The H23 C6 paper that has been given a hydrophobic treatment to the carbon fibres (left) and the H23 C2 paper that has not received any treatment (right).

This hydrophobic treatment coats the carbon fibres of the GDL, which may have a small influence on the porosity and flexibility, but largely leaves the microstructure unchanged. The main impact of the hydrophobic treatment would be on the wetting of the Sn onto the GDL, leading to different interaction. It is hypothesised that the presence of the PTFE will reduce the wetting properties, leading to poorer contact between the GDL and Sn, as visualised in Figure 8.2.2. This poorer wetting between the GDL and Sn could lead to fewer contact points, higher ICR and worse electrochemical performance. However, the presence of the hydrophobic treatment prevents the adsorption of electrolyte into the GDL fibres, which would cause oxidation of Sn along the Sn/GDL interface and could be detrimental to the ICR.

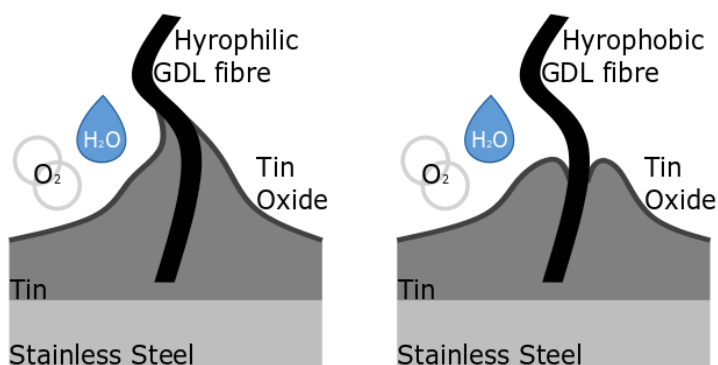


Figure 8.2.2. A drawing of the proposed impact of the PTFE treatment on the wetting properties of the GDL to the Sn, with the hydrophilic GDL having a greater contact area with the Sn than the hydrophobic GDL.

On an *in-situ* level, a low hydrophobicity can lead to adsorption of water into the GDL fibres, which reduces gas permeability and leads to an increased mass transport overpotential [252], therefore PTFE treated GDLs are most commonly used inside operating fuel cells.

The second type of GDL employed in this work is from Toray (TGP-H-120). It consists of a composite material of carbon fibre and carbon that has been pressed together at high temperature to form strong, stiff carbon papers with a high electrical conductivity, good corrosion resistance and high gas permeability. Two types of Toray paper, one with a hydrophobic treatment and one without, were identified as being of interest, to be analogous to the two types of Freudenberg paper. They are shown in Figure 8.2.3.

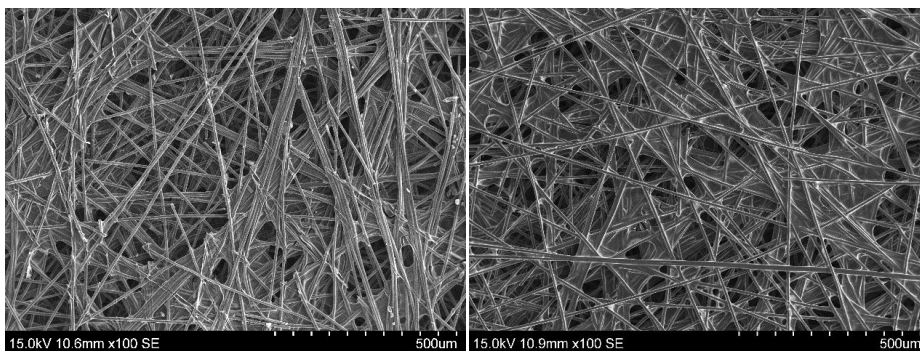


Figure 8.2.3. The two types of Toray paper used in this work, one with a hydrophobic treatment (left) and one without such treatment (right).

In contrast to the Freudenberg GDL fibres, the Toray fibre should extend further into Sn, due to their more rigid, non-flexible nature. This deeper penetration will increase the contact area with the Sn and reduce the ICR, as demonstrated in Figure 8.2.4. The more brittle paper will also deform less during the hot pressing procedure, keeping the pores more open and allowing better gas and water transport through the lifetime of the cell.

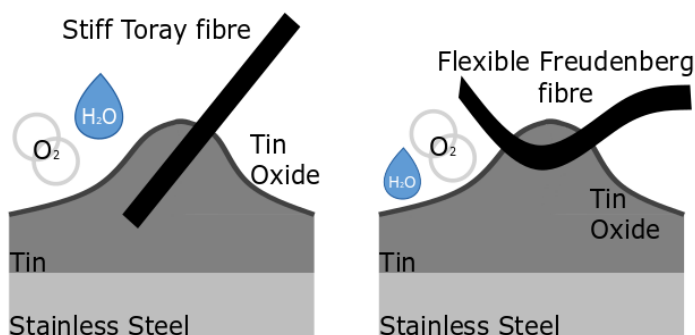


Figure 8.2.4. A drawing of the hypothesised impact of having a stiffer GDL fibre, with the Toray paper going deeper into the Sn layer, forming a larger contact area and therefore a lower ICR.

Additional differences between the Toray and Freudenberg GDLs are that the Toray GDLs have a higher porosity than the Freudenberg GDLs [267]. The porosity of the GDL will have an effect on the infiltration of Sn and contact with the GDL, as well as the amount of electrolyte that can reach the surface of the Sn during electrochemical testing.

Therefore, in order to determine which properties are the most important, analysis of the ICR before and after exposure to a simulated PEM environment, and the corrosion current during exposure can be performed.

## 8.2.2. Electrochemical testing

Each of the GDLs was hot pressed onto a Sn BPP and tested electrochemically by applying a voltage of  $1.0 V_{SHE}$  for 1 hour and measuring the current response whilst in a simulated PEMFC environment. The current density transients are shown in Figure 8.2.5.

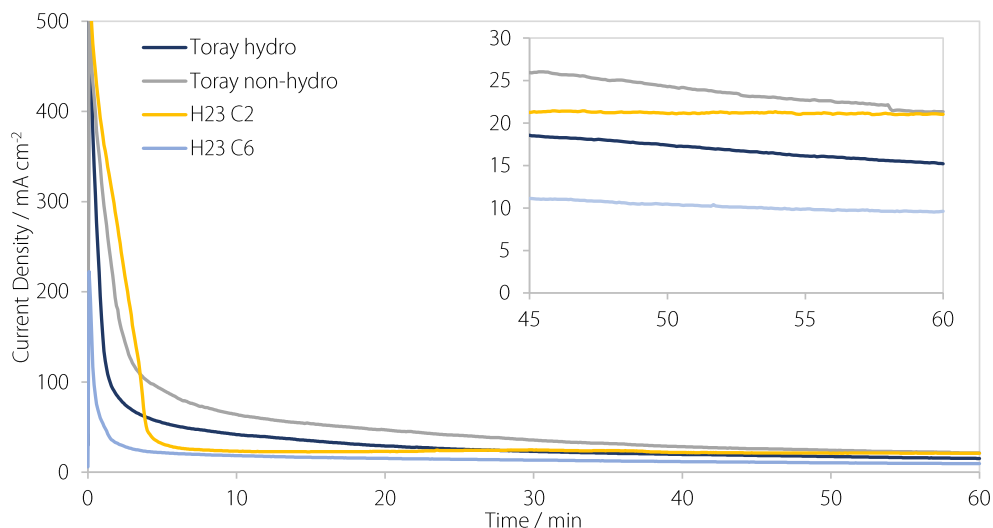


Figure 8.2.5. The current density response of different GDL types during exposure to  $1.0 V_{SHE}$  for 1 hour in a simulated PEM fuel cell environment. The inset shows the final 15 minutes of the test at low current densities.

The main difference between the different GDL types is that compared to the GDLs that have undergone hydrophobic treatment, the GDLs without hydrophobic treatment take longer to passivate, and end up with a higher corrosion current density. When the GDLs have no treatment, the electrolyte can be soaked into the carbon GDL fibres and gradually come into more contact with the Sn surface, leading to greater oxidation and greater current densities.

The difference between the Toray and Freudenberg type papers seems to be minimal, although the Freudenberg C6 paper with the hydrophobic treatment passivates most quickly and ends up with the lowest corrosion current. This could be due to its greater thickness and lower porosity than the equivalent Toray paper, leading to a smaller contact area between the Sn and the electrolyte.

The ICR before and after electrochemical testing of the BPPs hot pressed with the GDL is shown in Figure 8.2.6. Before testing, all the ICR values are similar, so the different GDL types must have similarly good electrical connection to the Sn.

After the CA test at  $1.0 V_{SHE}$  for 1 hour, the Toray papers seem to perform better, with a lower ICR. This could be due to the increased penetration depth of the GDL into the Sn layer, which occurs because of both the higher porosity and the stiffer fibres, which do not bend to remain near the surface during hot pressing. They remain deep in the Sn layer, so any oxide formed at the surface does not negatively impact the ICR to a large extent.

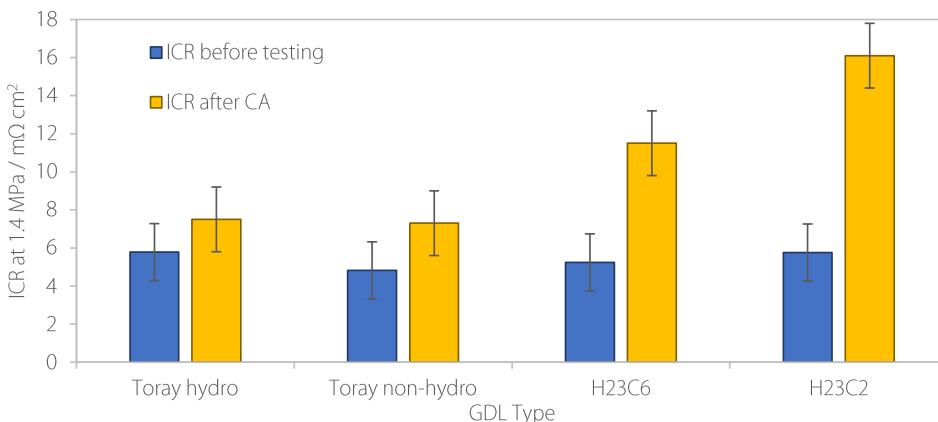


Figure 8.2.6. The ICR for each type of GDL after hot pressing (blue) and after electrochemical testing at  $1.0 V_{SHE}$  for 1 hour (yellow).

The Freudenberg GDLs are flexible and will have a higher tendency to bend and remain near the surface of the Sn, which means they are more susceptible to an increased ICR upon Sn removal and passivation. The H23 C2 GDL without hydrophobic treatment performs particularly poorly after the CA test as the fibres become saturated with electrolyte, so all Sn in contact with the GDL fibres can oxidise and the ICR increases.

### 8.2.3. Conclusions

From the electrochemical testing performed on the different types of GDL, we can conclude that the presence of a hydrophobic coating on the carbon GDL fibres is beneficial to the performance of the Sn/GDL system. This coating helps prevent the infiltration of electrolyte to the Sn/GDL boundary, which reduces the amount of oxidation taking place and the dissolution of the coating. Although these different types of GDL have not been tested *in-situ*, the presence of the hydrophobic treatment should help with the water management in a working fuel cell, allowing the easier movement of water from the three phase boundary where it is generated, to the outlet of the cell.

The stiffness of the GDL fibres was determined to be a less crucial factor than the presence of hydrophobic treatment, however the Toray GDL seems to have a lower ICR than the Freudenberg, probably due to deeper infiltration into the Sn during hot pressing improving the contact between the GDL and Sn. Despite this, the Toray GDL had a larger corrosion current density during electrochemical testing, due to the larger interaction area between the GDL and the Sn. The Freudenberg GDL with the hydrophobic treatment (H23 C6) was therefore used for all *in-situ* testing.

## 8.3. Carbon nanolayer to enhance the Sn/GDL interface

### 8.3.1. Introduction

It is hypothesised that adding carbon to the interface between the Sn and the GDL will increase the conductivity and longevity of the BPP. It has been observed that Sn alone is not a successful interface material due to the continual corrosion of the oxide layer. Although  $\text{SnO}_2$  is mostly stable, it can rupture or dissolve leading to a reduced thickness and poorer conductivity of the interface with the GDL and a reduced performance over time.

The addition of a carbon nanolayer between the Sn and GDL can both improve the conductivity of the interface by providing numerous contact points on the nanoscale to aid electron transfer through an increase in contact area between the Sn and the GDL, shown in Figure 8.3.1.

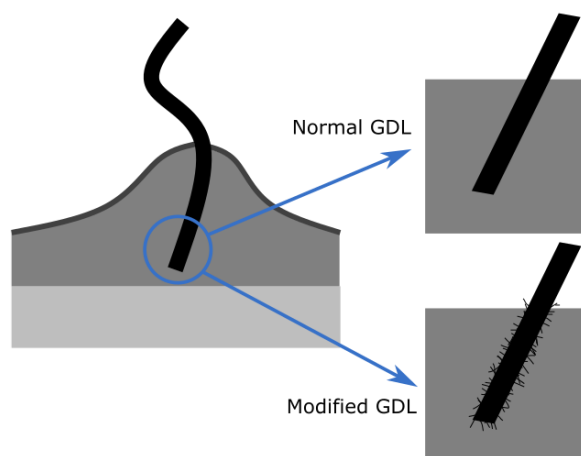


Figure 8.3.1. A drawing of the Sn/GDL interface, without (top) and with (bottom) carbon nanoparticles present.

The addition of carbon to the Sn/GDL interface can also provide improvements to the longevity of the system. Firstly, if there are more contact points between the Sn and the GDL, even if some of these are removed due to oxidation of Sn, there will still be more left than if there were no carbon present, thereby keeping the ICR as low as possible for longer. Additionally, the carbon layer can act as a barrier. During the hot pressing procedure, Sn can freely move through the GDL, spreading out and soldering to the GDL fibres. Although this is beneficial for the conductivity of the BPP, it provides an increased contact area between the electrolyte and the Sn, leading to more dissolution and performance degradation. If the carbon layer provides a barrier to this Sn penetration, there is a smaller surface area of Sn exposed to electrolyte, therefore less oxidation and removal of the Sn and an improved performance over time.

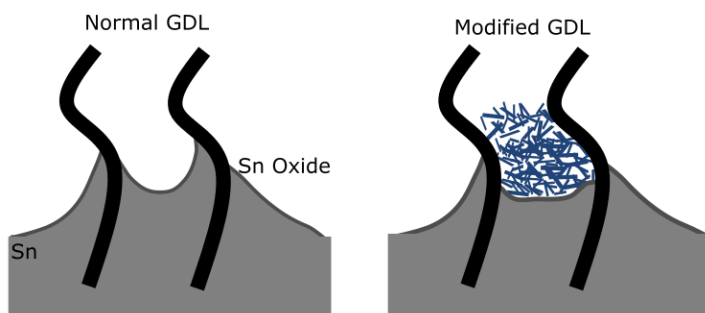


Figure 8.3.2. A drawing of the Sn/GDL interface unmodified (left) and modified with carbon (right) to block the movement of Sn into the GDL and reduce the surface area exposed to electrolyte.

In order to test this hypothesis, three types of carbon were obtained for spraying onto the GDL. These were carbon black, multi-walled carbon nanotubes, and graphitic carbon. The surface area, density, bulk conductivity and single particle conductivity of each particle type is listed in Table 8.3.1.

Carbon black is the simplest form of carbon tested, often produced by heating almost any type of carbon in an anaerobic environment. It often consists of small spheres (around 50 nm in diameter) which agglomerate to form larger particles of around 250 nm diameter [252]. It is commonly used as a catalyst support in fuel cells due to its low cost, good electrochemical performance and relatively high surface area [257]. Although carbon black is widely used, it does undergo some corrosion in a PEMFC environment, through oxidation to form  $\text{CO}_2$  when large potential differences occur during start-up and shutdown [260]. This process is catalysed by platinum, but does occur even without Pt present, so would still be a concern for carbon used in bipolar plates. Therefore, there has been a movement to use other types of carbon support in PEMFCs for enhanced durability.

Table 8.3.1. Selected properties of the different types of carbon used in this work, including the surface area [268] and density [269] of the carbon types, and both the conductivity of a single particle [268], and the bulk conductivity [268] which takes into account the packing and surface contact between the carbon particles of the same type.

Carbon Type	Surface Area / $\text{m}^2 \text{g}^{-1}$	Bulk conductivity / $\text{S m}^{-1}$	Single particle conductivity / $\text{S m}^{-1}$	Density / $\text{g cm}^{-3}$
Carbon Black	57	558	$10^3$	0.4
Graphitic carbon	3	2120	$10^5$	1.8
Multiwalled Carbon Nanotubes	272	543	$10^7$	0.3

It has been observed that increasing the surface area and conductivity of the carbon particles provides improved performance and longevity within a PEMFC [257], however it is unclear whether the same properties are required for the carbon layer between the Sn and GDL. Varying the type of carbon to increase the surface area or conductivity is therefore interesting. Graphitic carbon has a particularly high bulk conductivity [268] (Table 8.3.1), indicating that their shape leads to a good packing density with lots of contact points, and the interfacial contact resistance between two graphite particles is low. This is ideal for a BPP, which requires a very low ICR. It has also been proposed that carbon with a higher graphite like quality is more stable [258], so the longevity of the BPP should be improved with the presence of graphitic carbon over carbon black. Graphite particles in general are much larger than

carbon black [270]. Although there are many types of graphitic particles available, the ones used in this work have a rough platelet shape of around 1 to 10  $\mu\text{m}$  diameter, as seen in [65]. This leads to a lower surface area than the other, smaller carbon types.

Multiwalled carbon nanotubes (MWCNT) have an extremely high surface area and single particle conductivity [268], therefore could provide a good interface between the Sn and GDL, with large areas for the Sn to solder onto, and easy transfer of electrons. Due to their tubular shape, MWCNT may infiltrate deeper into the Sn during hot pressing, which could further decrease ICR compared to the other carbon geometries. Additionally, it has been shown that carbon nanotubes are more stable than carbon black in a simulated PEMFC environment, with a lower corrosion current density and less surface oxide formation [271].

Therefore, three types of carbon (carbon black, graphitic carbon and multiwalled carbon nanotubes) were investigated to determine whether the presence of carbon has a beneficial effect on the performance of the Sn/GDL system, and which type of carbon performs best in a simulated PEMFC environment.

### 8.3.2. Determining the correct carbon loading

The Sn/C/GDL BPPs were first optimised to find the carbon loading that produced the lowest ICR. The carbon loading is an important parameter because a good coverage of the GDL should be obtained, so each fibre has some carbon present to generate contact points on the nanoscale and reduce the ICR. However, if there is too much carbon present, the pores in the GDL will be obscured by the carbon nanolayer, and the tin will not be able to infiltrate during the hot pressing process, leading to fewer contact points and a higher ICR.

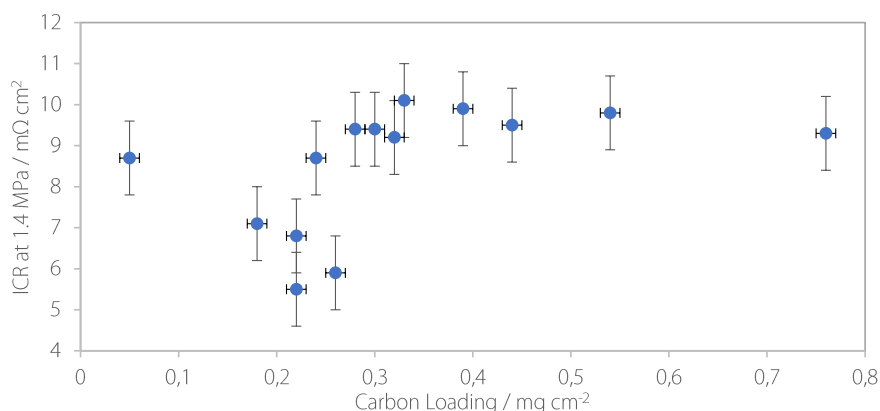


Figure 8.3.3. The ICR of bipolar plates hot pressed to GDLs with different amount of carbon black sprayed on.

This phenomenon can be observed in Figure 8.3.3, where the ICR goes through a minimum at a carbon black loading of between 0.15 and 0.25  $\text{mg cm}^{-2}$ . Although the standard deviation in the weighing equipment used to calculate the carbon loading is very low, there are some discrepancies in the exact carbon loading due to local variations in the spraying procedure, which is done by hand. From the measurements, we can estimate that the optimum loading of carbon black is around 0.2  $\text{mg cm}^{-2}$  with an ICR at about 6  $\text{m}\Omega \text{ cm}^2$ .

However, this optimum does not necessarily apply to the other types of carbon used in this work. Each type of carbon has a different density (Table 8.3.1), therefore using the same mass of carbon corresponds to a different volume and can lead to different surface coverages. This can be seen in Figure 8.3.4, which shows light microscope images of a GDL sprayed with a loading of  $0.2 \text{ mg cm}^{-2}$  of each type of carbon.

It is clear that the carbon black and nanotubes form a much higher surface coverage than the graphitic carbon, due to their significantly lower density and therefore higher number of particles. The underlying GDL is almost completely covered for carbon black and nanotubes, whereas the GDL is clearly visible under the graphitic carbon layer, which consists of fewer large particles dispersed over the GDL.

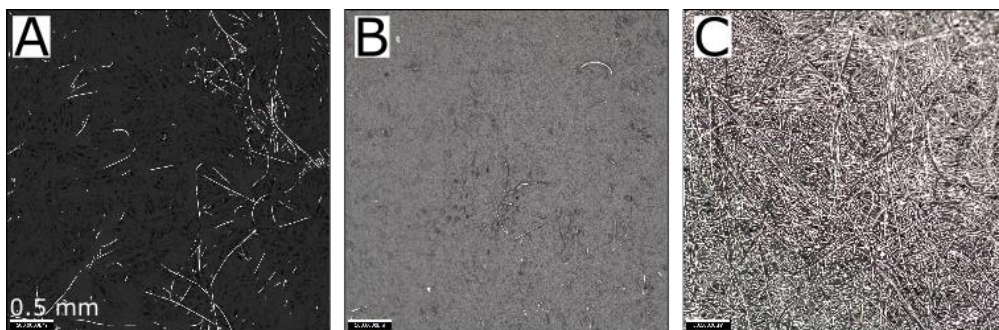


Figure 8.3.4. Light Microscope images of a GDL sprayed with around  $0.2 \text{ mg cm}^{-1}$  of A: Carbon Black, B: Multiwalled Carbon Nanotubes, C: Graphite.

As described previously, this will have an impact on the ICR and electrochemical performance. The thick layer of carbon black or nanotubes can block the GDL pores, leading to problems with water balance and mass transport. Conversely, if there is very little graphitic carbon on the GDL surface, it will not have a large impact on the ICR and performance, meaning that a higher loading may be more suitable.

Therefore, the density of the carbon types should be taken into account when determining the correct loading, and perhaps the coverage of the carbon over the GDL surface is the more important factor than the mass of carbon present. This should be further optimised when using different types of carbon in the future.

### 8.3.3. Comparing the Different Types of Carbon

In order to determine whether the addition of carbon improves performance, and which type of carbon represents the better choice given the conditions, electrochemical testing in a simulated fuel cell environment was performed. The samples, including the bare SS 304L substrate and Sn/GDL with no carbon, were exposed to a potential of  $1.2 V_{\text{SHE}}$  for 1 hour, and the ICR was monitored before and after exposure.

Initially before any corrosion testing has been performed, the ICR of each sample with the carbon nanolayer is much lower than that of the Sn alone. This is as expected, because of the larger contact area between the Sn and the GDL with the carbon fibres present. The carbon black has the lowest ICR, but

it is within the standard deviation of the other carbon particle types. The addition of carbon reduces the initial ICR compared to the Sn/GDL alone, which again has a lower ICR than the bare substrate due to the beneficial hot pressing process.

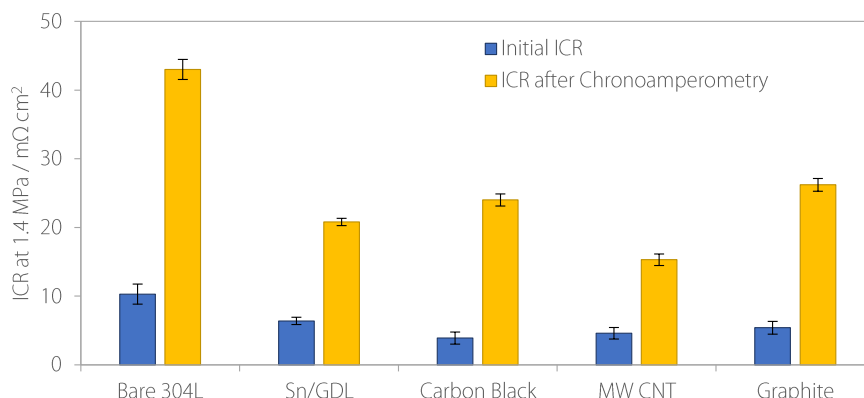


Figure 8.3.5. The ICR of the samples before and after exposure to  $1.2 V_{SHE}$  for 1 hour in a simulated PEMFC environment.

After the corrosion testing, the ICR of all samples increased. The stainless steel substrate increased significantly, due to the formation of a stable and poorly conductive surface oxide, confirmed also by the very low corrosion current density, Figure 8.3.6. For the Sn/C/GDL samples, the ICR after corrosion testing corresponds well to the shape and size of the carbon types, and therefore the surface area. The MWCNT have an elongated structure, unlike the more spherical carbon black and graphite used in this thesis [65]. This means that when hot pressed, the MWCNT infiltrate deeper into the Sn, leading to an increased contact area and therefore a lower increase in ICR.

After corrosion testing, the carbon black and graphitic carbon modified samples have a similar ICR, 24 and 26 mΩ cm<sup>2</sup>, respectively, but both now have a slightly higher ICR than the Sn sample, with an ICR of around 21 mΩ cm<sup>2</sup>. The percentage increase is high, perhaps implying that the addition of these types of carbon is actually detrimental to the corrosion resistance of the BPPs. This could be because the carbon particles lie between the Sn and the GDL, meaning that when the surface of the Sn is dissolved and passivated to form Sn(OH)<sub>4</sub>, the hot pressed particles lying on the surface are cut off from contact with the Sn. Additionally, if the layer of carbon introduces some porosity to the Sn/GDL interface, there may be increased contact with the electrolyte and increased dissolution, leading to worse performance. For the Sn alone, the GDL fibres go deeper into the Sn and conductivity is maintained despite the presence of surface oxides, which can passivate the surface.

Given that the carbon black and graphite particles are of a similar geometry, it can be determined that adding rounded particles rather than elongated particles is worse for the long-term ICR performance of the Sn/C/GDL BPP.

The corrosion current density of each BPP type after exposure to  $1.2 V_{SHE}$  for 1 hour in a simulated PEMFC environment can be seen in Figure 8.3.6. In confirmation of the findings by Wang et al. [271], the carbon nanotubes have a significantly lower corrosion current than carbon black, and have a lower ICR after exposure. This is due to the reduced oxidation of the MWCNT themselves, as well as the suppression of the dissolution and oxide formation of the Sn. This can be confirmed by the EDS

analysis of the samples after corrosion testing, where the Sn sample with no carbon present contained 17 % oxygen, compared to 7 % for the carbon black, and 0 % for the MWCNT. This reduction in oxidation of the surface and the stability the MWCNT can explain the smallest increase in ICR after corrosion testing, and the overall best performance.

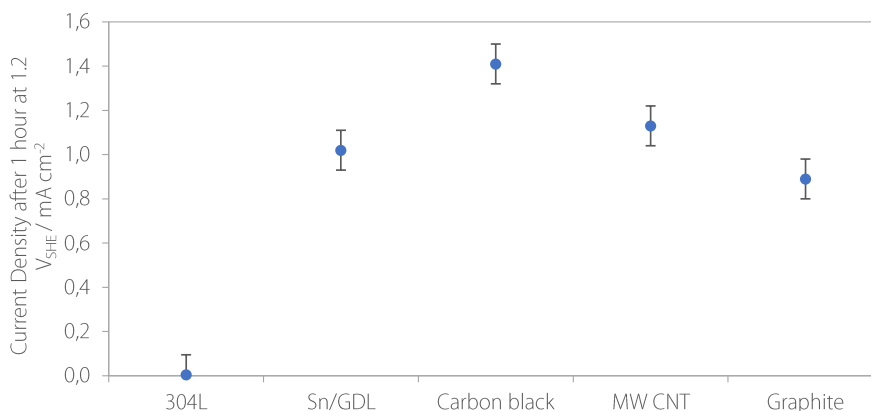


Figure 8.3.6. The corrosion current density of each bipolar plate type after exposure to 1.2 V<sub>SHE</sub> for 1 hour in a simulated PEMFC environment.

The graphitic sample has a lower corrosion current density, which could be due to both the smaller number and surface area of particles on the surface which can undergo oxidation, as well as the high stability of graphitized carbon [258,272]. There is little exposure of the carbon to the electrolyte, and the few graphite particles do not impact the exposure of the Sn surface to the electrolyte, therefore the corrosion current is similar to that of Sn alone.

### 8.3.4. Conclusions

The addition of a carbon based layer between the GDL and BPP has been shown to reduce the ICR of the Sn/GDL system, due to an increased number of electronic pathways. However, this low ICR is not necessarily sustained after exposure to the PEMFC environment. Spherical particles that do not infiltrate deeply into the Sn during hot pressing are susceptible to an increase in ICR after electrochemical testing, due to the growth of an oxide between the Sn and carbon, which blocks the electron transfer through the Sn/C/GDL system.

The best type of carbon particle investigated in this thesis was the multiwalled carbon nanotubes, which are both a more stable form of carbon, leading to less surface oxidation, and have a longer contact pathway deeper into the Sn due to their elongated shape. These two factors mean that the increase in ICR after exposure to the PEMFC environment is limited, and the bipolar plate is more stable. The multiwalled carbon nanotubes were then tested *in-situ*, the results of which can be found in chapter 9 of this thesis.

## In-situ Analysis of Bipolar Plates

### 9.1. Introduction

During the previous chapters of this thesis, the Sn/GDL type BPPs have been shown to have superior contact resistance and stability in an *ex-situ* simulated PEMFC environment when compared to bare stainless steel. *Ex-situ* testing is useful, but not always comparable to *in-situ* testing because of a number of factors, including: different electrolyte conditions, relative humidity, temperature, acidity not constant, variable load conditions, interactions with other components, and the release of metal ions which may affect performance. Additionally, when hot pressed with the GDL, the Sn may change the mass transport properties of the GDL in a way that should be quantified. Therefore, only *in-situ* testing can truly determine the long-term performance of the BPPs inside a working PEM fuel cell.

However, the varying conditions and interactions between different components make determining the performance of one specific component *in-situ* challenging. There are some developments in *in-situ* analysis of different components, for example an *in-situ* ICR technique has been developed to monitor the ICR at specific points in the cell (inlet, outlet, cathode, anode) through the lifetime [273]. However, at the moment, the technology is still in the early stages and is not suitably reliable.

In this thesis chapter, the time evolution of the performance of the Sn BPPs will be compared against standard BPPs using a testing protocol developed by the European commission [8]. This protocol is used to determine the long-term performance of bipolar plates inside a working PEM fuel cell, by applying accelerated stress protocols including drive cycles, polarisation curves, EIS and *ex-situ* ICR. Post-mortem analysis of the bipolar plates and membranes were also performed. The specific methodology used for the *in-situ* testing including all experimental details can be found in chapter 3.

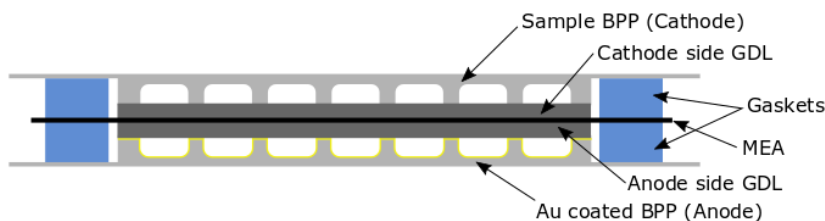


Figure 9.1.1. The *in-situ* fuel cell assembly, consisting of a MEA sandwiched between two bipolar plates, a gold coated stainless steel BPP on the anode side, and a variable BPP on the cathode.

In order to deconvolute the different processes happening at the anode and cathode bipolar plates, a standard gold coated stainless steel bipolar plate was used on the anode side, while the plate at the cathode side was changed depending on the experiment (Sn – from chapter 4, SnBi – from chapter 6 and Sn/C – from chapter 8 as well as gold coated and as-received stainless steel). The cell assembly is as shown in Figure 9.1.1. In general, the cathode side is expected to have a higher degradation rate due to

the harsh oxidising conditions [87], so the samples of interest were used on the cathode side. Also, the reducing atmosphere on the anode side of the fuel cell could degrade the protective Sn oxide which is formed on the Sn/GDL plates, so they are most suitable for the cathode side of the fuel cell.

This thesis chapter therefore aims to determine whether the Sn/GDL soldering process produces any significant advantages in performance and longevity of BPPs in an operating PEM Fuel Cell.

## 9.2. Interfacial Contact Resistance

Before the cell was assembled and started up, the interfacial contact resistance (ICR) of each bipolar plate was measured *ex-situ* in the apparatus described earlier in chapter 3 of this thesis.

By looking at the ICR before and after the cycling procedure, we can try and compare the decreases in cell voltage we see after the fuel cell has been operating for 200 hours and estimate how much of the performance loss can be attributed to the bipolar plate degradation.

### 9.2.1. Anode Side Bipolar Plates

Figure 9.2.1 shows the measured *ex-situ* ICR (at 1.4 MPa) between a GDL and the anode side bipolar plates from different fuel cell assemblies, both before and after 600 drive cycles of *in-situ* testing.

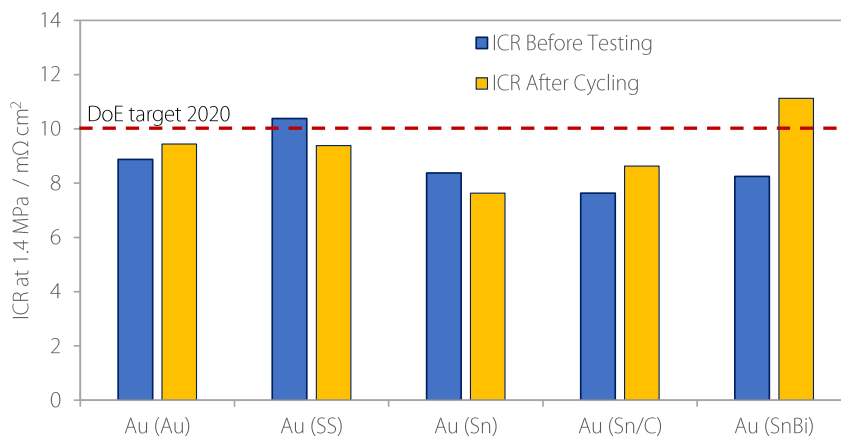


Figure 9.2.1. The *ex-situ* ICR at 1.4 MPa of bipolar plates placed on the anode side of a fuel cell before and after cycling. Each plate was gold-coated stainless steel, and the plate on the cathode side of the fuel cell is indicated in brackets. The red dashed line shows the DoE target for ICR to be reached by 2020.

The ICR values for each cell are similar and in the same range. Before cycling, the average ICR for the 5 cells was around 8.70 mΩ cm<sup>2</sup>, with a deviation of around ± 1.5 mΩ cm<sup>2</sup>, while after 600 drive cycles the average ICR was 9.24 mΩ cm<sup>2</sup>, an increase of about 6%. This is within the maximum ICR target for bipolar plates put forth by the US Department of Energy (DoE) for 2020 (10 mΩ cm<sup>2</sup>). As the bipolar plate coating at the anode side was comprised of the same material (Au) for all cells, we would indeed expect the measured ICR to be about the same. Furthermore, the Pourbaix diagram for gold [146] indicates that gold is stable in the anode environment of the fuel cell, and the similar ICR recorded after cycling is therefore as expected.

It is worth noticing that the observed ICR after 600 cycles of *in-situ* testing either increased or decreased slightly, indicating that small local changes in the coating during *in-situ* testing can change the overall contact with the GDL. Although gold is supposed to be stable, some changes in the gold coating are frequently observed when taking the bipolar plates out of the PEMFC (Figure 9.2.2), and minute changes in the ICR could be due to thinning or removal of the gold coating on the stainless steel. In fact, gold is known to oxidise when exposed to higher anodic potentials, which may occur in the fuel cell at certain conditions [274]. Subsequent gold oxide reduction leads to some dissolution and loss of gold, also roughening of the surface [275]. Cherevko et al. [276] used an ICP-MS with an electrochemical flow cell and showed that gold dissolution commenced at about 1.3 V vs RHE, coinciding with the onset of 2D surface oxide formation.

These changes in the gold surface can lead to changes in the ICR of the bipolar plates. A reduced ICR is hard to explain, but may be a result of a beneficial removal of gold increasing the contact points between the GDL and bipolar plate, hence reducing the constriction, and this way reducing the ICR slightly. Contrarily, an increased ICR may be expected if parts of the Au coating are removed, possibly reducing the number of contact points to the GDL as well as exposing the underlying stainless steel to the environment with the inevitable formation of lower conductive surface oxide.

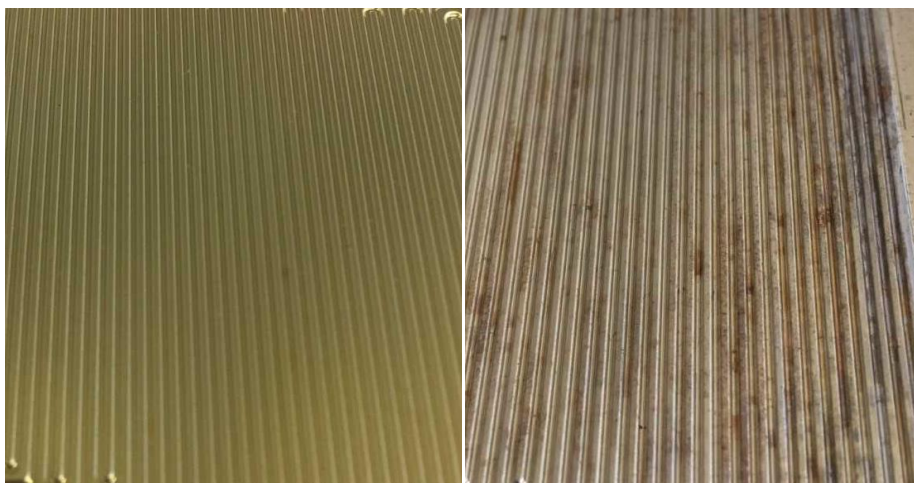


Figure 9.2.2. The flow-fields of a gold coated stainless steel bipolar plate, before (left) and after (right) 200 hours of *in-situ* testing. After testing, there is discolouration on the surface and the coating is faded in places, with brown spots along the channels.

It is important to note that some of the Au-coated BPPs were re-used for multiple *in-situ* tests, due to limited availability and the fact that their lifetime should be much greater than 200 hours given their supposed stability in PEMFC conditions. This cumulative use and degradation could be the reason behind some small variances in measured ICR (Figure 9.2.1).

In order to determine what impact these changes in contact resistance will have on the overall fuel cell performance, we can calculate the corresponding cell voltage increase. On average, the ICR has increased by  $0.54 \text{ m}\Omega \text{ cm}^2$  from before to after cycling, which using Ohm's law can be converted into a voltage loss at different current densities. Even at the highest current densities of  $1.2 \text{ A cm}^{-2}$ , the performance loss from the anode side bipolar plate is less than 1 mV. This indicates that the contact resistance increase from the anode side bipolar plate will play only a minor role in the total fuel cell

performance degradation. However, this does not consider other degradation that the bipolar plate might undergo, including reduction in water management due to changes in hydrophobicity, metal ion leaching due to coating defects or poorer gas transport due to channel blockages.

### 9.2.2. Cathode Side Bipolar Plates

The bipolar plates on the cathode side of the fuel cell are of more interest, as we can compare the quality of the custom-made BPPs to two standards, Au coated and bare stainless steel. The ICR values between a GDL and each BPP are presented in Figure 9.2.3, and measured was taken before being placed into the fuel cell (blue column), and after 600 drive cycles had been completed (yellow column).

The stainless steel bipolar plate obtained a significantly higher initial ICR than all of the other bipolar plates. This can be attributed to the formation of a less conductive oxide layer on the stainless steel surface when being stored before *in-situ* testing. For the gold plate, no oxide is formed because of its extremely low reactivity with air [277], hence it has good conductivity and a low ICR. For the Sn-based plates, the oxide on the stainless steel substrate is removed before Sn electrodeposition, and then immediately hot pressed with the GDL after electrodeposition, to limit oxide formation between the GDL and BPP. When the oxide does form, it acts as a protective layer and does not impede the conduction of electrons, hence the low ICR before *in-situ* testing.

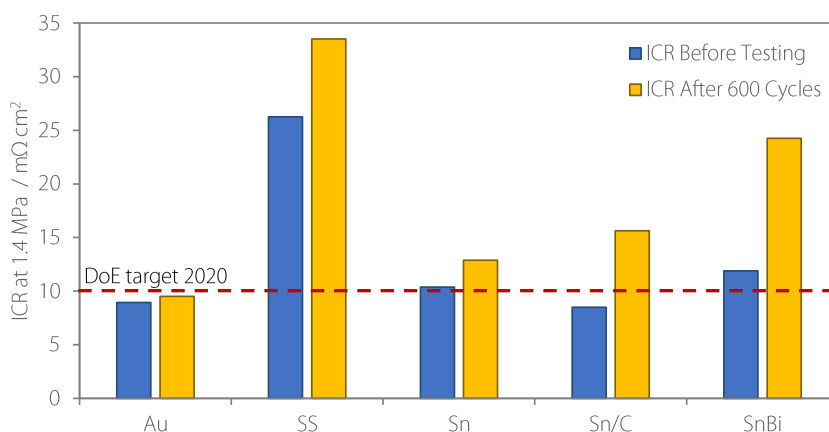


Figure 9.2.3. The ICR of bipolar plates placed on the cathode side of the fuel cell, before and after 600 drive cycles. The red dashed line shows the DoE target for ICR to be reached by 2020.

There is some variation in the initial ICR of the Sn-based BPPs. As seen in chapter 7.2, the addition of the sprayed carbon layer produces a lower ICR than Sn alone likely due to the higher number of contact points between the GDL and BPP, whereas the SnBi alloy has a higher ICR than the others because of its naturally higher resistivity ( $13 \times 10^{-7} \Omega \text{ m}$  compared to  $1 \times 10^{-7} \Omega \text{ m}$  for tin[144]). In general, the ICR of the Sn based BPPs are higher for the larger area *in-situ* BPPs compared to the samples tested *ex-situ*. This is because the hot pressing process is less accurate on the larger scale, leading to a larger variance in the applied pressure over the BPP surface. This leads to some areas of the BPP having poorer contact with the GDL and therefore higher ICR than expected. The outcome of this uneven hot pressing is that only the Sn/C/GDL plate reaches the DoE targets for 2020 before cycling. After optimisation of the hot pressing process, the ICR of all the Sn-based BPPs could be lower and similar to the gold coated sample.

The measured ICR of the cathode BPPs increased for all samples after being exposed to 600 drive cycles of *in-situ* testing. In general, the ICR values increased significantly more than the anode side did (Figure 9.2.1). This could be due to harsher conditions on cathode, including the presence of O<sub>2</sub> and high positive cell voltages.

The stainless steel bipolar plate exhibits a large increase in ICR of around 7 mΩ cm<sup>2</sup>, or 28 %, after 600 drive cycles of testing. This is comparable to previous work [273] and can be attributed to a thickening of the non-conductive oxide layer, or to the formation of other corrosion products on the surface of the BPP. Furthermore, it is a well-known phenomenon that in PEM fuel cell, stainless steel bipolar plates release Fe<sup>3+</sup> ions which can go on to contaminate the nafion membrane and degrade performance [87]. In the oxidising conditions at the cathode side of a PEM fuel cell, dissolved metal ions could also form oxides which can stick to the BPP surface, increasing contact resistance and reducing performance.

As for the Sn-based bipolar plates, the ICR after the *in-situ* testing varies quite widely. The BPP with Sn alone seems most stable, with a small increase in ICR of 24 % after cycling for 200 hours. This increase is lower than all of the other bipolar plates except for the Au-coated plates, implying that the Sn/GDL BPP is relatively stable in the PEM environment, with the protective surface oxide remaining in place, whilst maintaining good conductivity. The increase in ICR could be attributed to growth in the thickness of this oxide film, when oxygen atoms diffuse through the film and oxidise the underlying Sn. This would reduce the amount of contact between the Sn and the GDL, with the less conductive SnO<sub>2</sub> forming in between.

For the Sn/C/GDL plate, there is a significant increase in ICR after *in-situ* testing, of 7.2 mΩ cm<sup>2</sup>, or 84 %. This larger increase in ICR can be understood because of possible degradation and delamination of the multiple interfaces that the electron has to travel through with this type of BPP. Carbon corrosion will occur quite readily at high potentials, in particular potentials that are experienced during start up and shutdown [87] as well as starvation conditions [274], which can lead to the removal of conduction pathways between the BPP and GDL, increasing the ICR. Additionally, oxidation of the Sn underneath the carbon nanolayer can lead to poorer contact, or adhesion, with the carbon, which reduces conductivity. The carbon nanoparticles sit on the surface of the Sn whereas the GDL fibres penetrate much deeper into the bulk, meaning that any changes to the surface oxide of the Sn will affect the BPP with carbon more than the other types of BPP.

Surprisingly, the SnBi BPP underwent the largest increase in ICR from before to after the *in-situ* testing despite the promising *ex-situ* electrochemical results (Chapter 6). The ICR increased by over 12 Ω cm<sup>2</sup>, or 104 %. This is a significant increase compared to the Sn/GDL BPP, and the reasoning may be due to phase separation (as was observed for longer hot pressing times) or selective corrosion in the SnBi alloy reducing the number of contact points with the GDL. In either case, the adhesion between the BPP and the GDL was clearly degraded in some way, and the ICR therefore increased.

Finally, the ICR of the Au bipolar plate on the cathode side increased by less than 1 mΩ cm<sup>2</sup>, around 6 %, showing that it is relatively stable in the acidic environment of the cathode. This value is within the expected variance between samples observed on the anode side of the fuel cell, indicating that the gold coated plates are inert in both the anode and cathode environment. Therefore, we can conclude that

the increases in ICR for the other BPPs are not due to the harsher conditions on the cathode side, but rather a worse overall performance.

Overall, we can conclude that from the ICR measurements before and after *in-situ* testing, the Au BPP performs best, the stainless steel has the highest absolute contact resistance, and the SnBi/GDL BPP has the largest increase in ICR after *in-situ* testing, around  $15 \text{ m } \Omega \text{ cm}^2$ . This corresponds to a cell voltage decrease of 18 mV at a current density of  $1.2 \text{ A cm}^{-2}$ , which is a very small contribution compared to the overall performance degradation, as will be seen in the remainder of this thesis chapter.

### 9.3. Polarisation curves

As outlined in chapter 3.1 of this thesis, a polarisation curve of each fuel cell was performed every 50 drive cycles. Here, a current density of between 0 and  $1.2 \text{ A cm}^{-2}$  is applied and the cell voltage is measured. An example of an initial polarisation curve and the changes expected after cycling is seen in Figure 9.3.1.

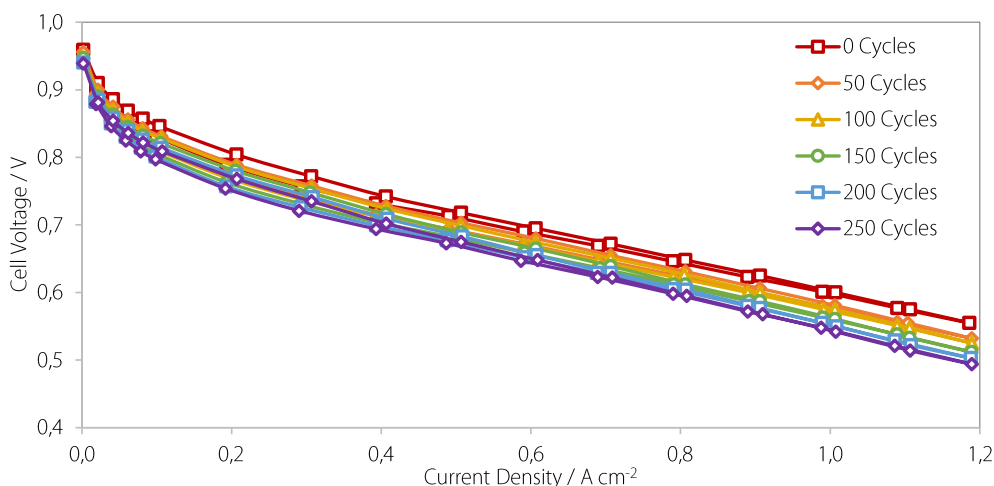


Figure 9.3.1. An example of the progression of polarisation curves with increasing numbers of drive cycles.

There are two main ways to analyse the polarisation curves for each fuel cell. The first is by taking the cell voltage at two specific current densities ( $0.2$  and  $1.0 \text{ A cm}^{-2}$ ), which are thought to represent the activation and ohmic loss dominating regions of the polarisation curve, respectively. These cell voltages can be plotted over time to determine a reversible and irreversible degradation in cell performance, which can be compared to other fuel cells.

Although the thermodynamic cell voltage is close to  $1.2 \text{ V}$  at the operating temperature, this is never accessible in an operating fuel cell. Internal currents from reactant cross over or leak currents from Pt and carbon support corrosion reduces the open circuit voltage to values below  $1 \text{ V}$ . Furthermore, voltage performance in the low current density region is dominated by electrode kinetics (activation losses) and quickly dwarves the effect of internal currents. The activation loss is a result of degradation of the catalytic layer, or more specifically the 3-phase region where reaction occurs, and is due to loss

of active area by carbon support corrosion, catalyst particle removal, catalyst dissolution, Ostwald ripening and agglomeration of small catalyst particles or poisoning/blocking of the catalyst active sites by fuel contaminants (e.g. CO, SOx or others) [87,278,279]. The cell voltage development in the medium current density ohmic loss region is more representative of the bipolar plate, with reduction in performance due to increase in ICR from oxide growth, or poor connection between the GDL and BPP. However, the cell voltage in the ohmic loss region also includes other losses related to the membrane as well as losses related to electrode kinetics as before, so it is important to analyse the performance trends with time in more detail.

Additionally, the linear region of the polarisation curve, in the ohmic loss area, can be used to estimate the resistance of the fuel cell over time. This again can be compared to other fuel cells to determine the performance of the bipolar plates, as they dominate the ohmic losses in the fuel cell.

### 9.3.1. Cell Voltage in the Activation Region

The cell voltage in the activation loss region of each fuel cell, at  $0.2 \text{ A cm}^{-2}$  was extracted from the respective polarisation curves and plotted against the number of drive cycles run in Figure 9.3.2.

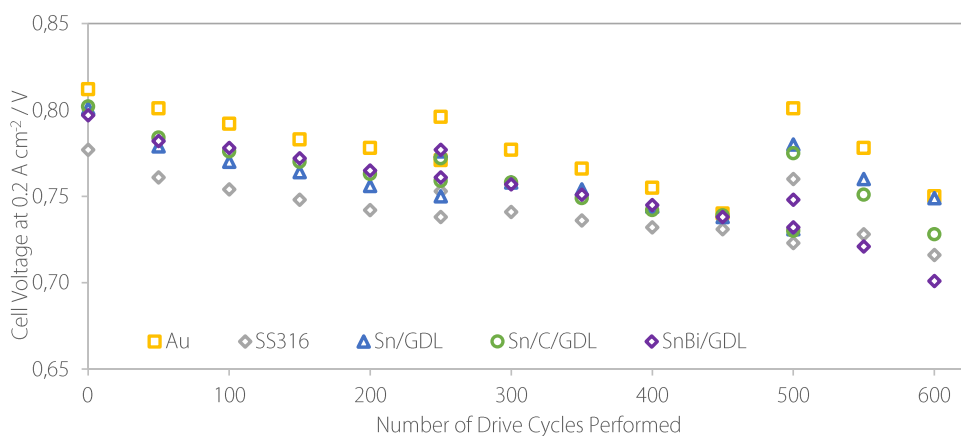


Figure 9.3.2. The progression of the cell voltage at  $0.2 \text{ A cm}^{-2}$  for each fuel cell as the number of drive cycles performed increases.

The first thing to notice from Figure 9.3.2 is the absolute cell voltages at the beginning of the cycling procedure. Here, after very little degradation had occurred, the Sn-based BPPs performed a little worse than would be expected from the ICR values alone. The exact cause for this difference is not readily extracted from the measurements. It could be related to the hot pressing procedure which led to some infiltration of Sn into the GDL affecting transport processes within the layer.

All the fuel cells experienced a steady decline in performance with increasing number of drive cycles. Some of the degradation was then recovered after performing a shut-down and start-up of the cell. The shutdown was performed after 250 and 500 drive cycles and the recovered voltage divided by the number of drive cycles is referred to as the reversible degradation rate. Irreversible degradation rate is given as the difference between the initial voltage and the voltage after the start-up at 500 drive cycles divided on the number of drive cycles. Both reversible and irreversible degradation rates of the cells in

Figure 9.3.2 are plotted in Figure 9.3.3. Furthermore, the voltage recovery after the shutdown and start-up procedures at 250 and 500 drive cycles are summarized in Figure 9.3.4.

The degradation rates of all fuel cells are highest during the final set of drive cycles and were significantly worse than during the first sets of drive cycles. This is most likely due to the damaging conditions experienced during the shutdown and start-up procedures. Very high, or even negative cell voltages can be experienced during shutdown and start-up procedures [87,259], which can lead to various degradation mechanisms of the MEA and bipolar plate constituents, lowering the performance significantly.

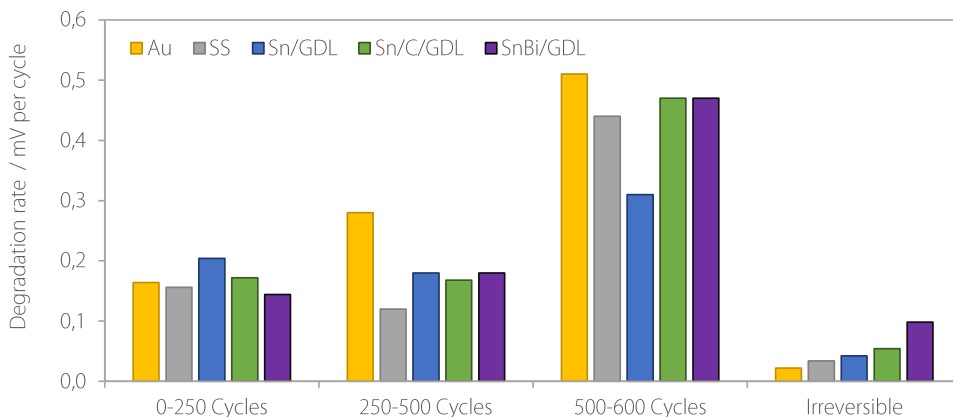


Figure 9.3.3. Average degradation rate of each fuel cell in mV per cycle at 0.2 A cm<sup>2</sup>. Both the reversible degradation rates in each set of 250 drive cycles, as well as the overall irreversible degradation rate after 500 drive cycles are shown.

From Figure 9.3.2 and Figure 9.3.3, the fuel cell with Au BPPs showed consistently the highest cell voltage, but also the highest reversible degradation rate in the second and third set of cycles. Additionally, it also showed a very low irreversible degradation rate. This shows that any reduction in performance was probably caused by reduced hydrophobicity and poor water management that slowly dried out the membrane during continuous operation, which then was almost recovered after shutdown that allowed for humidification of the membrane before start-up.

The stainless steel plate showed the second lowest irreversible degradation, and one of the lowest reversible degradation rates, in particular in the 250-500 drive cycles region. However, it also consistently showed the lowest cell performance up to 500 drive cycles, indicating that it does not represent a high quality BPP.

The Sn/GDL BPP showed a relatively good performance, both with respect to reversible and irreversible degradation. Its final cell voltage after 600 drive cycles was approximately the same as the Au coated plate, showing that it experienced the lowest drop in cell performance over the complete cycling procedure at 0.2 A cm<sup>2</sup>. It seems likely that the Sn/GDL BPP would even surpass the Au coated BPP if the cycling procedure were allowed to be continued.

The Sn/C/GDL plate showed a similar performance and degradation rate, as the Sn/GDL sample up to the second shutdown and start-up procedure at 500 drive cycles. After the second start-up, the cell voltage dropped significantly between 500 and 600 cycles, rendering the overall cell performance worse than the Sn/GDL and Au coated ones. Although the exact reason for the sudden rapid decline in

performance after 500 drive cycles is not clearly understood, it may be attributed to corrosion of the extra carbon sprayed on to the GDL and subsequent deterioration of the interface between the GDL and the substrate affiliated effects.

For the SnBi/GDL BPP, the performance over the first 500 cycles was good and it obtained both the lowest degradation and highest cell voltage at 500 cycles, although by a small margin only. However, the voltage recovery after the second shutdown was much lower than expected and was a mere 2.0 %, significantly lower than the other cells that obtained an average recovery of 6.0 % (Figure 9.3.4).

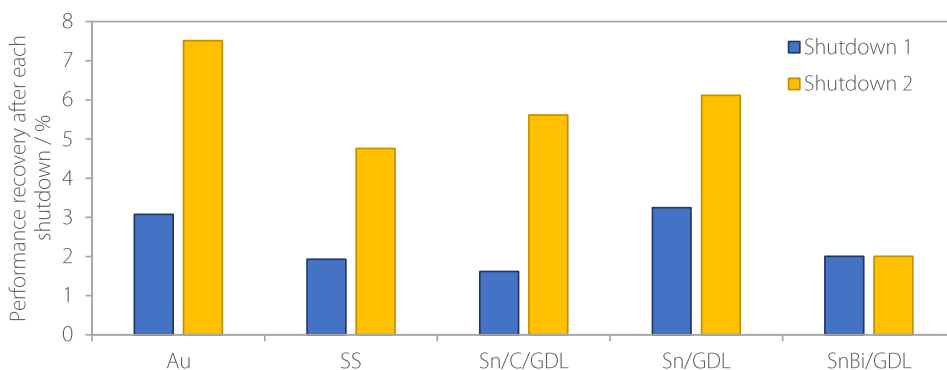


Figure 9.3.4. The recovery of each fuel cell after the first and second shutdowns as a percentage of the initial cell performance.

This was not the case after the first shutdown, where the recovery of the SnBi was also 2.0 %, compared to the average of 2.4 % for the other cells. This small recovery after the second shutdown is also shown in the high irreversible degradation rate of the SnBi cell (Figure 9.3.3). This could imply that there is some problem with the membrane, for example if bismuth ions have entered the membrane and caused some irrevocable damage. Alternatively, the SnBi cell could have experienced some particularly challenging conditions during the second shutdown, leading to more carbon corrosion than normal and therefore poorer performance recovery.

In conclusion, the progression of the cell voltage in the activation region over time tells us that the Au coated and Sn/GDL BPPs have performed well. As expected, the Au BPP has a very low irreversible degradation rate, with a consistently high cell voltage. The Sn/GDL BPP also has a fairly low degradation rate, and it seems that if cycling were continued, it would likely obtain the highest cell voltage. The addition of carbon or bismuth to the Sn/GDL system does not provide any substantial beneficial effect on the performance over 600 cycles, but before the second shutdown, each BPP was performing as well if not better than the Sn alone. Therefore, more frequent shutdown and start-up cycles may be a better way to identify more durable BPPs.

### 9.3.2. Cell Voltage in the Ohmic Region

In the same way that the voltage in the activation region can be plotted against drive cycle number, the voltage in the ohmic losses region, at 1.0 A cm<sup>-2</sup>, can be analysed, and is plotted in Figure 9.3.5. The trends in the voltage progression between the different bipolar plates are very similar to the trends in the activation region (Figure 9.3.2).

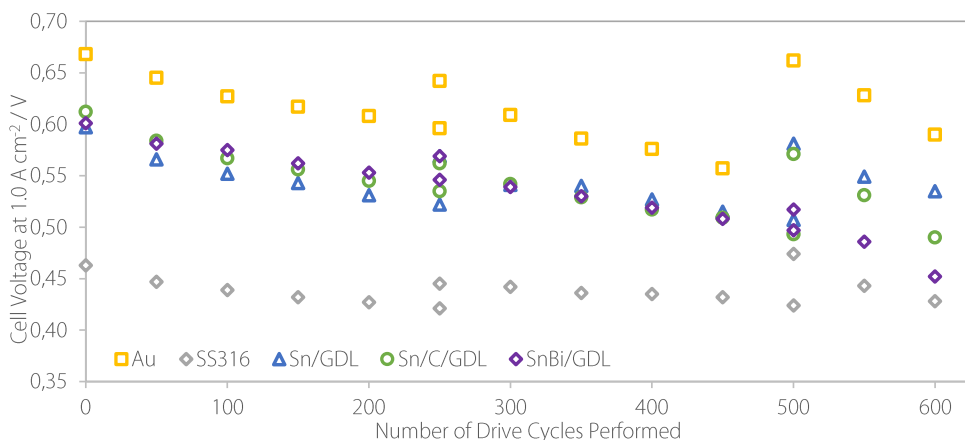


Figure 9.3.5. The progression of the cell voltage at 1.0 A cm<sup>-2</sup> during cycling for each fuel cell.

Again, at the beginning of the cycling procedure, we can correlate the relative cell voltages with the *ex-situ* ICR. The gold coated BPP performed the best and the uncoated stainless steel BPP performed the worst. All the Sn-based BPPs showed similar performance initially with the Sn/C/GDL slightly higher. However, the cell voltage degradation rate was also slightly higher for the Sn/C/GDL sample over the first 250 drive cycles, while the SnBi/GDL showed the lowest and surpassed the former.

The degradation rates of each cell over the groups of drive cycles, are plotted in Figure 9.3.6, including both reversible and irreversible degradation rates. The stainless steel BPP has an extremely low degradation rate, and surprisingly even gains performance after the second shutdown. This increase in cell voltage could be due to several reasons, for instance abnormal electrode potential fluctuations during the shutdown reducing the contact resistance due to removal of surface oxide, or removal of water in the channels during the shutdown leading to a better distribution of gasses. The performance reduction seen during cycling is therefore not due to increasing ICR but could mainly be due to metal ions leaching into the proton exchange membrane and impeding the proton transport through the membrane.

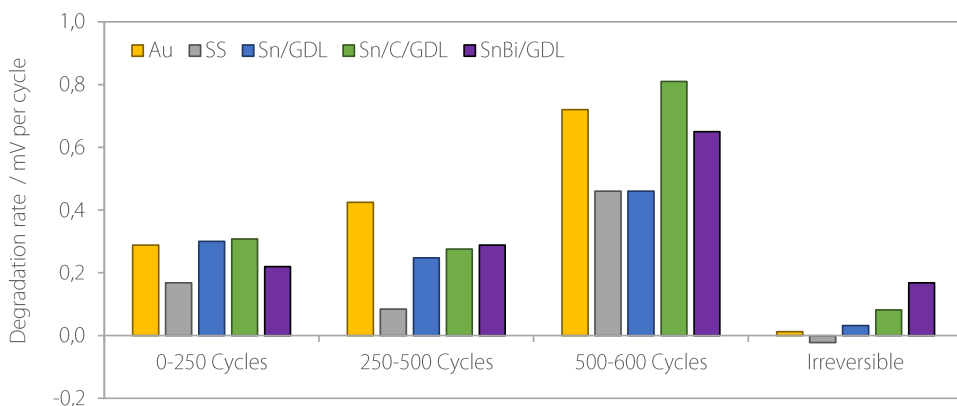


Figure 9.3.6. The degradation rate of each fuel cell during cycling at 1.0 A cm<sup>-2</sup>. Both the reversible degradation rate during each group of drive cycles, and the irreversible rate after the first 500 cycles are shown.

The Sn based bipolar plates showed similar performance during the first cycles, but after 500 cycles, the Sn/C/GDL BPP exhibited a particularly high degradation rate, in a similar manner as was observed at the lower current density (Figure 9.3.2). As explained previously, this was perhaps due to a breakdown in the conduction between the Sn and the carbon nanoparticles, which are not deeply imbedded into the Sn. This could be the consequence of oxide formation on the Sn surface, carbon corrosion or thermal cycling during the start-up and shutdown procedures, which could cause physical delamination of the carbon from the Sn and deterioration of the interface. These processes are irreversible, which can explain the higher irreversible degradation rate observed for the Sn/C BPPs as compared to those with Sn alone.

The SnBi/GDL BPP obtained a high irreversible degradation rate, due to the poor performance recovery after the second shutdown, again in accordance with the low current density results (Figure 9.3.2). This could be because of an unexpected cell voltage behaviour during the shutdown and start-up procedure, which could in fact reverse the current in case of incomplete purging; i.e. when the anode is partially exposed to both hydrogen and air [259]. Alternatively, there could be some delamination of the GDL from the BPP due to thermal cycling, although it is unclear why this would affect the SnBi BPP more than the Sn or Sn/C BPPs.

In total, analysing the cell voltage in the ohmic region of the polarisation curve can give some information about the performance of the bipolar plate, however it is difficult to separate the losses related to the bipolar plate from other loss mechanisms in the fuel cell, such as the activation losses, which dominate the degradation rates.

### 9.3.3. Slope of the Ohmic Region

The slope of the polarization curve in the ohmic region may be used in an attempt to separate out the impact of the bipolar plate on the fuel cell performance from the activation losses, which should be of less importance at higher current densities. Resistance values were calculated from the slope of the polarization curves for every 50 drive cycles for each fuel cell and are provided in Figure 9.3.7.

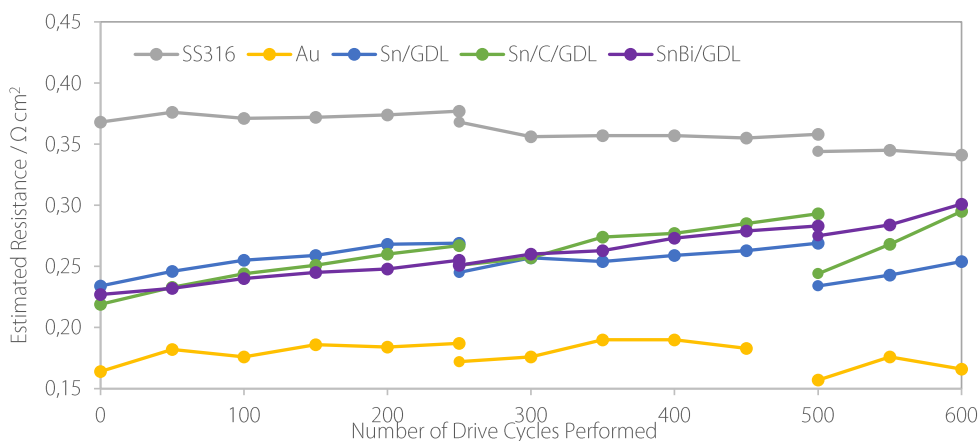


Figure 9.3.7. The estimated resistance from the slope of the ohmic region of the polarisation curve for each cell plotted against the number of drive cycles performed.

First of all, it is worth pointing out that the calculated resistances are approximately 10 times higher than the ICR resistances measured *ex-situ* of the BPPs shown in Figure 9.2.1 (anode side) and Figure 9.2.3 (cathode side). While the *ex-situ* ICR is measured to a combined value between 15 and 45  $\text{m}\Omega \text{ cm}^{-2}$  (Figure 9.3.8) the estimated resistances from the polarization curves ranges from about 160 (Au) to 370  $\text{m}\Omega \text{ cm}^{-2}$  (SS316) (Figure 9.3.7). This is because the resistances estimated from the polarisation curves include all other resistance contributions of the fuel cell, including the membrane, catalyst layers, cell housing and wiring.

Despite this discrepancy, the trend of resistances estimated from the slope of the polarisation curve agrees with the *ex-situ* ICR and the cell voltages in the ohmic region, both before and at the end of the cycling procedure. The Au plates having the lowest resistance and the SS the highest. However, the trends for each individual set of BPPs do not necessarily agree before and after cycling. From the *ex-situ* ICR measurements at the cathode side (Figure 9.2.3) we see that all BPPs have increased their contact resistance after 600 cycles. In fact, while the Sn-based BPPs showed an increase in their estimated *in-situ* resistance values over the duration of the measurements, these resistance values were surprisingly slightly reduced for both the Au and SS BPPs. This is hard to explain and to fully understand this, more in-depth analysis is needed. However, this could be due to the impact the Sn-based BPP would have on the flow field channel geometry, potentially influencing the gas distribution and water management reducing fuel cell performance to a greater extent than the case would be for the smoother Au coated and SS BPPs. Some variation may also be attributed to the change in the surface of the BPPs that occurs when they are removed from the fuel cell and exposed to the atmosphere to perform the *ex-situ* ICR test.

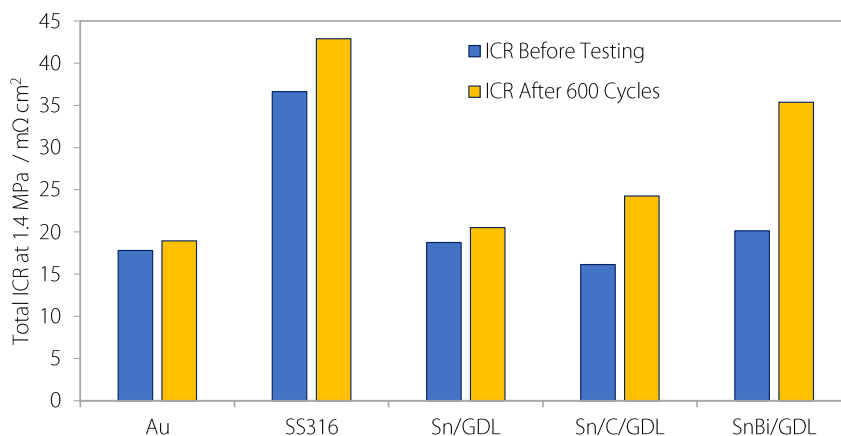


Figure 9.3.8. The total ICR from the anode and cathode side bipolar plates for each cell, before (blue) and after (yellow) operation.

For the Au coated plates, which are fairly stable in PEM conditions, the surface is not suspected to corrode heavily within the fuel cell, although some removal of the Au coating may occur leading to some exposure of the underlying substrate (see section 9.2.1). When stainless steel is actively corroding, in particular during acidic conditions, an associated reduction in the *in-situ* ICR can be observed (e.g. [44]). However, any significant reduction or removal of the surface oxide is not expected during ordinary fuel cell operation, although shutdown and start-up conditions evidently influences the estimated *in-situ* resistance perhaps due to removal of surface oxide. It should be noted that although

the estimated *in-situ* resistances decreased slightly during operation for Au-coated and stainless steel bipolar plates, the overall cell performance still decreased for both BPPs due to degradation of other cell components.

As already mentioned, there is a steady increase in the estimated *in-situ* resistance as the number of cycles increases for all Sn-based BPPs. This could be due to oxidation of the Sn surface, which eventually produces SnO<sub>2</sub> with a higher resistance than metallic Sn, or delamination with the GDL due to dissolution of the oxide before complete oxidation of the surface is reached (see chapter 4). It was hoped that the addition of carbon or bismuth to the tin would reduce the degradation of the surface, hence maintain a low ICR and increase the longevity of the bipolar plate. However, it seems that both additions have increased the rate at which the resistance increases. Deterioration of the Sn/C/GDL ICR is likely because any Sn oxidation that occurs on the surface would break contact between the carbon and the metallic Sn, having a large negative impact on conductivity. This is not a problem for the Sn/GDL BPP (without carbon), since the Sn would penetrate deeply into the GDL securing superior contact, therefore dissolution of the top layer of Sn does not affect the total conductivity as much. For the SnBi/GDL BPP, the rate of conductivity increase is low, but the usual improvement in performance seen after shutdown is much smaller for the second shutdown than for the other BPPs. As the temperature and humidity varies during the shutdown and start-up process, the expansion and contraction can make contact between the BPP and GDL worse, so although the MEA recovers performance after the shutdown, the BPP is heavily degraded, leading to poor performance recovery and a high *ex-situ* ICR.

From the estimated resistances, we can say that the Au BPP obtained the best performance, as expected, and the Sn/GDL did not degrade as much as the other Sn-based BPPs. The SnBi BPP was performing well until the second shutdown. Further optimization of the hot pressing equipment and procedure for large bipolar plates, in particular for the SnBi/GDL BPPs, are needed to obtain more reproducible *in-situ* measurements and to determine the longevity of such plates, preferably including more shutdown and start-up cycles.

## 9.4. Electrochemical Impedance Spectroscopy

Electrochemical impedance spectroscopy (EIS) is a versatile technique that can be used *in-situ* as a diagnostic tool for fuel cell performance [280]. The high frequency intercept of the impedance curve with the real axis shows the ohmic resistance of the fuel cell [111], commonly referred to as the high frequency resistance (HFR), and is typically collected from visual inspection of either a Nyquist or Bode plot. However, the actual real axis intercept may be influenced by high frequency artefacts, leading to erroneous readings and fitting to an appropriate equivalent circuit or other measurement strategies are often recommended.

In this work, the impedance spectra typically showed two arcs, one at low frequencies and one at higher frequencies. In PEMFC these arcs are often ascribed to the cathode (oxygen reduction reaction) and associated to charge transfer (high frequency) and mass transport (low frequency) [280]. The existence of a 45° slope towards the high frequency intercept is suggested to be related to the coupling between

double layer charging effects and proton transport within the porous catalyst layer [8]. This can be modelled as a one-dimensional transmission line [281]. In addition, a blocking or inductive behaviour was found at the highest frequencies in some of the spectra, making it difficult to read of the HFR values. This behaviour was observed for frequencies higher than about 4 kHz, which can be considered to be above the highest characteristic frequencies in the spectrum, of the electron and proton transport [282,283]. Additionally, this feature is quite random, implying that it is most likely not a result of fuel cell processes, but instead stray conductance in the connecting cables.

Here, it was found that an LR(QR)(QR) circuit was needed to fit the data, where the two arcs are represented by the QR parallel combinations (the second representing the low frequency arc), the HFR as the first resistor and where the inductive or capacity high frequency behaviour was fitted by adding an inductor (L) in series. An inductor was added for simplicity in both cases, with a negative value in the latter case. Zsimpwin with modulus weighting was used to fit the impedance data. For the SnBi and SS plates, good fits to this circuit were not possible without discarding datapoints above 4 kHz. Good fits were obtained when double layer capacitance were modelled using constant phase elements (CPE, admittance  $Q(i\omega)^\alpha$ ) rather than capacitors. The fitted parameters are summarized in Table 9.4.1 for the impedance spectra recorded initially and at the end during the *in-situ* testing and presented graphically in the respective Nyquist plots along with the experimental data.

Table 9.4.1. The fitted parameters for the impedance spectra of each fuel cell, initially and after 600 cycles.

	HFR / mΩ cm <sup>2</sup>	R1 / mΩ cm <sup>2</sup>	Q1 / mF cm <sup>-2</sup>	α1	R2 / mΩ cm <sup>2</sup>	Q2 / mF cm <sup>-2</sup>	α2 <sup>1</sup>	L / mH
Sn initial	112 ±0.8	179 ±9	132 ±16	0.59 ±0.02	43 ±10	1.1E3 ±1.8E2	1.0 ±0.1	-1.5E-4 ±5E-6
Sn final	85 ±1.1	190 ±14	163 ±27	0.56 ±0.02	31 ±15	1.6E3 ±5.7E2	1.0 ±0.2	-1.5E-4 ±6E-6
SnBi initial <sup>2</sup>	106 ±1.8	169 ±10	99 ±16	0.63 ±0.02	47 ±10	925 ±146	1.0 ±0.01	6.9E-5 ±5.1E-5
SnBi final <sup>2</sup>	94 ±3.1	183 ±13	174 ±35	0.55 ±0.03	49 ±7.5	(899) <sup>2</sup> (±207)	(1.0) <sup>2</sup>	9.2E-5 ±7.2E-5
SS initial <sup>2</sup>	240 ±3.5	127 ±15	74 ±26	0.68 ±0.05	45 ±13	600 ±132	1.0 ±0.01	2.5E-4 ±1.1E-4
SS final <sup>2</sup>	186 ±2.9	138 ±16	83 ±26	0.69 ±0.48	50 ±15	747 ±179	1.0 ±0.015	3.8E-4 ±1.0E-4
Au initial	52.8 ±0.5	147 ±11	176 ±22	0.63 ±0.02	86 ±14	575 ±63	1.0 ±0.01	-1.8E-4 ±4E-6
Au final	47.1 ±0.5	164 ±18	204 ±28	0.63 ±0.02	141 ±22	430 ±43	1.0 ±0.01	-1.9E-4 ±4E-6

<sup>1</sup> In most cases, converging fits with reasonable values were only obtained with two QRs although the second CPE exponent ( $\alpha_2$ ) indicates an equal fit with a pure capacitor instead.

<sup>2</sup> Fitted to an LR(QR)(CR) circuit.

The development of the high frequency resistance is of interest in this work, and this value was assumed to be similar to the real part of the impedance at 1 kHz. Figure 9.4.1 plots the real part of impedance at 1 kHz recorded for every 50 drive cycles. Unfortunately, the impedance spectra for the Sn/C/GDL cell is not reported here due to a measurement error.

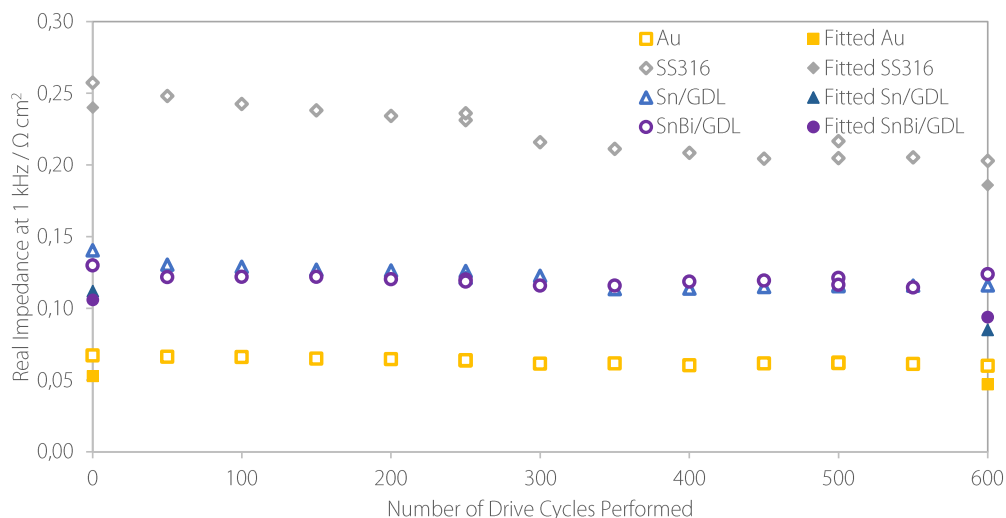


Figure 9.4.1. The real impedance of each fuel cell at 1 kHz, plotted over cycle number (unfilled shaped). The fitted HFR at 0 and 600 cycles (filled shapes) is also plotted for comparison.

Firstly, it should be noted that the real impedance at 1 kHz corresponds reasonably well with the fitted HFR. The HFR is lower than the real impedance at 1 kHz, which is expected, but the trends from before to after the cycling procedure are consistent in both analyses.

It can be seen from Figure 9.4.1 that for all of the fuel cells, the high frequency resistance either decreased or barely changed over the lifetime of the cell. This is in contrast to what we see from the *ex-situ* ICR, where all the pairs of bipolar plates increased their contact resistance after cycling and removal from the fuel cell. However, from the slope of the polarisation curves and now the EIS, it is clear that the total fuel cell, including all components, undergoes a much smaller change in total ohmic resistance than the *ex-situ* ICR implies. Furthermore, it is known that changes in the HFR are indicative that the membrane is changing resistivity due to differing levels of hydration [110]. Therefore, this process is offsetting the increasing contact resistance from the BPPs and is difficult to quantify.

In order to observe any changes in the resistance of the other components, the impedance spectra of each fuel cell can be analysed. The spectra taken initially and after 200 hours of cycling procedure are shown in Figure 9.4.2 to Figure 9.4.5 with the fitted parameters summarized in Table 9.4.1.

For the Au fuel cell, Figure 9.4.2, the change in the ohmic region (high frequency) of the impedance spectrum is minimal from before cycling (blue, HFR =  $52.8 \pm 0.5 \text{ m}\Omega \text{ cm}^2$ ) to after 600 cycles have been performed (yellow, HFR =  $47.1 \pm 0.5 \text{ m}\Omega \text{ cm}^2$ ). However, the activation losses that can be related to the charge transfer resistance ( $R_1$ ) on the cathode side increased slightly (from  $147 \pm 11$  to  $164 \pm 18 \text{ m}\Omega \text{ cm}^2$ ), while the low frequency resistance associated with mass transport resistance [110] almost doubled, from  $86 \pm 14$  to  $141 \pm 22 \text{ m}\Omega \text{ cm}^2$ . Therefore, the impedance data for the gold coated bipolar plate indicates a small decrease in ohmic resistance ( $R_s$ ) but an increase in the charge transfer resistance ( $R_1$ ) and a larger increase in the mass transport resistance ( $R_2$ ) over 600 cycles, which correlates well with the performance of the fuel cell based on the polarisation curves and *ex-situ* ICR.

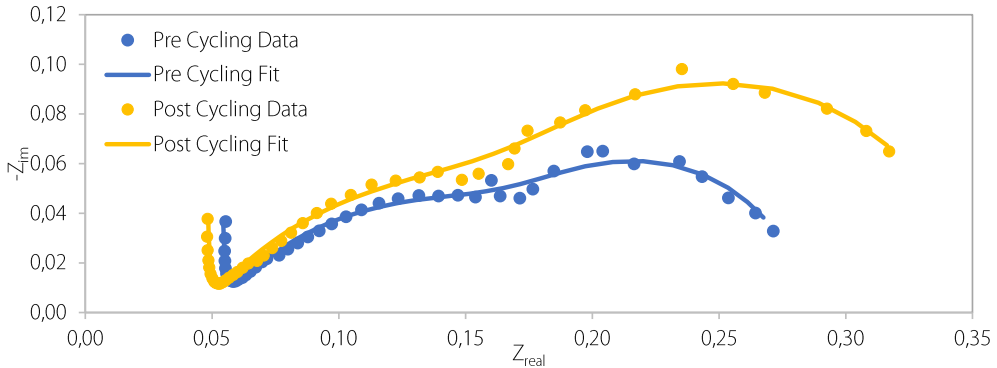


Figure 9.4.2. Nyquist plots showing the measured and fitted impedance of the gold coated BPP fuel cell before (blue) and after (yellow) 600 drive cycles.

Of all the BPPs investigated, the fuel cell with the Au coated BPP showed the lowest HFR change, but is the only one that showed such a significant increase in mass transport resistance. This has been shown to indicate poor transport of oxygen to the electrode surface [110], and particularly blockage of the flow channels by flooding [284], which could be due to changes in surface hydrophobicity of the BPPs, or over compression of the GDL.

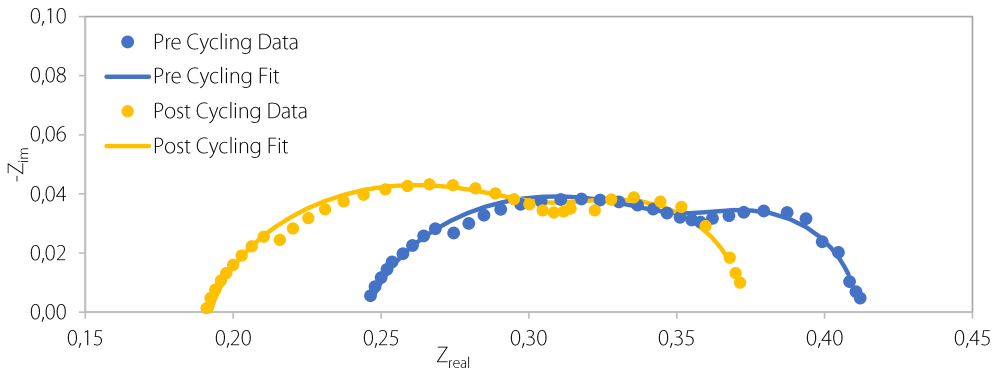


Figure 9.4.3. Nyquist plots showing the measured and fitted impedance of the stainless steel fuel cell before (blue) and after (yellow) 600 drive cycles.

For the stainless steel BPP fuel cell, the size of each of the features on the impedance spectrum, shown in Figure 9.4.3 and summarized in Table 1, remains similar from before ( $R1 = 127 \pm 15 \text{ m}\Omega \text{ cm}^2$ ,  $R2 = 45 \pm 13 \text{ m}\Omega \text{ cm}^2$ ) to after cycling ( $R1 = 138 \pm 16 \text{ m}\Omega \text{ cm}^2$ ,  $R2 = 50 \pm 15 \text{ m}\Omega \text{ cm}^2$ ). The main difference is that the whole Nyquist plot is translated along the real axis to more negative values after cycling, implying that there has been a quite large reduction in the ohmic resistance of this fuel cell (from  $\text{HFR} = 240 \pm 4$  to  $186 \pm 3 \text{ m}\Omega \text{ cm}^2$ ), but not much else changed. Here, a large decrease in ohmic resistance when correlated with the poor performance observed from the polarisation curves shows that the cell may be flooding [110,285]. Again, the slight increase in the measured contact resistance from the stainless steel bipolar plates may be offsetting some of the decreased resistance in the membrane, but this is difficult to determine from the impedance spectrum alone. It is also unclear why the flooding in this case effects the membrane resistance but has no impact on the mass transport of oxygen to the electrode surface at the cathode, as seen for the fuel cell with the gold coated BPPs.

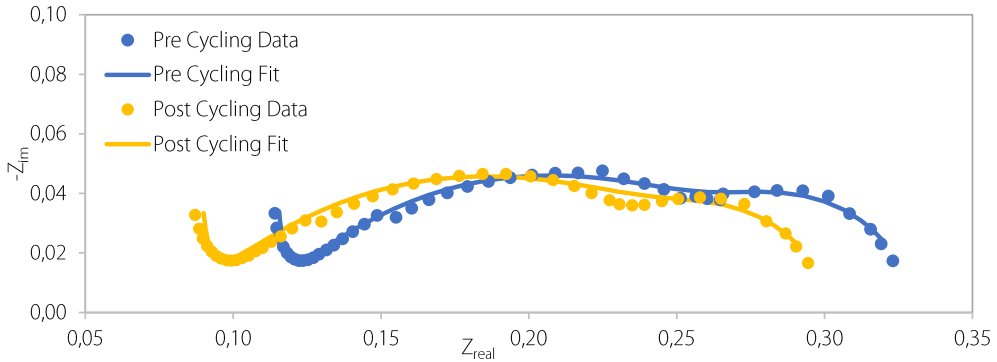


Figure 9.4.4. Nyquist plots showing the measured and fitted impedance of the Sn/GDL fuel cell before (blue) and after (yellow) 600 drive cycles.

The Sn/GDL fuel cell, Figure 9.4.4, has also undergone a similar negative shift of the Nyquist plot to lower real impedance values, indicating that the ohmic resistance has decreased (from  $112 \pm 1$  to  $85 \pm 1$   $\text{m}\Omega \text{ cm}^2$ ), although not as much as the stainless steel fuel cell. This again may be an indication of increased membrane hydration, but without the increased mass transport resistance. In fact, an apparent decrease in mass transport resistance was observed for the Sn/GDL fuel cell from  $43 \pm 10$  to  $31 \pm 15$   $\text{m}\Omega \text{ cm}^2$ , although within the errors of the fits. The other features of the impedance spectra remained similar, so the main change that occurred in the cell was a decrease in ohmic resistance.

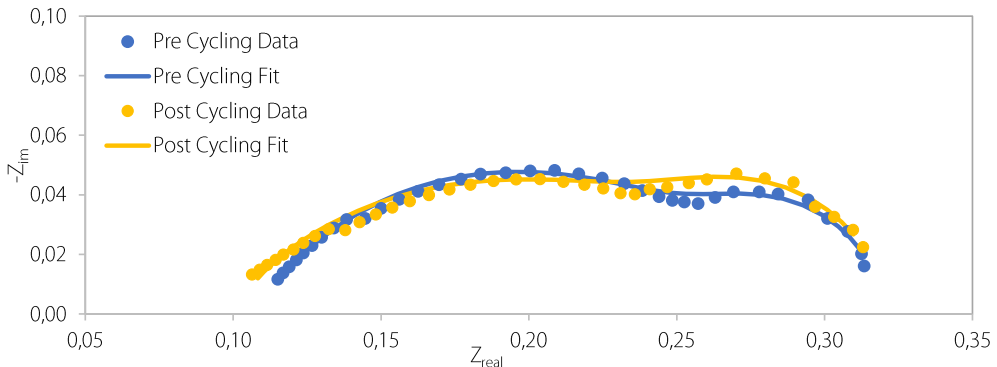


Figure 9.4.5. Nyquist plots showing the measured and fitted impedance of the SnBi/GDL fuel cell before (blue) and after (yellow) 600 drive cycles.

Finally, the SnBi/GDL cell did also experience a change in impedance after cycling, as seen in the spectra in Figure 9.4.5. The ohmic resistance was again decreased slightly (from  $106 \pm 2$  to  $94 \pm 3$   $\text{m}\Omega \text{ cm}^2$ ), presumably due to increased hydration of the membrane. In this case a small increase in the activation loss may be seen, reflected in the increase charge transfer resistance (from  $169 \pm 10$  to  $183 \pm 13$   $\text{m}\Omega \text{ cm}^2$ ) although within the error margins of the fits. If there was some catalyst degradation from e.g. corrosion of the carbon support, it would explain the increased activation resistance and poorer overall performance, and particularly the poor performance recovery seen after the second shutdown.

In conclusion, the impedance spectra give us more information about the different processes happening within the fuel cell, and in many of the cells, we see that the main process occurring is in fact a decrease in ohmic resistance. From the *ex-situ* ICR we can determine that this is not coming from the

BPP, and most likely it is a result of an altered conductivity of the membrane as a consequence of changing water content.

## 9.5. Post-mortem Analysis

Post-mortem analysis of the fuel cells was performed after the cycling procedure finished. As reported in chapter 8.2.1, *ex-situ* ICR of the BPP is performed and compared against the same measurement that was taken before cycling. This provides important information about the performance of the bipolar plate, and how much an altered resistance could affect the cell-voltage. However, the bipolar plate can also damage the MEA through the leaching of metal ions from degradation mechanisms. In order to determine whether this happened during the drive cycle procedure, EDS mapping of the cathode side of each MEA was performed to identify any metal ions from the BPP that may have entered the membrane.

The SEM and EDS images in Figure 9.5.1 show a section of the MEA, which consists of a platinum catalyst supported on carbon, and the Nafion membrane, a sulfonated polymer based on PTFE. The membrane is the source of some of the carbon observed in the EDS, as well as the sulfur, oxygen and fluorine.

Although there are no unexpected metal ions from the BPPs visible from the EDS analysis in Figure 9.5.1 and Table 9.5.1, it is difficult to conclude whether there is leaching of metal ions into the membrane. This is a well known phenomenon for stainless steel bipolar plates [87], so the absence of any Fe or Cr ions in the membrane of the stainless steel fuel cell can imply that the *in-situ* accelerated stress tests were not performed for long enough to observe ion leaching and absorption into the membrane. It should also be noted that the EDS technique is not very accurate for concentrations of less than 1 %, even of the heavier elements [286], so there could be some ions in the membrane that are not visible using this analysis method. A technique such as ICP-MS which fully decomposes the sample into its constituent elements, and then analyses them using mass spectroscopy [287] could be used in the future. ICP-MS has been used to accuracies of much less than 1 %, however it completely destroys the sample so no further analysis can be done [287].

Table 9.5.1. The EDS analysis of each MEA from the various fuel cells, showing the elemental composition.

Sample	Element / %								
	C	Pt	S	O	F	Fe	Au	Sn	Bi
Au	47	36	1	3	12	0	0	0	0
SS	48	38	1	3	11	0	0	0	0
Sn	47	34	1	3	15	0	0	0	0
SnBi	42	45	0	2	10	0	0	0	0
Sn/C	46	34	1	4	15	0	0	0	0

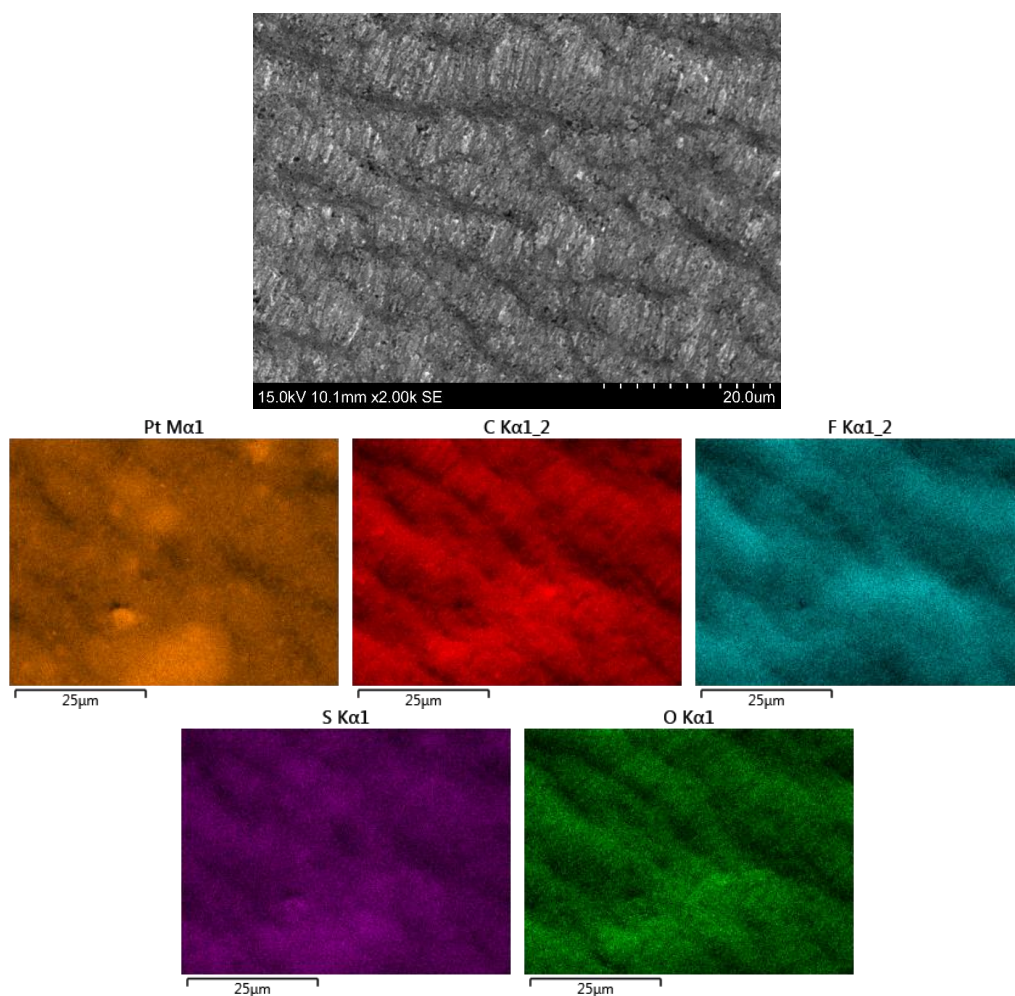


Figure 9.5.1. A SEM image of the MEA from the Stainless Steel fuel cell (top), with EDS analysis of the area to show the distribution of platinum (orange), carbon (red) fluorine (teal), sulfur (purple) and oxygen (green).

Despite this inaccuracy in the EDS measurement, there is also no evidence of any ion leaching from the Sn, SnBi, or Sn/C BPPs. Therefore, it can be concluded that they have a similar (or at least not worse) stability to the stainless steel BPPs. Interestingly, the MEA analysis shows that the SnBi sample is slightly depleted in carbon but enriched in platinum compared to the others. This implies that there has been some removal of the carbon support during the cycling procedure, which is likely the reason for the poor performance of this BPP after the second shutdown procedure.

In order to conclusively determine whether the leaching of metal ions into the membrane is a problem for the Sn/GDL type of BPPs, longer *in-situ* testing and a more accurate analysis method should be employed.

## 9.6. Conclusions

From these *in-situ* results, it can be concluded that the Au coated BPP fuel cell had the best overall performance, but it also had a very high degradation rate. This can be attributed to an increased mass transport resistance. The Sn based BPP fuel cells performed very similar to each other, with small variations in degradation rates. The Sn BPP performed best of the three, with the best performance after 600 cycles, and the smallest increase in ICR. SnBi looked initially very promising but had a poor recovery after the second shutdown likely due to corrosion of the carbon catalyst support. The Sn/C BPP also performed poorly, with a large increase in ICR and a larger performance degradation due to delamination of the carbon from the Sn/GDL interface, breaking conduction pathways. The stainless steel BPP fuel cell performed worst overall but had a very low degradation rate due to a large decrease in the ohmic resistance of the cell during cycling.

Post-mortem analysis of the MEA for each fuel cell did not reveal any ion leaching. However, using a more accurate analysis technique such as ICP-MS, or testing the samples for a much longer time would provide more information as to whether the ions do in fact eventually leech into the MEA and cause damage.

The overall increase in the *ex-situ* ICR of the bipolar plates, which is around  $15 \text{ m}\Omega \text{ cm}^{-2}$  for the worst performing SnBi BPP fuel cell, led to the maximum observed performance decrease of 15 mV at  $1 \text{ A cm}^{-2}$ . The corresponding average reduction in performance from cycle 0 to cycle 600 for each fuel cell was 90 mV at the same current density. Based on this, it can be concluded that an increased ICR at the bipolar plate / GDL interface plays only a small role in the total performance degradation.

In summary, although *in-situ* testing is a long process, it provides valuable information about the continued performance of the bipolar plates. In the future, the *in-situ* ICR analysis technique would be valuable to use in order to separate out and monitor the resistance of the individual components more easily. Finally, for more conclusive results about the performance of the Sn-based BPPs as compared to the Au, it is suggested to optimise hot pressing procedures to further investigate the SnBi BPP as it has the most potential.

# 10

## The feasibility of Sn/GDL BPPs on an industrial scale

### 10.1. Introduction

During the 2017 Bipolar Plate workshop, organised by the U.S. Department of Energy and Argonne National Laboratory, participants from industry, government agencies, universities and national laboratories with expertise in the field of bipolar plates for PEM Fuel Cells gathered. In a report summarising the workshop [9], a number of research and development needs were identified for metallic bipolar plate materials. These needs are crucial in order to meet the cost and performance targets set for bipolar plates for the automotive industry by the US Department of Energy [30]. The most notable challenges in this field are meeting the high annual production rates needed for mass-production of fuel cell systems and doing so at a low cost. Therefore, new materials and coatings for bipolar plates that are cheap and easily manufactured are crucial to the future of PEM Fuel Cells in transport applications.

In this chapter, the novel Sn/GDL bipolar plates that have been developed throughout this thesis are evaluated against the identified needs for bipolar plates, in order to determine their feasibility on an industrial scale.

### 10.2. Requirements for robust coating materials

A summary of the identified needs for robust coating materials are [9]:

1. The coating material and method must enable pre-forming deposition and mitigate coating defects, such as cracks and delamination, during the stamping process.
2. The coating must provide self-protection from corrosion/degradation at coating defect areas.
3. The coating must provide chemical stability, particularly the mitigation of leaching of metal ions which are harmful for other components, e.g. the membrane.
4. The elimination of PGMs or precious metals.
5. The coating method must be amenable to high-throughput manufacturing and joining processes.
6. The cost for each plate must be under \$3 / kW.

Although these targets are not official, they constitute an informed opinion on the limitations of current bipolar plates, and what is needed to overcome such limitations.

Looking at each of the identified needs, they can be divided broadly into three groups designed to increase the durability (targets 2 and 3), decrease the cost (targets 4 and 6) and improve manufacturability of bipolar plates (targets 1 and 5).

### 10.2.1. Durability

The durability of the bipolar plate is crucial for use in large scale transport applications. Busses, for which PEMFCs are used today, require operation lifetimes of over 25 000 hours. By the end of 2018, a number of fuel cell busses in operation in the USA had reached over 20 000 operational hours without stack replacement [288]. For smaller scale transport in personal vehicles, the US DoE has identified the need for over 8 000 hours of fuel cell operation with less than 10 % performance degradation in order for PEM systems to be commercially competitive [289].

Common failure mechanisms of the PEMFC include membrane degradation from either physical damage e.g. holes, which can be caused by heat/water build-up, or leaching of metal ions into the membrane from the BPP or catalyst layers. The metal ions can interact with membrane constituents forming radicals and destroying the polymer chains [87]. In perfluorosulfonic acid-type ionomer membranes (e.g. Nafion®) metal ions can also attach to x sulphonic acid groups (where the metal ion is  $M^{x+}$ ), leaving fewer groups for the  $H^+$  ions to attach to and therefore lower the proton conductivity of the membrane and hence the fuel cell performance [49]. If either of these things happen, the membrane must be replaced, and the cell lifetime is shortened. Therefore, bipolar plates that do not leech metal ions are required.

Common metallic bipolar plate substrates such as stainless steel and aluminium will build up a surface oxide layer with low conductivity and potentially leech metal ions over time, so a coating is required to meet durability targets [51]. This coating should form a barrier between the substrate and electrolyte, and if the coating is damaged, the underlying metal will be exposed, and corrosion can occur. Thereby, as target 2 states, any coating on the bipolar plate should either have a self-healing property or provide cathodic protection of the bipolar plate material to prevent the leaching of unwanted metal ions.

Although self-healing coatings are being developed, they are often organic and have high contact resistances, or are not truly self-healing as they must be activated by an external trigger [290–292]. Therefore, cathodic protection is preferred for metallic coatings on bipolar plates. This means that if the coating is damaged and the underlying substrate is exposed, the coating material will be in galvanic contact with the substrate and should preferentially corrode, acting as a sacrificial anode. As the coating material is of much greater area than the exposed BPP, the amount of coating that is corroded will be small overall, and the corrosion products can block the exposed substrate and stop any further corrosion. This process is visualised in Figure 10.2.1.

If the coating is cathodic in relation to the substrate, then the substrate will preferentially corrode. This may lead to the release of metal ions, further corrosion of the BPP under the coating surface and possible pitting corrosion that can completely penetrate the BPP, leading to gas crossover, leaking of coolant and other problems.

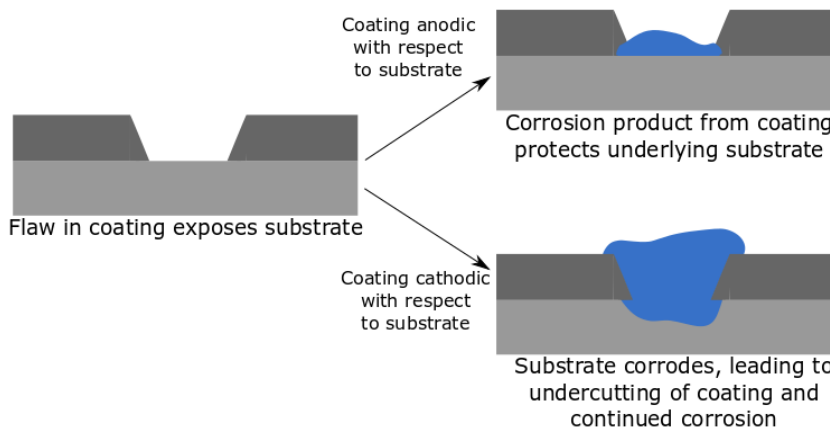


Figure 10.2.1. The two possible corrosion processes when the substrate is exposed. If the coating is anodic with respect to the substrate, the coating will start to corrode, producing a corrosion product that passivates the surface. If the coating is cathodic with respect to the substrate, the coating will not corrode, but the substrate will begin to corrode underneath the coating, producing a large amount of corrosion products and deep pits.

The corrosion product formed upon breaking of the coating does not necessarily need to be conductive, as long as there is sufficient coating remaining to provide good electron transport. The most important factor is that the exposed coating should be passivated.

The second target relating to BPP durability is target 3, which states that the coating must provide chemical stability, particularly the mitigation of leaching of metal ions which are harmful for other components, e.g. the membrane. If the coating is anodic in relation to the substrate, then the leaching of metal ions from the substrate should ideally not occur. Therefore, as long as the coating itself does not leech any harmful metal ions, this target should be fulfilled.

## 10.2.2. Cost

One of the reasons why PEMFCs are not widely prevalent today is that they are expensive compared to traditional combustion engines, and targets 4 and 6 set out requirements to reduce this cost. Bipolar plates account for between 18 % and 28 % of the cost of the PEMFC stack, depending on the scale of production [56], so by reducing the cost of materials and production of BPPs, the overall fuel cell stack cost can be vastly reduced.

A 2017 report from Strategic Analysis inc. showed that the current BPP target of 3 \$ / kW for bipolar plates in 2020 [30] are not being met. The stainless steel substrate alone, which contributes to 54 % of the BPP cost (29 % of the cost is from the stamping and manufacturing process, and 17 % is from the TreadStone DOTS-R coating [293]), leads to a cost of 2.9 USD / kW if 500 thousand systems are manufactured a year [294]. In order to reduce costs, the report suggested moving to a substrate of 304 stainless steel instead of 316, which would produce a cost saving of 0.30 USD / kW, but in order to make further cost savings, the performance of the stack should be improved. Therefore, the cost and durability targets are linked.

The coating can contribute significantly to the cost of the bipolar plate. Although platinum group metals (PGMs) provide corrosion resistant and highly conductive coatings for BPPs, they are extremely

expensive. Additionally, the environmental considerations of extracting and refining such metals cannot be ignored. For each kilogram of platinum group metal extracted in South Africa, there is an energy consumption of over 200 GJ, water consumption of around 400 m<sup>3</sup>, and CO<sub>2</sub> emissions of over 40 tonnes [295]. Therefore, for both cost and ethical reasons, PGMs should be avoided.

### 10.2.3. Manufacturability

Targets 1 and 5 address the need for bipolar plates that are manufactured in a time- and cost efficient manner. In general, metallic bipolar plates are produced from large sheets of metal, which are then stamped or etched to form a flow field before they are cut into a bipolar plate shape. These two processes can be done in any order, but it is favourable to form the flow field before cutting, as it takes more time and manufacturing to form a flow field on each individual cut bipolar plate [82]. Therefore, forming first is cheaper and quicker, both of which are extremely important if mass production of PEMFCs is to be realised.

In the same way, it is much easier to coat a large sheet of material, and then form bipolar plates from it, compared to coating each individual bipolar plate after it has already been formed. Therefore, any coating process and material must be able to withstand the mechanical forces of the forming and cutting process without causing irreversible damage and defects that affect the performance of the BPP. This is outlined in target 1, which states that the coating material and method must enable pre-forming deposition and mitigate coating defects, such as cracks and delamination, during the stamping process.

Target 5 addresses the joining process that occurs when each individual cell is joined to form a fuel cell stack. During this process, sets of two individual coated plates must be welded together to form a combined BPP that acts as the cathode on one side facing one MEA and anode on the other side, facing an adjacent MEA. Given the electron transfer through the BPP, the welding process must not unduly increase the contact resistance, meaning it is often time-consuming and therefore costly. Target 5 then states that the coating method for any bipolar plate must be amenable to high-throughput manufacturing and joining processes, meaning it should not be easily damaged by the joining process.

This stamping/welding process has been identified as the most efficient method, and is anticipated to be used for stack manufacture for the next generations [294], therefore durable BPPs that can withstand this processing are crucial.

## 10.3. Meeting the requirements for robust coating materials

In this section the Sn/GDL system is evaluated with respect to the criteria explained above, in order to determine whether it would provide a durable, cost-effective and easily manufacturable BPP for use in the future generations of PEM fuel cells.

## 10.3.1. Durability

### Self-protection in coating defect areas

As identified earlier, for a coating to self-protect in defect areas, it should be anodic with respect to the substrate. The galvanic potential of SS316 can vary depending on whether the steel is active or passive, so the exact value, and the relation to tin depends on the environment that it is in and the pre-treatment of the steel. In both 0.1 M citric acid [198] and 0.1 M NaCl [296] the presence of oxygen has been found to determine whether tin is anodic or cathodic with respect to the carbon steel substrate. In both cases, the tin coating is anodic to steel and therefore protective in deaerated solutions, but not in the presence of oxygen, where the electrolyte moves through the tin and corrodes the underlying substrate.

The high alloy SS 316 steel is significantly more cathodic than both carbon steel and tin when it is in a passive environment [297], and in this case the Sn will form a good protective layer. However, when in the presence of acidic or chloride containing media, the SS 316 becomes active, and its galvanic potential is significantly more anodic [297]. Under these conditions, the galvanic potential of SS 316 can in some cases become more anodic than that of Sn and the layer will no longer be protective. Therefore, it is difficult to accurately predict whether the coating will be of a protective nature if any defects form.

The addition of Bi to the Sn/GDL system would not help the self-protection mechanism, as Bi is more noble than Sn, and may potentially lead to more corrosion of the SS316 substrate. However, indium would have the opposite effect and would likely lead to better self-protection.

### Chemical stability and mitigation of metal leaching

In order to determine whether the BPPs tested in this work exhibit good stability, and mitigate the leaching of metal ions, post-mortem analysis of the cells that had been cycled *in-situ* was performed. After 200 hours of *in-situ* operation, each cell was disassembled and the membrane electrode assembly (MEA) was analysed to determine the metal content. Any metal ions from the bipolar plate that enter the membrane during operation can be identified using SEM imaging with EDS analysis, and it can be determined whether contamination and damage to the membrane is occurring.

From the EDS analysis shown in Chapter 8 of this thesis, no metal ions were found in the membranes of any of the samples, indicating that the leaching of metal ions from the Sn-based BPPs is not a problem. Given the reduced accuracy of the EDS method at low concentrations, leaching cannot be completely excluded. However, there were no visible signs of corrosion on the stainless steel bipolar plate. Leaching of metal ions from stainless steel bipolar plates has been previously documented after long term *in-situ* operation [87,298], so the lack of ions could be due to an insufficient exposure time to the PEM conditions. Therefore, it cannot conclusively be said whether leaching of Sn ions into the membrane is a problem until a longer experiment is performed and a more accurate analysis method is used.

In general, if the leaching of metal ions does take place, it has been shown in the literature that Fe<sup>3+</sup> ions are detrimental to membrane performance, and that SS316 under operation in a fuel cell releases such ions, which contaminate the membrane [49,161]. It has been shown that Sn ions have little effect on

the performance of membrane materials [165], and that the presence of Sn oxides may in fact improve membrane performance [166–168]. Therefore, the chemical stability of the Sn BPPs should meet the required chemical stability targets.

### 10.3.2. Manufacturability

#### Pre-forming Coating

Target 1 states that in order to reduce processing cost and time, it is preferential to coat large sheets of substrate material with a protective coating before the stamping and cutting process. Any coating materials must therefore be able to withstand the stamping process, where a large amount of force is applied to the sheets, leaving the coating susceptible to cracking or delamination from the substrate.

Although the Sn coating is liable to crack during the stamping process, the fact that it should be hot pressed with the GDL after forming means that any cracks could theoretically be healed by the melting process. Even if there are cracks in the coating, the addition of the GDL to the land areas does not necessarily require a 100 % tin coverage. As long as the Sn coating is adhered to the substrate, the GDL should successfully hot press and form the Sn/GDL soldered BPP.

Although access to stamping machines is difficult, the process can be simulated by bending the Sn-coated substrate, and then exposing any cracks to the hot pressing temperature to determine how the coating reacts. A Sn layer of 30  $\mu\text{m}$  thickness was deposited onto a SS 316 substrate, as reported in Chapter 3 of this work. The substrate was bent at an angle of  $90^\circ$  to simulate the formation of a vertical channel wall, and then flattened again to allow hot pressing to take place. Ideally, the GDL should be in place for this, however that would obscure the substrate so was removed for this experiment.

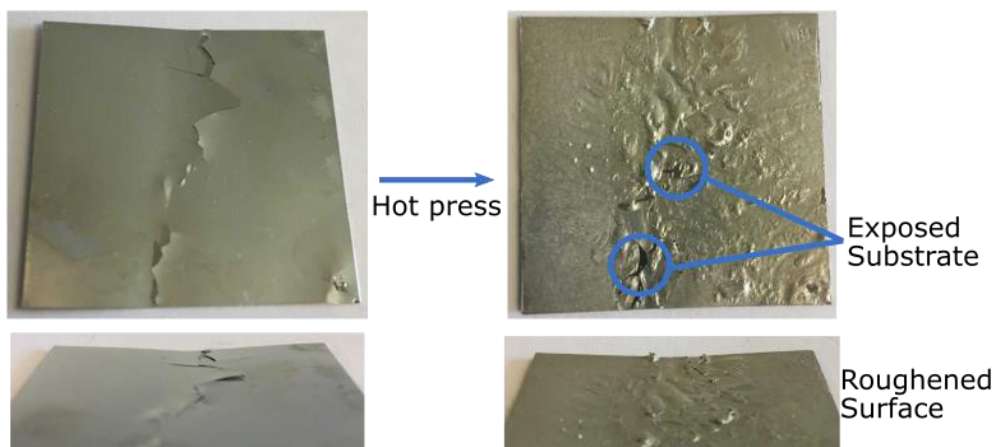


Figure 10.3.1. A series of photographs of a Sn-coated SS316 coupon, having been bent to crack the Sn surface, then hot pressed to repair the damage.

As can be seen from the images in Figure 10.3.1, after bending there is a visible crack in the Sn coating. This crack is somewhat repaired after the hot pressing process, however there is some underlying substrate visible and the crack has not completely healed. The small exposed areas should not impact the ICR, as good contact with the GDL will be secured through hot pressing of the majority of the Sn

surface. However, the presence of exposed substrate is unwanted as it can lead to the leaching of metal ions from the substrate and negative impacts on the fuel cell performance. It is difficult to say whether this would still form a functional Sn/GDL BPP without simulating the stamping process in a more realistic way.

In addition to stamping, the technique of laser etching can be used to form the flow fields in the bipolar plates. The process involves taking a single sheet of metal, and removing material using a laser to form a flow field structure. This is interesting for the Sn/GDL concept because electrodeposition onto flat sheets of metal is very simple, with fewer edge effects than deposition onto uneven structures such as BPPs.

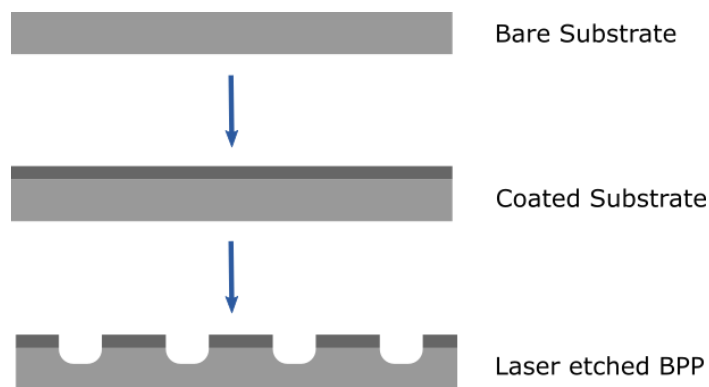


Figure 10.3.2. A diagram of a BPP fabricated by electrodeposition onto the bare substrate, followed by laser etching of the channels, which leaves the coating on the land area.

The laser etching process does not deform the substrate like the stamping process does, meaning that there will be no cracks in the coating or delamination from the substrate. The main downside of the laser etching process is the exposure of the BPP substrate in the channels, which may go on to leech ions into the membrane and cause other detrimental effects. Additionally, there is a large wastage of coating and substrate material, as the substrate must be thicker than the stamped BPPs, and a portion of it is removed during the etching process.

The Sn/GDL BPP could be amenable to the stamping or laser etching processes, however more experiments should be performed on a larger scale before the best forming method is found.

## High throughput manufacturing and joining methods

The Sn/GDL concept provides a fast and simple joining method to form the BPPs into a stack. There is only a one-step hot pressing process needed to form a unit cell with gas diffusion media, anodic and cathodic bipolar plates with a coolant channel in the centre, as outlined in Figure 10.3.3. The stack can then be assembled by simply layering these combined BPP/GDL sets with the MEAs. This removes many of the welding and assembly steps that are necessary for other bipolar plate materials, making it a quick (high throughput) and cheap method with the only equipment needed being a hot press. This technique would also work for both the stamped and laser etched BPPs, as long as there is Sn present on the land area of each bipolar plate to solder the GDL to the BPP.

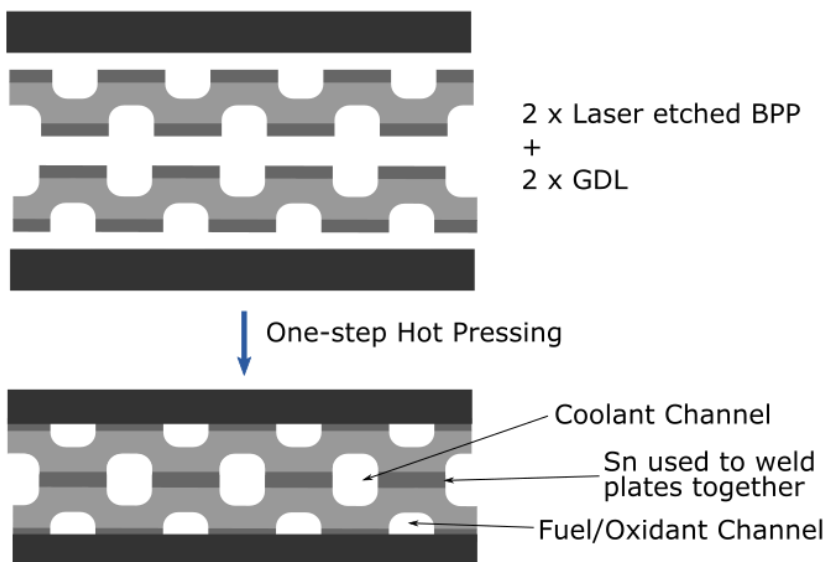


Figure 10.3.3. A summary of the one-step hot pressing procedure used to combine two BPPs and two GDLs to make a single BP/GDL unit that can be combined with a MEA into a fuel cell stack.

Although the success of this joining technique is hard to quantify on a large scale, we can determine whether it is effective on a lab-scale by comparing it with the BPPs we use for *in-situ* testing. These are mass produced by ElringKlinger and consist of a stamped flow field plate which is laser-welded onto a back plate. In this process, it is the laser welding that takes up most time as each weld must be individually made. Therefore, if the back plate can be reliably hot pressed to the flow field using Sn, it would make the process much cheaper and easier.

The one-step joining process was simulated by electroplating a thin (10  $\mu\text{m}$ ) layer of Sn onto the back plate, which was then hot pressed with a Sn coated flow field as described in Chapter 3 of this work, to form a complete BPP that can be used inside a fuel cell. The ICR of this plate was compared against a standard laser-welded plate with a Sn coating applied to it, Figure 10.3.4.

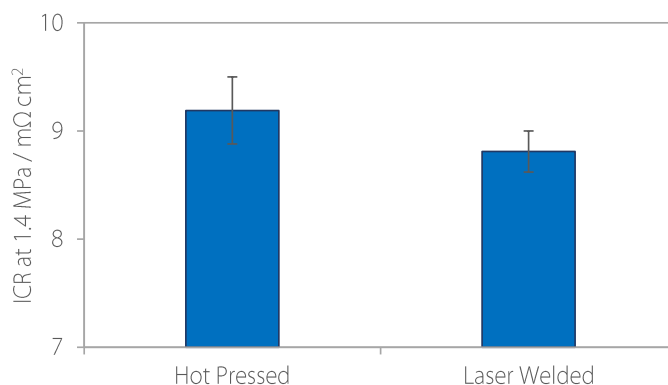


Figure 10.3.4. The ICR of a commercially prepared welded BPP and back plate, compared to a BPP electroplated with Sn and hot pressed to a back plate

Both samples show ICR values below the DoE recommendation of  $10 \Omega \text{ cm}^{-2}$ , implying that hot pressing is a technique that can be used to form bipolar plates in this way. The hot pressed sample has a slightly higher ICR than the laser welded sample,  $9.2 \pm 0.3 \Omega \text{ cm}^{-2}$  compared to  $8.8 \pm 0.2 \Omega \text{ cm}^{-2}$ . However, this is almost within the error margin, and with some optimisation of the Sn coating thickness and hot pressing procedure, the hot pressed BPP should perform as well as the laser welded BPP.

The Sn coated plates produced by this welding technique have not been tested *in-situ* under high pressures or for a prolonged amount of time. Additionally, the large-scale hot pressing has not been attempted in this work, but all of this would be interesting to look at in future work.

### 10.3.3. Reduced cost

Firstly, the Sn/GDL system does not contain PGMs in any of its iterations, fulfilling target 4. In this section, a basic cost analysis of the Sn/GDL concept has been performed to determine whether it meets the \$3/kW requirements set out in target 6. It should be noted that the technology is at a low TRL at this point, and thus not all factors can be included.

The Strategic Analysis report on the cost estimation of PEM Fuel Cell systems [294] is based on the use of 80 kW stacks containing 379 individual fuel cells, with two coated bipolar plates per cell. This leads to 758 bipolar plates in total, of which the 316 stainless steel substrate contributes 54 % of the cost. These bipolar plate substrates have a surface area of  $280 \text{ cm}^2$  [294], so in order to compare directly with the BPPs used in this thesis, we can calculate the cost of a similar  $50 \text{ cm}^2$  BPP substrate, at varying production volumes.

Table 10.3.1. A cost estimate of bipolar plates at varying production volumes, showing the cost for a complete stack of coated BPPs, then the individual BPP, the uncoated substrate, and a scaled  $50 \text{ cm}^2$  substrate, for comparison to the BPPs used in this thesis.

Systems each year	Stack BPP cost / \$	Individual BPP cost / \$	Substrate cost / \$	$50 \text{ cm}^2$ substrate cost / \$
1000	1 707	2.25	1.22	0.218
50 000	455	0.60	0.32	0.057
500 000	433	0.57	0.31	0.055

Even at the smallest production volume in Table 10.3.1, the number of bipolar plates produced is very high due to the hundreds of BPPs present in each stack. Given that the Sn/GDL system is not going to be mass-produced at anywhere near this scale, we can take the smallest volume of systems, and use the calculated substrate cost of 0.218 USD to determine how much each coated BPP used in this thesis would cost and compare them to the commercial BPP.

It is reported that the commercial TreadStone coating contributes 17 % of the total BPP cost [294], leading to a coating cost of 0.07 USD for a single  $50 \text{ cm}^2$  BPP. This is undoubtedly significantly lower than the actual cost of processing BPPs on the scale performed in this thesis. However, given how little we know about coating processes for the TreadStone or gold coated BPPs, the total cost of BPP production including all equipment, labour and chemicals is very difficult to estimate.

For the Gold-coated BPP, the cost of the gold layer can be calculated. Although fluctuating, the US Geological Survey values gold at a cost of around 39 USD / g [299]. The average thickness of a PVD coating is between 1 and 5  $\mu\text{m}$ , so if the coating is 1  $\mu\text{m}$  thick, this gives a volume of 0.005  $\text{cm}^3$  over a 50  $\text{cm}^2$  BPP. Therefore, the mass of this coating is 0.09 g, and the cost would be 3.76 USD. Again, the gold PVD targets and processing costs for coating the BPP are undoubtedly much higher, so this cost is a low estimate

For the Sn/GDL BPP, we can calculate the cost of the actual Sn material that is deposited onto the BPP. This is a 30  $\mu\text{m}$  thick layer over an area of 50  $\text{cm}^2$ , leading to a total volume of 0.15  $\text{cm}^3$ . The density of Sn is 7.31  $\text{g}/\text{cm}^3$  [144], so the total mass of Sn on the BPP is 1.10 g, and if the cost of Sn is on average 0.02 USD / g [299], then the total cost of this layer of Sn would be around 0.02 USD. This total does of course not account for the electroplating bath, anodes, processing equipment, power consumption or manual labour, however, the material cost is immediately much cheaper than the similar gold coating, and a little cheaper than the commercial coating.

By combining these values with the maximum power density obtained from the polarization curves in chapter 8, the cost of the total BPP in USD / kW can be calculated (Figure 10.3.5). In this case, the maximum power for each cell occurs at the maximum current density. However, if the test station were capable of increased current density, it is clear that the maximum power for some (and perhaps all) of the cells would increase.

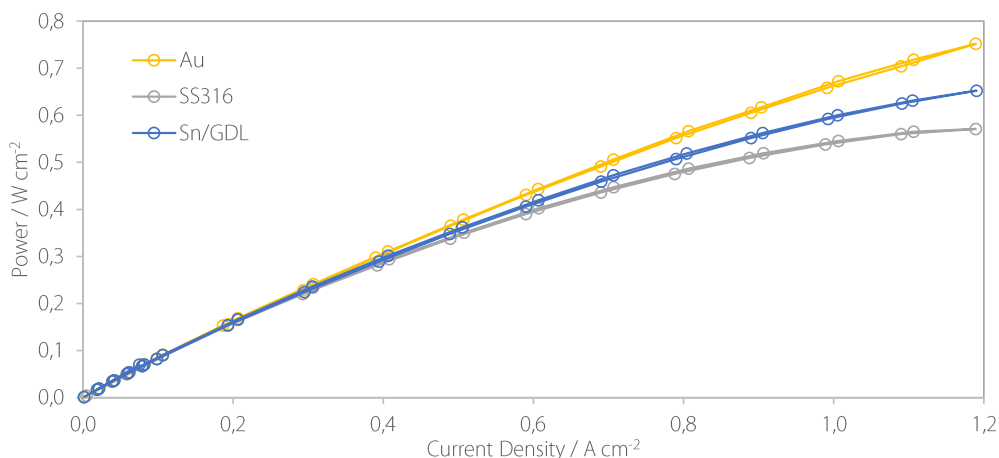


Figure 10.3.5. The variations on the power of each fuel cell with current density.

As described in the Strategic Analysis report [294], the commercial BPP has a power density of 1095  $\text{mW cm}^{-2}$ , which is significantly higher than the performance of the BPPs in this thesis.

From Table 10.3.2, it is clear that neither the commercial BPP nor the Sn/GDL BPP meet the cost requirements set by the US DoE of \$3 / kW for BPPs in 2020. However, this cost estimate is based on a production of 1000 systems a year, and if the number of systems increases, the commercial BPP can meet the cost requirements. The Sn/GDL system is a cheaper alternative to both the uncoated and the gold coated BPPs, and if it were sufficiently scaled up it might also reach the target of \$3 / kW.

Table 10.3.2. The calculation of the cost in USD / kW for each BPP type, with the maximum power calculated from the initial polarisation curves, then converted to a total BPP cost by adding the cost of the coating to that of the BPP substrate and accounting for the power obtained from each cell.

BPP Type	Max Power / mW cm <sup>-2</sup>	50 cm <sup>2</sup> cell Power / W	Coating Cost / \$	Total BPP Cost / \$	BPP Cost / \$ kW <sup>-1</sup>
Au	751	38	3.76	3.98	105
SS316	570	28	-	0.218	7.79
Sn/GDL	652	33	0.022	0.240	7.27
Commercial	1 095	55	0.068	0.287	5.22

Additionally, it can be investigated whether a different substrate material could be used for the bipolar plate. The cost of carbon steel is only 20 % of the cost of SS316 [300], and is easier to stamp than SS316 due to the absence of alloying elements. Since the Sn coating is impervious, the type of substrate should not impact the final performance of the BPP. As long as the deposition can take place on that substrate, and it is able to be stamped, this should be feasible. The use of carbon steel leads to a significantly lower substrate cost, and a total BPP cost of under 2.12 \$ / kW. However, this total cost does not consider the processing costs of the electrodeposition methods, nor any additional performance decrease that may be associated with using carbon steel instead of 316.

Overall, it can be confirmed that the Sn/GDL concept is a significantly cheaper alternative to Au-coated BPPs, even if it does not yet meet the specific requirements outlined in this work.

## 10.4. Conclusions

In conclusion, the Sn/GDL concept bipolar plates meet many of the requirements set out for robust coating materials for bipolar plates in PEM fuel cells. They are particularly amenable to a cheap, high-throughput, one-step manufacturing process, which although unproven is unique to this type of bipolar plate and would be very interesting for further study. In addition, the Sn coating is a low cost alternative to both bare stainless steel and Au coated BPPs, with an estimated cost of 7.3 \$ / kW compared to 8.7 \$ / kW for SS316 alone, and 105 \$ / kW for Au-coated SS316. Although this does not meet the cost targets outlined by the US DoE, this could be possible with upscaling of the system.

Therefore, it can be said that the Sn/GDL system is commercially very interesting, and in the future could be used as a bipolar plate for PEM fuel cells.



## Conclusions and Future Work

The main objective in this work has been to determine whether the electrodeposition of tin is a viable low-cost coating method for bipolar plates. When electroplated onto a stainless steel substrate and then hot pressed with a gas diffusion layer, the tin acts as a solder to provide excellent conduction of electrons through the fuel cell. The conductivity is maintained after exposure to the oxidising conditions within the fuel cell, as the surface of the tin oxidises, providing a protective barrier against further corrosion whilst maintaining conductivity through the GDL fibres. This is a completely novel concept for BPPs in PEMFCs and has never been tried before.

In this thesis, several aspects of tin and tin alloy deposition have been investigated for BPPs in PEMFCs, to find the optimum deposition and hot pressing parameters, firstly with respect to the lowest interfacial contact resistance, and then for the highest corrosion resistance in a simulated PEM fuel cell environment. The bipolar plates were then tested inside an operating fuel cell to determine their long term performance. Finally, the tin-based bipolar plates were investigated in relation to a set of criteria outlined in the 2017 Bipolar Plate Workshop to determine whether they meet the requirements for upscaling to industrially relevant scales.

This work has shown that the electrodeposition of Sn to form a thin layer on a bipolar plate has successfully been achieved. The deposition and hot pressing processes have been optimised to the following: A 30  $\mu\text{m}$  thick layer of Sn is electroplated onto a stainless steel BPP with a current density of 15  $\text{mA cm}^{-2}$ , before hot pressing with a Freudenberg H23 C6 GDL. The sample was hot pressed at a temperature of 230  $^{\circ}\text{C}$ , and a pressure of 0.5 bar for 20 minutes, before being slowly cooled to room temperature. This procedure resulted in a BPP/GDL system that showed a very low contact resistance of 6.5  $\text{m}\Omega \text{cm}^2$  at 140  $\text{Ncm}^{-2}$ , well below U.S DoE targets. Additionally, the Sn/GDL BPPs had lower resistance compared to uncoated stainless steel after being tested in a simulated PEMFC environment, with an ICR of 13.2  $\text{m}\Omega \text{cm}^2$  being recorded after exposure to 1.2  $\text{V}_{\text{SHE}}$  for 1 hour. This increase in ICR was attributed to the dissolution of Sn to form the soluble  $\text{Sn}(\text{OH})_4$ , leading to reduced contact between the Sn and GDL. Precipitation of  $\text{SnO}_2$  on the BPP surface leads to passivation and good stability.

Testing of the Sn/GDL BPP *in-situ* showed that the low-cost coating performed much better than the uncoated stainless steel substrate, but was not as good as the gold coated BPPs over the duration of the tests in this thesis. However, looking at the performance degradation, the indications are that the Sn/GDL BPP will eventually outperform the gold coated BPP, so the conduction of longer term *in-situ* tests would be interesting in the future. The *in-situ* tests performed in this thesis were 200 hours, corresponding to under 7000 km of real-world driving. The EU harmonised testing protocol recommends that 500 hours of testing, corresponding to 16000 km or one year of vehicular usage, are performed. Due to the time limitations of a PhD, it would be unfeasible to perform 500 hours of testing

on each bipolar plate, but in the future, it would be interesting to determine the performance over longer periods of time.

A number of variations on the Sn/GDL concept were also investigated, including the alloying of Sn with Bi or In, and the addition of a carbon nanolayer to the Sn/GDL interface.

The addition of bismuth into the tin layer has been hypothesised to aid in the formation of a protective oxide by increasing the rate of the  $\text{Sn}(\text{OH})_4$  to  $\text{SnO}_2$  passivation step. This should improve performance due to reduced Sn dissolution which should mitigate the increases in contact resistance. This hypothesis was proven to be correct, with a SnBi alloy containing 4.0 % Bi exhibiting a lower ICR and greater stability in a simulated PEM environment compared to Sn samples. It was determined that increasing the Bi content above 4 % led to phase separation and reduced performance due to enrichment of Bi in the phase boundary, hindering the oxidation process. Additionally, exposure of the SnBi alloy to elevated temperature for a prolonged time during hot pressing resulted in similar phase separation and reduced performance. Therefore, the synthesis of a SnBi/GDL BPP was optimised to deposit a SnBi alloy containing 4.0 % Bi, then hot pressing for 8 minutes at a temperature of 226 °C and a pressure of 0.5 bar.

The SnBi/GDL BPP was also tested *in-situ*, with good performance over the first 500 cycles observed. The degradation rate was low, with high cell voltages being observed. However, the performance recovery after the second shutdown was minimal, implying that the irreversible degradation rate was unusually high. Impedance spectroscopy showed that this was due to an increase in activation overpotential on the anode side, and EDS analysis of the MEA indicated that the carbon content of the membrane was lower than expected. Together, these imply that the SnBi cell went into reversal during shutdown or start-up, leading to corrosion of the carbon catalyst support and poor overall performance. Given the promising initial performance, it would be interesting to repeat the *in-situ* measurement of the SnBi BPP, to more accurately determine the long-term performance.

Due to the well-known stability and conductivity of indium tin oxide, alloys of tin and indium (<10 % In) were also investigated for BPPs in this thesis. A full parameter study was performed on a multiple types of deposition bath, but an alloy of Sn and In was not obtained. Although some SnIn alloys were obtained, they either had an extremely low current efficiency due to the favourable hydrogen evolution kinetics or contained unwanted impurities such as oxygen or sulfur. It would of course be interesting to obtain a suitable coated SnIn BPP for *in-situ* testing, and using alkaline, sulfonic acid or borate baths are possibilities that have been recorded in literature.

Since electrodeposition was unsuccessful, hot-dipping of a stainless steel substrate into a SnIn melt was performed. A number of varying compositions of SnIn alloys were obtained, and after re-flowing in the hot press, the coatings were tested in a simulated PEMFC environment. Due to poor adhesion to the substrate, the SnIn coated BPPs did not perform well. It is thus suggested that future work on SnIn coated stainless steel BPPs is focused on the optimisation of the hot-dipping process.

Due to the limited time frame of this PhD, only two different alloying elements for Sn have been identified and investigated, but additional variations on the Sn/GDL are also possible. Adding dopants such as fluorine and zinc to tin oxide is a popular choice, and it would be interesting to see how such elements impact the Sn/GDL system in terms of oxide stability and contact resistance.

Other than the Sn layer, variations in the type of GDL and the interface between the Sn and GDL were identified as areas of interest. Two types of GDL with different hydrophobicity and fibre stiffness were obtained. It was determined that the hydrophobicity of the GDL had a significant impact on performance, with the presence of the hydrophobic treatment preferable. As well as helping with the water management of the fuel cell, the hydrophobic treatment prevents infiltration of the electrolyte into the Sn surface, which reduces the amount of dissolution and maintains the excellent conductivity. It was also found that GDLs with stiffer fibres penetrated deeper into the Sn, preserving the conduction pathways and maintaining a low ICR for longer.

The addition of a carbon nanolayer to the Sn/GDL interface was investigated by spraying a thin layer of different types of carbon nanoparticles onto the GDL, and hot pressing with the Sn. The addition of multiwalled carbon nanotubes to the interface was shown to reduce the initial contact resistance, due to a higher number of contact points and electronic pathways. This low ICR was sustained after electrochemical testing due to a combined effect of carbon nanotubes being a more stable form of carbon, and also the deeper penetration of the nanotubes into the Sn. This means that any surface dissolution and oxidation did not break down the conduction pathways, as was the case with the different geometries of carbon particles. However, after *in-situ* testing for 200 hours, the Sn/C/GDL BPP performed worse than the BPP without carbon. This is because prolonged contact with the PEMFC environment including shutdown and start-up cycles led to more surface dissolution, and fracture of the interface with the carbon nanoparticles. Therefore, the conduction pathways are broken, leading to a larger performance decrease.

Finally, in order to place this thesis in context, the industrial suitability of the Sn/GDL BPPs was investigated. A small study has been performed, comparing the material cost of Sn/GDL BPPs to the gold coated and bare stainless steel BPPs used in this thesis, as well as an industrial BPP. It was found that the Sn/GDL BPP was a significantly cheaper alternative to the Au-coated and bare SS BPPs, and only slightly more expensive than the commercial BPPs. However, with some slight performance increases, the Sn BPPs will be able to compete with the industrial standards. Additionally, a novel one-step joining method was proposed for the Sn/GDL BPPs, involving hot pressing multiple BPPs and GDLs together into a stack. This should provide easy manufacturing, leading to future cost reductions.

When the Sn based coatings have reached a higher TRL level, a more thorough cost and life cycle analysis should be performed to accurately determine if the US DoE targets are reached. Additionally, the novel joining method of hot pressing two BPPs together to form an easily stackable fuel cell should be quantitatively investigated. Testing a hot pressed BPP *in-situ* under high-pressure operation would be interesting to see whether the long-term performance matches that of the welded BPPs. Also, if the Sn/GDL BPP does not meet cost targets, the relatively expensive SS 316 substrate can be replaced with carbon steel. However, a number of *ex-situ* and *in-situ* tests must be conducted to determine how changing the substrate will impact the performance.

Overall, the objectives outlined in the earlier chapters of this thesis have been achieved. A low-cost bipolar plate consisting of a stainless steel substrate with an electroplated layer of Sn which is hot pressed with a GDL has been investigated and found to out-perform gold coated and bare stainless steel BPPs at a much lower cost.



# References

- [1] IEA. Tracking Transport. Track Transp 2019:1–8. [www.iea.org/reports/tracking-transport-2019](http://www.iea.org/reports/tracking-transport-2019).
- [2] Wishart J. Fuel Cells vs Batteries In the Automotive Sector. 2014. doi:10.13140/RG.2.2.24357.70882.
- [3] Henning M, Thomas A, Smyth A. An Analysis of the Association between Changes in Ambient Temperature, Fuel Economy, and Vehicle Range for Battery Electric and Fuel Cell Electric Buses. 2020.
- [4] Deloitte-Ballard white paper on fuel cells for fueling future mobility. *Fuel Cells Bull* 2020;2020:12. doi:10.1016/s1464-2859(20)30076-6.
- [5] Thompson ST, James BD, Huya-Kouadio JM, Houchins C, DeSantis DA, Ahluwalia R, et al. Direct hydrogen fuel cell electric vehicle cost analysis: System and high-volume manufacturing description, validation, and outlook. *J Power Sources* 2018;399:304–13. doi:10.1016/J.JPOWSOUR.2018.07.100.
- [6] Jayakumar K, Pandiyan S, Rajalakshmi N, Dhathathreyan KS. Cost-benefit analysis of commercial bipolar plates for PEMFC's. *J Power Sources* 2006;161:454–9. doi:10.1016/J.JPOWSOUR.2006.04.128.
- [7] McCay K, Kongstein OE, Oedegaard A, Barnett AO, Seland F. Soldering a gas diffusion layer to a stainless steel bipolar plate using metallic tin. *Int J Hydrogen Energy* 2018;43:9006–14. doi:10.1016/J.IJHYDENE.2018.03.188.
- [8] De Marco G, Malkow T, Tsotridis G, Pilenga A. EU harmonised test protocols for PEMFC MEA testing in single cell configuration for automotive applications. 2015. doi:10.2790/54653.
- [9] Kopasz JP, Benjamin TG. 2017 Bipolar Plate Workshop Summary Report. 2017.
- [10] Barbir F. PEM Fuel Cells: Theory and Practice. 2005. doi:10.1016/b978-012078142-3/50002-1.
- [11] Bagotsky VS. *Fuel Cells. Fundam. Electrochem.*, 2005, p. 361–8. doi:10.1002/047174199X.ch20.
- [12] Hussain MM, Baschuk JJ, Li X, Dincer I. Thermodynamic analysis of a PEM fuel cell power system. *Int J Therm Sci* 2005;44:903–11. doi:10.1016/j.ijthermalsci.2005.02.009.
- [13] Hissel D, Gualous H. *Electrochemical Components*. 1st ed. Wiley; 2013.
- [14] Steele BC, Heinzel A. Materials for fuel-cell technologies. *Nature* 2001;414:345–52. doi:10.1038/35104620.
- [15] Grot WG. Perfluorinated Ion-Exchange Polymers and Their Use in Research and Industry. *Macromol Symp* 1994;82:161–72.
- [16] Talbot D (David EJ, Talbot J (James DR. *Corrosion science and technology*. CRC Press; 2007.
- [17] Peng L, Yi P, Lai X. Design and manufacturing of stainless steel bipolar plates for proton exchange membrane fuel cells. *Int J Hydrogen Energy* 2014;39:21127–53. doi:10.1016/j.ijhydene.2014.08.113.
- [18] LI X, SABIR I. Review of bipolar plates in PEM fuel cells: Flow-field designs. *Int J Hydrogen Energy* 2005;30:359–71. doi:10.1016/j.ijhydene.2004.09.019.
- [19] Nguyen PT, Berning T, Djilali N. Computational model of a PEM fuel cell with serpentine gas flow channels. *J Power Sources* 2004;130:149–57. doi:10.1016/j.jpowsour.2003.12.027.
- [20] Trogadas P, Cho JIS, Neville TP, Marquis J, Wu B, Brett DJL, et al. A lung-inspired approach to scalable and robust fuel cell design. *Energy Environ Sci* 2018;11:136–43. doi:10.1039/c7ee02161e.
- [21] Ozden A, Ercelik M, Ouellette D, Colpan CO, Ganjehsarabi H, Hamdullahpur F. Designing, modeling and performance investigation of bio-inspired flow field based DMFCs. *Int J Hydrogen Energy* 2017;42:21546–58. doi:10.1016/j.ijhydene.2017.01.007.
- [22] Sauermoser M, Kjelstrup S, Kizilova N, Pollet BG, Flekkøy EG. Seeking minimum entropy production for a tree-like flow-field

- in a fuel cell. *Phys Chem Chem Phys* 2020;22:6993–7003. doi:10.1039/c9cp05394h.
- [23] Kloess JP, Wang X, Liu J, Shi Z, Guessous L. Investigation of bio-inspired flow channel designs for bipolar plates in proton exchange membrane fuel cells. *J Power Sources* 2009;188:132–40. doi:10.1016/j.jpowsour.2008.11.123.
- [24] Tang Y, Yuan W, Pan M, Wan Z. Feasibility study of porous copper fiber sintered felt: A novel porous flow field in proton exchange membrane fuel cells. *Int J Hydrogen Energy* 2010;35:9661–77. doi:10.1016/j.ijhydene.2010.06.101.
- [25] Kozakai M, Date K, Tabe Y, Chikahisa T. Improving gas diffusivity with bi-porous flow-field in polymer electrolyte membrane fuel cells. *Int J Hydrogen Energy* 2016;41:13180–9. doi:10.1016/j.ijhydene.2016.05.131.
- [26] Huang X, Solasi R, Zou Y, Feshler M, Reifsnider K, Condit D, et al. Mechanical endurance of polymer electrolyte membrane and PEM fuel cell durability. *J Polym Sci Part B Polym Phys* 2006;44:2346–57. doi:10.1002/polb.20863.
- [27] Sulek M, Adams J, Kaberline S, Ricketts M, Waldecker JR. In situ metal ion contamination and the effects on proton exchange membrane fuel cell performance. *J Power Sources* 2011;196:8967–72. doi:10.1016/j.jpowsour.2011.01.086.
- [28] Inaba M, Kinumoto T, Kiriake M, Umabayashi R, Tasaka A, Ogumi Z. Gas crossover and membrane degradation in polymer electrolyte fuel cells. *Electrochim Acta* 2006;51:5746–53. doi:10.1016/j.electacta.2006.03.008.
- [29] Kinumoto T, Inaba M, Nakayama Y, Ogata K, Umabayashi R, Tasaka A, et al. Durability of perfluorinated ionomer membrane against hydrogen peroxide. *J Power Sources* 2006;158:1222–8. doi:10.1016/j.jpowsour.2005.10.043.
- [30] US Department of Energy office of energy efficiency and renewable energy U. US DOE Technical Targets for Polymer Electrolyte Membrane Fuel Cell Components 2017. <https://energy.gov/eere/fuelcells/doe-technical-targets-polymer-electrolyte-membrane-fuel-cell-components> (accessed August 10, 2017).
- [31] Barbir F, Braun J, Neutzler J. Properties of Molded Graphite Bi-Polar Plates for PEM Fuel Cell Stacks. *J New Mater Electrochem Syst* 1999;2:197–200.
- [32] Yuan XZ, Wang HJ, Zhang JJ, Wilkinson DP. Bipolar plates for PEM fuel cells - From materials to processing. *J New Mater Electrochem Syst* 2005;8:257–67.
- [33] Lee S-J, Huang C-H, Lai J-J, Chen Y-P. Corrosion-resistant component for PEM fuel cells. *J Power Sources* 2004;131:162–8. doi:10.1016/j.jpowsour.2004.01.008.
- [34] Cunningham B, Baird DG. The development of economical bipolar plates for fuel cells. *J Mater Chem* 2006;16:4385. doi:10.1039/b611883f.
- [35] Andrzej J, Antoni L, Petit JP. Corrosion resistance of stainless steel bipolar plates in a PEFC environment: A comprehensive study. *Int J Hydrogen Energy* 2010;35:3684–97. doi:10.1016/j.ijhydene.2010.01.062.
- [36] Wind J, Spöhr R, Kaiser W, Böhmer G. Metallic bipolar plates for PEM fuel cells. *J Power Sources* 2002;105:256–60. doi:10.1016/S0378-7753(01)00950-8.
- [37] Mawdsley JR, Carter JD, Wang X, Niyogi S, Fan CQ, Koc R, et al. Composite-coated aluminum bipolar plates for PEM fuel cells. *J Power Sources* 2013;231:106–12. doi:10.1016/j.jpowsour.2012.12.074.
- [38] Barranco J, Barreras F, Lozano A, Maza M. Influence of CrN-coating thickness on the corrosion resistance behaviour of aluminium-based bipolar plates. *J. Power Sources*, vol. 196, 2011, p. 4283–9. doi:10.1016/j.jpowsour.2010.11.069.
- [39] Wang SH, Peng J, Lui WB, Zhang JS. Performance of the gold-plated titanium bipolar plates for the light weight PEM fuel cells. *J Power Sources* 2006;162:486–91. doi:10.1016/j.jpowsour.2006.06.084.
- [40] Wang SH, Peng J, Lui WB. Surface modification and development of titanium bipolar plates for PEM fuel cells. *J Power Sources* 2006;160:485–9. doi:10.1016/j.jpowsour.2006.01.020.
- [41] De Las Heras N, Roberts EPL, Hodgson DR, Langton R. Metal separator plates for automotive fuel cells. CHISA 2008 - 18th Int. Congr. Chem. Process Eng., 2008.
- [42] Nikiforov AV, Petrushina IM, Christensen E, Tomás-García AL, Bjerrum NJ. Corrosion behaviour of construction materials for high temperature steam electrolyzers. *Int J Hydrogen Energy* 2011;36:111–9. doi:10.1016/j.ijhydene.2010.09.023.
- [43] Mahabunphachai S, Cora Ömer Necati, Kök M. Effect of manufacturing processes on formability and surface topography of proton exchange membrane fuel cell metallic bipolar plates. *J Power Sources* 2010;195:5269–77. doi:10.1016/j.jpowsour.2010.03.018.
- [44] Lædre S, Kongstein OE, Oedegaard A, Seland F, Karoliussen H. The effect of pI and halides on the corrosion process of stainless

- steel bipolar plates for proton exchange membrane fuel cells. *Int J Hydrogen Energy* 2012;37:18537–46. doi:10.1016/j.ijhydene.2012.09.021.
- [45] Mele C, Bozzini B. Localised corrosion processes of austenitic stainless steel bipolar plates for polymer electrolyte membrane fuel cells. *J Power Sources* 2010;195:3590–6. doi:10.1016/j.jpowsour.2009.11.144.
- [46] Pozio A, Silva RF, De Francesco M, Giorgi L. Nafion degradation in PEFCs from end plate iron contamination. *Electrochim Acta* 2003;48:1543–9. doi:10.1016/S0013-4686(03)00026-4.
- [47] Tawfik H, Hung Y, Mahajan D. Metal bipolar plates for PEM fuel cell-A review. *J Power Sources* 2007;163:755–67. doi:10.1016/j.jpowsour.2006.09.088.
- [48] Woodman a S, Anderson EB, Jayne KD, Kimble MC. Development of corrosion-resistant coatings for fuel cell bipolar plates. *Proc AESF Annu Tech Conf* 1999:717–25.
- [49] Collier A, Wang H, Zi Yuan X, Zhang J, Wilkinson DP. Degradation of polymer electrolyte membranes. *Int J Hydrogen Energy* 2006;31:1838–54. doi:10.1016/j.ijhydene.2006.05.006.
- [50] Miyazawa A, Tada E, Nishikata A. Influence of corrosion of SS316L bipolar plate on PEFC performance. *J Power Sources* 2013;231:226–33. doi:10.1016/j.jpowsour.2012.12.088.
- [51] Taherian R. A review of composite and metallic bipolar plates in proton exchange membrane fuel cell: Materials, fabrication, and material selection. *J Power Sources* 2014;265. doi:10.1016/j.jpowsour.2014.04.081.
- [52] Leng Y, Ming P, Yang D, Zhang C. Stainless steel bipolar plates for proton exchange membrane fuel cells: Materials, flow channel design and forming processes. *J Power Sources* 2020;451:227783. doi:10.1016/J.JPOWSOUR.2020.227783.
- [53] Asri NF, Husaini T, Sulong AB, Majlan EH, Daud WRW. Coating of stainless steel and titanium bipolar plates for anticorrosion in PEMFC: A review. *Int J Hydrogen Energy* 2016. doi:10.1016/j.ijhydene.2016.06.241.
- [54] Karimi S, Fraser N, Roberts B, Foulkes FR. A review of metallic bipolar plates for proton exchange membrane fuel cells: Materials and fabrication methods. *Adv Mater Sci Eng* 2012;2012. doi:10.1155/2012/828070.
- [55] Hermann A, Chaudhuri T, Spagnol P. Bipolar plates for PEM fuel cells: A review. *Int. J. Hydrogen Energy*, vol. 30, 2005, p. 1297–302. doi:10.1016/j.ijhydene.2005.04.016.
- [56] Wang Y, Ruiz Diaz DF, Chen KS, Wang Z, Adroher XC. Materials, technological status, and fundamentals of PEM fuel cells – A review. *Mater Today* 2020;32:178–203. doi:10.1016/j.mattod.2019.06.005.
- [57] Zhang Y, Blawert C, Tang S, Hu J, Mohedano M, Zheludkevich ML, et al. Influence of surface pre-treatment on the deposition and corrosion properties of hydrophobic coatings on a magnesium alloy. *Corros Sci* 2016;112:483–94. doi:10.1016/j.corsci.2016.08.013.
- [58] Wu Y, Li Y-F, Zhang E-G, Zhao J, Liv B. Experimental Study on the Impact of Pre-treatment Cleaning Process on DLC Coating Performance. *Asia-Pacific Eng. Technol. Conf. (APETC 2017)*, 2017. doi:10.12783/dtetr/apetc2017/11410.
- [59] Sharifi Golru S, Attar MM, Ramezanzadeh B. Effects of surface treatment of aluminium alloy 1050 on the adhesion and anticorrosion properties of the epoxy coating. *Appl Surf Sci* 2015;345:360–8. doi:10.1016/j.apsusc.2015.03.148.
- [60] Braccini M, Dupeux M. *Mechanics of Solid Interfaces*. 2013. doi:10.1002/9781118561669.
- [61] Özdemir A, Kocabaş İ, Svanda P. Improving the strength of adhesively bonded joints through the introduction of various surface treatments. *J Adhes Sci Technol* 2016;30:2573–95. doi:10.1080/01694243.2016.1188872.
- [62] Husby H. *Carbon Based Coatings for Metallic Bipolar Plates in PEM Fuel Cells*. Norwegian University of Science and Technology, 2013.
- [63] Bishopp JA, Sim EK, Thompson GE, Wood GC. Effects of the environment on bonded aluminium joints: an examination by electron microscopy. In: Allen KW, editor. *Adhes*. 13, Springer Netherlands; 1989, p. 201–20. doi:10.1007/978-94-010-9082-7.
- [64] Critchlow GW, Brewis DM. Review of surface pretreatments for aluminium alloys. *Int J Adhes Adhes* 1996;16:255–74. doi:10.1016/S0143-7496(96)00014-0.
- [65] Husby H, Kongstein OE, Oedegaard A, Seland F. Carbon-polymer composite coatings for PEM fuel cell bipolar plates. *Int J Hydrogen Energy* 2014;39:951–7. doi:10.1016/j.ijhydene.2013.10.115.
- [66] Mine EF, Ito Y, Teranishi Y, Sato M, Shimizu T. Surface coating and texturing on stainless-steel plates to decrease the contact resistance by using screen printing. *Int J Hydrogen Energy* 2017;42:20224–9. doi:10.1016/j.ijhydene.2017.06.154.

- [67] Chen P, Fang F, Zhang Z, Zhang W, Wang Y. Self-assembled graphene film to enable highly conductive and corrosion resistant aluminum bipolar plates in fuel cells. *Int J Hydrogen Energy* 2017;42:12593–600. doi:10.1016/j.ijhydene.2017.03.214.
- [68] Bi F, Hou K, Yi P, Peng L, Lai X. Mechanisms of growth, properties and degradation of amorphous carbon films by closed field unbalanced magnetron sputtering on stainless steel bipolar plates for PEMFCs. *Appl Surf Sci* 2017;422:921–31. doi:10.1016/j.apsusc.2017.06.122.
- [69] Jin J, Zhu Z, Zheng D. Influence of Ti content on the corrosion properties and contact resistance of CrTiN coating in simulated proton exchange membrane fuel cells. *Int J Hydrogen Energy* 2017;42:11758–70. doi:10.1016/j.ijhydene.2017.02.014.
- [70] Yu Y, Shironita S, Mizukami T, Nakatsuyama K, Souma K, Umeda M. Corrosion-resistant characteristics of nitrided Ni-free stainless steel for bipolar plate of polymer electrolyte fuel cell. *Int J Hydrogen Energy* 2017;42:6303–9. doi:10.1016/j.ijhydene.2017.01.211.
- [71] Wang S, Hou M, Zhao Q, Jiang Y, Wang Z, Li H, et al. Ti/(Ti,Cr)N/CrN multilayer coated 316L stainless steel by arc ion plating as bipolar plates for proton exchange membrane fuel cells. *J Energy Chem* 2017;26:168–74. doi:10.1016/j.jechem.2016.09.004.
- [72] Pugal Mani S, Rajendran N. Corrosion and interfacial contact resistance behavior of electrochemically nitrided 316L SS bipolar plates for proton exchange membrane fuel cells. *Energy* 2017;133:1050–62. doi:10.1016/j.energy.2017.05.086.
- [73] Abreu CM, Cristóbal MJ, Figueroa R, Nóvoa XR, Pena G. Evolution of corrosion behavior for AA7075 aluminum alloy implanted with nitrogen. *Nucl Instruments Methods Phys Res Sect B Beam Interact with Mater Atoms* 2019;442:1–12. doi:10.1016/j.nimb.2019.01.013.
- [74] Feng K, Li Z, Cai X, Chu PK. Silver implanted 316L stainless steel as bipolar plates in polymer electrolyte membrane fuel cells. *Mater Chem Phys* 2011;126:6–11. doi:10.1016/j.matchemphys.2010.11.029.
- [75] Huang N, Liang C, Wang H, Xu L, Xu H. Corrosion behavior of passivated 316LSS with Ag coating as PEMFC bipolar plate. *Int J Corros* 2011;2011. doi:10.1155/2011/103785.
- [76] Lin K, Li X, Dong H, Du S, Lu Y, Ji X, et al. Surface modification of 316 stainless steel with platinum for the application of bipolar plates in high performance proton exchange membrane fuel cells. *Int J Hydrogen Energy* 2017;42:2338–48. doi:10.1016/j.ijhydene.2016.09.220.
- [77] Wang L, Sun J, Kang B, Li S, Ji S, Wen Z, et al. Electrochemical behaviour and surface conductivity of niobium carbide-modified austenitic stainless steel bipolar plate. *J Power Sources* 2014;246:775–82. doi:10.1016/j.jpowsour.2013.08.025.
- [78] Zhao Y, Wei L, Yi P, Peng L. Influence of Cr-C film composition on electrical and corrosion properties of 316L stainless steel as bipolar plates for PEMFCs. *Int J Hydrogen Energy* 2016;41:1142–50. doi:10.1016/j.ijhydene.2015.10.047.
- [79] Yi P, Peng L, Zhou T, Wu H, Lai X. Cr-N-C multilayer film on 316L stainless steel as bipolar plates for proton exchange membrane fuel cells using closed field unbalanced magnetron sputter ion plating. *Int J Hydrogen Energy* 2013;38:1535–43. doi:10.1016/j.ijhydene.2012.11.030.
- [80] Huang NB, Yu H, Xu LS, Zhan S, Sun M, Kirk DW. Corrosion kinetics of 316L stainless steel bipolar plate with chromium carbide coating in simulated PEMFC cathodic environment. *Results Phys* 2016;6:730–6. doi:10.1016/j.rinp.2016.10.002.
- [81] Borup RL, Vanderborgh NE. Design and testing criteria for bipolar plate materials for PEM fuel cell applications. *Mater Res Soc Symp - Proc* 1995;393:151–5. doi:http://dx.doi.org/10.1557/PROC-393-151.
- [82] Turan C, Cora ÖN, Koç M. Investigation of the effects of process sequence on the contact resistance characteristics of coated metallic bipolar plates for polymer electrolyte membrane fuel cells. *J Power Sources* 2013;243:925–34. doi:10.1016/j.jpowsour.2013.05.182.
- [83] Mendizabal L, Oedegaard A, Kongstein OE, Lædre S, Walmsley J, Barriga J, et al. TaNX coatings deposited by HPPMS on SS316L bipolar plates for polymer electrolyte membrane fuel cells: Correlation between corrosion current, contact resistance and barrier oxide film formation. *Int J Hydrogen Energy* 2017;42:3259–70. doi:10.1016/j.ijhydene.2017.01.070.
- [84] Manso AP, Marzo FF, Garicano X, Alegre C, Lozano A, Barreras F. Corrosion behavior of tantalum coatings on AISI 316L stainless steel substrate for bipolar plates of PEM fuel cells. *Int J Hydrogen Energy* 2020;45:20679–91. doi:10.1016/j.ijhydene.2019.12.1157.
- [85] Shi K, Li X, Zhao Y, Li WW, Wang SB, Xie XF, et al. Corrosion behavior and conductivity of TiNb and TiNbN Coated Steel For Metallic Bipolar Plates. *Appl Sci* 2019;9. doi:10.3390/app9122568.
- [86] Gao P, Xie Z, Wu X, Ouyang C, Lei T, Yang P, et al. Development of Ti bipolar plates with carbon/PTFE/TiN composites

- coating for PEMFCs. *Int J Hydrogen Energy* 2018;43:20947–58. doi:10.1016/j.ijhydene.2018.09.046.
- [87] Borup R, Meyers J, Pivovar B, Kim YS, Mukundan R, Garland N, et al. Scientific aspects of polymer electrolyte fuel cell durability and degradation. *Chem Rev* 2007;107:3904–51. doi:10.1021/cr050182l.
- [88] Gago AS, Garcia-Sanchez D, Ansar SA, Gazdzicki P, Wagner N, Arnold J, et al. Improved Water Management with Thermally Sprayed Coatings on Stainless Steel Bipolar Plates of PEMFC. *ECS Trans* 2015;69:223–39. doi:10.1149/06917.0223ecst.
- [89] Lettenmeier P, Wang R, Abouatallah R, Burggraf F, Gago AS, Friedrich KA. Coated Stainless Steel Bipolar Plates for Proton Exchange Membrane Electrolyzers. *J Electrochem Soc* 2016;163:F3119–24. doi:10.1149/2.0141611jes.
- [90] Dearnaley G. Ion Implantation and Ion Assisted Coatings for Wear Resistance in Metals. *Surf Eng* 1986;2:213–22. doi:10.1179/sur.1986.2.3.213.
- [91] Fu Y, Wu X, Han E-H, Ki W, Yang K, Jiang Z. Effects of nitrogen on the passivation of nickel-free high nitrogen and manganese stainless steels in acidic chloride solutions. *Electrochim Acta* 2009;54:4005–14. doi:10.1016/j.electacta.2009.02.024.
- [92] Wang H, Turner JA. Modifying a stainless steel for PEMFC bipolar plates via electrochemical nitridation. *Fuel Cells* 2013;13:917–21. doi:10.1002/fuce.201300068.
- [93] Lin K, Li X, Sun Y, Luo X, Dong H. Active screen plasma nitriding of 316 stainless steel for the application of bipolar plates in proton exchange membrane fuel cells. *Int J Hydrogen Energy* 2014. doi:10.1016/j.ijhydene.2014.04.102.
- [94] Stoot AC, Camilli L, Spiegelhauer SA, Yu F, Bøggild P. Multilayer graphene for long-term corrosion protection of stainless steel bipolar plates for polymer electrolyte membrane fuel cell. *J Power Sources* 2015;293:846–51. doi:10.1016/j.jpowsour.2015.06.009.
- [95] Hashempour M, Sharma S, Gonzalez D, Vicenzo A, Bestetti M. The effect of electrodeposited PANI on corrosion behavior of 316 stainless steel coated by CVD grown MWCNTs under PEMFC bipolar plate working condition. *ECS Trans*, vol. 63, 2014. doi:10.1149/06301.0261ecst.
- [96] Melo RL, Casciano PNS, Correia AN, Lima-Neto P de. Characterisation of electrodeposited and heat-treated Ni–Mo–P coatings. *J Braz Chem Soc* 2012;23:328–34. doi:10.1590/S0103-50532012000200020.
- [97] Zhu XB, Cai C, Zheng GQ, Zhang Z, Li JF. Electrodeposition and corrosion behavior of nanostructured Ni-TiN composite films. *Trans Nonferrous Met Soc China (English Ed)* 2011;21:2216–24. doi:10.1016/S1003-6326(11)60998-9.
- [98] Wang H-C, Hou K-H, Lu C-E, Ger M-D. The study of electroplating trivalent CrC alloy coatings with different current densities on stainless steel 304 as bipolar plate of proton exchange membrane fuel cells. *Thin Solid Films* 2014;570:209–14. doi:10.1016/j.tsf.2014.03.034.
- [99] Kim KM, Kim JH, Lee YY, Kim KY. Electrodeposition of ruthenium oxide on ferritic stainless steel bipolar plate for polymer electrolyte membrane fuel cells. *Int J Hydrogen Energy* 2012;37:1653–60. doi:10.1016/j.ijhydene.2011.10.028.
- [100] Andrew G. Howell, Heli Wang, Scott W. Cowley, John A. Turner. Characterization and performance of UNS S63019 (21-4N) as bipolar plate material in a simulated polymer electrolyte membrane fuel cell environment. *J Power Sources* 2011;196:5922–7. doi:10.1016/j.jpowsour.2011.02.055.
- [101] Kumagai M, Myung S-T, Kuwata S, Asaishi R, Yashiro H. Corrosion behavior of austenitic stainless steels as a function of pH for use as bipolar plates in polymer electrolyte membrane fuel cells. *Electrochim Acta* 2008;53:4205–12. doi:10.1016/j.electacta.2007.12.078.
- [102] Feng K, Wu G, Li Z, Cai X, Chu PK. Corrosion behavior of SS316L in simulated and accelerated PEMFC environments. *Int J Hydrogen Energy* 2011;36:13032–42. doi:10.1016/j.ijhydene.2011.07.058.
- [103] Orsi A, Kongstein OE, Hamilton PJ, Oedegaard A, Svenum IH, Cooke K. An investigation of the typical corrosion parameters used to test polymer electrolyte fuel cell bipolar plate coatings, with titanium nitride coated stainless steel as a case study. *J Power Sources* 2015;285. doi:10.1016/j.jpowsour.2015.03.111.
- [104] Hinds G, Brightman E. Towards more representative test methods for corrosion resistance of PEMFC metallic bipolar plates. *Int J Hydrogen Energy* 2015;40:2785–91. doi:10.1016/j.ijhydene.2014.12.085.
- [105] Wang H, Sweikart MA, Turner JA. Stainless steel as bipolar plate material for polymer electrolyte membrane fuel cells. *J Power Sources* 2003;115:243–51. doi:10.1016/S0378-7753(03)00023-5.
- [106] Madadi F, Rezaeian A, Edris H, Zhiani M. Influence of surface roughness and hydrophobicity of bipolar plates on PEM performance. *Surf Coatings Technol* 2020;389. doi:10.1016/j.surfcoat.2020.125676.

- [107] Lin CH, Tsai SY. An investigation of coated aluminium bipolar plates for PEMFC. *Appl Energy* 2012;100:87–92. doi:10.1016/j.apenergy.2012.06.045.
- [108] Nowak AP, Salguero TT, Kirby KW, Zhong F, Blunk RH. A conductive and hydrophilic bipolar plate coating for enhanced proton exchange membrane fuel cell performance and water management. *J Power Sources* 2012;210:138–45. doi:10.1016/j.jpowsour.2012.03.005.
- [109] Boyaci San FG, Isik-Gulsac I. Effect of surface wettability of polymer composite bipolar plates on polymer electrolyte membrane fuel cell performances. *Int J Hydrogen Energy* 2013;38:4089–98. doi:10.1016/j.ijhydene.2013.01.135.
- [110] Wu J, Yuan XZ, Wang H, Blanco M, Martin JJ, Zhang J. Diagnostic tools in PEM fuel cell research: Part I Electrochemical techniques. *Int J Hydrogen Energy* 2008;33:1735–46. doi:10.1016/j.ijhydene.2008.01.013.
- [111] Yuan X, Wang H, Colin Sun J, Zhang J. AC impedance technique in PEM fuel cell diagnosis-A review. *Int J Hydrogen Energy* 2007;32:4365–80. doi:10.1016/j.ijhydene.2007.05.036.
- [112] Ivers-Tiffée E, Weber A, Schichlein A. *Electrochemical Impedance Spectroscopy. Handb. fuel cells Fundam. Technol. Appl. Volume 2*, New York: Wiley; 2003, p. 220–35.
- [113] Zhu WH, Payne RU, Tatarchuk BJ. PEM stack test and analysis in a power system at operational load via ac impedance. *J Power Sources* 2007;168:211–7. doi:10.1016/j.jpowsour.2007.02.071.
- [114] Spiegel C. *Designing and Building Fuel Cells*. 2007.
- [115] Cooper KR. in Situ Pem Fuel Cell Electrochemical Surface Area and Catalyst Utilization Measurement. *Fuel Cell Mag* 2009;1–3. doi:10.1016/S1464-2859(00)80060-7.
- [116] Cooper KR. In situ pem fuel cell fuel: Fuel crossover and electrical short circuit measurement. *Fuel Cell* 2008;8:34–5.
- [117] Lædre S, Kongstein OE, Oedegaard A, Seland F, Karoliussen H. Measuring In Situ Interfacial Contact Resistance in a Proton Exchange Membrane Fuel Cell. *J Electrochem Soc* 2019;166:F853–9. doi:10.1149/2.1511912jes.
- [118] Gamburg YD, Zangari G. Introduction to Electrodeposition: Basic Terms and Fundamental Concepts. *Theory Pract. Met. Electrodepos.*, 2011, p. 1–25. doi:10.1007/978-1-4419-9669-5\_1.
- [119] Paunovic M, Schlesinger M. Kinetics and Mechanism of Electrodeposition. *Fundam. Electrochem. Depos.*, 2005, p. 77–112. doi:10.1002/0470009403.ch6.
- [120] Pletcher D, Greff R, Peat R, Peter LM, Robinson J. *Instrumental methods in electrochemistry*. 2001. doi:10.1533/9781782420545.
- [121] Paunovic M, Schlesinger M. Metal-Solution Interphase. *Fundam. Electrochem. Depos.*, 2005, p. 41–54. doi:10.1002/0470009403.ch4.
- [122] Gamburg YD, Zangari G. Thermodynamics and Kinetics of Nucleation. *Theory Pract. Met. Electrodepos.*, 2011, p. 97–122. doi:10.1007/978-1-4419-9669-5\_5.
- [123] Paunovic M, Schlesinger M. Nucleation and Growth Models. *Fundam. Electrochem. Depos.*, 2005, p. 113–38. doi:10.1002/0470009403.ch7.
- [124] Gamburg YD, Zangari G, Gamburg YD, Zangari G. Morphology of the Growing Metal Surface. *Theory Pract. Met. Electrodepos.*, 2011, p. 123–41. doi:10.1007/978-1-4419-9669-5\_6.
- [125] Xu S, Lu GQ. Effect of atomic substrate surface mobility on the nucleation and island growth of thin films. *J Mater Sci Lett* 1994;13:1629–31. doi:10.1007/BF00704522.
- [126] Gamburg YD, Zangari G. Structure and Microstructure of Electrodeposited Metals and Alloys. *Theory Pract. Met. Electrodepos.*, 2011, p. 317–33. doi:10.1007/978-1-4419-9669-5\_14.
- [127] Gamburg YD, Zangari G. Potential Distribution in the Electrolyte and Current Distribution on the Electrode Surface. *Theory Pract. Met. Electrodepos.*, 2011, p. 143–67. doi:10.1007/978-1-4419-9669-5\_7.
- [128] Hull RO. Apparatus and process for the study of plating solutions. 2149344, 1935.
- [129] Paunovic M, Schlesinger M. Effect of Additives. *Fundam. Electrochem. Depos.*, 2005, p. 177–98. doi:10.1002/0470009403.ch10.
- [130] Gamburg YD, Zangari G. Codeposition of Impurities. *Theory Pract. Met. Electrodepos.*, 2011, p. 233–52. doi:10.1007/978-1-4419-9669-5\_11.

- [131] Brenner A. Variation in the Composition of Electrodeposited Alloys with the Composition of the Bath. *Electrodepos. Alloy.*, 1963, p. 75–121. doi:10.1016/b978-1-4831-9808-8.50012-5.
- [132] Meibuhr S, Yeager E, Kozawa A, Hovorka F. The Electrochemistry of Tin. *J Electrochem Soc* 1963;110:190. doi:10.1149/1.2425709.
- [133] Brenner A. Some Theoretical Aspects of Complexing Agents and Addition Agents in Alloy Plating. *Electrodepos. Alloy.*, 1963, p. 388–408. doi:10.1016/b978-1-4831-9808-8.50021-6.
- [134] Brenner A. Effect of Operating Variables on the Composition of Electrodeposited Alloys. *Electrodepos. Alloy.*, 1963, p. 122–74. doi:10.1016/b978-1-4831-9808-8.50013-7.
- [135] Brenner A. Practical Considerations Involved in the Electrodeposition of Alloys. *Electrodepos. Alloy.*, 1963, p. 44–74. doi:10.1016/b978-1-4831-9808-8.50011-3.
- [136] Brenner A. Properties of Electrodeposited Alloys. *Electrodepos. Alloy.*, 1963, p. 208–64. doi:10.1016/b978-1-4831-9808-8.50015-0.
- [137] Zhang Y. Tin and Tin Alloys for Lead-Free Solder. *Mod. Electroplat. Fifth Ed.*, 2011, p. 139–204. doi:10.1002/9780470602638.ch6.
- [138] Chason E, Jadhav N, Pei F, Buchovecky E, Bower A. Growth of whiskers from Sn surfaces: Driving forces and growth mechanisms. *Prog Surf Sci* 2013;88:103–31. doi:10.1016/j.progsurf.2013.02.002.
- [139] Oh CS, Shim JH, Lee BJ, Lee DN. A thermodynamic study on the Ag-Sb-Sn system. *J Alloys Compd* 1996;238:155–66. doi:10.1016/0925-8388(95)02191-4.
- [140] Lee BJ, Oh CS, Shim JH. Thermodynamic assessments of the Sn-In and Sn-Bi binary systems. *J Electron Mater* 1996;25:983–91. doi:10.1007/BF02666734.
- [141] Shim JH, Oh CS, Lee BJ, Lee DN. Thermodynamic assessment of the Cu-Sn system. *Zeitschrift Fuer Met Res Adv Tech* 1996;87:205–12.
- [142] Lau JH, Wong CP, Lee N-C, Lee S-WR. *Electronics Manufacturing: With Lead-Free, Halogen-Free, and Conductive-Adhesive Materials.* The McGraw-Hill Companies, Inc.; 2003.
- [143] Chriateľová J, Ožvold M. Properties of solders with low melting point. *J Alloys Compd* 2008;457:323–8. doi:10.1016/j.jallcom.2007.03.062.
- [144] Haynes WM. *CRC Handbook Chemistry and Physics.* CRC Press 2016:2670.
- [145] Hinds G, Brightman E. In situ mapping of electrode potential in a PEM fuel cell. vol. 17. 2012. doi:10.1016/j.elecom.2012.01.007.
- [146] Pourbaix M. *Atlas of Electrochemical Equilibria in Aqueous Solutions Version 2.* vol. 52. 2016. doi:10.1039/c5cc08796a.
- [147] Jiang Y, Sun W, Xu B, Yan M, Bahlawane N. Unusual enhancement in electrical conductivity of tin oxide thin films with zinc doping. *Phys Chem Chem Phys* 2011;13:5760–3. doi:10.1039/c0cp00816h.
- [148] Khilli MA, Hanafi ZM, Mohamed AK. The electrical conductivity of chromium trioxide and its suboxides. *Thermochim Acta* 1982;56:291–8. doi:10.1016/0040-6031(82)87037-8.
- [149] Patapis SK. Electrical resistivity of  $\alpha$ -Fe<sub>2</sub>O<sub>3</sub> and comparison to TEP at the first order Morin transition. *Solid State Commun* 1984;52:925–8. doi:https://doi.org/10.1016/0038-1098(84)90857-3.
- [150] Guziewicz M, Grochowski J, Borysiewicz M, Kaminska E, Domagala JZ, Rzdokiewicz W, et al. Electrical and optical properties of NiO films deposited by magnetron sputtering. *Opt. Appl.*, vol. 41, 2011, p. 431–40.
- [151] He L, Chen L, Xue X, Chen R, Li W. *Electromagnetism of ultramafic rocks from the Luobusa ophiolite studied at room temperatures and pressures.* 2016. doi:10.2991/iceeg-16.2016.13.
- [152] Fontana MG. *High Temperature corrosion.* Corros. Eng., 1986.
- [153] Cramer SD, Covino BS. *ASM Handbook Vol. 13a: Corrosion - Fundamentals, Testing, and Protection.* Asm 2003;13:1135. doi:10.1002/jbm.b.31896.
- [154] Xu C, Gao W. Pilling-bedworth ratio for oxidation of alloys. *Mater Res Innov* 2000;3:231–5. doi:10.1007/s100190050008.
- [155] Stürup BN, Hampson NA. Electrochemical reactions of tin in aqueous electrolytic solutions. *Surf Technol* 1977;5:429–62. doi:10.1016/0376-4583(77)90011-5.

- [156] Boggs WE, Kachik RH, Pellissier GE. The Effect of Alloying Elements on the Oxidation of Tin. *J Electrochem Soc* 1963;110:4–11.
- [157] Pardo A, Merino MC, Carboneras M, Coy AE, Arrabal R. Pitting corrosion behaviour of austenitic stainless steels with Cu and Sn additions. *Corros Sci* 2007;49:510–25. doi:10.1016/j.corsci.2006.06.004.
- [158] Pardo A, Merino MC, Carboneras M, Viejo F, Arrabal R, Muñoz J. Influence of Cu and Sn content in the corrosion of AISI 304 and 316 stainless steels in H<sub>2</sub>SO<sub>4</sub>. *Corros Sci* 2006;48:1075–92. doi:10.1016/j.corsci.2005.05.002.
- [159] Li H, Yu H, Zhou T, Yin B, Yin S, Zhang Y. Effect of tin on the corrosion behavior of sea-water corrosion-resisting steel. *Mater Des* 2015;84:1–9. doi:10.1016/j.matdes.2015.06.121.
- [160] Pourcelly G, Oikonomou A, Gavach C, Hurwitz HD. Influence of the water content on the kinetics of counter-ion transport in perfluorosulphonic membranes. *J Electroanal Chem* 1990;287:43–59. doi:10.1016/0022-0728(90)87159-11.
- [161] Cheng X, Shi Z, Glass N, Zhang L, Zhang J, Song D, et al. A review of PEM hydrogen fuel cell contamination: Impacts, mechanisms, and mitigation. *J Power Sources* 2007;165:739–56. doi:10.1016/j.jpowsour.2006.12.012.
- [162] Dahl PI, Barnett AO, Monterrubio FA, Colmenares LC. The use of tin oxide in fuel cells. *Tin Oxide Mater* 2020;379–410. doi:10.1016/B978-0-12-815924-8.00013-X.
- [163] Pitussi I, Schechter A, Teller H, Natan A, Kornweitz H. Tailored Pt Coatings on Metallic Tin—An Effective Catalyst for Fuel Cells Anodes. *J Electrochem Soc* 2020;167:44512. doi:10.1149/1945-7111/ab754b.
- [164] Kim JM, Lee YJ, Kim Shoon, Chae KH, Yoon KR, Lee KA, et al. High-performance corrosion-resistant fluorine-doped tin oxide as an alternative to carbon support in electrodes for PEM fuel cells. *Nano Energy* 2019;65. doi:10.1016/j.nanoen.2019.104008.
- [165] Iwai Y, Yamanishi T. Thermal stability of ion-exchange Nafion N117CS membranes. *Polym Degrad Stab* 2009;94:679–87. doi:10.1016/j.polymdegradstab.2008.12.020.
- [166] Nørgaard CF, Nielsen UG, Skou EM. Preparation of Nafion 117<sup>TM</sup>/SnO<sub>2</sub> composite membranes using an ion-exchange method. *Solid State Ionics* 2012;213:76–82. doi:10.1016/j.ssi.2011.10.014.
- [167] Taghizadeh MT, Vatanparast M. Preparation and evaluation of Nafion/SnO<sub>2</sub> nanocomposite for improving the chemical durability of proton exchange membranes in fuel cells. *RSC Adv* 2016;6. doi:10.1039/c6ra07849d.
- [168] Poulsen MG, Larsen MJ, Andersen SM. Improved durability of proton exchange membrane fuel cells by introducing Sn (IV) oxide into electrodes using an ion exchange method. *J Power Sources* 2017;343:174–82. doi:10.1016/j.jpowsour.2017.01.046.
- [169] Yang L, Qin Z, Pan H, Yun H, Min Y, Xu Q. Corrosion protection of 304 stainless steel bipolar plates of PEMFC by coating SnO<sub>2</sub> film. *Int J Electrochem Sci* 2017;12:10946–57. doi:10.20964/2017.11.67.
- [170] Wang H, Turner JA. SnO<sub>2</sub>:F coated ferritic stainless steels for PEM fuel cell bipolar plates. *J Power Sources* 2007;170:387–94. doi:10.1016/j.jpowsour.2007.04.028.
- [171] Wang H, Turner JA, Li X, Bhattacharya R. SnO<sub>2</sub>:F coated austenite stainless steels for PEM fuel cell bipolar plates. *J Power Sources* 2007;171:567–74. doi:10.1016/j.jpowsour.2007.03.086.
- [172] Wang H, Turner J. SnO<sub>2</sub>:F Coated Duplex Stainless Steel in for PEM Fuel Cell Bipolar Plates. *ECS Meet Abstr* 2008;16. doi:10.1149/ma2008-02/11/1081.
- [173] Park JH, Byun D, Lee JK. Employment of fluorine doped zinc tin oxide (ZnSnOx:F) coating layer on stainless steel 316 for a bipolar plate for PEMFC. *Mater Chem Phys* 2011;128:39–43. doi:10.1016/j.matchemphys.2011.01.020.
- [174] Holm R, Holm R. The contact resistance. General theory. *Elektrische Kontakte / Electr. Contacts Handb.*, 1958, p. 10–2. doi:10.1007/978-3-662-25893-4\_3.
- [175] Netwall CJ, Gould BD, Rodgers JA, Nasello NJ, Swider-Lyons KE. Decreasing contact resistance in proton-exchange membrane fuel cells with metal bipolar plates. *J Power Sources* 2013;227:137–44. doi:10.1016/j.jpowsour.2012.11.012.
- [176] Zhou Y, Lin G, Shih AJ, Hu SJ. A micro-scale model for predicting contact resistance between bipolar plate and gas diffusion layer in PEM fuel cells. *J Power Sources* 2007;163:777–83. doi:10.1016/j.jpowsour.2006.09.019.
- [177] Avasarala B, Haldar P. Effect of surface roughness of composite bipolar plates on the contact resistance of a proton exchange membrane fuel cell. *J Power Sources* 2009;188:225–9. doi:10.1016/j.jpowsour.2008.11.063.
- [178] Kraysberg A, Auinat M, Ein-Eli Y. Reduced contact resistance of PEM fuel cell's bipolar plates via surface texturing. *J Power*

Sources 2007;164:697–703. doi:10.1016/j.jpowsour.2006.11.033.

- [179] Lai Y-H, Rapaport PA, Ji C, Kumar V. Channel intrusion of gas diffusion media and the effect on fuel cell performance. *J Power Sources* 2008;184:120–8. doi:10.1016/j.jpowsour.2007.12.065.
- [180] Pero-Sanz Elorz JA, Quintana Hernández MJ, Verdeja González LF. Solidification and Solid-State Transformations of Metals and Alloys. 2017.
- [181] Stefanescu D, Ruxanda R. Fundamentals of Solidification. *ASM Handb. vol. 9 – Metallogr. Microstruct.*, vol. 9, 2004, p. 71–92.
- [182] Maveety JG, Liu P, Vijayan J, Hua F, Sanchez EA. Effect of cooling rate on microstructure and shear strength of pure Sn, Sn-0.7Cu, Sn-3.5Ag, and Sn-37Pb solders. *J. Electron. Mater.*, vol. 33, 2004, p. 1355–62. doi:10.1007/s11664-004-0165-z.
- [183] Hurtony T, Szakál A, Almásy L, Len A, Kugler S, Bonyár A, et al. Characterization of the microstructure of tin-silver lead free solder. *J Alloys Compd* 2016;672:13–9. doi:10.1016/j.jallcom.2016.02.177.
- [184] Ralston KD, Birbilis N, Davies CHJ. Revealing the relationship between grain size and corrosion rate of metals. *Scr Mater* 2010;63:1201–4. doi:10.1016/j.scriptamat.2010.08.035.
- [185] Ralston KD, Birbilis N. Effect of grain size on corrosion: A review. *Corrosion* 2010;66:0750051–07500513. doi:10.5006/1.3462912.
- [186] Osório WR, Spinelli JE, Afonso CRM, Peixoto LC, Garcia A. Microstructure, corrosion behaviour and microhardness of a directionally solidified Sn-Cu solder alloy. *Electrochim Acta* 2011;56:8891–9. doi:10.1016/j.electacta.2011.07.114.
- [187] Van Bennekom A, Robinson FPA. Effect of cooling rate on corrosion properties of 3CR12 type alloys. *Br Corros J* 1992;27:224–30. doi:10.1179/000705992798268576.
- [188] Yu C, Wang H, Gao X. Effect of cooling rate on microstructure and corrosion behavior of low alloy steel under H<sub>2</sub>S/CO<sub>2</sub>-saturated saline solution environment. *Int J Electrochem Sci* 2018;13:1527–41. doi:10.20964/2018.02.42.
- [189] Ochoa F, Williams J, Chawla N. Effects of cooling rate on the microstructure and tensile behavior of a Sn-3.5wt.%Ag solder. *J Electron Mater* 2003;32:1414–20.
- [190] El Din AMS, El Wahab FMA. On the anodic passivity of tin in alkaline solutions. *Electrochim Acta* 1964;9:883–96. doi:10.1016/0013-4686(64)85039-8.
- [191] Giannetti BF, Sumodjo PTA, Rabockai T. Electrochemical studies with tin electrodes in citric acid solutions. *J Appl Electrochem* 1990. doi:10.1007/BF01008881.
- [192] Ammar IA, Darwish S, Khalil MW, Galal A. The anodic behaviour and Passivity of Tin in sulphate solutions. *Materwiss Werksttech* 1983;14:330–6. doi:10.1002/mawe.19830141007.
- [193] Laitinen T, Salmi K, Sundholm G, Viinikka P, Yli-Pentti A. The anodic behaviour of tin in sulphuric acid solutions. *Electrochim Acta* 1992;37:1797–803. doi:10.1016/0013-4686(92)85083-W.
- [194] Jiang L, Volovitch P, Sundermeier U, Wolpers M, Ogle K. Dissolution and passive film formation of Sn and Sn coated steel using atomic emission spectroelectrochemistry. *Electrochim Acta* 2011;58:322–9. doi:10.1016/j.electacta.2011.09.046.
- [195] Alvarez PE, Ribotta SB, Folquer ME, Gervasi CA, Vilche JR. Potentiodynamic behaviour of tin in different buffer solutions. *Corros Sci* 2002;44:49–65. doi:10.1016/S0010-938X(01)00032-4.
- [196] Abd El-Rehim SS, Taha F, Saleh MB, Mohamed SA. On the pitting corrosion of tin by sulphate anion. *Corros Sci* 1992;33:1789–96. doi:10.1016/0010-938X(92)90009-R.
- [197] Abd El Rehim SS, El Samahi AA, El Sayed A. Breakdown of tin passivity in aqueous sodium stannate solution. *Br Corros J* 1985;20:196–200. doi:10.1179/000705985798272669.
- [198] Che Y, Han Z, Luo B, Xia D, Shi J, Gao Z, et al. Corrosion mechanism differences of tinplate in aerated and deaerated citric acid solution. *Int J Electrochem Sci* 2012;7:9997–10007.
- [199] Minami T, Miyata T, Yamamoto T. Stability of transparent conducting oxide films for use at high temperatures. *J Vac Sci Technol A Vacuum, Surfaces, Film* 1999;17:1822–6. doi:10.1116/1.581897.
- [200] Wild RN. SOME FATIGUE PROPERTIES OF SOLDERS AND SOLDER JOINTS., 1974, p. 105–17.
- [201] Fukuda M, Imayoshi K, Matsumoto Y. Effect of polyoxyethylenelauryl ether on electrodeposition of Pb-free Sn-Bi alloy. *Electrochim Acta* 2001;47:459–64. doi:10.1016/S0013-4686(01)00741-1.

- [202] Medvedev GI, Makrushin NA, Dubenkov AN. Electrodeposition of tin-bismuth alloy from sulfate bath containing organic additives. *Zashchita Met* 2003;39:424–7.
- [203] Medvedev GI, Rybin AA, Makrushin NA. Electrodeposition of tin-indium alloy from a sulfate electrolyte in the presence of organic substances. *Russ J Appl Chem* 2012;85:604–11. doi:10.1134/S107042721204012X.
- [204] Zorkina O V., Perelygin YP. Electrodeposition of the tin-indium alloy from the sulfate electrolyte. Proc. All-Russian Conf. "Progressive Technol. Ecol. issues Electroplat. Prod. Print. circuit boards," 2000, p. 48–9.
- [205] Indira KS, Udupa HVK. INDIUM AND INDIUM ALLOY DEPOSITION. *Met Finish* 1972;70:57–61.
- [206] Jo J-L, Nagao S, Hamasaki K, Tsujimoto M, Sugahara T, Suganuma K. Mitigation of Sn Whisker Growth by Small Bi Additions. *J Electron Mater* 2014;43:1–8. doi:10.1007/s11664-013-2706-9.
- [207] Suganuma K. Advances in lead-free electronics soldering. *Curr Opin Solid State Mater Sci* 2001;5:55–64. doi:10.1016/S1359-0286(00)00036-X.
- [208] Abtew M, Selvaduray G. Lead-free solders in microelectronics. *Mater Sci Eng R Reports* 2000;27:95–141. doi:10.1016/S0927-796X(00)00010-3.
- [209] Rajamani AR, Jothi S, Datta M, Rangarajan M. Electrodeposition of Tin-Bismuth Alloys: Additives, Morphologies and Compositions. *Journal Electrochem Soc* 2018;165:D50–7. doi:10.1149/2.1281714jes.
- [210] Tsai Y Da, Hu CC, Lin CC. Electrodeposition of Sn-Bi lead-free solders: Effects of complex agents on the composition, adhesion, and dendrite formation. *Electrochim Acta* 2007;53:2040–7. doi:10.1016/j.electacta.2007.09.002.
- [211] Sandnes E, Williams ME, Vaudin MD, Stafford GR. Equi-axed grain formation in electrodeposited Sn-Bi. *J Electron Mater* 2008;37:490–7. doi:10.1007/s11664-007-0369-0.
- [212] Heong CY, Haseeb ASMA, Goh Y, Fang LS. Effects of Sn concentration and current density on Sn-Bi electrodeposition in additive free plating bath. Proc. 4th Asia Symp. Qual. Electron. Des. ASQED 2012, 2012, p. 286–90. doi:10.1109/ACQED.2012.6320517.
- [213] Gao Y, Hu W, Gao X, Duan B. Electrodeposition of SnBi coatings based on deep eutectic solvent. *Surf Eng* 2014;30:59–63. doi:10.1179/1743294413Y.0000000198.
- [214] Vieira L, Burt J, Richardson PW, Schloffer D, Fuchs D, Moser A, et al. Tin, Bismuth, and Tin–Bismuth Alloy Electrodeposition from Chlorometalate Salts in Deep Eutectic Solvents. *ChemistryOpen* 2017;6:393–401. doi:10.1002/open.201700045.
- [215] Suh MS, Park CJ, Kwon HS. Effects of plating parameters on alloy composition and microstructure of Sn-Bi electrodeposits from methane sulphonate bath. *Surf Coatings Technol* 2006;200:3527–32. doi:10.1016/j.surfcoat.2004.08.162.
- [216] Kabassis H, Rutter JW, Winegard WC. Phase relationships in Bi–In–Sn alloy system. *Mater Sci Technol (United Kingdom)* 1986;2:985–8. doi:10.1179/mst.1986.2.10.985.
- [217] Wild RN. Properties of some low melting fusible alloys. 1971.
- [218] Mahmudi R, Geranmayeh AR, Mahmoodi SR, Khalatbari A. Effect of cooling rate on the room-temperature indentation creep of cast lead-free Sn-Bi solder alloys. *Phys Status Solidi Appl Mater Sci* 2007;204:2302–8. doi:10.1002/pssa.200622583.
- [219] Alfantazia A., Moskalyk R. Processing of indium: a review. *Miner Eng* 2003;16:687–94. doi:https://doi.org/10.1016/S0892-6875(03)00168-7.
- [220] Downs AJ. Chemistry of Aluminium, Gallium, Indium and Thallium. 1993. doi:10.1007/978-94-011-2170-5.
- [221] Geiger S, Kasian O, Mingers AM, Mayrhofer KJJ, Cherevko S. Stability limits of tin-based electrocatalyst supports. *Sci Rep* 2017;7. doi:10.1038/s41598-017-04079-9.
- [222] Glazer J. Metallurgy of low temperature pb-free solders for electronic assembly. *Int Mater Rev* 1995;40:65–93. doi:10.1179/imr.1995.40.2.65.
- [223] Mei Z, Morris JW. Superplastic creep of low melting point solder joints. *J Electron Mater* 1992;21:401–7. doi:10.1007/BF02660403.
- [224] Das Mahapatra S, Majumdar BS, Dutta I, Bhassyanantha S. Eliminating Whisker Growth by Indium Addition in Electroplated Sn on Copper Substrate. *J Electron Mater* 2017;46:4062–75. doi:10.1007/s11664-016-5177-y.
- [225] Shimauchi H, Suzuki K. Tin whisker-free tin or tin alloy plated article and coating technique thereof. US4959278A, 1989.

- [226] Makrushin NAE, Iosifovich MG, Rybin AA. METHOD OF ELECTROPLATING OF STANNUM-INDIUM ALLOY. RU2458188C1, 2011.
- [227] Tsunoda K, Tamura T. Tin-indium alloy electroplating solution. US6331240B1, 2000.
- [228] Dyer JR, Rowan TJ. Electrodeposition of indium and its alloys. US2458839A, 1949.
- [229] Walsh FC, Gabe DR. The electrodeposition of indium alloys. *Surf Technol* 1981;13:305–14. doi:10.1016/0376-4583(81)90104-7.
- [230] Das Mahapatra S, Dutta I. Co-electrodeposition of tin with 0.2–20% indium: Implications on tin whisker growth. *Surf Coatings Technol* 2018;337:478–83. doi:10.1016/J.SURFCOAT.2018.01.061.
- [231] SUZUKI H. The Plating of Indium-Tin Alloy. *J Met Finish Soc Japan* 1964;15:283–8. doi:10.4139/sfj1950.15.283.
- [232] OTA J, ISHIKAWA T, KOSAKAI K. Plating of Indium-Tin Alloy. *J Met Finish Soc Japan* 1965;16:246–50. doi:10.4139/sfj1950.16.246.
- [233] Mogilev VM, Falicheva AI. ELECTRODEPOSITION OF INDIUM-TIN ALLOYS. *Prot Met* 1974;10:182–3.
- [234] Abd el Rehim SS, Mostafa MA, Ahmed AM. Structural studies on electrodeposited indium on steel surfaces. *J Mater Sci Lett* 1988;7:1350–2. doi:10.1007/BF00719980.
- [235] TZENG G-S. Effects of additive agents on the kinetics of tin electrodeposition from an acidic solution of tin(II) sulfate. *Plat Surf Finish* 1995;82:67–71.
- [236] Lovrecek B, Markovac V. Studies of the Electrochemical Kinetics of Indium. *J Electrochem Soc* 1962;109:727. doi:10.1149/1.2425538.
- [237] Chung Y-H, Lee C-W. Electrochemical behaviors of Indium. *J Electrochem Sci Technol* 2012;3:1–13. doi:10.5229/jecst.2012.3.1.1.
- [238] Piercy R, Hampson NA. The indium electrode in chloride electrolytes. A kinetic study. *J Electroanal Chem* 1975;59:261–71. doi:10.1016/S0022-0728(75)80181-1.
- [239] Kongstein OE, Haarberg GM, Thonstad J. Current efficiency and kinetics of cobalt electrodeposition in acid chloride solutions. Part I: The influence of current density, pH and temperature. *J Appl Electrochem* 2007;37:669–74. doi:10.1007/s10800-007-9299-z.
- [240] Yuan B, Kongstein OE, Haarberg GM. Electrowinning of Iron in Aqueous Alkaline Solution Using a Rotating Cathode. *J Electrochem Soc* 2009;156:D64. doi:10.1149/1.3039998.
- [241] Kongstein OE, Haarberg GM, Thonstad J. Proton Transport during Electrodeposition of Cobalt in Chloride Electrolytes. *ECS Trans* 2011;33:3–17. doi:10.1149/1.3573584.
- [242] Ernst S, Hamann CH. The pH-dependence of the hydrogen exchange current density at smooth platinum in alkaline solution (KOH). *J Electroanal Chem* 1975;60:97–100. doi:10.1016/S0022-0728(75)80206-3.
- [243] Goldstein JI, Newbury DE, Michael JR, Ritchie NWM, Scott JHJ, Joy DC. Scanning electron microscopy and x-ray microanalysis. 2017. doi:10.1007/978-1-4939-6676-9.
- [244] Azizi O, Jafarian M, Gopal F, Heli H, Mahjani MG. The investigation of the kinetics and mechanism of hydrogen evolution reaction on tin. *Int J Hydrogen Energy* 2007;32:1755–61. doi:10.1016/j.ijhydene.2006.08.043.
- [245] Kita H. Electrocatalysis by d and sp Metals. *Electrochemistry*, 1977, p. 117–37. doi:10.1007/978-1-4615-6884-1\_11.
- [246] Brenner A. Theory of Electrodeposition of Alloys. General Considerations and Literature. *Electrodepos. Alloy.*, 1963, p. 267–75. doi:10.1016/b978-1-4831-9808-8.50017-4.
- [247] Goh Y, Lee SF, Haseeb ASMA. Formation of Sn-Bi solder alloys by sequential electrodeposition and reflow. *J Mater Sci Mater Electron* 2013;24:2052–7. doi:10.1007/s10854-012-1055-4.
- [248] Biswal A, Panda PK, Acharya AN, Mohapatra S, Swain N, Tripathy BC, et al. Role of Additives in Electrochemical Deposition of Ternary Metal Oxide Microspheres for Supercapacitor Applications. *ACS Omega* 2020;5:3405–17. doi:10.1021/acsomega.9b03657.
- [249] Anicai L, Petica A, Costovici S, Moise C, Brincoveanu O, Visan T. Electrodeposition of Sn-In Alloys Involving Deep Eutectic Solvents. *Coatings* 2019;9. doi:10.3390/coatings9120800.

- [250] Morimitsu M, Nakahara Y, Matsunaga M. Electrodeposition of indium-tin alloys from EMI-BF<sub>4</sub>-Cl melts. *Electrochemistry* 2005;73:754–7. doi:10.5796/electrochemistry.73.754.
- [251] Nawafune H, Nakatani T, Akamatsu K, Mizumoto S, Obata K, uchida E. Electrodeposition of Sn-In Eutectic Alloy from Sulfosuccinate Bath for Flip-Chip Interconnection. *J Japan Inst Electron Packag* 2002;5:349–52. doi:10.5104/jieip.5.349.
- [252] Dicks AL. The role of carbon in fuel cells. *J Power Sources* 2006;156:128–41. doi:10.1016/j.jpowsour.2006.02.054.
- [253] Yi P, Zhang D, Qiu D, Peng L, Lai X. Carbon-based coatings for metallic bipolar plates used in proton exchange membrane fuel cells. *Int J Hydrogen Energy* 2019;44:6813–43. doi:10.1016/j.ijhydene.2019.01.176.
- [254] Antunes RA, De Oliveira MCL, Ett G, Ett V. Carbon materials in composite bipolar plates for polymer electrolyte membrane fuel cells: A review of the main challenges to improve electrical performance. *J Power Sources* 2011;196:2945–61. doi:10.1016/j.jpowsour.2010.12.041.
- [255] Gervasio D. Fuel Cells - Proton-Exchange Membrane Fuel Cells | Gas Diffusion Layers. *Encycl. Electrochem. Power Sources*, 2009, p. 806–9. doi:10.1016/B978-044452745-5.00225-2.
- [256] Cindrella L, Kannan AM, Lin JF, Saminathan K, Ho Y, Lin CW, et al. Gas diffusion layer for proton exchange membrane fuel cells-A review. *J Power Sources* 2009;194:146–60. doi:10.1016/j.jpowsour.2009.04.005.
- [257] Shahgaldi S, Hamelin J. Improved carbon nanostructures as a novel catalyst support in the cathode side of PEMFC: A critical review. *Carbon N Y* 2015;94:705–28. doi:10.1016/j.carbon.2015.07.055.
- [258] Yu X, Ye S. Recent advances in activity and durability enhancement of Pt/C catalytic cathode in PEMFC: Part II: Degradation mechanism and durability enhancement of carbon supported platinum catalyst. *J Power Sources* 2007;172:145–54. doi:https://doi.org/10.1016/j.jpowsour.2007.07.048.
- [259] Reiser CA, Bregoli L, Patterson TW, Yi JS, Yang JD, Perry ML, et al. A reverse-current decay mechanism for fuel cells. *Electrochem Solid-State Lett* 2005;8. doi:10.1149/1.1896466.
- [260] Macauley N, Papadias DD, Fairweather J, Spornjak D, Langlois D, Ahluwalia R, et al. Carbon Corrosion in PEM Fuel Cells and the Development of Accelerated Stress Tests. *J Electrochem Soc* 2018;165:F3148–60. doi:10.1149/2.0061806jes.
- [261] Mehta V, Cooper JS. Review and analysis of PEM fuel cell design and manufacturing. *J Power Sources* 2003;114:32–53. doi:10.1016/S0378-7753(02)00542-6.
- [262] Borup RL, Vanderborgh NE. Design and testing criteria for bipolar plate materials for PEM fuel cell applications. *Mater. Res. Soc. Symp. - Proc.*, vol. 393, 1995, p. 151–5. doi:10.1557/proc-393-151.
- [263] Heo SI, Oh KS, Yun JC, Jung SH, Yang YC, Han KS. Development of preform moulding technique using expanded graphite for proton exchange membrane fuel cell bipolar plates. *J Power Sources* 2007;171:396–403. doi:10.1016/j.jpowsour.2007.05.110.
- [264] Fukutsuka T, Yamaguchi T, Miyano SI, Matsuo Y, Sugie Y, Ogumi Z. Carbon-coated stainless steel as PEFC bipolar plate material. *J Power Sources* 2007;174:199–205. doi:10.1016/j.jpowsour.2007.08.096.
- [265] Feng K, Shen Y, Sun H, Liu D, An Q, Cai X, et al. Conductive amorphous carbon-coated 316L stainless steel as bipolar plates in polymer electrolyte membrane fuel cells. *Int J Hydrogen Energy* 2009;34:6771–7. doi:10.1016/j.ijhydene.2009.06.030.
- [266] Wang WL, He SM, Lan CH. Protective graphite coating on metallic bipolar plates for PEMFC applications. *Electrochim Acta* 2012;62:30–5. doi:10.1016/j.electacta.2011.11.026.
- [267] El-kharouf A. Understanding GDL Properties and Performance in Polymer Electrolyte Fuel Cells. University of Birmingham, 2014.
- [268] Marinho B, Ghislandi M, Tkalya E, Koning CE, de With G. Electrical conductivity of compacts of graphene, multi-wall carbon nanotubes, carbon black, and graphite powder. *Powder Technol* 2012;221:351–8. doi:10.1016/j.powtec.2012.01.024.
- [269] American Elements n.d. <https://www.americanelements.com/> (accessed September 12, 2020).
- [270] Guo N, Leu MC. Effect of different graphite materials on the electrical conductivity and flexural strength of bipolar plates fabricated using selective laser sintering. *Int J Hydrogen Energy* 2012;37:3558–66. doi:10.1016/j.ijhydene.2011.11.058.
- [271] Wang X, Li W, Chen Z, Waje M, Yan Y. Durability investigation of carbon nanotube as catalyst support for proton exchange membrane fuel cell. *J Power Sources* 2006;158:154–9. doi:10.1016/j.jpowsour.2005.09.039.
- [272] Mohanta PK, Regnet F, Jörissen L. Graphitized Carbon: A promising stable cathode catalyst support material for long term

- PEMFC applications. *Materials* (Basel) 2018;11. doi:10.3390/ma11060907.
- [273] Laedre S, Kongstein OE, Oedegaard A, Seland F, Karoliussen H. In Situ and Ex Situ Contact Resistance Measurements of Stainless Steel Bipolar Plates for PEM Fuel Cells. *ECS Trans* 2013;50:829–39. doi:10.1149/05002.0829ecst.
- [274] Yousfi-Steiner N, Moçotéguy P, Candusso D, Hissel D. A review on polymer electrolyte membrane fuel cell catalyst degradation and starvation issues: Causes, consequences and diagnostic for mitigation. *J Power Sources* 2009;194:130–45. doi:10.1016/j.jpowsour.2009.03.060.
- [275] Hoare JP. Adsorption of oxygen on gold electrodes in aqueous solutions. *Electrochim Acta* 1964;9:1289–94. doi:10.1016/0013-4686(64)87005-5.
- [276] Cherevko S, Topalov AA, Katsounaros I, Mayrhofer KJJ. Electrochemical dissolution of gold in acidic medium. *Electrochem Commun* 2013;28:44–6. doi:10.1016/j.elecom.2012.11.040.
- [277] Canning NDS, Outka D, Madix RJ. The adsorption of oxygen on gold. *Surf Sci* 1984;141:240–54. doi:10.1016/0039-6028(84)90209-7.
- [278] Borup RL, Kusoglu A, Neyerlin KC, Mukundan R, Ahluwalia RK, Cullen DA, et al. Recent developments in catalyst-related PEM fuel cell durability. *Curr Opin Electrochem* 2020;21:192–200. doi:10.1016/j.coelec.2020.02.007.
- [279] Meier JC, Galeano C, Katsounaros I, Witte J, Bongard HJ, Topalov AA, et al. Design criteria for stable Pt/C fuel cell catalysts. *Beilstein J Nanotechnol* 2014;5:44–67. doi:10.3762/bjnano.5.5.
- [280] Rezaei Niya SM, Hoorfar M. Study of proton exchange membrane fuel cells using electrochemical impedance spectroscopy technique - A review. *J Power Sources* 2013;240:281–93. doi:10.1016/j.jpowsour.2013.04.011.
- [281] Eikerling M, Kornyshev AA. Electrochemical impedance of the cathode catalyst layer in polymer electrolyte fuel cells. *J Electroanal Chem* 1999;475:107–23. doi:10.1016/S0022-0728(99)00335-6.
- [282] Meland AK, Bedeaux D, Kjelstrup S. A Gerischer phase element in the impedance diagram of the polymer electrolyte membrane fuel cell anode. *J Phys Chem B* 2005;109:21380–8. doi:10.1021/jp050635q.
- [283] Reshetenko T, Kulikovskiy A. On the Origin of High Frequency Impedance Feature in a PEM Fuel Cell. *J Electrochem Soc* 2019;166:F1253–7. doi:10.1149/2.1201915jes.
- [284] Ciureanu M, Roberge R. Electrochemical impedance study of PEM fuel cells. Experimental diagnostics and modeling of air cathodes. *J Phys Chem B* 2002;105:3531–9. doi:10.1021/jp003273p.
- [285] Barbir F, Gorgun H, Wang X. Relationship between pressure drop and cell resistance as a diagnostic tool for PEM fuel cells. *J Power Sources* 2005;141:96–101. doi:10.1016/j.jpowsour.2004.08.055.
- [286] Newbury DE, Ritchie NWM. Is Scanning Electron Microscopy/Energy Dispersive X-ray Spectrometry (SEM/EDS) Quantitative? *J Scanning Microsc* 2013;35:141–68. doi:https://doi.org/10.1002/sca.21041.
- [287] Wilschefski S, Baxter M. Inductively Coupled Plasma Mass Spectrometry: Introduction to Analytical Aspects. *Clin Biochem Rev* 2019;40:115–33. doi:10.33176/aacb-19-00024.
- [288] Eudy I, Post M. Fuel Cell Buses in U.S. Transit Fleets: Current Status 2018. Golden, CO: 2018.
- [289] Drive U. Fuel Cell Technical Team Roadmap. 2017.
- [290] Zhang F, Ju P, Pan M, Zhang D, Huang Y, Li G, et al. Self-healing mechanisms in smart protective coatings: A review. *Corros Sci* 2018;144:74–88. doi:10.1016/j.corsci.2018.08.005.
- [291] Cui G, Bi Z, Wang S, Liu J, Xing X, Li Z, et al. A comprehensive review on smart anti-corrosive coatings. *Prog Org Coatings* 2020;148. doi:10.1016/j.porgcoat.2020.105821.
- [292] Samadzadeh M, Boura SH, Peikari M, Kasiriha SM, Ashrafi A. A review on self-healing coatings based on micro/nanocapsules. *Prog Org Coatings* 2010;68:159–64. doi:https://doi.org/10.1016/j.porgcoat.2010.01.006.
- [293] Zhang L, Finch J, Gontarz G, Wang C. Development of Low Cost PEMFC Metal Bipolar Plate. *ECS Trans* 2010;33:955–61. doi:10.1149/1.3484589.
- [294] James BD, Huya-Kouadio J, Houchins C, Desantis D. Mass Production Cost Estimation of Direct H<sub>2</sub> PEM Fuel Cell Systems for Transportation Applications: 2017 Update. 2017. doi:10.13140/RG.2.2.36532.55683.
- [295] Cairncross E. Health and environmental impacts of platinum mining: Report from South Africa. 2014.

- [296] Zhou D, Wang J, Han Z, Liu X, Mao J. Corrosion behavior of tinplate in aerated and deaerated NaCl solution. *Int J Electrochem Sci* 2017;12:639–51. doi:10.20964/2017.01.23.
- [297] G82-98(2009). Standard Guide for Development and Use of a Galvanic Series for Predicting Galvanic Corrosion Performance. ASTM B Stand 2003;98:1–7. doi:10.1520/G0082-98R09.2.
- [298] Papadias DD, Ahluwalia RK, Thomson JK, Meyer HM, Brady MP, Wang H, et al. Degradation of SS316L bipolar plates in simulated fuel cell environment: Corrosion rate, barrier film formation kinetics and contact resistance. *J Power Sources* 2015;273:1237–49. doi:10.1016/j.jpowsour.2014.02.053.
- [299] USGS. Mineral Commodity Summaries 2020. 2020. doi:<https://doi.org/10.3133/mcs202>.
- [300] Management Engineering and Production Services International Ltd Company Website n.d. <https://www.meps.co.uk> (accessed May 26, 2020).

# Appendices

## Scientific Paper

McCay K, Kongstein OE, Oedegaard A, Barnett AO, Seland F. “Soldering a gas diffusion layer to a stainless steel bipolar plate using metallic tin”, *Int. J. Hydrogen. Energy.* 43, 9006–14 (2018)



Available online at [www.sciencedirect.com](http://www.sciencedirect.com)

ScienceDirect

journal homepage: [www.elsevier.com/locate/ijhe](http://www.elsevier.com/locate/ijhe)

## Soldering a gas diffusion layer to a stainless steel bipolar plate using metallic tin

Katie McCay<sup>a,b,\*</sup>, Ole Edvard Kongstein<sup>b</sup>, Anders Oedegaard<sup>b</sup>,  
Alejandro Oyarce Barnett<sup>b</sup>, Frode Seland<sup>a</sup>

<sup>a</sup> Norwegian University of Science and Technology (NTNU), Department of Materials Science and Engineering, Norway

<sup>b</sup> SINTEF Materials and Chemistry, Norway

### ARTICLE INFO

#### Article history:

Received 27 November 2017

Received in revised form

23 March 2018

Accepted 27 March 2018

Available online 11 April 2018

#### Keywords:

PEM fuel cell

Stainless steel bipolar plate

Electrodeposition

Tin

Interfacial contact resistance

### ABSTRACT

A novel investigation to decrease the interfacial contact resistance of stainless steel bipolar plates was performed. A thin layer of Sn was electrodeposited onto a bipolar plate and subsequently joined with a gas diffusion layer through hot-pressing at a temperature around the melting point of tin. This procedure was optimised, depositing 30  $\mu\text{m}$  of Sn onto the stainless steel bipolar plate before hot-pressing at 230 °C and 0.5 bar for 20 min. A contact resistance of 5.45  $\text{m}\Omega\text{ cm}^2$  at 140  $\text{N cm}^{-2}$  was obtained, with low values maintained after exposure to both in-situ and ex-situ conditions. The in-situ testing in a fuel cell produced excellent results, with minor increases in contact resistance from 8.8 to 9.2  $\text{m}\Omega\text{ cm}^2$  and decreases in cell voltage from 0.714 to 0.667 V after 200 h of operation. These values are comparable to gold plated stainless steel, showing that combining a gas diffusion layer with electrodeposited Sn through hot-pressing is a promising low-cost coating for bipolar plates in PEM fuel cells.

© 2018 Hydrogen Energy Publications LLC. Published by Elsevier Ltd. All rights reserved.

### Introduction

In recent years, a greater demand for substitutes to fossil fuels has prompted the development of Proton Exchange Membrane (PEM) Fuel Cells. PEMFCs represent highly efficient energy conversion devices that are a viable alternative to combustion engines in the automobile industry [1]. Large car manufacturing companies, such as Toyota, Honda and Hyundai have set up long term plans to develop and introduce fuel cell technology for this industry [2–4]. However, a number of challenges have to be overcome before such electrochemical energy conversion devices are economically and

practically feasible for mass implementation, including intrinsic limitations concerning durability, longevity and costs.

Numerous studies have looked into development of improved catalysts [5–7], ion conducting membranes [8–10] and catalytic layers [11–13] for optimised performance. Over the last few decades, more attention has been devoted to the bipolar plate (BPP) which is estimated to contribute 11–45% of the overall fuel cell cost and 45–80% of the stack weight [14–17]. BPPs must allow even distribution and separation of the anode and cathode feeds, facilitate removal of the waste products, manage heat produced during operation, and

\* Corresponding author. Department of Materials Science and Engineering, Norwegian University of Science and Technology (NTNU), 7491 Trondheim, Norway.

E-mail address: [katie.mccay@ntnu.no](mailto:katie.mccay@ntnu.no) (K. McCay).

<https://doi.org/10.1016/j.ijhydene.2018.03.188>

0360-3199/© 2018 Hydrogen Energy Publications LLC. Published by Elsevier Ltd. All rights reserved.

provide mechanical support for the stack as well as the membrane electrode assembly (MEA) [17,18]. Due to their numerous tasks within the cell, the BPP must meet a strict series of criteria. The plates must be lightweight yet mechanically supportive to minimise overall weight, have high electrical conductivity and low interfacial contact resistance to both anode and cathode to minimise ohmic losses [19]. They must also be thermally conductive to remove excess heat, have high corrosion resistance to be long lasting and avoid contamination of catalyst and electrolyte as well as being impermeable to the reactant gases to minimise fuel crossover [20].

Consequently, a vast number of different BPP materials have been investigated [21–24]. Due to the inherent limitations of graphite [25] and other carbon based BPPs [17], metal plates are now considered the most promising candidates, with stainless steel found to be more suitable than titanium [26], nickel [27] or aluminium [28] alloy plates. Stainless steels have a significantly lower manufacturing cost and a higher strength than graphite [29], as well as a high electrical conductivity and low gas permeability. The main drawback of a metallic BPP is its struggle to maintain both low contact resistance and high corrosion resistance inside the fuel cell environment. When undergoing corrosion processes, the stainless steel releases metal ions that could lead to poisoning of the membrane and catalyst [17]. Another issue is the non-conductive oxide layer (e.g. chromium oxide,  $\text{Cr}_2\text{O}_3$ ) that forms on the surface of the stainless steel upon contact with air and water, increasing contact resistance [30]. In order to limit the formation of such oxides and ions, a series of protective coatings have been developed for the stainless steel BPPs. A large amount of research has been done into different coating materials, including carbon based coatings [31–33], metal nitrides [34–36], carbides [37–39] and noble metals [40,41], many of which have improved the corrosion resistance and the Interfacial Contact Resistance (ICR) of the BPP to the standards set by the US Department of Energy [42]. However, the coating methods for many of these BPPs, such as physical vapour deposition (PVD) or plasma nitriding, are costly, so a cheaper alternative must be found if stainless steel bipolar plates are to become commercially viable.

Tin is widely used as a solder in the electronics industry due to its high electrical conductivity, good wettability, low cost and reliability [43,44]. It is also easy to produce a well-defined layer of Sn by electrodeposition onto a metallic substrate, a technique that is popular due to its low cost, simplicity and good controllability of coating morphology and thickness [45,46]. As similar criteria need to be met for fuel cell applications, electrodeposition can be considered a good candidate for further research.

Tin has also been proven to improve the corrosion properties of stainless steels through the formation of a dense  $\text{SnO}_2$  passive layer, which inhibits further corrosion [47–49]. Despite this, Sn has been thought unsuitable for PEM applications due to the potential poisoning of the membrane and catalyst by Sn ions. This has proven not to be the case by Iwai et al., who reported no decomposition of nafion membranes when exposed to Sn [50], in fact, the proton conductivity and Young's modulus of nafion membranes is improved upon small additions of Sn [51]. It has been reported that  $\text{SnO}_2$

modified membranes have improved durability, reduced release of  $\text{F}^-$  ions and retained a higher Pt loading through the cell lifetime [52,53]. Sn based catalysts have also been used extensively for methanol oxidation with promoting effects [54–56], indicating that Sn has no negative impact on the catalyst or membrane during operation.

In this work we cover stainless steel bipolar plates with a thin and uniform layer of electroplated Sn in order to exploit the high electrical conductivity as well as the high corrosion resistance offered by metallic Sn and Sn oxide, respectively. The novel idea in this work is to join (solder) the tin-plated stainless steel bipolar plate with a pre-cut gas diffusion layer (GDL) through hot pressing at a temperature around the melting point of tin. This process softens the Sn coating, and the addition of mechanical pressure forces it into the pores of the GDL where it cools and solidifies, soldering the materials together as demonstrated in Fig. 1. This should produce improved through-plane electrical and thermal conductivity, yielding extremely low contact resistances.

The BPP will be exposed to operating PEM conditions, including a slightly acidic environment and voltages up to 1.4  $V_{\text{SHE}}$ , that may occur during start up and shut down [57]. During exposure, the outer layer of the deposited Sn will oxidise to form a passive  $\text{SnO}_2$  layer [58], as indicated by the Pourbaix diagram [59]. This layer remains conductive and protects the underlying Sn and stainless steel substrate from further oxidation, whilst maintaining a good conductivity and low contact resistance.

The preparation procedure and quality of the joined BPP/GDL material are studied with respect to conductivity and durability through a series of measurements, including interfacial contact resistance (ICR), ex-situ chronoamperometry and electron microscope imaging with elemental analysis. Finally, long-term in-situ testing in a simulated fuel cell environment is performed. The produced plates show good adhesion and low contact resistance, even after being exposed to a simulated fuel cell environment. Thus, the method described in this work brings a move towards simple, yet reliable, coating methods for BPPs in PEM systems.

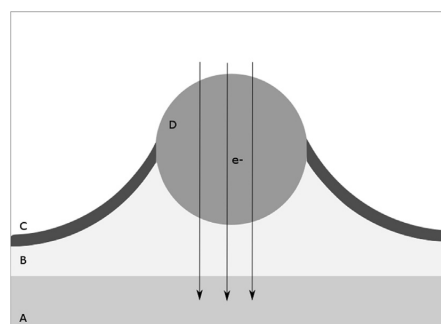


**Fig. 1 – The combined Sn/GDL concept. A is the steel bipolar plate, B the deposited Sn, C the  $\text{SnO}_2$  layer and D the carbon fibre from the GDL. Electrons can move through the system without obstruction whilst the  $\text{SnO}_2$  prevents further oxidation of Sn.**

## Experimental

AISI 316L bipolar plates were used as received from Elring Klinger for all tests. The total surface area of the plates was 39.2 cm<sup>2</sup>, with a land area of 6.2 cm<sup>2</sup> for ICR measurements. Potentiostatic and ICR measurements were recorded ex-situ, as well as Scanning Electron Microscopy (SEM) and Energy Dispersive Spectroscopy (EDS) analysis using a Hitachi S-3400N. In-situ fuel cell testing of the plates was performed using a Greenlight G-40 Fuel Cell Test Station equipped with a Gamry Reference 3000 Potentiostat.

### Construction of combined bipolar plate with GDL

Prior to all experimental work, the stamped SS316L BPP was etched in HCl (12.8 wt%, 3.5 M, room temperature, 15 min) to remove any oxide layer, followed by rinsing in deionized water and drying under nitrogen at room temperature. A coating of peel-able Micro super XP 2000 stop-off lacquer was then applied to the backside of the BPP with a paintbrush.

The electroplating solution was prepared as follows: Tin(II) sulfate (36.17 g, purity  $\geq$  95%, Sigma Aldrich) was dissolved in 700 ml deionized water (Milli-Q Integral pure water system). Sulphuric acid (98%, 100 ml, Sigma Aldrich) was added dropwise, and left to cool. SLOTTIN 71™ (Schlötter, 20 ml) starter and SLOTTIN 72™ (Schlötter, 3 ml) brightener were added to the solution, which was then diluted with deionized water to a total volume of 1.0 L. The stainless steel bipolar plate was immersed in the electroplating bath and connected to the negative pole of the current source. A pair of Sn electrodes were used as the counter electrode (positive pole) and a current density of 1.5 A dm<sup>-2</sup> was applied to obtain a deposition rate of 0.7  $\mu$ m min<sup>-1</sup> assuming 100% current efficiency.

After removal of the plate from the solution, it was cleaned with deionized water and the lacquer peeled from the back side. Immediately after, the cleaned plate was placed on top of a pre-cut GDL (H23C6 GDL, Freudenberg FFCT) [60], and hot-pressed at a set pressure, temperature and time before cooling to room temperature either slowly under applied pressure or rapidly at atmospheric pressure. This process was repeated for three identical plates to obtain a standard deviation.

### Interfacial contact resistance (ICR) measurements

ICR measurements were performed before and after each corrosion test using a setup adapted from Wang et al. [61] and identical to the one used in Ref. [62]. The sample was placed between two gold-coated copper conducting plates, and a current of 2 A was passed between the bottom plate and the top plate. The voltage between a spring-loaded gold pin and the top plate, through the sample, was recorded as the compaction force was increased from 70 to 650 N cm<sup>-2</sup>. All quoted values for ICR are recorded at 140 N cm<sup>-2</sup>, which is the standard in-situ compaction pressure [61]. It was assumed that the bulk resistance of the gold and copper plates, as well as the bulk resistance of the SS316L BPP and GDL were negligible.

### Ex-situ corrosion testing

The bipolar plate specimens were evaluated for their corrosion characteristics through potentiostatic measurements using a Gamry Ref 600 potentiostat. The combined BPP/GDL functioned as the working electrode, and was submerged in a Na<sub>2</sub>SO<sub>4</sub> (0.1M)/H<sub>2</sub>SO<sub>4</sub> mixture adjusted to pH 5.5. A Pt mesh was used as the counter electrode. Prior to potentiostatic testing, electrolyte was injected into the channels of the bipolar plate with a syringe. A mercury-mercurous sulfate reference electrode (Hg/Hg<sub>2</sub>SO<sub>4</sub>/K<sub>2</sub>SO<sub>4</sub>sat, 0.64 V<sub>SHE</sub>) was connected to the working electrolyte compartment via a salt bridge. The electrolyte was heated to 80 °C and purged with nitrogen prior to all testing. All potentials in this work are recalculated and expressed versus a standard hydrogen electrode unless stated otherwise. For potentiostatic measurements, the samples were first stabilised at open circuit potential before applying a voltage of 1.4 V<sub>SHE</sub> for 1 h.

### In-situ fuel cell testing

A fuel cell test station equipped with a cell of active area of 15 cm<sup>2</sup> was used. The MEA was a GORE® PRIMEA® MEA of thickness 15  $\mu$ m, Pt content of 0.1 mg cm<sup>-2</sup> at the anode and 0.4 mg cm<sup>-2</sup> at the cathode. H23C6 GDL (Freudenberg FFCT) [60] was used throughout this study.

The fuel cell was constructed with two of the combined BPP and GDL plates, one placed on each side of a membrane electrode assembly (MEA) with the back side of the steel bipolar plates in direct contact with gold current collectors, and then clamped together. The clamping pressure was piston-regulated and separated from the sealing pressure at 200 kPa over the area of the bipolar plate, equivalent to 140 N cm<sup>-2</sup>. The cell was operated at 70 °C, with synthetic air supplied in excess at the cathode (AGA 99.999%, stoichiometry 5) and hydrogen in excess at the anode (AGA 99.999%, stoichiometry 3). The excess of gas ensured a stable performance and minimum variation in reactant concentration throughout the entire length of the bipolar plate. Backpressures of 20 kPa and 30 kPa were applied to the anode and cathode, respectively.

The catalytic layers and membrane interactions were activated for 1 h in fully humidified N<sub>2</sub>, 70 °C, at both the anode and cathode, followed by cycling for 3 h between 0.7 V and 0.5 V under H<sub>2</sub>/air.

A cycling procedure of high and low current densities (1.2 and 0.5 A cm<sup>-2</sup>), interspaced with shut-downs and start-ups, as seen in Fig. 2, was performed for 170 h.

After completion of the initial 170 h test procedure, the cell was shut-down and purged with nitrogen overnight before the test was resumed until a total of 200 h of testing was complete.

Over the course of the in-situ testing, impedance measurements were recorded during high current density operation, over a frequency range of 10 kHz–100 mHz. The real value of the impedance recorded at 1 kHz was used as the high frequency resistance (HFR), and assumed to represent the ohmic resistance in the circuit. Cyclic voltammetry of the fuel cell was conducted with H<sub>2</sub> on the anode and N<sub>2</sub> on the cathode to provide an estimate of the change in the electrochemical active surface (ECSA) area at the cathode.

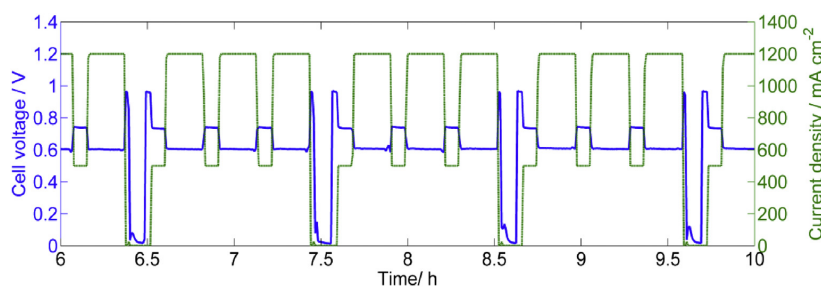


Fig. 2 – The cycling procedure during in-situ testing.

The same procedure was implemented for two control plates, gold coated SS316L and TiN + C coated SS316L, both provided by Elring Klinger.

## Results & discussion

### Optimisation of procedure: combining BPP and GDL with Sn

The procedure for combining the metallic plate with the GDL through Sn impregnation via hot pressing was optimised firstly with respect to lowest possible ICR and then to highest corrosion resistance. The effects on interfacial contact resistance and corrosion rate of various preparation parameters such as hot press pressure, temperature and time, as well as deposition charge (coating thickness) and cooling method, were investigated. Before the Sn/GDL plates could be tested in-situ, each of these parameters was optimised to increase performance.

#### Hot pressing

When hot pressing, the pressure was set at  $140 \text{ N cm}^{-2}$ , equivalent to the in-situ pressure. Increasing the pressure could cause flattening of the BPP channels, compromising the structure. Blocking of the channels by the GDL could also occur, reducing the cell performance by hindering the transport of reactants into and waste products out of the cell. Lower pressures reduce adhesion between the GDL and BPP as permeation of the Sn into the GDL is lessened, reducing the length of the conduction pathway and the conductivity.

When optimising the hot pressing temperature, those around the melting point of Sn ( $231.9 \text{ }^\circ\text{C}$  [63]) were selected to investigate how the degree of melting of Sn could produce a best possible electronic contact between the metallic plate and the carbon based GDL. Table 1 shows the ICR values recorded

Table 1 – Contact resistance ( $\text{m}\Omega \text{ cm}^2$ ) at various hot press times and temperatures.

Press temp ( $^\circ\text{C}$ )	226	228	230	232
Press time (min)				
1	7.9	6.5	6.6	5.4
10	8.3	8.4	5.4	7.6
60	6.0	9.2	4.4	5.6

after pressing at temperatures between 226 and  $232 \text{ }^\circ\text{C}$ . At temperatures above  $230 \text{ }^\circ\text{C}$ , the Sn becomes ductile enough to penetrate the GDL more effectively, ensuring an increased contact area and a better pathway for current, lowering the average ICR from  $8.0 \text{ m}\Omega \text{ cm}^2$  at  $228 \text{ }^\circ\text{C}$  down to  $5.4 \text{ m}\Omega \text{ cm}^2$  at  $230 \text{ }^\circ\text{C}$ . In addition to an improved through-plane electronic conductivity, the plates prepared with a hot press temperature of  $230 \text{ }^\circ\text{C}$  offered an improved adhesion due to the infiltration of GDL fibres into the tin, something that did not occur at temperatures lower than  $230 \text{ }^\circ\text{C}$ . Raising the temperature even further causes the Sn to run into the channels.

For this reason, a temperature of  $230 \text{ }^\circ\text{C}$  was used for all further plates.

The time required for hot pressing was also investigated. Varying the hot-press time from 1 to 60 min produced variations in contact resistance with no clear pattern, as seen in Table 1. 20 min was found to be a suitable duration to allow the Sn to reach the desired temperature.

#### Cooling method

The effect on ICR of cooling the samples using two different methods was investigated (Fig. 3). The ICRs for both cooling rapidly under atmospheric pressure (fast cool) or slowly under applied pressure (slow cool) were comparable before corrosion, at 6.8 and  $7.1 \text{ m}\Omega \text{ cm}^2$  at  $140 \text{ N cm}^{-2}$ . After polarization to 1.4 V for 1 h, a significantly improved ICR was observed for the slowly cooled plate, 13.2 compared to  $17.9 \text{ m}\Omega \text{ cm}^2$  at  $140 \text{ N cm}^{-2}$ . The slow cooling is suggested to result in increased grain sizes and fewer grain boundaries and

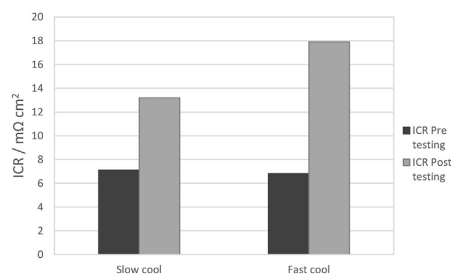


Fig. 3 – Comparison of the quickly vs slowly cooled plates before and after corrosion testing.

therefore fewer active sites for corrosion [64]. In addition, leaving the sample under continuous pressure when being cooled forces the Sn to stay in contact with the GDL whilst solidifying.

This shows the importance of precise control of processing parameters. The slower cooling procedure was used in the production of all further plates.

#### Thickness of Sn layer

It is important that the Sn layer is thick enough to allow the Sn to permeate into the GDL and form a good contact. ICR measurements before and after corrosion testing were done for a series of Sn thicknesses from 10 to 60  $\mu\text{m}$  (Fig. 4).

Before corrosion testing, all ICR values were lower than DoE requirements, and decreased with an increasing tin-plating thickness, most likely due to greater permeation of the Sn into the GDL and increased electrical contact between the layers. In addition, the bulk resistance of Sn is low ( $1.09 \times 10^{-7} \Omega \text{ m}$  [65]), so a thicker layer does not impact negatively on the conductivity. In fact, the contact resistance measured initially was lower than values obtained from gold and cleaned stainless steel plates using the same equipment. This is a clear indication that hot-pressing the tin-plated BPP with the GDL produces a better conduction pathway than simply placing the GDL on top of the BPP.

After potentiostatic testing for 1 h at 1.4 V, the ICR of the samples increased vastly, up to 560% for the thinner coatings. The significant increase in through-plane resistivity must be due to detrimental oxidation processes occurring during the high potential operation. Fig. 5 shows cross-sectional EDS images for the series of tin-plating thicknesses after corrosion testing. It is clear that the corrosion testing led to a significant removal of tin. In fact, the deposited Sn layer (green colour) in Fig. 5A (10  $\mu\text{m}$ ) was reduced from a thickness of 10  $\mu\text{m}$  to being non-existent. Furthermore, the GDL (red colour) is also not present in Fig. 5A. The removal of Sn during corrosion testing reduced adhesion between the GDL and BPP enough that the GDL entirely delaminated from the plate. From Fig. 5B (20  $\mu\text{m}$ ), there is also very little of the Sn layer remaining, but just

enough to continue to adhere the GDL to the BPP. The Sn is oxidised to  $\text{SnO}_2$  during the corrosion testing, but instead of providing corrosion protection to the underlying Sn bulk deposit it delaminates and falls off the plate into the electrolyte.

As the thickness of the Sn layer increases, in Fig. 5C, D, E and F, there is more Sn left after corrosion and consequently greater adhesion. Interestingly, the ICR of the thickest coatings, 50 and 60  $\mu\text{m}$ , also increased by a large amount, up to 570%, after polarization to 1.4 V for 1 h. This is possibly due to the larger volume of  $\text{SnO}_2$  formed during the corrosion process.  $\text{SnO}_2$  has a lower conductivity than metallic Sn [63], contributing to the observed increase in ICR. Additionally, the  $\text{SnO}_2$  produced after testing has a larger volume than Sn, so falls off the surface of the Sn and causes delamination between the remaining Sn layer and the GDL. This excess  $\text{SnO}_2$  is not visible in the EDS images, as it is removed during the corrosion testing, as observed by a milky white suspension in the electrolyte.

From Fig. 4, the best performing bipolar plate was found to have a Sn layer thickness of around 30  $\mu\text{m}$ , which was then used for all subsequent plates. As seen in the images in Fig. 5(C and D), it is obvious that the Sn has permeated into the GDL during the hot-pressing stage, so despite the loss of Sn that took place during the high voltage procedure, there is still a good conduction pathway and the ICR remains low. The ICR increased by around 260% after corrosion testing. Despite this being less than for the other thicknesses, all of which showed better performance than bare SS316L, there is still a necessity to improve the deposition process or stabilise the  $\text{SnO}_2$  layer that is formed after exposure to the PEM environment.

#### In-situ analysis

An in-situ study of the optimised Sn/GDL BPP was performed and compared to identical tests on Au and TiN + C coated SS316L BPPs. Both before and after the 200 h cycling procedure, a full series of standard measurements including electrochemical active surface area (ECSA), H-cross-over and high

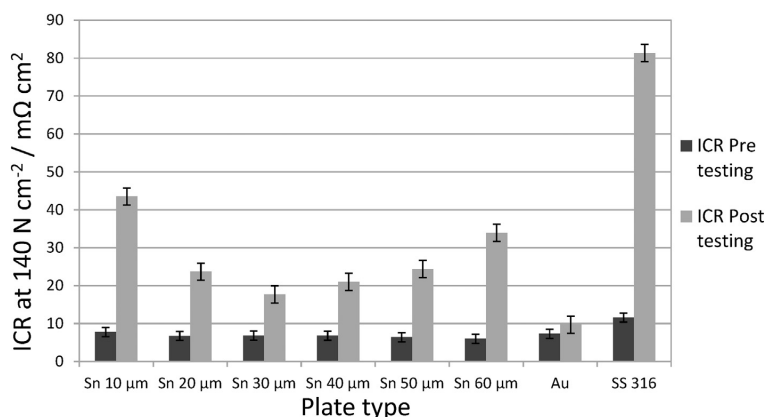
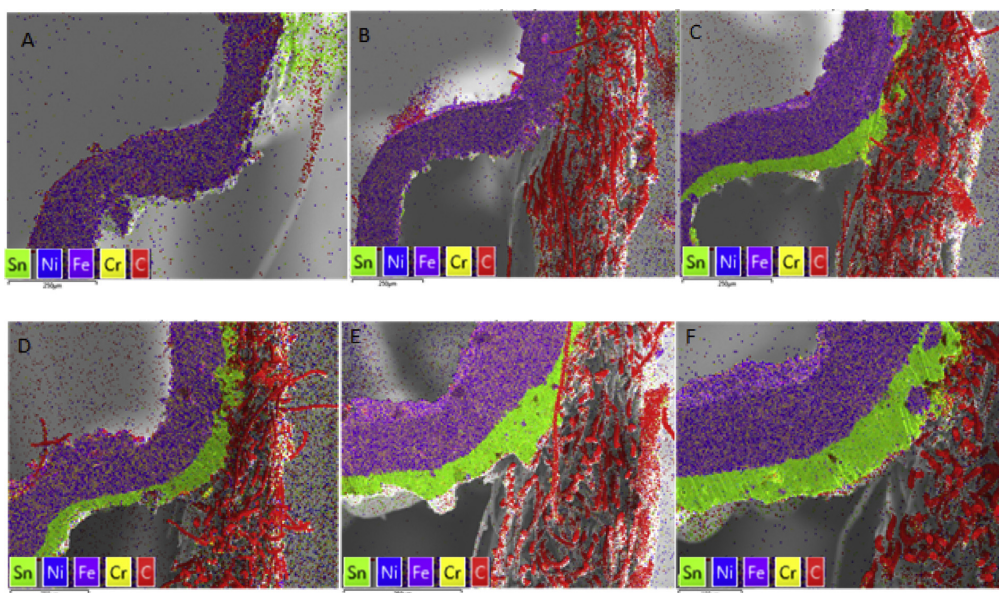
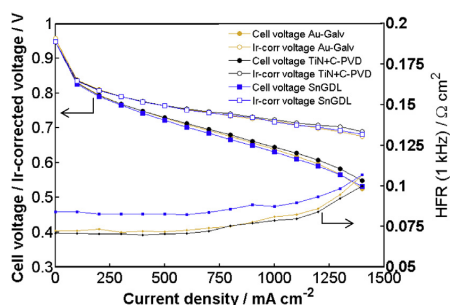


Fig. 4 – Comparison of coating thickness against ICR before and after ex-situ testing.



**Fig. 5 – Cross-sectional EDS images of BPPs & GDL with varying thickness of Sn after ex-situ testing, purple representing the bipolar plate, green the Sn and red the GDL. The initial thickness of deposits was 10, 20, 30, 40, 50 and 60  $\mu\text{m}$  on figure A to F respectively. (For interpretation of the references to color in this figure legend, the reader is referred to the Web version of this article.)**



**Fig. 6 – Beginning of life performance of the fuel cell equipped with Au (yellow) TiN + C (black) and Sn/GDL (blue) bipolar plates. (For interpretation of the references to color in this figure legend, the reader is referred to the Web version of this article.)**

frequency resistance (HFR) were undertaken to ensure normal operation of the cell.

Some differences in performance were observed at the beginning of life, as seen in Fig. 6. The HFR for the Sn/GDL plate is higher than for the other two plates, and the cell voltage is lower, 0.630 V at 1 A  $\text{cm}^{-2}$  compared to 0.639 V and 0.645 V for Au and TiN + C, respectively. These differences arise from differing resistances within the cell, which include all ohmic losses: membrane resistance, electronic resistances and all contact resistances.

During cycling, the cell voltage and HFR were monitored. A visible drop in cell voltage and an increase in HFR, as seen in Fig. 7, occurs for all plates due to the degradation of the membrane and a reduction in ECSA. The Sn/GDL bipolar plate is degrading at a slower rate than the other bipolar plates, despite its initially poorer performance. After 170 h of cycling, all plates show similar cell voltages. Moreover, after the shut down and a further 30 h of operation, the Sn/GDL and TiN + C plates outperform the Au standards, with a higher cell voltage maintained after a total of 200 h of operation.

There are no indications that any formation of  $\text{SnO}_2$  on the Sn/GDL plate is affecting performance, as was the case during potentiostatic ex-situ testing. Cyclic voltammetry confirmed that there is no adsorption of Sn onto the catalyst, and although a decrease in catalytic surface area was observed, this is consistent with the control plates, indicating no negative effect of Sn on the catalyst. Nor is the Sn affecting the membrane performance as the HFR after 200 h is equal for all plates (Fig. 7).

Comparing the voltage performance, the BPP that ended up with the smallest total drop in cell voltage was the Sn/GDL BPP, with a drop from 0.714 to 0.667, indicating that it would have the longest lifetime in the cell. More long term testing is needed to confirm this.

After testing for 200 h, the plates were removed from the cell and their ICR was tested ex-situ, as seen in Table 2.

The Sn/GDL combined plate performed well when compared with the control plates, with a very small increase in ICR being observed at the anode side. However, a significant increase was observed on the cathode side of the cell. As no

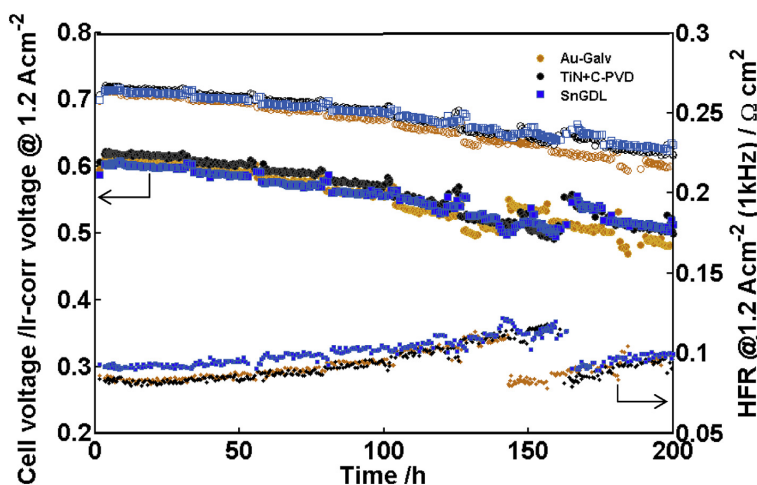


Fig. 7 – 200 h in-situ cell voltage and high frequency resistance performance of a PEM fuel cell equipped with Au (yellow circles), TiN + C (black circles) and Sn/GDL (blue squares) BPPs. (For interpretation of the references to color in this figure legend, the reader is referred to the Web version of this article.)

**Table 2 – Ex-situ interfacial contact resistance measurements before and after in-situ testing.**

Plate	ICR before (mOhm cm <sup>2</sup> )	ICR after - Anode (mOhm cm <sup>2</sup> )	ICR after - Cathode (mOhm cm <sup>2</sup> )
Au	7.7	7.2	7.4
TiN + C	8.4	9.3	10.3
Sn/GDL	8.8	9.2	19.7

corresponding sharp increase in HFR was observed in-situ, the increase observed during the ex-situ ICR could be due to post-mortem disassembly of the cell, during which the GDL may slightly delaminate from the Sn-coated BPP.

## Conclusions

A novel bipolar plate concept that significantly diminishes the interfacial contact resistance with the gas diffusion layer was successfully demonstrated. An optimised electrodeposition process was developed to produce a combined Sn/GDL protective layer on an SS316L bipolar plate. Very low ICR values were obtained before ex-situ corrosion testing, due to the uninhibited conduction pathways connecting the GDL and BPP through the soldered tin. If maintained in-situ, these pathways will provide easy conduction through the lifetime of the cell. However, the ICR increased after corrosion testing due to the instability of SnO<sub>2</sub> on the surface of the coating leading to the breakdown of the conduction pathways.

The optimised conditions for the deposition of Sn onto the SS316L BPP are as follows: A plating thickness of 30 μm was deposited onto the pre-cleaned BPP, before hot pressing with a pre-cut GDL at 230 °C for 20 min at a pressure of 0.5 bar, and cooling slowly to room temperature. This procedure obtained

the lowest contact resistance of 6.5 mΩ cm<sup>2</sup> at 140 Ncm<sup>-2</sup>, well below U.S DoE targets, and was tested both ex-situ and in-situ. The contact resistance increased to 13.2 mΩ cm<sup>2</sup> at 140 Ncm<sup>-2</sup> after ex-situ testing in Na<sub>2</sub>SO<sub>4</sub> at pH 5.5 and 80 °C, with 1.4 V<sub>SHE</sub> applied for 1 h. In-situ testing produced results equivalent to high-cost PVD coatings, with interfacial contact resistance values increasing from 8.8 to 9.2 mΩ cm<sup>2</sup> on the anode side and 19.7 mΩ cm<sup>2</sup> on the cathode side, and the cell voltage decreasing from 0.714 to 0.667 V over the course of 200 h. No degradation of the catalyst or membrane caused by the release of Sn ions from the bipolar plate was observed after 200 h.

Future work must focus on enhancing the stability of the SnO<sub>2</sub> oxide layer, and introducing alloying elements to improve long-term performance.

## Acknowledgements

The research leading to these results has received funding from the European Union's Seventh Framework Programme (FP7/2007-2013) for the Fuel Cells and Hydrogen Joint Technology Initiative under grant agreement number 303449 10.

KM thanks the Department of Materials Science and Engineering at NTNU for the award of a scholarship.

## REFERENCES

- [1] Wang Y, Chen KS, Mishler J, Cho SC, Adroher XC. A review of polymer electrolyte membrane fuel cells: technology, applications, and needs on fundamental research. *Appl Energy* 2011;88:981–1007. <https://doi.org/10.1016/j.apenergy.2010.09.030>.
- [2] Barrett S. Fuel cells power forward on the roads and for power generation. *Renew Energy Focus* 2017;18:29–32. <https://doi.org/10.1016/J.REF.2017.03.002>.

- [3] Samuelsen S. The automotive future belongs to fuel cells range, adaptability, and refueling time will ultimately put hydrogen fuel cells ahead of batteries. *IEEE Spectr* 2017;54:38–43. <https://doi.org/10.1109/MSPEC.2017.7833504>.
- [4] Kojima K, Fukazawa K. Current status and future outlook of fuel cell vehicle development in Toyota. *ECS Trans* 2015;69:213–9. <https://doi.org/10.1149/06917.0213ecst>.
- [5] Zhang S, Yuan X-Z, Hin JNC, Wang H, Friedrich KA, Schulze M. A review of platinum-based catalyst layer degradation in proton exchange membrane fuel cells. *J Power Sources* 2009;194:588–600. <https://doi.org/10.1016/j.jpowsour.2009.06.073>.
- [6] Shao Y, Sui J, Yin G, Gao Y. Nitrogen-doped carbon nanostructures and their composites as catalytic materials for proton exchange membrane fuel cell. *Appl Catal B Environ* 2008;79:89–99. <https://doi.org/10.1016/j.apcatb.2007.09.047>.
- [7] Dai L, Xue Y, Qu L, Choi H-J, Baek J-B. Metal-Free catalysts for oxygen reduction reaction. *Chem Rev* 2015;115:4823–92. <https://doi.org/10.1021/cr5003563>.
- [8] Kreuer K-D. Ion conducting membranes for fuel cells and other electrochemical devices. *Chem Mater* 2013;26:361–80. <https://doi.org/10.1021/cm402742u>.
- [9] Smitha B, Sridhar S, Khan AA. Solid polymer electrolyte membranes for fuel cell applications - a review. *J Membr Sci* 2005;259:10–26. <https://doi.org/10.1016/j.memsci.2005.01.035>.
- [10] Peighambaroust SJ, Rowshanzamir S, Amjadi M. Review of the proton exchange membranes for fuel cell applications. *Int J Hydrogen Energy* 2010;35:9349–84.
- [11] Banham D, Ye S. Current status and future development of catalyst materials and catalyst layers for proton exchange membrane fuel cells: an industrial perspective. *ACS Energy Lett* 2017;2:629–38. <https://doi.org/10.1021/acseenergylett.6b00644>.
- [12] Shao Y, Liu J, Wang Y, Lin Y. Novel catalyst support materials for PEM fuel cells: current status and future prospects. *J Mater Chem* 2009;19:46–59. <https://doi.org/10.1039/b808370c>.
- [13] Zhang J. PEM fuel cell electrocatalysts and catalyst layers: fundamentals and applications. 2008. <https://doi.org/10.1007/978-1-84800-936-3>.
- [14] Wang H, Turner JA. Reviewing metallic PEMFC bipolar plates. *Fuel Cell* 2010;10:510–9. <https://doi.org/10.1002/fuce.200900187>.
- [15] Yuan XZ, Wang HJ, Zhang JJ, Wilkinson DP. Bipolar plates for PEM fuel cells - from materials to processing. *J New Mater Electrochem Syst* 2005;8:257–67.
- [16] Mehta V, Cooper JS. Review and analysis of PEM fuel cell design and manufacturing. *J Power Sources* 2003;114:32–53. [https://doi.org/10.1016/S0378-7753\(02\)00542-6](https://doi.org/10.1016/S0378-7753(02)00542-6).
- [17] Antunes RA, Oliveira MCL, Ett G, Ett V. Corrosion of metal bipolar plates for PEM fuel cells: a review. *Int J Hydrogen Energy* 2010;35:3632–47. <https://doi.org/10.1016/j.ijhydene.2010.01.059>.
- [18] Peng L, Yi P, Lai X. Design and manufacturing of stainless steel bipolar plates for proton exchange membrane fuel cells. *Int J Hydrogen Energy* 2014;39:21127–53. <https://doi.org/10.1016/j.ijhydene.2014.08.113>.
- [19] Netwall CJ, Gould BD, Rodgers JA, Nasello NJ, Swider-Lyons KE. Decreasing contact resistance in proton-exchange membrane fuel cells with metal bipolar plates. *J Power Sources* 2013;227:137–44. <https://doi.org/10.1016/j.jpowsour.2012.11.012>.
- [20] Zhang JJ, Zhang H, Wu JJ, Zhang JJ, Zhang H. PEM fuel cell testing and diagnosis. 2013. <https://doi.org/10.1016/B978-0-444-53688-4.00007-3>.
- [21] Tawfik H, Hung Y, Mahajan D. Metal bipolar plates for PEM fuel cell-A review. *J Power Sources* 2007;163:755–67. <https://doi.org/10.1016/j.jpowsour.2006.09.088>.
- [22] Taherian R. A review of composite and metallic bipolar plates in proton exchange membrane fuel cell: materials, fabrication, and material selection. *J Power Sources* 2014;265. <https://doi.org/10.1016/j.jpowsour.2014.04.081>.
- [23] Asri NF, Husaini T, Sulong AB, Majlan EH, Daud WRW. Coating of stainless steel and titanium bipolar plates for anticorrosion in PEMFC: a review. *Int J Hydrogen Energy* 2016. <https://doi.org/10.1016/j.ijhydene.2016.06.241>.
- [24] Hermann A, Chaudhuri T, Spagnol P. Bipolar plates for PEM fuel cells: a review. *Int J Hydrogen Energy* 2005;30:1297–302. <https://doi.org/10.1016/j.ijhydene.2005.04.016>.
- [25] Kakati BK, Ghosh A, Verma A. Efficient composite bipolar plate reinforced with carbon fiber and graphene for proton exchange membrane fuel cell. *Int J Hydrogen Energy* 2013;38:9362–9. <https://doi.org/10.1016/j.ijhydene.2012.11.075>.
- [26] Wang SH, Peng J, Lui WB. Surface modification and development of titanium bipolar plates for PEM fuel cells. *J Power Sources* 2006;160:485–9. <https://doi.org/10.1016/j.jpowsour.2006.01.020>.
- [27] Brady MP, Wang H, Yang B, Turner JA, Bordignon M, Molins R, et al. Growth of Cr-Nitrides on commercial Ni-Cr and Fe-Cr base alloys to protect PEMFC bipolar plates. *Int J Hydrogen Energy* 2007;32:3778–88. <https://doi.org/10.1016/j.ijhydene.2006.08.044>.
- [28] Mawdsley JR, Carter JD, Wang X, Niyogi S, Fan CQ, Koc R, et al. Composite-coated aluminum bipolar plates for PEM fuel cells. *J Power Sources* 2013;231:106–12. <https://doi.org/10.1016/j.jpowsour.2012.12.074>.
- [29] Sun H, Cooke K, Eitzinger G, Hamilton P, Pollet B. Development of PVD coatings for PEMFC metallic bipolar plates. *Thin Solid Films* 2013. <https://doi.org/10.1016/j.tsf.2012.10.094>.
- [30] Lædre S, Kongstein OE, Oedegaard A, Seland F, Karoliusen H. The effect of pH and halides on the corrosion process of stainless steel bipolar plates for proton exchange membrane fuel cells. *Int J Hydrogen Energy* 2012;37:18537–46. <https://doi.org/10.1016/j.ijhydene.2012.09.021>.
- [31] Chung CY, Chen SK, Chin TS, Ko TH, Lin SW, Chang WM, et al. Catalyst layer-free carbon-coated steel-An easy route to bipolar plates of polymer electrolyte membrane fuel cells: characterization on structure and electrochemistry. *J Power Sources* 2009;186:393–8. <https://doi.org/10.1016/j.jpowsour.2008.10.047>.
- [32] Jin W, Feng K, Li Z, Cai X, Yu L, Zhou D, et al. Properties of carbon film deposited on stainless steel by close field unbalanced magnetron sputter ion plating. *Thin Solid Films* 2013;531:320–7. <https://doi.org/10.1016/j.tsf.2013.01.036>.
- [33] Husby H, Kongstein OE, Oedegaard A, Seland F. Carbon-polymer composite coatings for PEM fuel cell bipolar plates. *Int J Hydrogen Energy* 2014;39:951–7. <https://doi.org/10.1016/j.ijhydene.2013.10.115>.
- [34] Turan C, Cora OM, Koc M. Contact resistance characteristics of coated metallic bipolar plates for PEM fuel cells - investigations on the effect of manufacturing. *Int J Hydrogen Energy* 2012;37:18187–204. <https://doi.org/10.1016/j.ijhydene.2012.09.042>.
- [35] Jin J, Zhu Z, Zheng D. Influence of Ti content on the corrosion properties and contact resistance of CrTiN coating in simulated proton exchange membrane fuel cells. *Int J Hydrogen Energy* 2017;42:11758–70. <https://doi.org/10.1016/j.ijhydene.2017.02.014>.
- [36] Wang S, Hou M, Zhao Q, Jiang Y, Wang Z, Li H, et al. Ti/(Ti,Cr)N/CrN multilayer coated 316L stainless steel by arc ion plating as bipolar plates for proton exchange membrane fuel cells. *J Energy Chem* 2017;26:168–74. <https://doi.org/10.1016/j.jechem.2016.09.004>.
- [37] Wang L, Sun J, Kang B, Li S, Ji S, Wen Z, et al. Electrochemical behaviour and surface conductivity of niobium carbide-

- modified austenitic stainless steel bipolar plate. *J Power Sources* 2014;246:775–82. <https://doi.org/10.1016/j.jpowsour.2013.08.025>.
- [38] Zhao Y, Wei L, Yi P, Peng L. Influence of Cr-C film composition on electrical and corrosion properties of 316L stainless steel as bipolar plates for PEMFCs. *Int J Hydrogen Energy* 2016;41:1142–50. <https://doi.org/10.1016/j.ijhydene.2015.10.047>.
- [39] Huang NB, Yu H, Xu LS, Zhan S, Sun M, Kirk DW. Corrosion kinetics of 316L stainless steel bipolar plate with chromiumcarbide coating in simulated PEMFC cathodic environment. *Results Phys* 2016;6:730–6. <https://doi.org/10.1016/j.rinp.2016.10.002>.
- [40] Feng K, Li Z, Cai X, Chu PK. Silver implanted 316L stainless steel as bipolar plates in polymer electrolyte membrane fuel cells. *Mater Chem Phys* 2011;126:6–11. <https://doi.org/10.1016/j.matchemphys.2010.11.029>.
- [41] Lin K, Li X, Dong H, Du S, Lu Y, Ji X, et al. Surface modification of 316 stainless steel with platinum for the application of bipolar plates in high performance proton exchange membrane fuel cells. *Int J Hydrogen Energy* 2017;42:2338–48. <https://doi.org/10.1016/j.ijhydene.2016.09.220>.
- [42] US Department of Energy office of energy efficiency and renewable energy U. US DOE Technical Targets for Polymer Electrolyte Membrane Fuel Cell Components 2017. <https://energy.gov/eere/fuelcells/doe-technical-targets-polymer-electrolyte-membrane-fuel-cell-components> [Accessed August 10 2017].
- [43] Lau JH, Wong CP, Lee N-C, Lee S-WR. *Electronics manufacturing: with lead-free, halogen-free, and conductive-adhesive materials*. The McGraw-Hill Companies, Inc; 2003.
- [44] Chriástelová J, Özvold M. Properties of solders with low melting point. *J Alloy Comp* 2008;457:323–8. <https://doi.org/10.1016/j.jallcom.2007.03.062>.
- [45] Melo RL, Casciano PNS, Correia AN, Lima-Neto P de. Characterisation of electrodeposition and heat-treated Ni–Mo–P coatings. *J Braz Chem Soc* 2012;23:328–34. <https://doi.org/10.1590/S0103-50532012000200020>.
- [46] Zhu XB, Cai C, Zheng GQ, Zhang Z, Li JF. Electrodeposition and corrosion behavior of nanostructured Ni-TiN composite films. *Trans Nonferr Met Soc China (English Ed)* 2011;21:2216–24. doi:10.1016/S1003-6326(11) 60998–60999.
- [47] Pardo A, Merino MC, Carboneras M, Coy AE, Arrabal R. Pitting corrosion behaviour of austenitic stainless steels with Cu and Sn additions. *Corros Sci* 2007;49:510–25. <https://doi.org/10.1016/j.corsci.2006.06.004>.
- [48] Pardo A, Merino MC, Carboneras M, Viejo F, Arrabal R, Muñoz J. Influence of Cu and Sn content in the corrosion of AISI 304 and 316 stainless steels in H<sub>2</sub>SO<sub>4</sub>. *Corros Sci* 2006;48:1075–92. <https://doi.org/10.1016/j.corsci.2005.05.002>.
- [49] Li H, Yu H, Zhou T, Yin B, Yin S, Zhang Y. Effect of Sn on the corrosion behavior of sea-water corrosion-resisting steel. *Mater Des* 2015;84:1–9. <https://doi.org/10.1016/j.matdes.2015.06.121>.
- [50] Iwai Y, Yamanishi T. Thermal stability of ion-exchange Nafion N117CS membranes. *Polym Degrad Stab* 2009;94:679–87. <https://doi.org/10.1016/j.polymdegradstab.2008.12.020>.
- [51] Nørgaard CF, Nielsen UG, Skou EM. Preparation of Nafion 117™-SnO<sub>2</sub> composite membranes using an ion-exchange method. *Solid State Ionics* 2012;213:76–82. <https://doi.org/10.1016/J.SSI.2011.10.014>.
- [52] Taghizadeh MT, Vatanparast M. Preparation and evaluation of Nafion/SnO<sub>2</sub> nanocomposite for improving the chemical durability of proton exchange membranes in fuel cells. *RSC Adv* 2016;6. <https://doi.org/10.1039/c6ra07849d>.
- [53] Poulsen MG, Larsen MJ, Andersen SM. Improved durability of proton exchange membrane fuel cells by introducing Sn (IV) oxide into electrodes using an ion exchange method. *J Power Sources* 2017;(343):174–82. <https://doi.org/10.1016/J.JPOWSOUR.2017.01.046>.
- [54] Wang K, Gasteinger HA, Markovic NM, Ross Jr PN. On the reaction pathway for methanol and carbon monoxide electrooxidation on Pt-Sn alloy versus Pt-Ru alloy surfaces. *Electrochim Acta* 1996;41:2587–93. [https://doi.org/10.1016/0013-4686\(96\)00079-5](https://doi.org/10.1016/0013-4686(96)00079-5).
- [55] Janssen MMP, Moolhuysen J. Platinum–tin catalysts for methanol fuel cells prepared by a novel immersion technique, by electrocodeposition and by alloying. *Electrochim Acta* 1976;21:861–8. [https://doi.org/10.1016/0013-4686\(76\)85058-X](https://doi.org/10.1016/0013-4686(76)85058-X).
- [56] Lee SJ, Mukerjee S, Ticianelli EA, McBreen J. Electrocatalysis of CO tolerance in hydrogen oxidation reaction in PEM fuel cells. *Electrochim Acta* 1999;44:3283–93. [https://doi.org/10.1016/S0013-4686\(99\)00052-3](https://doi.org/10.1016/S0013-4686(99)00052-3).
- [57] Hinds G, Brightman E. In situ mapping of electrode potential in a PEM fuel cell, vol. 17; 2012. <https://doi.org/10.1016/j.elecom.2012.01.007>.
- [58] Abdel Rehim SS, Sayyah SM, El Deeb MM. Corrosion of Sn in citric acid solution and the effect of some inorganic anions. *Mater Chem Phys* 2003;80:696–703. [https://doi.org/10.1016/S0254-0584\(03\)00128-7](https://doi.org/10.1016/S0254-0584(03)00128-7).
- [59] Takeno N. Atlas of Eh-pH diagrams: intercomparison of thermodynamic databases. National Institute of Advanced Industrial Science and Technology Research Center for Deep Geological Environments; 2005.
- [60] Materials FP. Freudenberg technical data sheet. online. 2014. <https://fuelcellcomponents.freudenberg-pm.com/products/gas-diffusion-layers>. [Accessed 21 July 2017].
- [61] Wang H, Sweikart MA, Turner JA. Stainless steel as bipolar plate material for polymer electrolyte membrane fuel cells. *J Power Sources* 2003;115:243–51. [https://doi.org/10.1016/S0378-7753\(03\)00023-5](https://doi.org/10.1016/S0378-7753(03)00023-5).
- [62] Orsi A, Kongstein OE, Hamilton PJ, Oedegaard A, Svernum IH, Cooke K. An investigation of the typical corrosion parameters used to test polymer electrolyte fuel cell bipolar plate coatings, with titanium nitride coated stainless steel as a case study. *J Power Sources* 2015;285. <https://doi.org/10.1016/j.jpowsour.2015.03.111>.
- [63] Housecroft CE, Sharpe AG. *Inorganic chemistry*. 2012. [https://doi.org/10.1016/0022-2860\(73\)85197-X](https://doi.org/10.1016/0022-2860(73)85197-X).
- [64] Ochoa F, Williams J, Chawla N. Effects of cooling rate on the microstructure and tensile behavior of a Sn-3.5 wt% Ag solder. *J Electron Mater* 2003;32:1414–20.
- [65] Griffiths DJ, Inglefield C. Introduction to electrodynamic, vol. 73; 2005. <https://doi.org/10.1119/1.4766311>.

ISBN 978-82-471-9726-4 (printed ver.)  
ISBN 978-82-471-9984-8 (electronic ver.)  
ISSN 1503-8181 (printed ver.)  
ISSN 2703-8084 (online ver.)



**NTNU**

Norwegian University of  
Science and Technology